INVESTIGATING CRUSTAL STRUCTURE IN WESTERN WASHINGTON AND IN THE ROCKY MOUNTAINS: IMPLICATIONS FOR SEISMIC HAZARDS AND CRUSTAL GROWTH

CATHERINE M. SNELSON

Department of Geological Sciences

APPROVED:

Kate C. Miller, Co-Chair

G. Randy Keller, Co-Chair

Elizabeth Y. Anthony

Christopher L. Andronicos

Benjamin C. Flores

Thomas C. Brocher, U.S.G.S.

Charles H. Ambler
Dean of Graduate Studies

This dissertation is dedicated to my grandparents, Lucille and George Snelson. I wish they were here to see this accomplishment finally realized. To my mom, Mary Bishop, for raising me to be an independent woman. To my dad and mom, David and Dee Snelson, for their pride in me. The words do not describe how much joy that has given me. Thanks.

INVESTIGATING CRUSTAL STRUCTURE IN WESTERN WASHINGTON AND IN THE ROCKY MOUNTAINS: IMPLICATIONS FOR SEISMIC HAZARDS AND CRUSTAL GROWTH

by

CATHERINE M. SNELSON, B. S., M.S.

DISSERTATION

Presented to the Faculty of the Graduate School of

The University of Texas at El Paso

in Partial Fulfillment

of the Requirements

for the Degree of

DOCTOR OF PHILOSOPHY

Department of Geological Sciences

UNIVERSITY OF TEXAS AT EL PASO

December, 2001

ACKNOWLEDGEMENTS

I wish to thank all of those people that have helped me so much in making this dissertation happen. First, I wish to thank my co-chairs Kate C. Miller and G. Randy Keller for their guidance and expertise throughout this experience. Without them I would not have found the confidence to go off and find my way. Also thanks to the rest of my committee: Libby Anthony, Chris Andronicos, Ben Flores, and Tom Brocher for their guidance and expertise. Thanks to Carlos Montana, without you I would have never gotten to this point. Thanks to Steve Harder for the many opportunities for field work. Thanks to Ra'ed Al-Douri and John Kennedy for making the world of GIS more bearable.

Thanks to the many people involved in the Dry and Kingdome SHIPS projects. Thanks to the PIs, Kate Miller, Tom Brocher, Tom Pratt, and Anne Trehu for believing I could complete this work. Thanks to Tom Burdette, U.S. Geological Survey for organizing and permitting. Cindy Bartlett, Brian Laird, Craig Tiballi, Angie Williams, Elizabeth Barnett, Bob Norris, and Tom Yelin surveyed the profiles. Karen Meagher and Nancy Sandoval coordinated field logistics. Geoff Clitheroe, Karen Meagher, Tom Van Wagoner, Nicolas Weaver, and Brett Williams distributed leaflets to the public for Kingdome SHIPS. Volunteers included Jason Barnes, Elizabeth Barnett, Katherine Brown, Jonathon Cox, Don Farrell, Janice Murphey, Rob Nicholson, Bob Norris, Kaye Shedlock, Ray Sliter, Angie Williams, Tom Yelin, and Donna Criley, all of the U. S. Geological Survey. From UTEP, Brett Hiett and Kimberly Schramm. From Boise State University, Bill Clement and Lee Liberty. From OSU, Cindy Bartlett, Kyle Kinports, and J. D. Ousley. From the University of Washington, Gerick Bergsma, Peter Burkholder, Abdul Cherkaoui, Mary Edmunds, Amy Lindemuth, Arianne Lisi, Tony Qamar, Kari Sauers, Peter Shaw, Clare

Steedman, Eric Sommargren, Koji Tanno, George Thomas, Kathy Troost, Tom Van Wagoner, Wil Wilcock, Rob Willis, Bill Steele, and Steve Malone. From the local region, Nakib Ahmed, Milton Benz, Laurel Clark, David Cornwell, Mark Conway, Adekemi Liped, Gini Gandhok, Jeff Shragge, Kevin Smith, Robin Smith, Kristoffe Walker, Mary Bare, Tom Bush, Terry Butler, John Cass, Greg Civay, Lara Cramer, Dustin Cysensky, Greg Geehan, David Hay, Tom Hay, Lynn Hulrgrein, Tom Ise, Paul Manganelli, Pnina Miller, Debbie Milne, Jan Ramsey, Pat Reed, Colin Turnbull, Hans Van Wandelen, Jim Wilhite, and Amy Winchester. Thanks to the UTEP Instrument center for the use of the TEXANS. Steve Harder, Galen Kaip, and Steve Azevedo prepared the TEXANS. Thanks also to the IRIS/PASSCAL Instrument center for use of the RefTeks. Marcos Alvarez, Mike Fort, Ian Matchum, and William Zamora prepared the RefTeks. Thanks to the Canadian Geological Survey for the use of the PRS instruments. Isa Asudeh, John Meloche, and Marcel Gervay prepared the PRSs. Thanks to the U. S. Geological Survey for the use of the SGRs. Don Farell and Cathy Snelson prepared the SGRs. Harley Benz, Tom Burdette, Ed Criley, David Croker, Steve Harder, Ron Kaderabek, David Reneau, and John Van Schaack detonated the shots.

Additional thanks goes to the Washington State Departments of Forestry and Park and Recreation, Olympic National Forest, the Bureau of Land Management, Kitsap and King Counties, the Cities of Bainbridge Island, Seattle, and Redmond for permission to access land. Also Weyerhaeuser Corp., International Paper Co., and numerous smaller property owners for access to their land. Thanks to NOAA-PMEL for the use of their vessel and facilities for the use of the U. S. Geological Survey OBSs. Rodger Bartlett and Don Mast provided additional logistical support from NOAA-PMEL. Captain Speer, Uri ten Brink, Gregory Miller, Michael Taylor, Alvin Buchholtz for their help with the U. S. Geological Survey OBSs. Video of the Kingdome implosion was provided by Glenn Farley and Channel 5 TV. This work in western Washington was supported by U.S. Geological Survey NEHRP contract 99HQGR0054.

I would like to thank everyone who helped make CD-RoM seismic refraction experiment happen. Thanks to the CD-RoM Working group for making this project come to life. Thanks to Randy Keller, Kate Miller, and Claus Prodehl for their guidance with this aspect of my dissertation. There were people from several universities that participated in the experiment. Volunteers from UTEP where Alberto Barud, Hairani Blanchard, Melyssa Boswell, Raquel Diaz, Miguel Dominguez, Greg Dumond, Tefera Eshete, Lizbet Guijarro, Steve Harder, Brett Hiett, Jimmy Hincapie, Betsy Julian, Galen Kaip, Randy Keller, Mike Mansfield, Matt Miles, Kate Miller, Pete Muela, Al Munoz, Arlene Perez, Kim Schramm, Cathy Snelson, Frank Tate, and Yvette Villegas. Volunteers from Rice University where Aron Azaria, Diana Dana, Kara Hackwith, and Alan Levander. From Leicester University, UK were Duncan Ansell, Lee Bailey, Helen Basford, and Chris Purcell. Volunteers from the University of Karlsruhe were Alexander Gerst, Alexander Goertz, Franz Hauser, Philipp Heidinger, Sonja Hofmann, Werner and Ange Kaminski, Uli Micksch, Claus and Sieglinde Prodehl, Hanna-Maria Rumpel, Baerbel Traub, and Andreas Wuestefeld. Also there was Colin Shaw (University of New Mexico), Dan Pope (University of Washington), Todd Shearer (Whitman College), Matt Averill (University of Montana), and Gerrit Bulman (Brown University). Thanks to the UTEP instrument center for the use of the TEXANS and personnel during the experiment. Thanks to the IRIS/PASSCAL Instrument center for the use of the RefTeks. Marcos Alvarez, Steve Azevedo,

Mike Fort, Jim Fowler, Ian Matchum, Mary Templeton, and Tim Parker prepared the Refteks. Thanks to the survey crew, Kim Schramm, Hanna-Maria Rumpel, and Alex Goerst. Thanks to Steve Harder, Randy Keller, Alan Levander, Ed Criley, Nick Boyd, BLM, Microgeophysics, Buckley Powder, Crass Drilling, and Youngs Drilling. Additional thanks goes to the land owners who allowed access to their property, those include Hage & Webb Land and Cattle (Carol Webb), Fallon Ranch (Mr. Wilson), Pettigrew Ranch, Carlos Pena, Vermejo Park Ranch (David Vacker), Tercio Ranch (Peter Trexler), Fred Harte, Stella Wheatley, the Brand's Ranch (Jody & Janie Brands), the Boettcher Ranch (Jerry & Lance Towle), Kim & Felix Najera, and Robert Wrigley. Funding was provided by the National Science Foundation - Continental Dynamics Program (EAR-9614269) and Deutsche Forschungsgemeinschaft (DFG).

Thanks to my family, Mary Bishop, Dave and Dee Snelson, Dawn, Todd, Brandon, and Jacob Lengel, Nicole Netsen, Deidre and Bill Plavsic, and Jason Snelson for their moral support. Thanks to my friends for whom I would not have survived without the laughter. I apologize in advance if I leave anyone out. In particular, thanks to the “boys”, Oscar Quezada, Brett Hiett, and Tefera Eshete. Thanks to Kelly Latter for the ashes on the steps, proper lab instruction, and too much more. Thanks to Imana Ekal for a constant source of support, a true friend. Thanks to the Hayward bunch, Gwyneth Terry, Andrew Passerelli, Steve Newton, Nancy Fegan, Phil Garbutt, and many more whom without your support I would not have made it this far. Thanks to Leandro Trevino another Hayward buddy whom I kidnapped from the Bay Area. Thanks to Paul Wilson, Pierre-Andre Depret, Wesley Brown, Christina Rodriguez, and Jimmy Hincapie for the laughs. Thanks to Alfredo Ruiz for touching my heart. Thanks to John Comstock for a continued boost to

my ego. Thanks to Ryan Lieske for the good times we had. Thanks to Vicki Harder for the support and generous use of her office space to help me finish. Thanks to Kerry Wilrich, a true inspiration for life, I miss you terribly.

ABSTRACT

This dissertation consists of two seismic studies, one in western Washington State and one in the Rocky Mountains. The study in western Washington State is one component of the SHIPS (Seismic Hazards Investigations of Puget Sound) experiments, a continuing effort to define Cenozoic basin and fault geometry beneath the densely populated Puget Lowland. In September 1999, the U. S. Geological Survey and a number of university collaborators collected the “Dry” SHIPS seismic profile across the Seattle basin of western Washington State. The objectives of the “Dry” SHIPS study were to define the geometry of the Seattle basin in an E-W direction and to determine the structure of the eastern and western boundaries of the basin. In addition, the experiment was designed to test the hypothesis that N-S trending faults lie beneath Puget Sound or the adjacent Lowland. One of these faults may form the eastern boundary of the Siletz terrane. The “Dry” SHIPS data are characterized by travel time advances associated with the Siletz terrane to the west and the Cascades to the east and by delays of as much as 2 s in the Seattle basin.

P-wave 3-D tomographic results show that the basin is about 70 km wide and contains sedimentary strata with velocities increasing gradually from 1.8 - 4.5 km/s. The contact with underlying basement rocks is characterized by a rapid increase in velocity from 4.5 to 5.0 km/s. At its center, the basin is 6 - 7 km deep along this profile. This result is consistent with results from a N-S trending reflection line collected in 1998 during the “Wet” SHIPS phase of the project that is tied to well control. The symmetry of the Seattle basin is consistent with thrust loading as the major contributor to the formation of the basin. The lower velocities within the upper part of the basement found east of the Puget Sound may be indicative of pre-Tertiary basement rocks of the Cascades. This

change is probably an expression of the Coast Range Boundary fault, which has previously been interpreted from gravity and magnetic data. Density modeling tied to the velocity model shows that the Olympic accretionary wedge is indistinguishable from surrounding rocks below a depth of about 20 km. The contact between the Siletz and Pre-Tertiary basement rocks is a subtle contact as inferred from the velocity and gravity models.

The study in the Rocky Mountains is one component of the Continental Dynamics - Rocky Mountains Project (CD-RoM '99), a collaborative interdisciplinary study involving 14 American universities and the University of Karlsruhe, Germany that focuses on Precambrian features and their effects on Phanerozoic deformation. One of the major field efforts in the CD-RoM project took place during August, 1999. The University of Texas at El Paso and the University of Karlsruhe, with the assistance of several other institutions, collected data along a ~ 950 km long seismic refraction/wide-angle reflection profile extending from Fort Sumner, New Mexico to the Gas Hills, Wyoming. Station spacing was nominally 800 m using ~ 600 instruments during two deployments. Eleven shots were fired ranging in size from 167.2 - 4540.9 kg and were nominally spaced at ~ 100 km intervals along the profile. The profile crosses major structural features of the continent including the Jemez lineament, the Colorado mineral belt, and the Cheyenne belt (a prominent Proterozoic suture).

Velocity modeling, employing several techniques, indicates that crustal thicknesses ranges from ~ 45 to 55 km in New Mexico and Colorado. In northern Colorado, the crust begins to thin from ~ 50 and reaches ~ 40 km in Wyoming, north of the Cheyenne belt. A mid-crustal interface is very prominent within the data and can be thought of as the Conrad discontinuity. This interface falls at depths of about 25 to 30 km and is a discontinuity below which velocities increase to about 6.8 km/s. A high-velocity lowermost crustal layer with a thickness ranging from 5 to 10 km is evident in the Southern Rocky Mountains - Great Plains (SRM-GP) portion of the model. The velocity of this layer ranges from 7.0 to 7.4 km/s, a value that is consistent with a composition of mafic garnet granulite. One interpretation of this high-velocity lower crustal layer is that it originally formed during assembly of the Proterozoic terranes. Magmatic underplating at 1.4 Ga may have increased the thickness of this layer beneath the SRM-GP. This is not to say that the depth to the Moho has not been locally modified during Phanerozoic events, but that major modification took place during the Precambrian.

TABLE OF CONTENTS

LIST OF FIGURES

CHAPTER 1: INTRODUCTION

This dissertation covers analysis of seismic and gravity data from two regions in the western United States. The first study is located in western Washington State and the second study is located in the southern Rocky Mountains. Data from these regions were analyzed using tomographic inversion techniques on seismic refraction data, forward gravity modeling, and for western Washington State reflection seismic data processing.

The study in western Washington State is one component of the SHIPS (Seismic Hazards Investigations of Puget Sound) experiments, a continuing effort to define Cenozoic basin and fault geometry beneath the densely populated Puget Lowland. In September 1999, the USGS and university collaborators collected the “Dry” SHIPS (Seismic Hazards Investigations of Puget Sound) seismic profile across the Seattle basin of western Washington State. In March 2000, this group collected additional seismic data in the city of Seattle using the implosion of the Kingdome sports arena as a seismic source (“Kingdome” SHIPS). The main “Dry” SHIPS experiment consisted of a ~ 112-km-long east-west seismic profile that extended from the Olympic Peninsula, through Seattle to the foothills of the Cascades. Station spacing along the line was nominally 100 m except at the far ends where spacing was nominally 200 m. During the experiment 38 shots ranging in size from 11.4 to 1136.4 kg were detonated at ~ 4 km intervals along the profile, including several shots within the city limits of Seattle.

The objectives of the “Dry” SHIPS study were to define the geometry of the Seattle basin in an E-W direction and to determine the structure of the eastern and western boundaries of the basin. In addition, the experiment was designed to test the hypothesis that N-S trending faults lie beneath Puget Sound or the adjacent Lowland. One of these faults may form the eastern boundary of the Siletz terrane. The main objective of “Kingdome” SHIPS was to look at the Seattle fault and shallow strata beneath Seattle to estimate site response in Seattle.

Chapter 2 discusses processing and analysis of the “Dry” SHIPS refraction data. A 3-D tomographic code (Hole, 1992) that inverts P-wave first arrivals from the seismic data to produce a velocity field was used. In addition, forward density modeling was conducted in order to test possible geometries of rocks at depth. Both these techniques were then used to define basin and fault geometry beneath the populated Puget Lowland.

Initial analysis of the S-wave component of the SHIPS dataset using the tomographic technique is also discussed. The S-waves are much more difficult to identify in the data, especially in an urban area, due to the large amount of cultural noise. Eventually the P and S-wave velocity field can be used together to obtain the Vp/Vs ratio and thus more detailed rock property information along the profile. Since S-wave cause the most damage during an earthquake, the results from the S-wave model furthers the effort to assess the seismic hazards for the Seattle basin.

Finally, Chapter 2 discusses the use of the seismic dataset to create a low-fold reflection image along the profile. The station and shot point spacing, by design, were small enough to make this possible. The stacked record will provide additional information on the mid- to lower-crust that the tomographic inversion techniques were not able to elucidate.

The second main study in this dissertation focuses on a seismic refraction profile along the Rocky Mountains and is presented in Chapter 3. The Continental Dynamics - Rocky Mountains Project (CD-RoM '99) is a collaborative interdisciplinary study involving ~14 American universities and the University of Karlsruhe, Germany and focuses on Precambrian features and their effects on Phanerozoic deformation. One of the major geophysical field efforts of the CD-RoM project took place during August, 1999. The University of Texas at El Paso and the University of Karlsruhe, with the assistance of several other institutions, collected data along a ~ 950 km long seismic refraction/wide-angle reflection profile from central New Mexico to central Wyoming. The profile crossed such geologic features as the Jemez lineament, the Colorado mineral belt, and the Cheyenne belt, a prominent Proterozoic suture.

In Chapter 3, the same technique described in the western Washington study is used to produce a velocity model. P-wave first arrivals were analyzed as well as the wide-angle reflections. This inversion provided a velocity field which then could be described in terms of gross structure in the subsurface. Forward density modeling was conducted in conjunction with the velocity modeling to provide an additional constraint for the interpretation.

CHAPTER 2: TOMOGRAPHIC RESULTS, LOW-FOLD STACK, AND DENSITY MODELING ALONG THE “DRY” AND “KINGDOME” SHIPS PROFILES

Introduction

The Pacific Northwest of North America has evolved from a series of tectonic events extending from Cambrian to recent time (e.g., Monger and Nokleberg, 1996). This tectonic history includes Mesozoic accretionary events, inception of a Tertiary subduction zone with associated volcanism, changes in plate motions leading to the formation and accretion of the Siletz terrane, and uplift of the accretionary wedge in late Tertiary time (e.g., Monger and Nokleberg, 1996). The current tectonic regime is an active subduction zone where the Juan de Fuca plate is subducting beneath the North American plate (Figure 1) (e.g., Riddihough, 1984). Because convergence is oblique, both dextral strike-slip faults and east-west trending thrust faults have formed in the fore-arc basin (Puget Lowland - Willamette Valley) (Figure 1) (e.g., Johnson et al., 1996; Pratt et al., 1997). Faulting in the Puget Lowland - Willamette Valley has been accompanied by formation of a series of deep, fault-bounded basins (Finn, 1990).

In September of 1999, the SHIPS (Seismic Hazards Investigations in Puget Sound) working group acquired seismic data (“Dry” SHIPS) along a high resolution seismic profile that started in the Olympic Peninsula and continued through the city of Seattle into the foothills of the Cascades (Figure 2). In March, 2000 the SHIPS working group acquired additional seismic data (Kingdome SHIPS) centered on the Kingdome sports arena implosion in downtown Seattle (Figure 3). These projects are components of a series of studies designed to assess the seismic hazard in the Seattle region (Brocher et al., 2000). The city of Seattle overlies a deep basin which may focus energy and enhance ground shaking

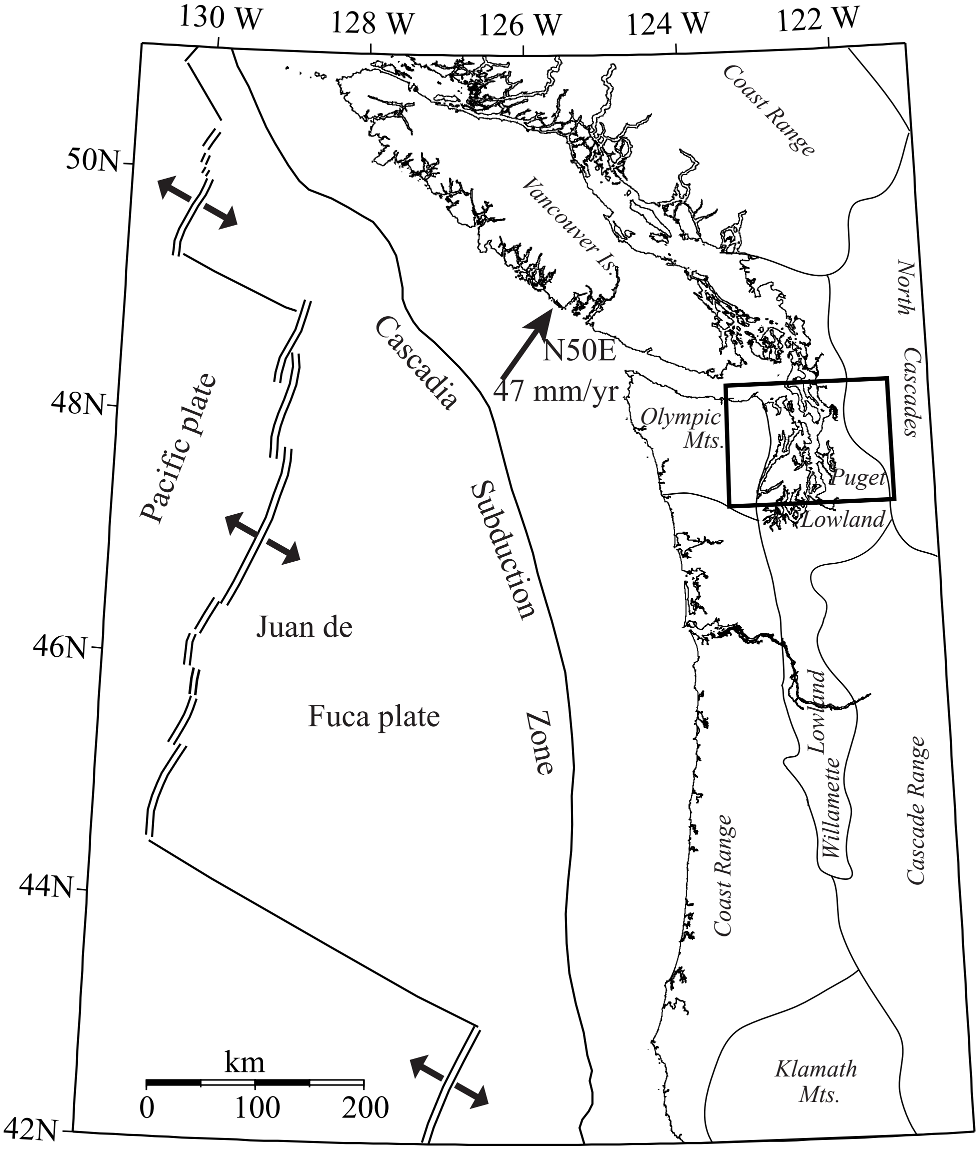

Figure 1. Basemap showing current tectonic plates, rate of motion, and physiotectonic provinces (after Ludwin et al., 1991). The study area is shown by the black box.

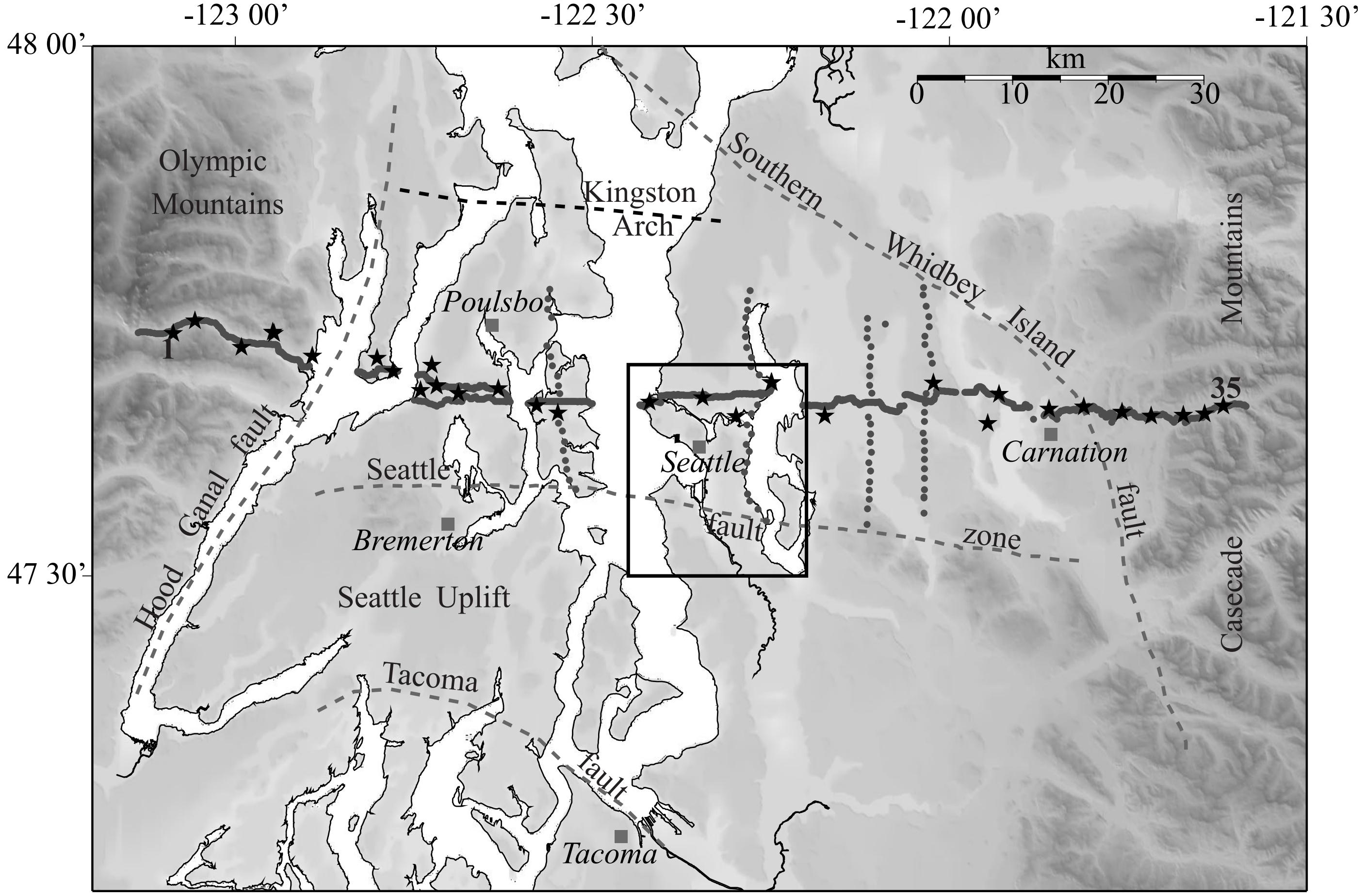

Figure 2. Topographic basemap of study area. Darker shades of gray represent higher elevations. “Dry” SHIPS profile is indicated by the gray dots (receiver stations) and stars (shotpoints). Kingdome SHIPS is represented by the square. Major faults are indicated by the dashed gray lines. Cities are in italics.

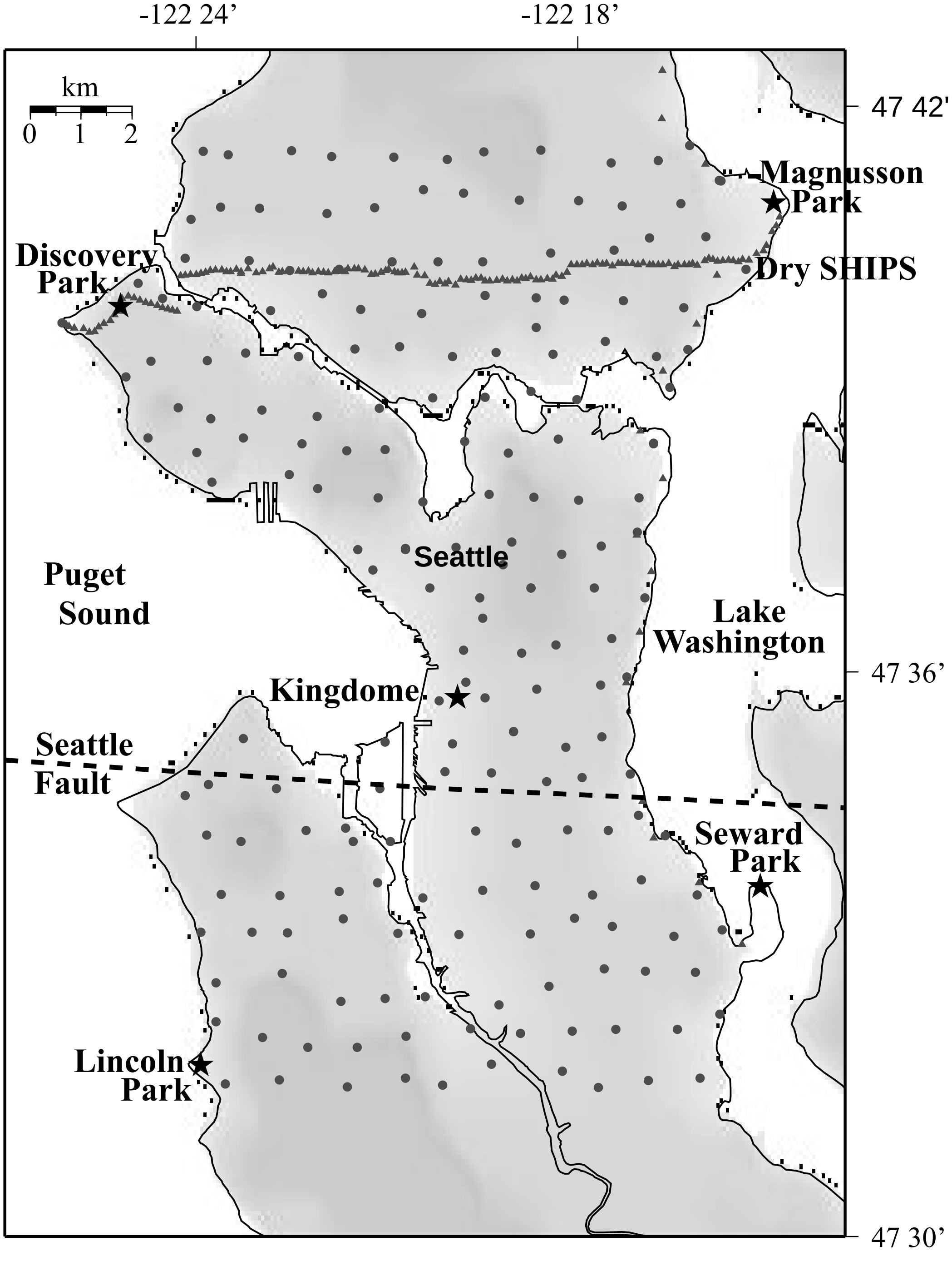

Figure 3. Topographic basemap of the Kingdome SHIPS study area. Kingdome stations are indicated by the gray dots and shot points are the stars. The black triangles are "Dry" SHIPS stations.

when an earthquake occurs (e.g., Frankel et al., 1999; Pratt et al., in review). The “Dry” and “Kingdome” SHIPS results provide data that help more fully determine the seismic hazard for the Seattle region.

Geologic Background

The building of the Pacific Northwest include a series of accretionary events; accretion leading to the docking of several terranes including the Eocene Siletz terrane, the inception of subduction leading to the Cascadia volcanic arc, the uplift of the accretionary wedge, and continued convergence of the Juan de Fuca plate with North America (Figure 4) (e.g., Snavely et al., 1968; Simpson and Cox, 1977; Tabor and Cady, 1978; Monger and Nokleberg, 1996).

Pre-Tertiary

The pre-Tertiary geologic history is dominated by two accretionary events during Jurassic and Cretaceous time (e.g., Atwater, 1989; Monger and Nokleberg, 1996). The first accretionary event occurred during sinistral convergence between the Farallon plate and North America, which ended by Early Cretaceous time (e.g., Atwater, 1989; Engebretsen et al., 1985; Monger and Nokleberg, 1996). The second event occurred during dextral plate convergence between the Kula or Farallon plate and North America at mid- to Late Cretaceous time. These terranes became part of the North American plate by early Tertiary time (ca. 60 Ma) (e.g., Monger and Nokleberg, 1996; Irving et al., 1979).

Tertiary to Recent

The main tectonic events from Tertiary to recent time include increased obliquity at the plate boundary by early Tertiary time (~ 55 Ma), docking of the Siletz terrane by late

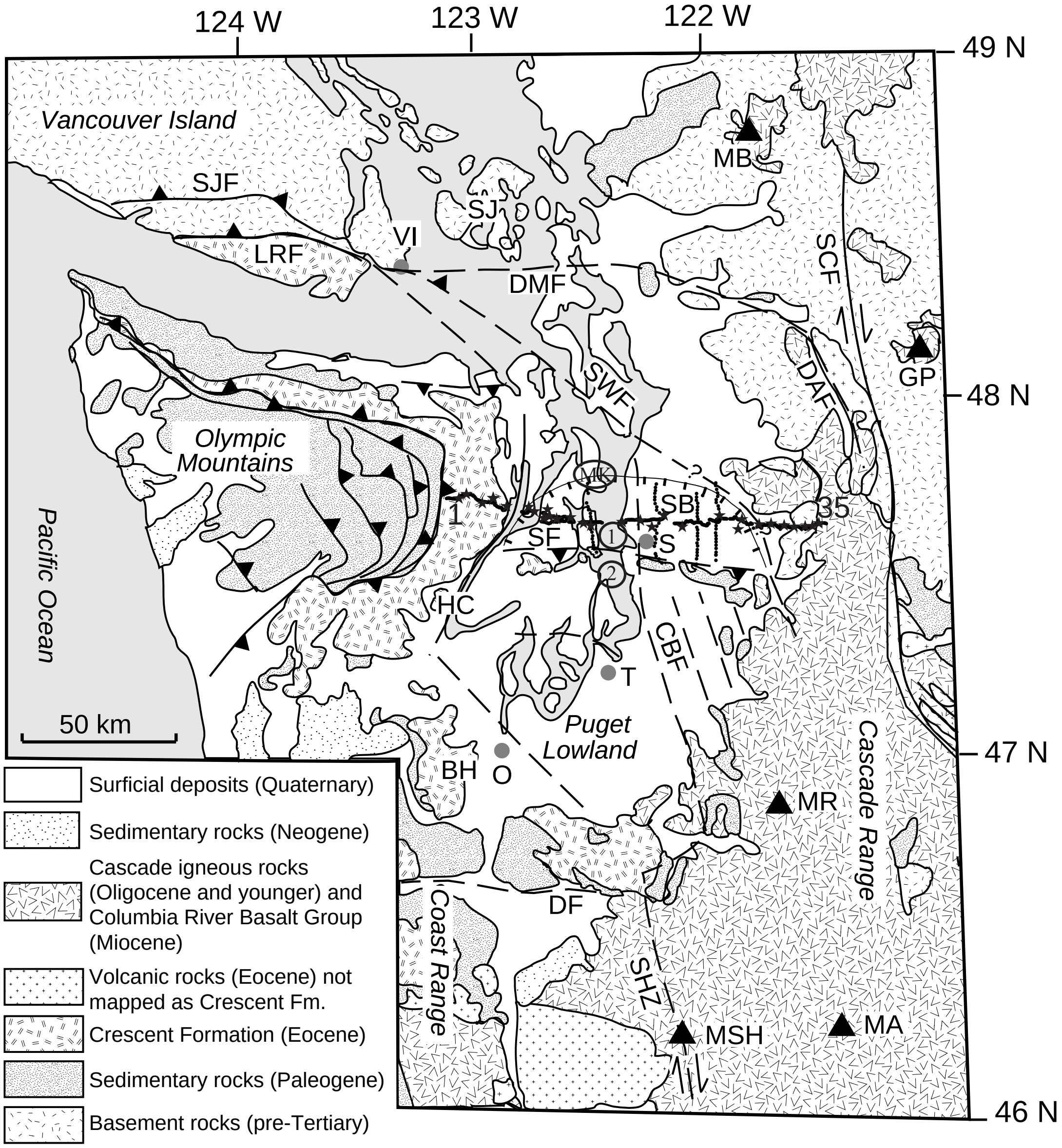

Figure 4. Generalized geologic map of western Washington state (modified from Johnson et al., 1999). Seismic stations for “Dry” SHIPS are the small black dots and shot points are the small stars. Abbreviations for cities: S - Seattle; T - Tacoma; O - Olympia; VI - Victoria. Circled 1, 2, and MK are stratigraphic column locations. Abbreviations for geologic features (fault - heavy lines; volcanoes - triangles): BH - Black Hills; CBF - Coast Range Boundary fault; DAF - Darrington fault; DF - Doty fault; DMF - Devils Mountain fault; GP - Glacier Peak; HC - Hood Canal fault; LRF - Leech River fault; MA - Mt. Adams; MB - Mt. Baker; MR - Mt. Rainer; MSH - Mt. St. Helens; SB - Seattle Basin; SCF - Straight Creek fault; SF - Seattle fault; SHZ - Saint Helens zone; SJ - San Juan Islands; SJF - San Juan fault; SWF - Southern Whidbey Island fault.

Eocene (~ 40 Ma), formation of the Olympic Mountains and subsequent uplift, evolution of the Cascade range, continued formation of the forearc basin, and rotation of the southwestern Washington (e.g., Atwater, 1989; Burchfiel et el., 1992; Monger and Nokleberg, 1996).

Siletz Terrane

This history of the Siletz terrane here is summarized from Duncan, 1982; Wells et al., 1984; Clowes et al., 1987; Beck, 1989; Babcock et al., 1992. The Siletz terrane is composed of Paleocene to mid-Eocene age basalts that are mainly pillows and massive flows (Figure 4). Two models exist for the formation of the Siletz terrane (Figure 5). The first proposes that the Siletz terrane is either hot-spot generated seamount chains or anomalously thick oceanic crust that entered the subduction zone in early Eocene time and was then accreted to North America.

The second model involves oblique rifting of a marginal basin within the North American plate where the basalts were formed. This geometry created a transform system whereby a volcanic arc was formed seaward of the continent. The arc was then transported northward along the transform fault, leaving behind a clean edge along the continental margin. This migration would have left little evidence of the previous subduction zone. This model also explains the continent-derived sediments found within the Eocene basalts (e.g., Wells et al., 1984; Clowes et al., 1987). Evidence for transcurrent faulting and continent truncations during the early Tertiary is consistent with the marginal basin model (e.g., Johnson, 1984; Clowes et al., 1987).

Cascade Range

The history of the Cascade Range is here summarized from Armstrong (1978).

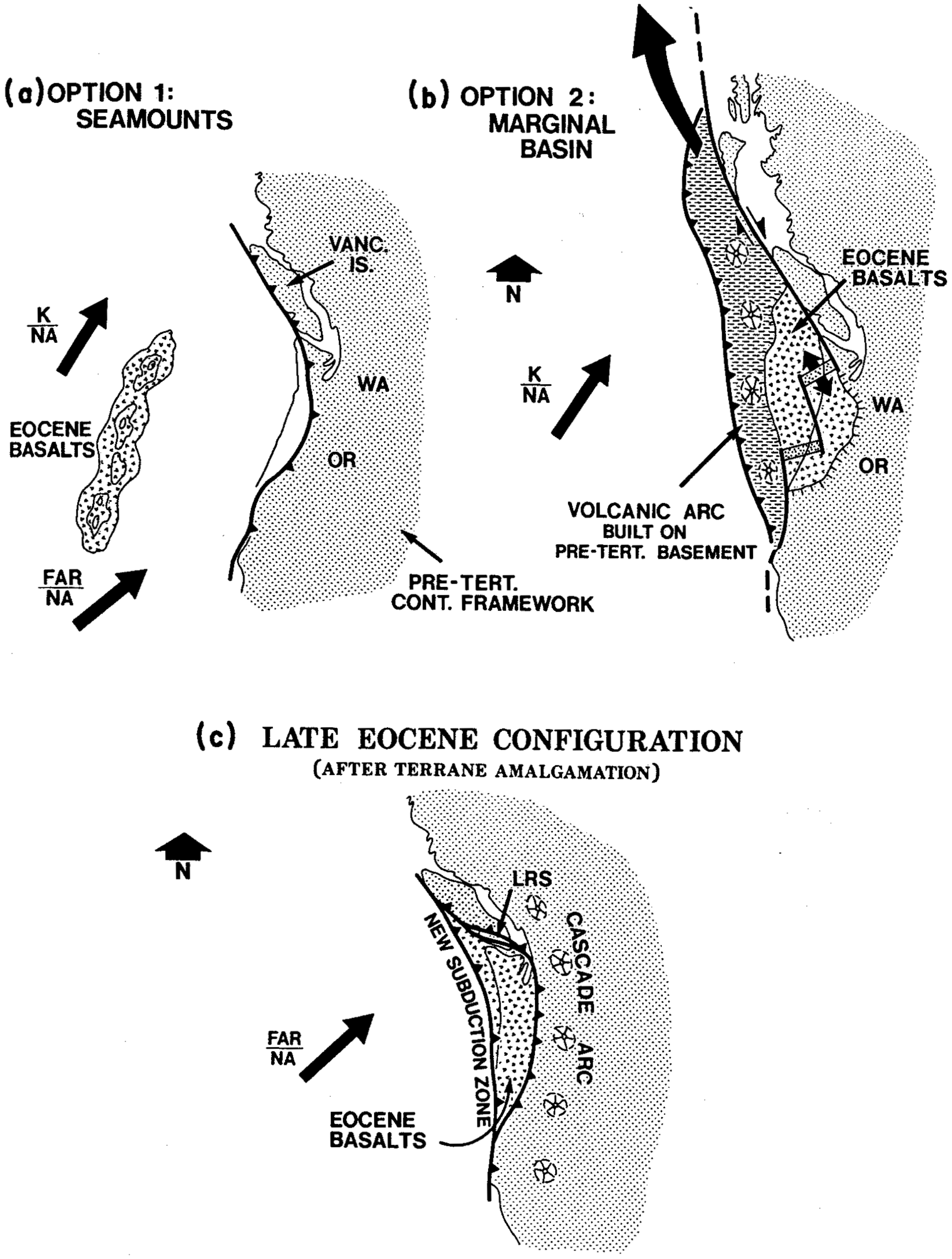

Figure 5. Two possible interpretations of the docking of the Siletz terrane. Arrows indicate the relative plate motions between the Kula (K) and North American (NA) plates and the Farallon (FAR) plates and North American (NA) plates (after Wells et al., 1984). A). Option 1 shows Siletz as a seamount chain which later collide with the margin. B). Option 2 shows Siletz forming in a marginal basin similar to the Andaman Sea (Curray et al., 1979). Siletz is left behind when oblique rifting occurs, causing the forearc to be translated northward. C). Regardless, by late Eocene, a new subduction zone had formed west of the Siletz terrane (after Wells et al., 1984; Clowes et al., 1987).

From Tertiary to recent time the Cascade Range were formed in response to the Cascadia subduction zone (e.g., Guffanti and Weaver, 1988). The Cascade Range was at the western edge of the continental margin in the pre-Tertiary (~ 55 Ma). Volcanism in the region was persistent from ~ 55 to 43 m.y. and then went through a time of magmatic quiescence. During this time, the Cascade Range shifted eastward in response to the accretion of the Siletz terrane. At about 36 Ma, volcanism became localized to what is the present-day Cascade volcanic arc. During Miocene time (~ 17 Ma), the Columbia flood basalts were deposited in a short span of time. This episode is coincident with the continued curvature of the plate boundary. The building of the shield volcanoes continued from ~ 10 Ma to present.

Olympic Mountains

The Cascadia accretionary wedge formed outboard of the Siletz terrane and has been subsequently uplifted in some areas with the Siletz terrane acting as a backstop for accretion of the accretionary wedge (Figure 6) (e.g., Tabor and Cady, 1978; Brandon and Calderwood, 1990; Brandon and Vance, 1992; Parsons et al., 1999). The origin of the present-day horseshoe shape of the Siletz terrane is something of an enigma (e.g., Beck and Engebretson, 1982). The horseshoe shape has been proposed to be either a primary or secondary feature (e.g., Beck and Engebretson, 1982). If the horseshoe is a primary feature then sediments were stacked up from off-scraping of oceanic debris during subduction against a curved buttress which led to the bending of the sediments (e.g., Tabor and Cady, 1978; Beck and Engebretson, 1982). If the horseshoe is a secondary feature or an orocline, then the bending would have occurred about a vertical axis (e.g., Tabor and Cady, 1978). As subduction continued, the northeastward push of the off-scraped debris

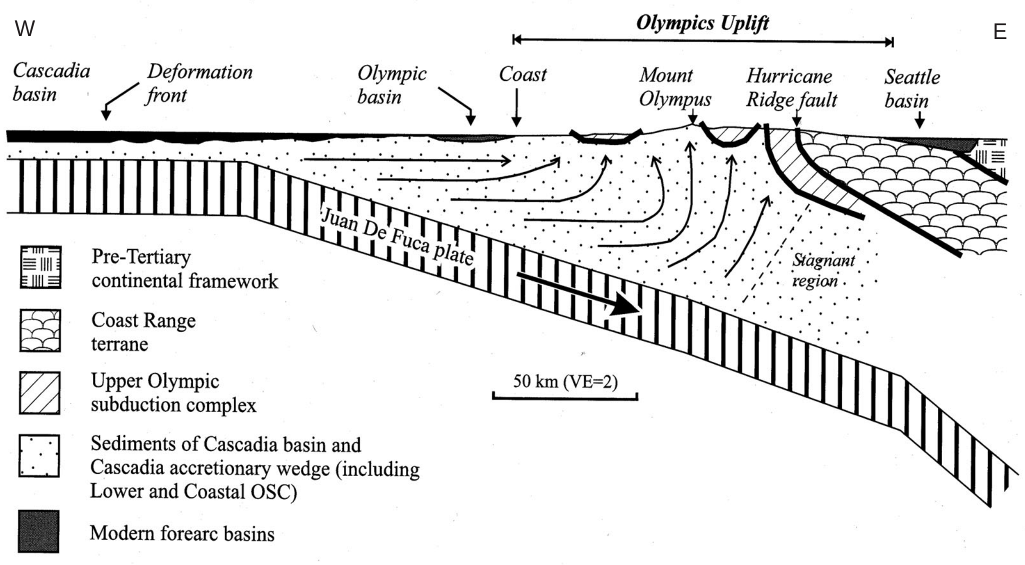

Figure 6. Schematic cross section west to east from the Olympic Mountains to the Seattle basin. Shows the relative position of the Siletz and Olympic accretionary rocks (after Brandon et al., 1998).

would reach the crystalline rocks of the North Cascades and Vancouver Island setting up the curved shape for the material to be deposited against (e.g., Beck and Engebretson, 1982). The change in direction of the Farallon plate at ~ 40 Ma to the northeast relative to the North American plate supports a mechanism for oroclinal bending, unfortunately the paleomagnetic data has not been able to resolve this issue (e.g., Beck and Engebretson, 1982). Alternatively, Parsons et al. (1999) speculates that the N-S compression is the primary cause for the bending of the Siletz terrane into the horseshoe shape and subsequently magnifies the uplift of the accretionary wedge.

The amount of uplift in the Olympic Mountains is more extreme then other subduction complexes (e.g., Tabor and Cady, 1978; Brandon and Calderwood, 1990; Brandon and Vance, 1992; Parsons et al., 1999). The Olympic Mountains are comprised of part of the accretionary wedge of the current subduction zone. Additional curvature of the plate boundary at ~ 15 Ma is thought to have caused an arch beneath the Olympic Mountains (Figure 7) (e.g., Weaver and Baker, 1988; Brandon and Calderwood, 1990; Parsons et al., 1999). As the plate margin became more oblique, the Olympic Mountains were uplifted (e.g., Wells et al., 1984; Weaver and Baker, 1988; Brandon and Calderwood, 1990). The concave nature of the arch has magnified the amount of uplift that the Olympic Mountains has experienced (e.g., Brandon and Calderwood, 1990; Parsons et al., 1999).

> 15 Ma

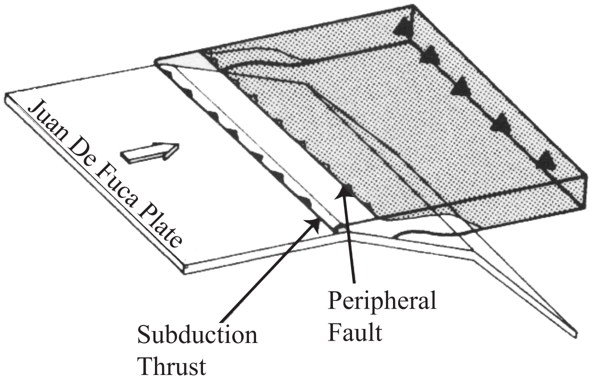

15 Ma To Present

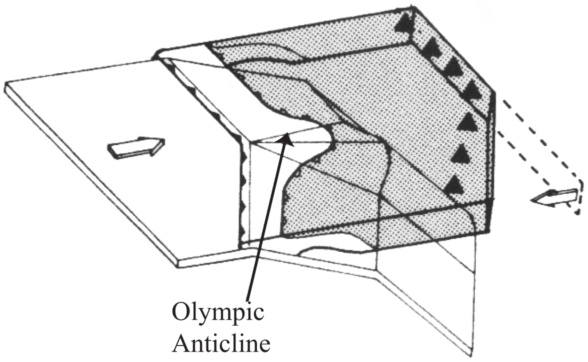

Figure 7. Schematic drawing of the slab arch model (after Brandon and Calderwood, 1990).

Puget Lowland

The Puget Lowland is a series of basins and uplifts in the forearc of the Cascadia subduction zone (e.g., Finn, 1990; Brocher et al., 2001). A major feature within the Puget Lowland is the Seattle fault zone. It is made up of several east-west trending segments and bounds the Seattle basin to the south (e.g., Johnson et al., 1994; Pratt et al., 1997; Wells et al., 1998). The Seattle fault zone is thought to have originated as a restraining bend in a transfer zone that was created by the increased obliquity of the Cascadia subduction zone (e.g., Johnson et al., 1994; Wells et al., 1998). This transfer zone allow right-lateral strike-slip fault motion from south to north (e.g., Johnson et al., 1994; Pratt et al., 1997; Wells et al., 1998). As a result, the Seattle basin was produced by flexural loading (e.g., Johnson et al., 1994; Pratt et al., 1997). Motion across the Seattle fault zone can be directly related to the asymmetry of the basin in the north-south direction (e.g., Johnson et al., 1994; Pratt et al., 1997; Wells et al., 1998; ten Brink, in review). The Seattle basin is deepest nearest the fault and thins dramatically at its northern edge (e.g., Johnson et al., 1994; Pratt et al., 1997; ten Brink, in review). The western edge of the fault is thought to lie at the edge of the Olympic Mountains as interpreted from gravity and magnetic data (Figures 8 & 9) (e.g., Finn, 1990; Pratt et al., 1997; Brocher et al., 2001). The eastern edge of the fault is interpreted to be at the base of the Cascades along an inferred north-northwest trending fault zone (e.g., Gower et al., 1985; Johnson et al., 1994).

Seattle Basin

The Seattle basin has been interpreted to overlie the contact (or suture zone) between the Siletz terrane (Crescent basalt) and the pre-Tertiary Cascade basement rocks (e.g., Finn, 1990). The stratigraphy within the Seattle basin is known from the Mobil-Kingston well #1 as well as other wells in the region (Figure 10) (e.g., Johnson et al., 1994; Jones, 1996). The upper 2 km of the basin is filled with primarily unconsolidated

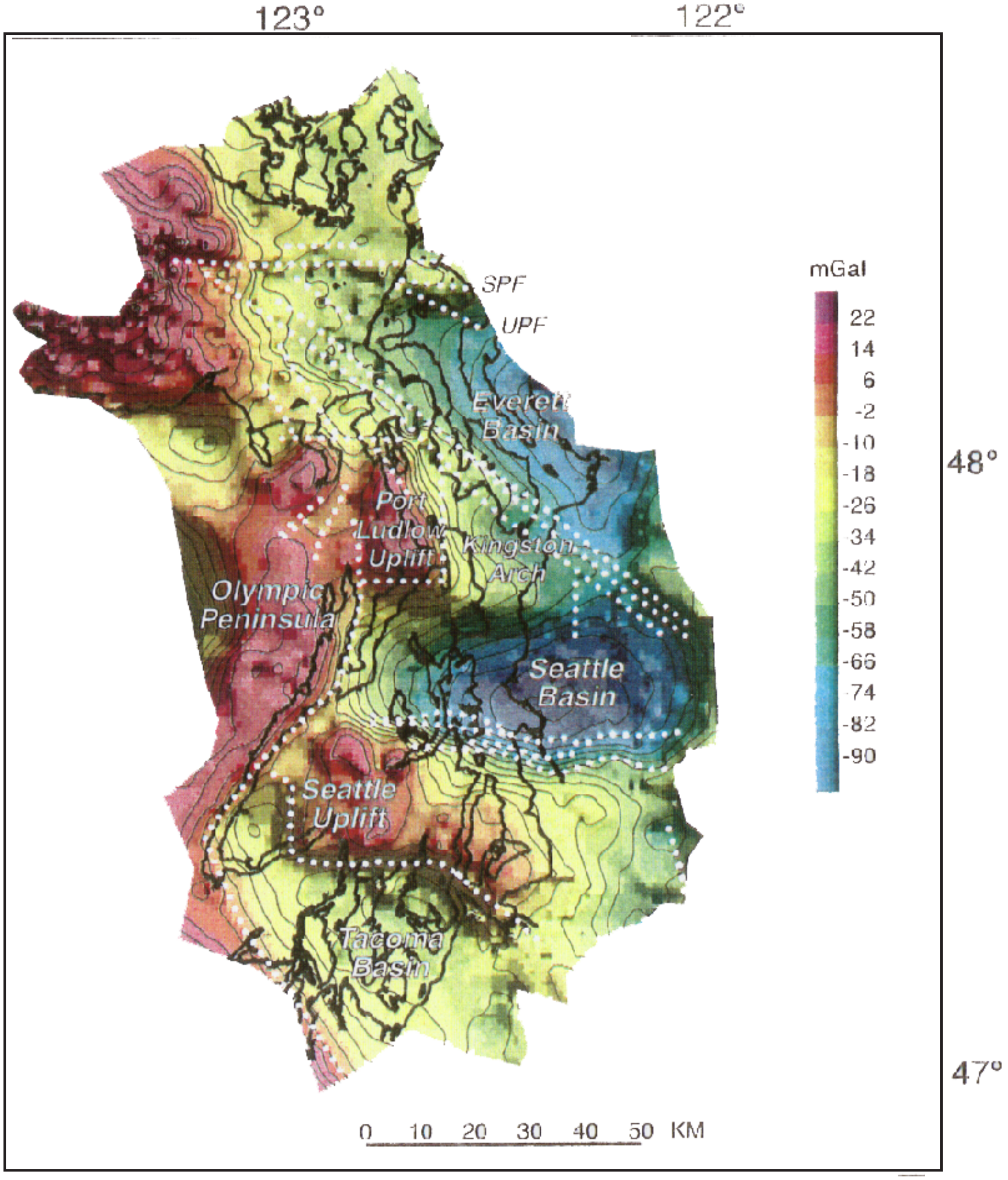

Figure 8. Observed gravity map (after Brocher et al., 2001). Faults are dotted white lines from Johnson et al. (1994; 1996) and Blakely et al., (2000). Abbreviations for geologic and geographic features are SPF - Strawberry Point fault, UPF - Utsulady Point fault, DB - Discovery Bay, PS - Port Susan, and TP - Toandos Peninsula.

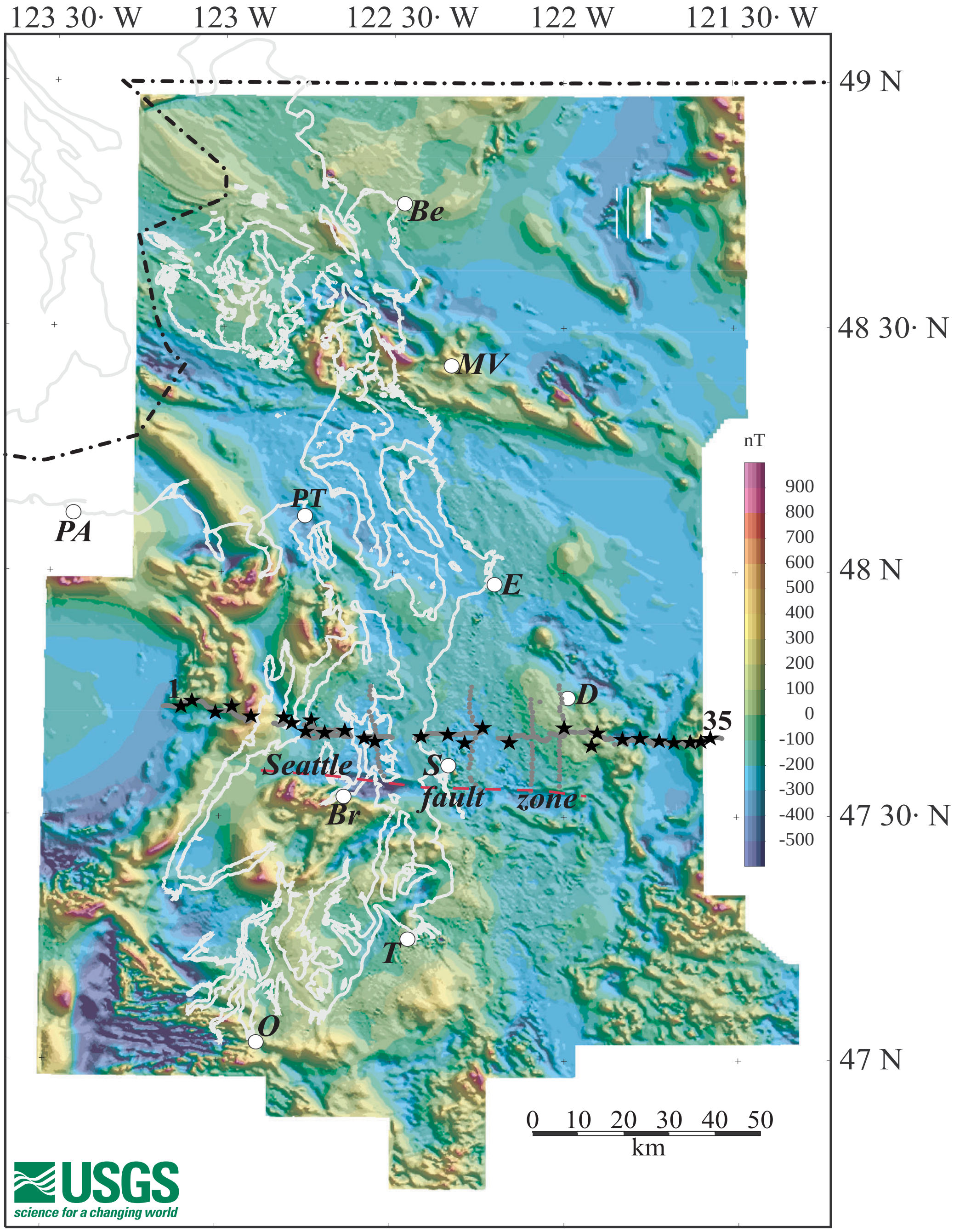

Figure 9. Aeromagnetic anomalies over Puget Sound, Washington (after Blakely et al., 1999). “Dry” SHIPS receivers are gray dots and shots are black stars. Red dashed line is the Seattle fault zone. Abbreviations for towns are PA - Port Angeles, Be - Bellingham, MV - Mount Vernon, PT - Port Townsend, E - Everett, D - Duvall, S - Seattle, Br - Bremerton, T - Tacoma, O - Olympia.

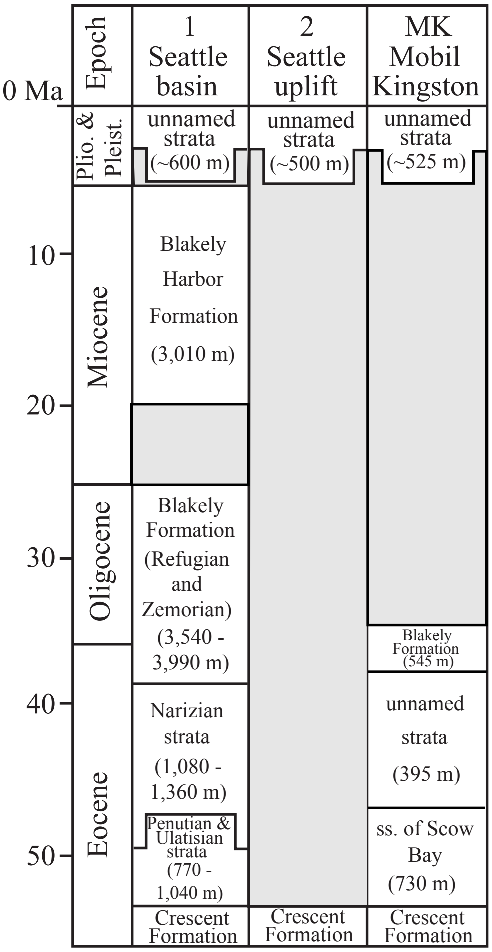

Figure 10. Stratigraphic column for the Puget Lowland. Columns are located in Figure 4. Shaded areas are intervals of non-deposition and/or erosion (modified from Johnson et al.,

sediments, which are thought to be the major contributor to amplification of seismic energy (e.g., Frankel et al., 1999; Pratt et al., in review).

The stratigraphy of the Seattle basin is here summarized from Johnson et al. (1994; 1996; 1997), Jones (1996), Brocher and Ruebel (1998), and Rau and Johnson (1999) (Figure 10). The upper 600 m of the basin are glacial and interglacial non-marine and marginal marine sequences which consist of poorly to semi-consolidated clay, sand, and gravel of Pleistocene age. The Blakely Harbor formation consists of non-marine sandstone, conglomerate, and siltstone. The conglomerate clasts are poorly sorted, well rounded pebbles, cobbles, and boulders of which ~ 85% are from the Siletz terrane. This formation marks the uplift on the Seattle fault in the early Miocene. The Blakely formation consists of various deep marine sequences. The Refugian and Zemorian of the Blakely formation consists of siltstone, claystone, and minor sandstone. Tuffaceous interbeds and rare macerated carbonaceous material are common. Forams suggest an upper bathyal depositional environment. The Narizian strata consist of sandstone and siltstone, claystone and tuffaceous interbeds are common. Depositional environment is interpreted as upper bathyal depths. Penutian and Ulatisian strata consist of siltstone and claystone with interbeds of tuff and very fine grained to granular sandstone. Depositional environment is interpreted as middle bathyal depths. The Crescent formation (Siletz terrane) consist of basalt and minor interbeds of siltstone, tuff, and conglomerate. Depositional environment suggests neritic depths.

Dextral strike-slip faults trending north-south are inferred to be common throughout the Puget Lowland. Paleomagnetic studies in southwestern Washington indicate clockwise rotation of ~ 16E since 12 m.y. (Figure 11) (e.g., Simpson and Cox, 1977; Magill et al., 1982; Wells and Heller, 1988; Wells et al., 1998). Two tectonic models have been proposed to explain this rotation. The first is a rigid plate model which proposes that southwestern Washington rotated as a rigid body separated from the western Cascades (e.g., Simpson and Cox, 1977; Magill et al., 1982; Wells and Heller, 1988; Wells et al., 1998). The second is a shear model where dextral shearing along transcurrent faults caused the rotation (e.g., Simpson and Cox, 1977; Magill et al., 1982; Wells and Heller,

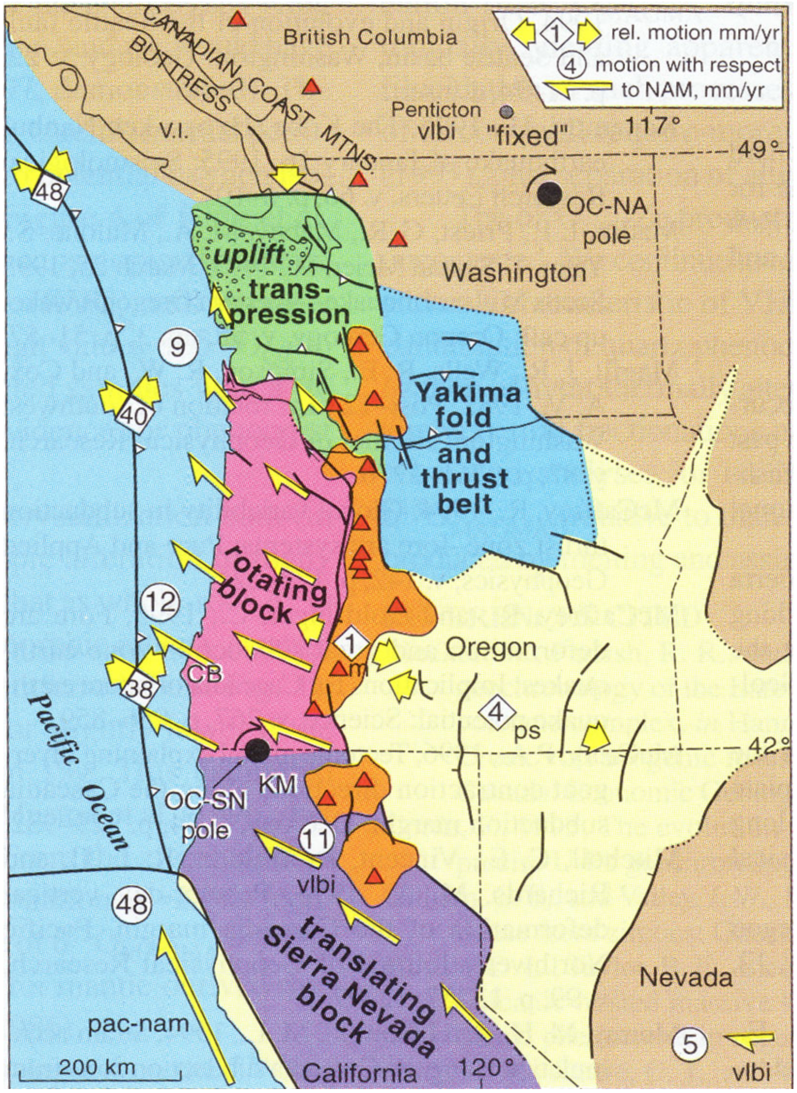

Figure 11. Rates of motion for the Cascadia forearc (after Wells and Simpson, 2001).

1988; Wells et al., 1998). Paleomagnetic evidence is consistent with dextral shearing from interaction with the subducting plate and overlying plate (e.g., Simpson and Cox, 1977; Magill et al., 1982; Wells and Heller, 1988; Wells et al., 1998). The rigid body model is also consistent with rotation caused by extension in the adjacent Basin and Range (e.g., Simpson and Cox, 1977; Magill et al., 1982; Wells and Heller, 1988; Wells et al., 1998).

Seismotectonics

The three major source regions for earthquakes in Cascadia are great quakes at the subducting plate boundary (M 8.5 - 9.0), large crustal earthquakes (M 7.0+), and large intra-slab earthquakes (M 7.0+). Seven great subduction zone quakes are estimated to have occurred over the past 4000 years, with the most recent occurred ~ 300 years ago (e.g., Clague, 1997; Goldfinger and Nelson, 2001). Evidence for these earthquakes are in drowned and buried soils along the coast, tsunami deposits, and liquefaction features (e.g., Atwater and Hemphill-Haley, 1996; Clague, 1997). The most recent of these earthquake has been estimated to have occurred in January, 1700 based on records from Japan, oral history of native people in western Washington State, and tree ring dating (e.g, Satake et al., 1996; Clague, 1997). The re-occurrence interval for such earthquakes is estimated to be ~ 600 years (e.g, Clague, 1997; Goldfinger and Nelson, 2001).

Slab events occur at depths of about 40 to 60 km (e.g., Crosson, 1972; Ludwin et al., 1991). Three slab events have occurred in the last 50 years, with the most recent being the M=6.8 Nisqually event (Malone et al., 2001), 18 February 2001, in the Olympia area (Figure 12). Several large crustal earthquakes have also occurred in the late Holocene (e.g., Ludwin et al., 1991; Bucknam et al., 1992; Dewberry and Crosson, 1996). The largest of these occurred about 1000 to 1100 years ago along the Seattle fault as is evidenced by uplift at Restoration Point at the edge of Bainbridge Island (e.g., Yount and Gower, 1991; Bucknam et al., 1992). It has been estimated that the Puget Lowland could expect a large crustal earthquake of M 7.0+ on the Seattle fault in the future (e.g., Pratt et al., 1997).

Two prominent zones of seismicity occur in the Puget Lowland (Figure 13) (e.g., Crosson, 1972; Ludwin et al., 1991). The first zone defines the subducting slab and the

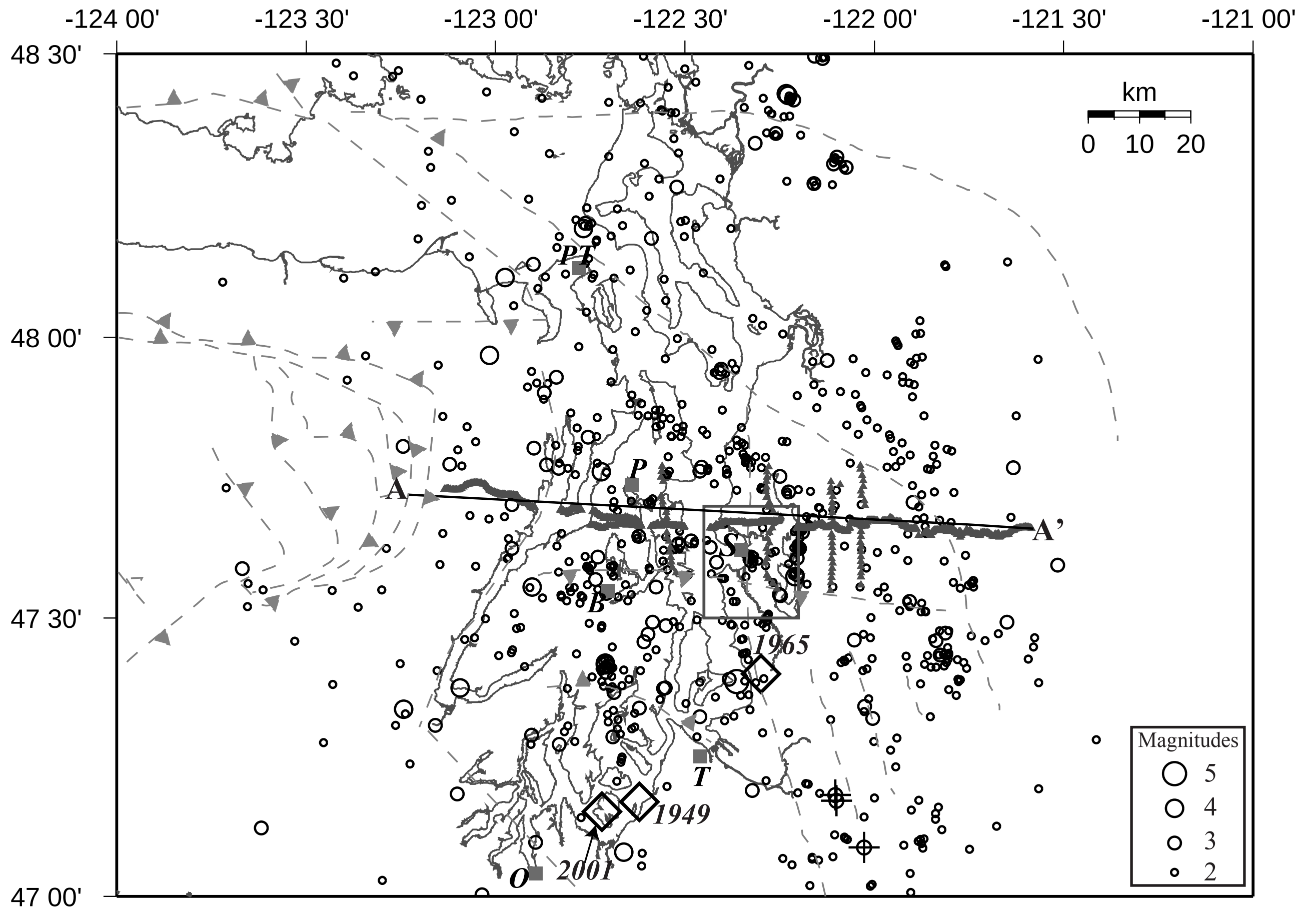

Figure 12. Basemap showing seismicity within the Puget Lowland. Events size is relative to the size of the circles. Events plotted only reach a maximum depth of 60 km. Large slab events are noted by the diamonds. Inferred faults are labeled and dashed. “Dry” SHIPS profile is represented by the gray line with stars as the shotpoint locations. Kingdome SHIPS is represented by the gray box. A cross section of seismicity, A-A’ along the “Dry” SHIPS profile in shown in Figure 13.

second lies within the crust (e.g., Crosson, 1972; Taber and Smith, 1985; Ludwin et al., 1991). Slab events can be large, but are less likely to cause a tremendous amount of damage compared to a shallower event of the same magnitude (e.g., Crosson, 1972; Ludwin et al., 1991). The seismic zone within the crust is about 20 km deep with few events near the surface (e.g., Crosson, 1972; Ludwin et al., 1991). The recurrence rate for large crustal earthquakes in the Puget Lowland can not be reliably estimated currently, because of the lack of large recent events and surface exposures (e.g., Johnson et al., 1996; Pratt et al., 1997). Seismicity related to Mt. St. Helens and Mt. Rainier can greatly effect the region but may not be as damaging as a large local crustal earthquake (e.g., Weaver and Smith, 1983; Ludwin et al., 1991).

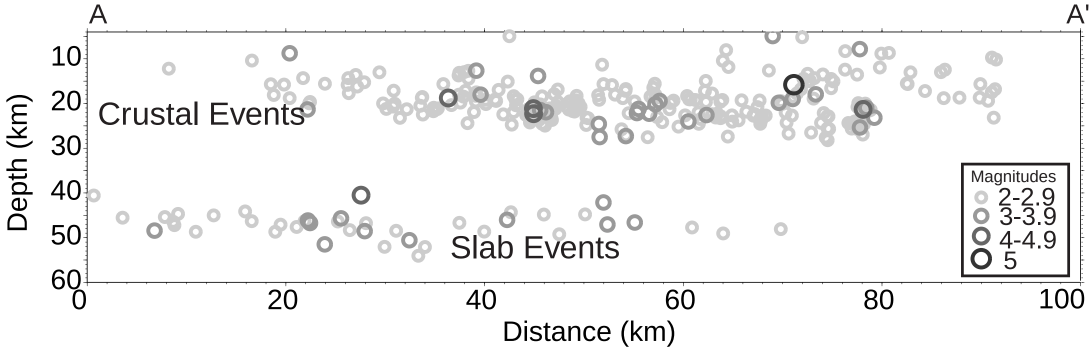

Figure 13. Cross section A-A’ is located on Figure 12. The cross section of seismicity along the “Dry” SHIPS profile shows the two distinct zones of seismicity, the diffuse crustal component and the slab events. Events were compiled from the University of Washington catalog. A search width of 30 km from the strike line were used.

Previous Geophysical Work

Gravity and Magnetics

Interpretation of gravity and magnetic data has delineated linear features which may be associated with faults in the Puget Lowland (Figures 8 & 9) (e.g., Finn, 1990; Danes, 1985; Gower et al., 1985; Blakely et al., 2000). Both the magnetic and gravity data have been tied to geologic mapping and seismic reflection interpretations (e.g., Finn, 1990; Pratt et al., 1997; Blakely et al., 2000). A gravity inversion based on 3-D tomography from “Wet” SHIPS data provided additional sub-surface information, but is limited because it assumes a single density for the basin and crust (e.g., Brocher et al., 2001).

Passive Source Seismic Studies

A number of earthquake studies have been conducted in the area since the first network was installed in 1970 (e.g., Ludwin et al., 1991). A study of earthquakes from the Olympic Peninsula has shown that seismicity is lower on the Peninsula compared to Puget Sound (e.g., Taber and Smith, 1985). This study determined the angle of subduction was ~ 11E and that focal mechanisms show there is active subduction under Washington state (e.g., Taber and Smith, 1985; Weaver and Baker, 1988). In addition, tomographic studies show that lower velocity rocks associated with the Olympic accretionary prism are thrusted under the Siletz terrane (e.g., Lees and Crosson, 1990; Symons and Crosson, 1997). They also show that the Olympic Peninsula (2 to 12 km depth) is associated with fast P-wave velocities and that the crust under Puget Sound at 4 to 6 km depth is slow. These studies also showed faster velocities at about 10 to 20 km depth under the Puget Sound which has been interpreted as Siletz (Lees and Crosson, 1990; Symons and Crosson, 1997). A pseudo-refraction study using earthquakes provided additional information on the crustal thickness and dip of the Moho along a profile from 47.55E, -122.79E to 46.02E, 118.57E, which trended southeast in Washington State (Schultz and Crosson, 1996). This study determined that the dip of the Moho to be 4.4E to the east in western Washington and 2.7E to the west in eastern Washington along their profile (Schultz and Crosson, 1996). The crustal thickness in the Puget Lowland was determined to be 35 km

(Schultz and Crosson, 1996). These earthquake studies have yielded valuable information on the structure of the region, but do not provide detailed structural information on the Seattle basin or the contact between the Siletz and Pre-Tertiary Cascade basement rocks (e.g., Lees and Crosson, 1990; Schultz and Crosson, 1996; Symons and Crosson, 1997).

Active Source Seismic Studies

Three crustal scale studies have been conducted in the Puget Lowland. Interpretation of industry seismic reflection data suggests that the Seattle fault has been active in recent times (Johnson et al., 1994; 1996). Re-interpretation of industry seismic reflection data have led to a hypothesis that the Puget Lowland rides on a north-verging décollement at about 20 km depth (Pratt et al., 1997). The décollement is interpreted to lie within the Siletz terrane and the Seattle fault is interpreted to terminate into the décollement (Pratt et al., 1997). The result provides a working hypothesis for deformation in the Puget Lowland (Pratt et al., 1997).

In 1991, a seismic refraction profile crossed the Puget Lowland along the Cascade front (Miller et al., 1997). The velocity model obtained from the profile provides starting velocities along the eastern edge of the “Dry” SHIPS profile. Interpretation of seismic refraction data collected in 1995 along an east-west profile near ~ 46.5E shows the location of the contact between the Siletz terrane and Cascade basement rocks at the Mt. St. Helens seismic zone (~ 46.5E, -122.0E) as represented by a sharp decrease in velocity from west to east (Parsons et al., 1999). These data are also interpreted to suggest that the Siletz terrane is a backstop for the accretionary prism (Parsons et al., 1999).

The first phase of SHIPS, “Wet” SHIPS, took place in 1998. A tomographic model from this experiment has yielded an image much of the Puget Lowland to a depth of ~ 11 km (Brocher et al., 2001). The velocity model shows the Seattle basin is about 7 to 10 km deep and that the basin appears to be asymmetric in the north-south direction (Brocher et al., 2001). From this model, the Seattle basin appears to be asymmetric in the east-west direction, probably a result of lack of coverage in the eastern edge of the model (Brocher et al., 2001). Although this experiment covered the region well, the data do not provide a very detailed picture of the upper part of the Seattle basin nor do they define the contact between the Crescent terrane and Pre-Tertiary Cascade basement rocks. A north-south reflection line acquired in the Puget Sound during “Wet” SHIPS ties the Mobil-Kingston well #1 to provide stratigraphic control (Fisher et al., 2000; Calvert et al., 2001; ten Brink et al., in review). This line crosses the “Dry” SHIPS profile and thus provides stratigraphic control for the “Dry” SHIPS model.

Data Acquisition

In order to define the geometry of the Seattle basin and its contact with the Siletz terrane and the Cascades, the 1999 SHIPS (Seismic Hazards Investigation of Puget Sound) experiment (“Dry” SHIPS) was conducted in September, 1999 (Brocher et al., 2000). The main goal of this experiment was to determine the velocity information on the basin fill to aid in site response calculations for earthquake response. The seismic line is ~112 km in length, and extends from the Olympic Mountains, thru Seattle to the foothills of the Cascades (Figure 2). In addition, four crosslines were acquired to further constrain the shallow structure in 3-D for the eastern side of the Seattle basin (Figure 2). For many of our ~ 1000 stations, spacing was nominally ~ 100 m. A variety of portable seismic recording systems, Texans (440 units), RefTeks (231 units), SGRs (129 units), PRSs (200 units), and ocean-bottom seismometers (8 units) were used during this experiment. The

RefTeks and some of the PRSs used 3-component geophones. All of the instruments were programmed to begin prior to the shot window and recorded for at least 60 s. There were 38 shots detonated ranging in size from 11.4 to 1136.4 kg. The data were merged at the IRIS DMC (Data Management Center) and were processed using the ProMAX® seismic data processing software at UTEP.

A subsequent experiment in March of 2000, the “Kingdome SHIPS” phase, was designed to look directly at the site response within the upper 2 km of the Seattle basin (Brocher et al., 2000). Approximately 206 TEXANS and RefTeks were deployed in a hexagonal grid in the city of Seattle, with a nominal station spacing of about 1 km (Figure 3). In addition to recording the implosion of the Kingdome sports arena, four additional shots were fixed at the corners of the grid. The four corner shots were ca. 68 kg in size, whereas the Kingdome implosion was ca. 100,000 kg.

Overall the data quality was very high with “Dry” SHIPS, with several shots carrying the length of the profile. The Seattle basin is a very distinct in the record sections and is associated with as much as a 2 s traveltime delay (Figures 14 & 15). The Kingdome data recorded offsets out to about 10 km which is sufficient for studying the upper 2 km of the Seattle basin.

P-Wave Tomography

Over 13,000 P-wave first arrivals were picked from the seismic data for use in a traveltime tomography code. The picking error for the first arrivals is ~ 100 ms in high signal to noise ratio portion of the seismic data and is ~ 150 ms is areas of the data with

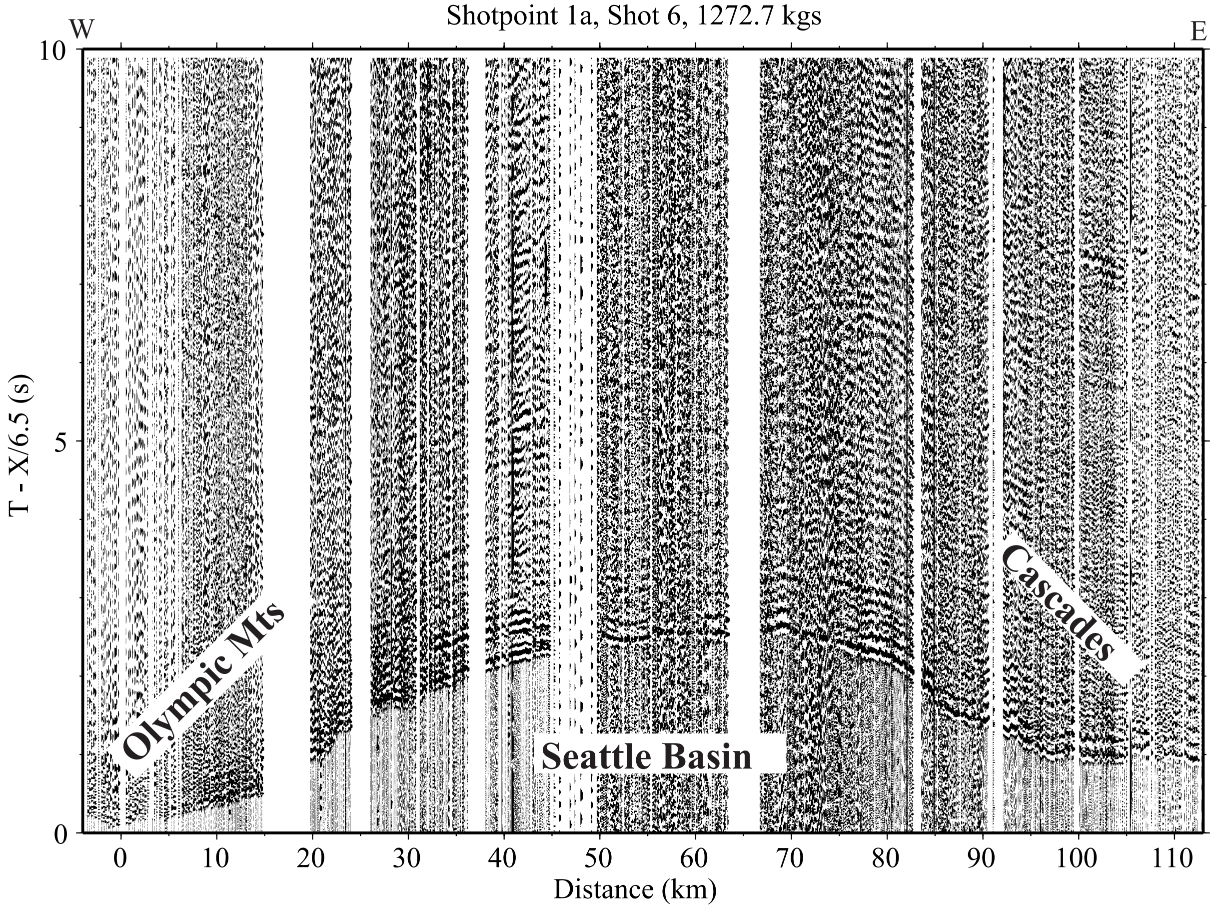

Figure 14. Shot point 1a at the west end of the profile as seen on figure 2. The Seattle basin is distinguished by a 2 s traveltime delay. The data are reduced at 6.5 km/s.

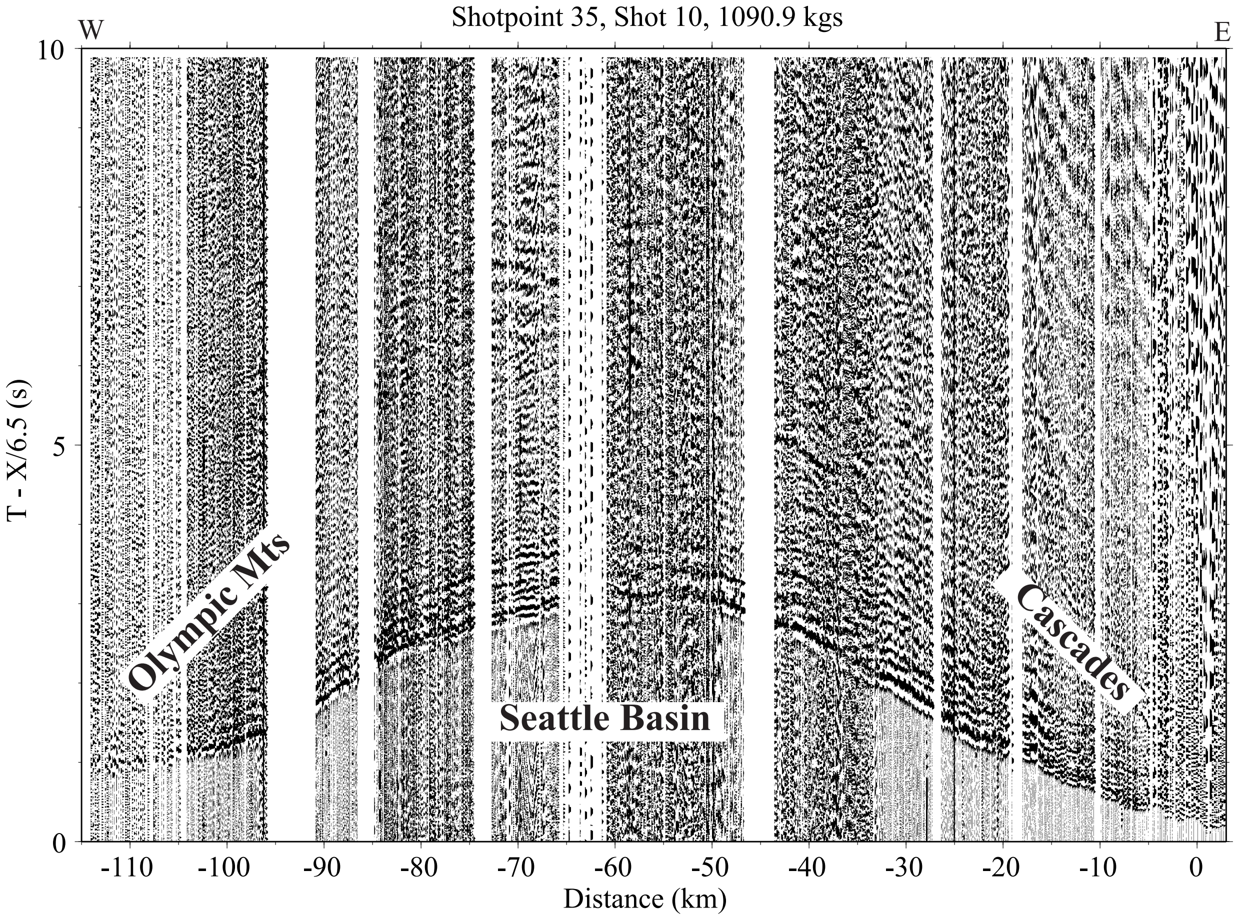

Figure 15. Shot point 35 at the east end of the profile as seen on figure 2. The Seattle basin is distinguished by a 2 s traveltime delay. The data are reduced at 6.5 km/s.

low signal to noise ratios. We used a 3-D approach for this problem because of the crooked-line geometry of the profile. This approach solves any geometrical effects that would have occurred in 2-D modeling. We chose the Hole (1992) code, which is a non-linear high resolution tomographic technique. The code is computationally efficient and handles large velocity contrasts (Hole, 1992). The code uses a finite difference approximation to the eikonal equation to calculate traveltimes (Vidale, 1988; 1990). The model space consists of a 3-D velocity model defined on a uniformly spaced grid. Initial traveltimes are calculated to all grid points by a finite difference operator which uses the average slowness across each cell (Hole, 1992). Ray paths are back-projected through the array of calculated traveltimes to obtain the traveltime at any given receiver for a source in the model space.

The inversion requires a linearization of the eikonal equation with a Taylor series expansion that ignores higher order terms (Hole, 1992). The linearized equation is solved iteratively for perturbations to the velocity model until the RMS residual no longer changes or reaches the traveltime uncertainty. The technique is non-linear because traveltimes are re-calculated through an updated model after each inversion.

Procedures for running the inversion were as follows. First, an initial 1-D model is expanded into a 3-D volume and used to calculate initial ray paths. Second, traveltime residuals are calculated. Third, a slowness perturbation model is found in the inversion, which minimizes the differences between calculated and observed traveltimes. Next, the initial model is updated and smoothed using a moving average filter. Finally, the new model is input to the next iteration and traveltimes are recalculated. The smoothing factor or moving average filter is reduced, by almost half, for every iteration until the size of the smoother is equal to that of the receiver spacing. These iterations continue until the change in RMS becomes insignificant.

The model space used in this study has corners at -123.28E, 47.43E at the origin and -121.45E, 47.88E for the opposite corner. The stations and shot locations were transformed from latitude and longitude to x and y with a UTM zone 10 projection. The size of the model is 137 km in x (west-east) by 51 km in y (north-south) by 40 km in depth and has 400 m grid cells (Figure 16). The sides of the model have ~10 km of padding in x and y and 4 km in z to prevent rays, from the model, escaping. All of the 2-D figures were calculated based on weighted average in the 3-D volume using the ray coverage, where there was little or no ray coverage, the velocity cell was not averaged in the final 2-D slice.

The initial model was chosen from a priori information for the local area (e.g., Parsons et al., 1999; Hiett, 2000). The 1-D model was constructed with a gentle velocity gradient. At the base of the model a low velocity was assigned, which prevents rays from getting trapped or guided at the bottom of the model (Hole, 1992). The inversion is very sensitive to the starting model. For example, a slower model than the one used for the inversion would not calculate all ray paths after a couple of iterations. A model that was faster than the one chosen, produced a large starting RMS which was difficult to reduce to a reasonable RMS.

We carried out 3 runs of the code to produce the final model. The first run used a smoothing factor of 40 x 40 x 20 grid nodes (16 km x 16 km x 8 km) for 10 iterations (Figure 17). The starting RMS was 1.34 s for iteration 1. Iteration 4 from this run, which had a RMS of 0.26 s, was input to the 2nd run. The second run used a smoothing factor of 30 x 30 x 10 grid nodes (12 km x 12 km x 4 km) for 10 iterations. Iteration 4 from the 2nd run,

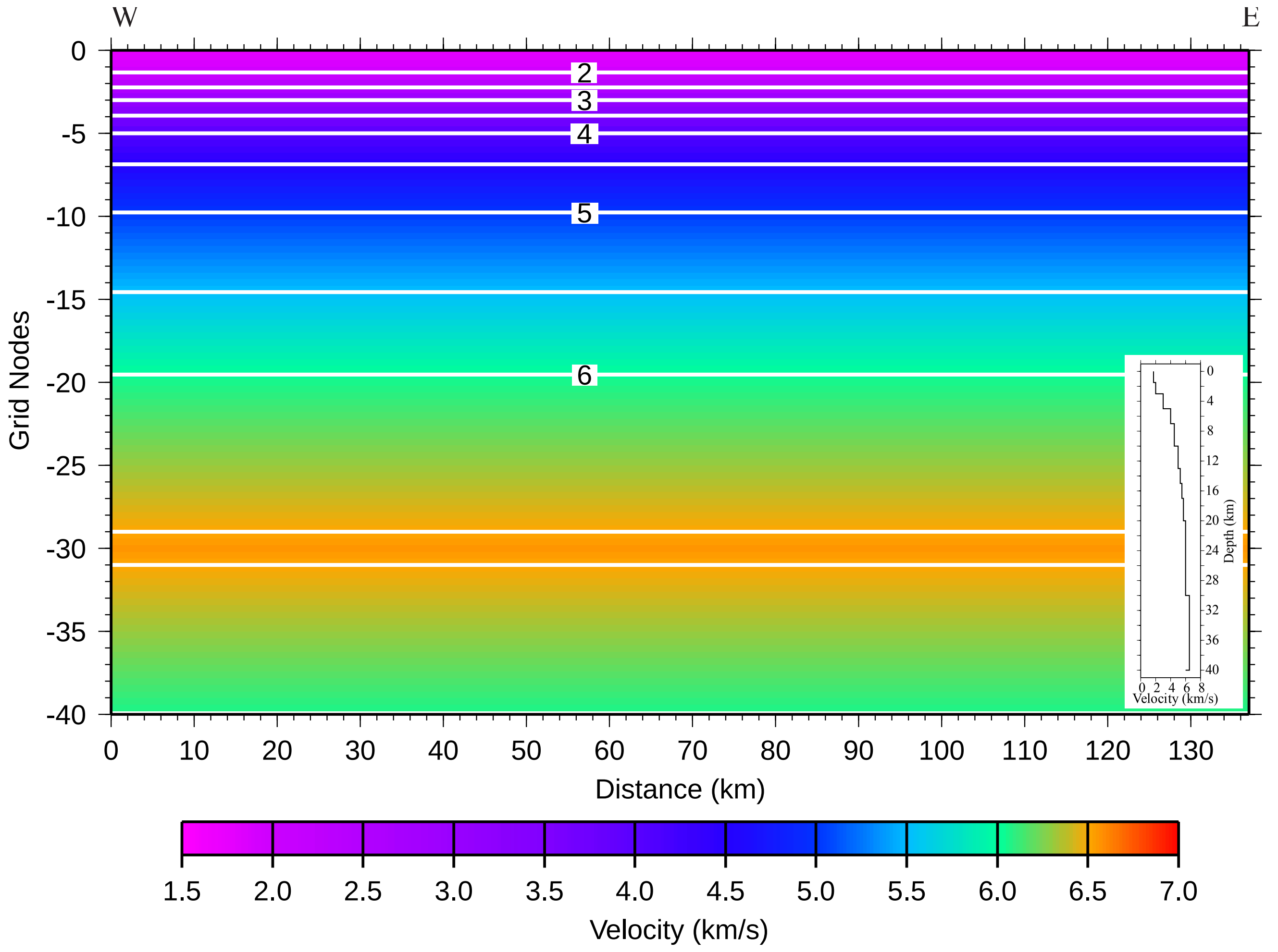

Figure 16. 2-D slice of the starting model from the 3-D volume. The initial 1-D model is shown inset in the bottom right corner.

which had a RMS of 0.14 s, was input to the 3rd run. The final run used a smoothing factor of 20 x 20 x 10 grid nodes (8 km x 8 km x 4 km) for 10 iterations. The final RMS for the model is ~ 0.10s with a final smoothing factor of 8 km x 8 km x 4 km.

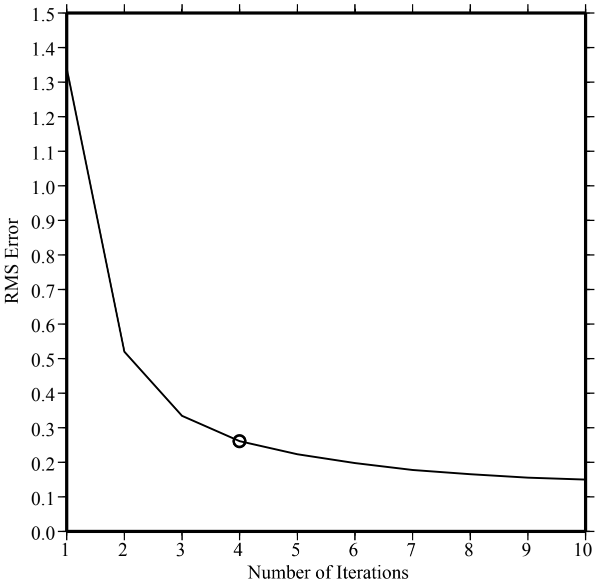

Figure 17. RMS error curve versus number of iterations run for the initial model. The circle represents the model that was input to the next run.

Overall the traveltime fits are excellent, although there are places where the misfit is as large as 200 ms (Figure 18). The observed traveltimes (red plus signs in Figure 18) are reduced at 6.5 km/s. The calculated traveltimes (blue triangles in Figure 18) overlay quite well. The residuals (green dots in Figure 18) all plot around zero which indicates and excellent fit of the data. This misfit appears to be caused by a systematic error within the inversion. If two rock types share the same cell then the slower material will prevail and the calculated traveltime will reflect a large misfit (Zelt et al., 1996).

Measures of Resolution

A sense for the resolution of the model can be gained by evaluating the RMS error,

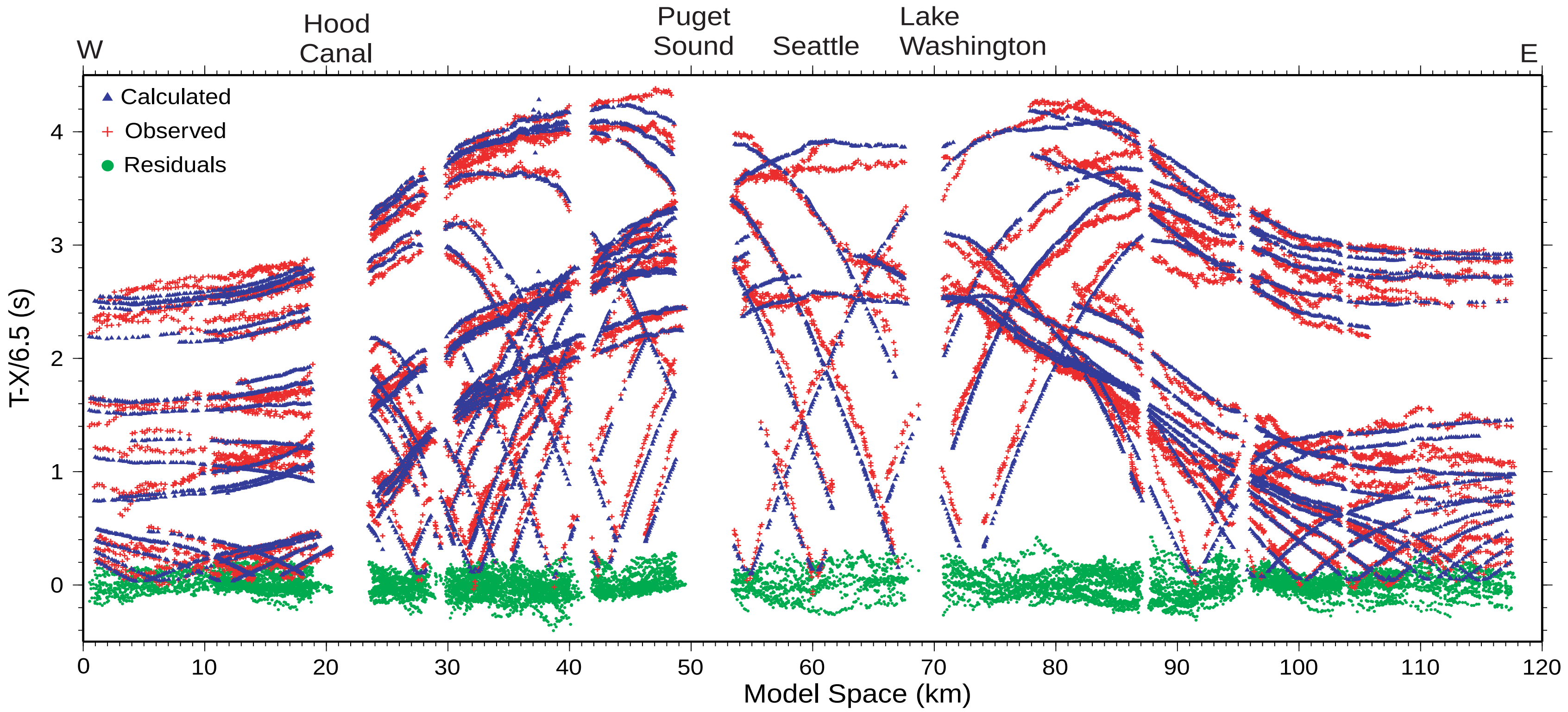

Figure 18. Traveltime fits for the “Dry” SHIPS data. These picks are reduced at 6.5 km/s. Red plus signs are the observed traveltimes, blue triangles are the calculated traveltimes from the inversion, and the green dots are the residuals or difference between the observed and calculated traveltimes.

traveltime fits, ray coverage, and the resolution matrix. Unfortunately with this technique, the resolution matrix is not created because the technique is non-linear (Hole, 1992). We have been able to provide RMS error, traveltime fits, and ray coverage for the velocity model. In an effort to further evaluate the resolution of the model, checkerboard tests and sensitivity tests were also carried out.

Ray Coverage - P-Wave Tomography

The ray coverage or hit count represents the number of rays traveling through a particular cell. The more hits for any given cell the better resolved that cell will be. Ray coverage is adequate throughout the model with a minimum of 5 hits and a maximum of 1884 hits per cell (Figure 19). The ray coverage is especially high, in an east-west direction, where there were duplicate shots. Ray coverage for the crosslines and Kingdome SHIPS was adequate in the upper 2 km but decreased rapidly with increasing depth (Figures 20-29). At the surface it is evident that the southwest corner shot for Kingdome SHIPS were not strong enough to carry the length of the grid (Figure 20). As a result the southern portion of the grid, which crossed the Seattle fault, provides limited information. The majority of hits are on the ends of the model where the signal to noise ratio was high compared to the center of the model, through the city of Seattle.

Checkerboard Tests

Following the technique of Zelt (1998), 16 km x 16 km sinusoidal checkers with amplitudes of +/- 5% were added to a smoothed 1-D version of the final velocity model (Figure 30). Traveltimes times for this model were calculated input to the inversion as the “observed” traveltimes along with the smoothed 1-D model. The inversion was then allowed to run for five iterations. Unfortunately, we were unable to recover the full

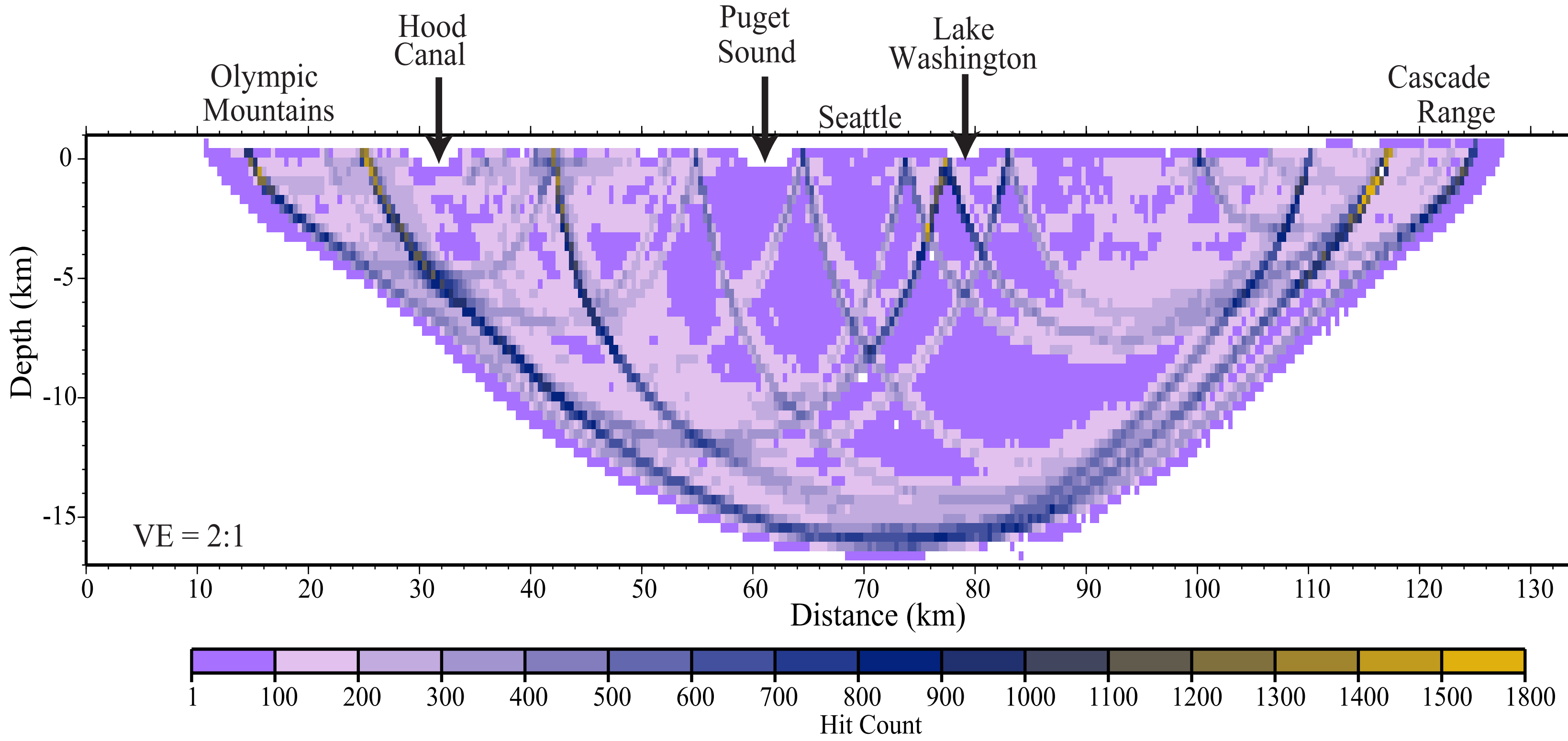

Figure 19. Hit count for the “Dry” SHIPS model. The minimum number of hits per cell is 5 and the maximum is 1884.

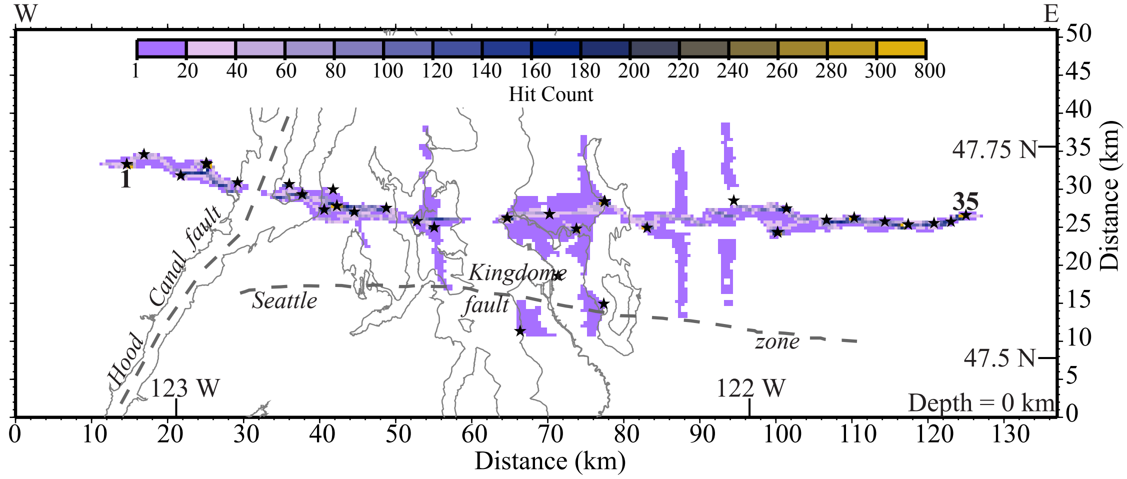

Figure 20. Ray coverage along the “Dry” SHIPS profile in map view at the surface. Small stars are shotpoint locations.

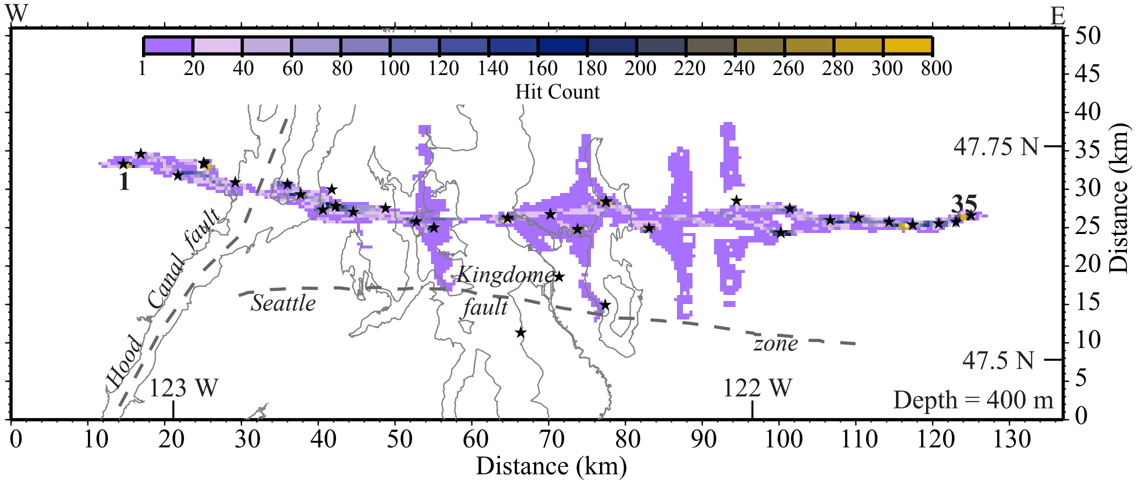

Figure 21. Ray coverage along the “Dry” SHIPS profile in map view at 400 m depth. Small stars are shotpoint locations.

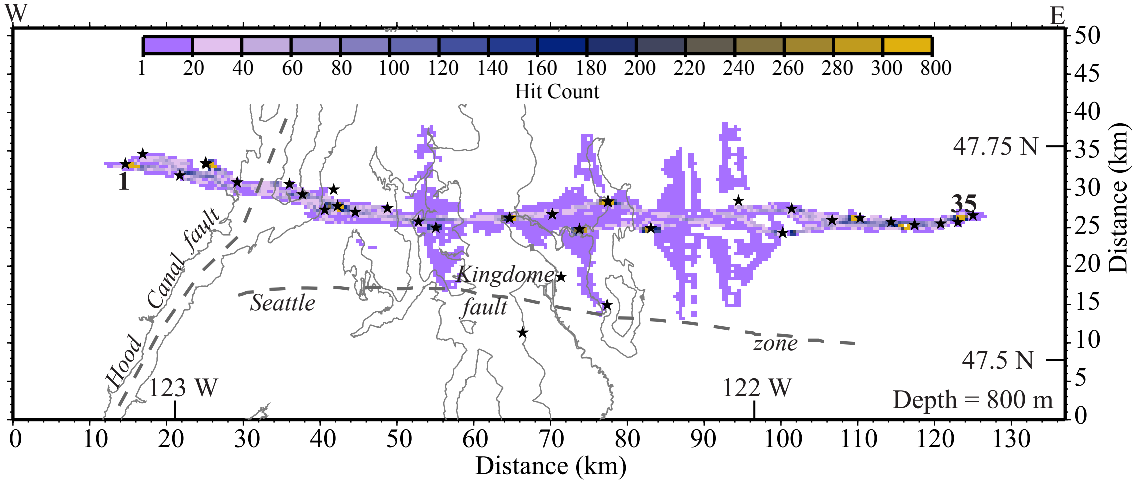

Figure 22. Ray coverage along the “Dry” SHIPS profile in map view at 800 m depth. Small stars are shotpoint locations.

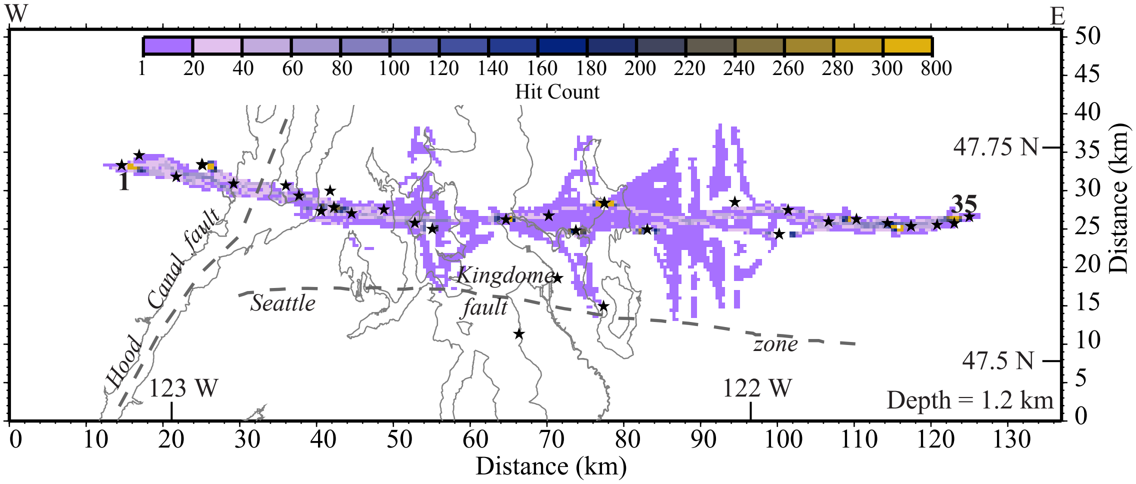

Figure 23. Ray coverage along the “Dry” SHIPS profile in map view at 1.2 km depth. Small stars are shotpoint locations.

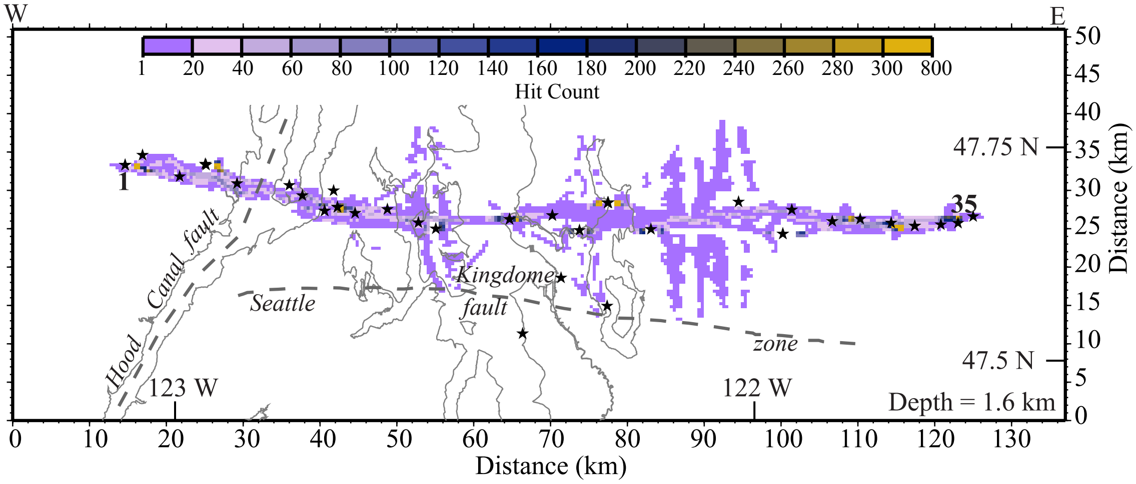

Figure 24. Ray coverage along the “Dry” SHIPS profile in map view at 1.6 km depth. Small stars are shotpoint locations.

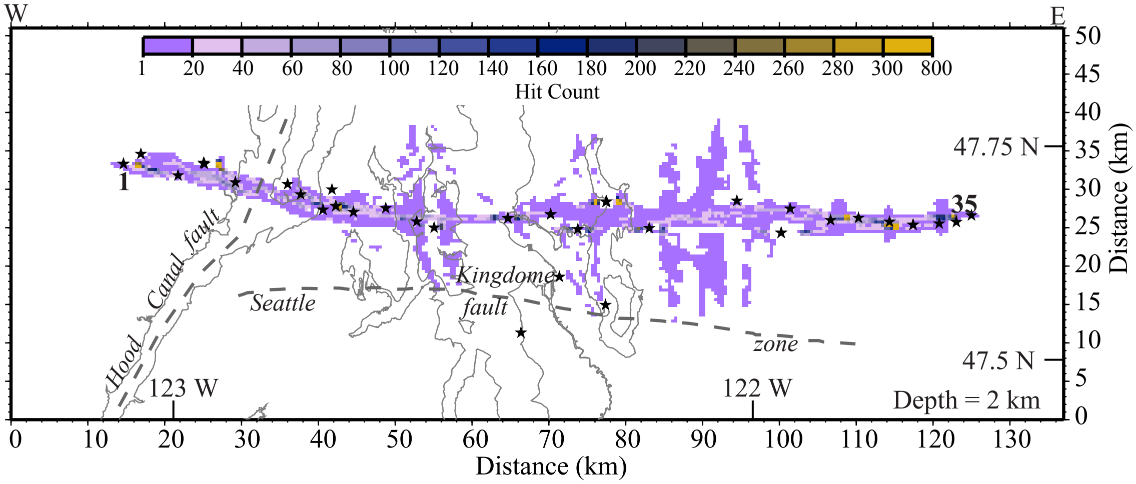

Figure 25. Ray coverage along the “Dry” SHIPS profile in map view at 2 km depth. Small stars are shotpoint locations.

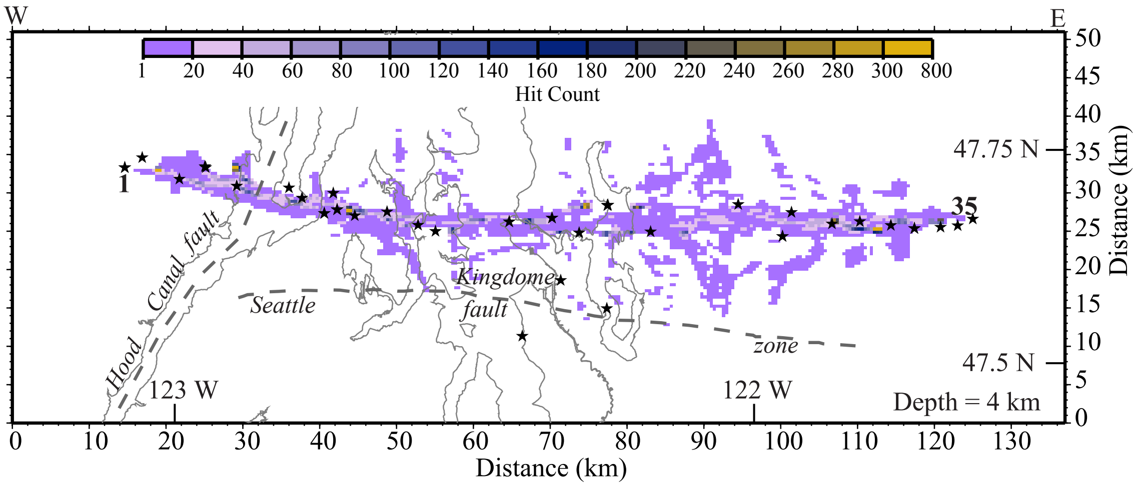

Figure 26. Ray coverage along the "Dry" SHIPS profile in map view at 4 km depth. Small stars are shotpoint locations.

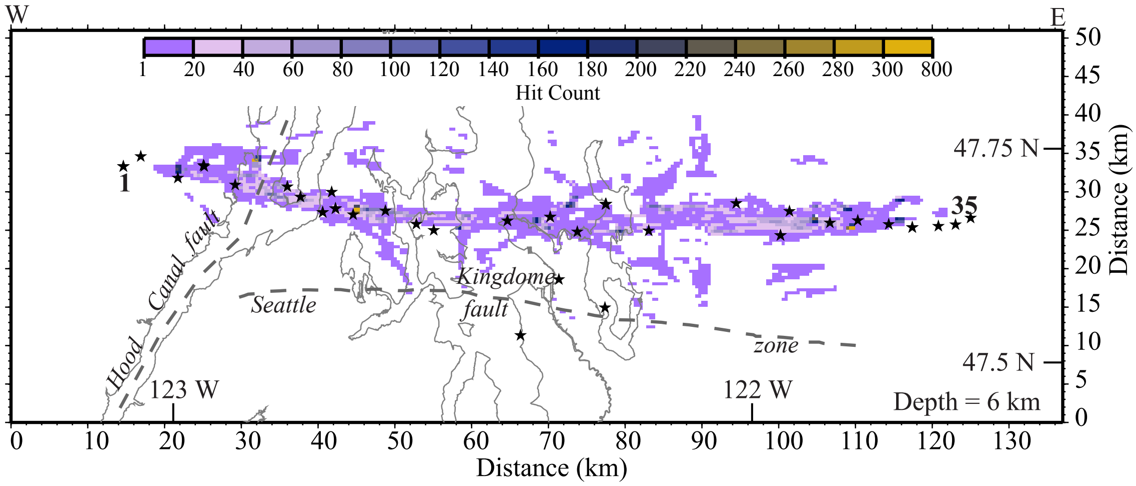

Figure 27. Ray coverage along the "Dry" SHIPS profile in map view at 6 km depth. Small stars are shotpoint locations.

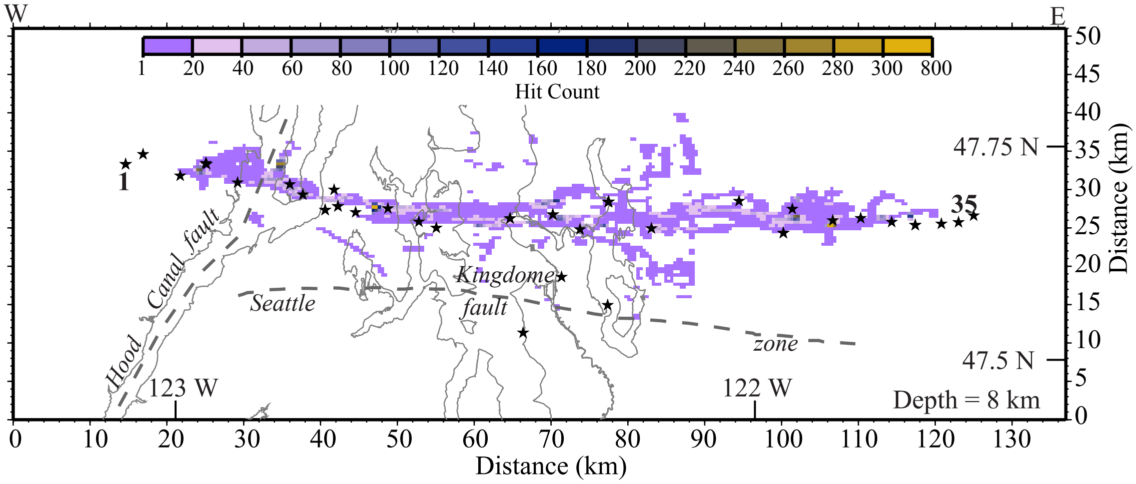

Figure 28. Ray coverage along the “Dry” SHIPS profile in map view at 8 km depth. Small stars are shotpoint locations.

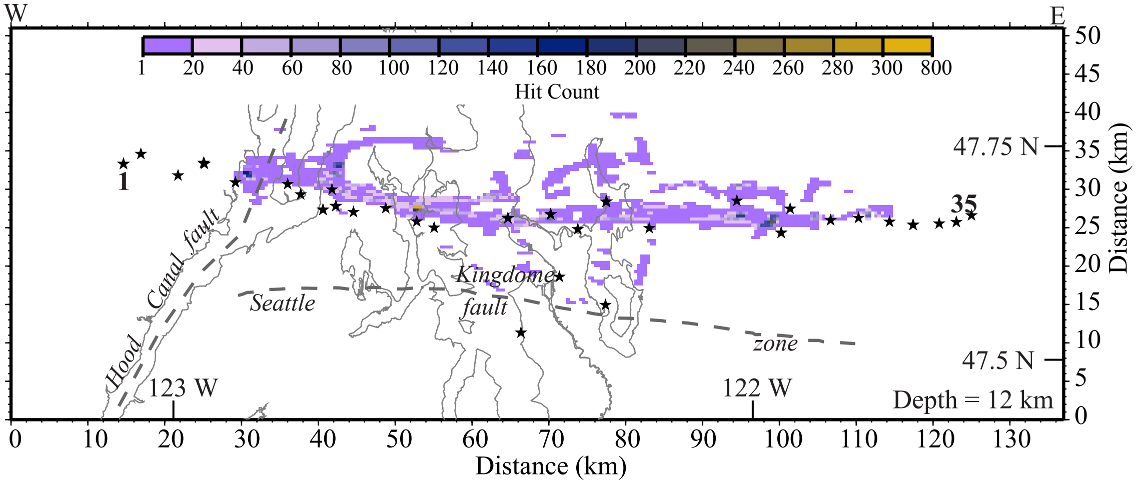

Figure 29. Ray coverage along the “Dry” SHIPS profile in map view at 12 km depth. Small stars are shotpoint locations.

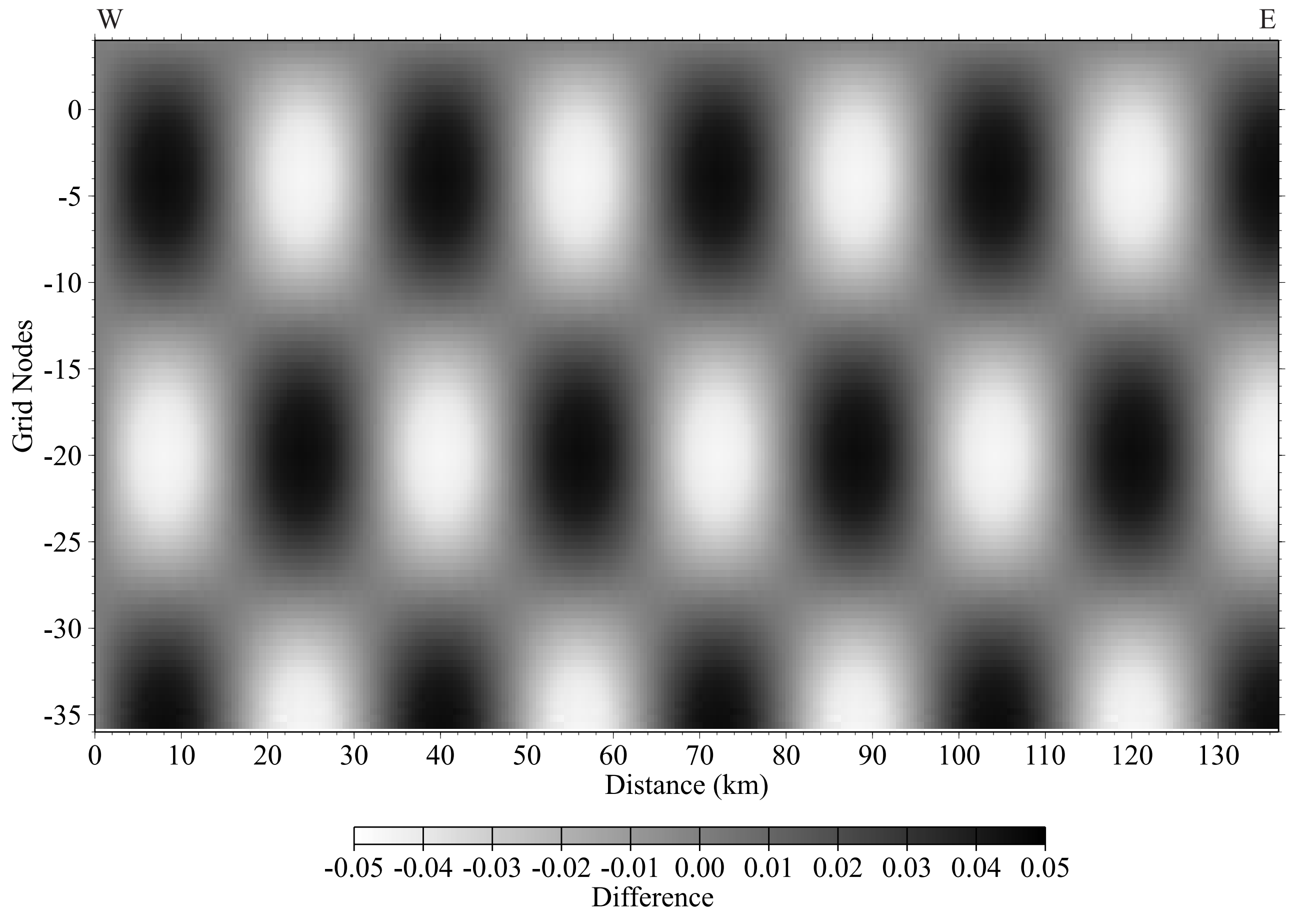

Figure 30. Original sinusoidal checkers. These checkers are 16 km x 16 km in the X-Z plane with a +/- 5% amplitude.

amplitude of the checkers (Figure 31). In addition, we were unable to resolve any checkers below 5 km depth. This suggests that the best resolution is in the upper 5 km of the model.

Traveltimes Sensitivity

We also applied another technique which uses a combination of a Gaussian fit and Monte Carlo approach to determine the sensitivity of the traveltimes (Doser et al., 1998). In this approach a random component with a RMS of the picking error (100 ms) is added to the observed traveltimes. The inversion procedure is then run ten times using the same steps used to obtain the final model. The suite of ten final models were then combined according to the approach using in the following equation (Doser et al., 1998).

$$\sqrt{\frac{1}{N}\sum_{r=1}^{N}(t_j^{(r)}-t_j)^2}$$

Here t_j is the velocity per perturbation, r is the traveltime perturbation, and N are the number of iterations (Doser et al., 1998).

The magnitude of changes to the velocity is a measure of sensitivity of the model. If the velocity variations from cell to cell are significant then the model is well resolved. Where there are few changes then the model is more uncertain. The extreme changes in velocity maybe related to picking of emergent arrivals and/or a sharp boundary within a particular cell. Application of this technique to the “Dry” SHIPS data show that the upper 5 km of the basin is well resolved (Figure 32). Below 5 km depth, the model shows little variation in the velocity field. Therefore, the upper 5 km of the model is better resolved

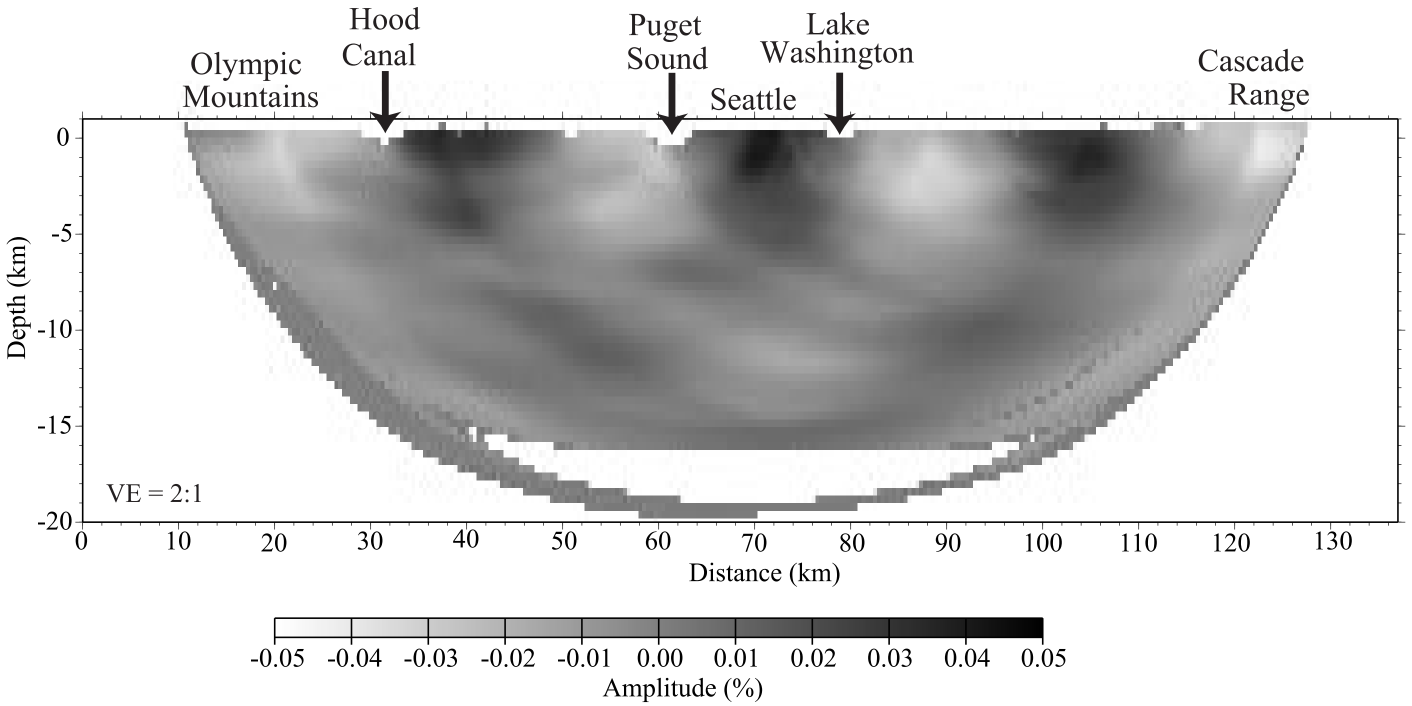

Figure 31. Recovered checkers along the “Dry” SHIPS profile. Colors represent the change in amplitude.

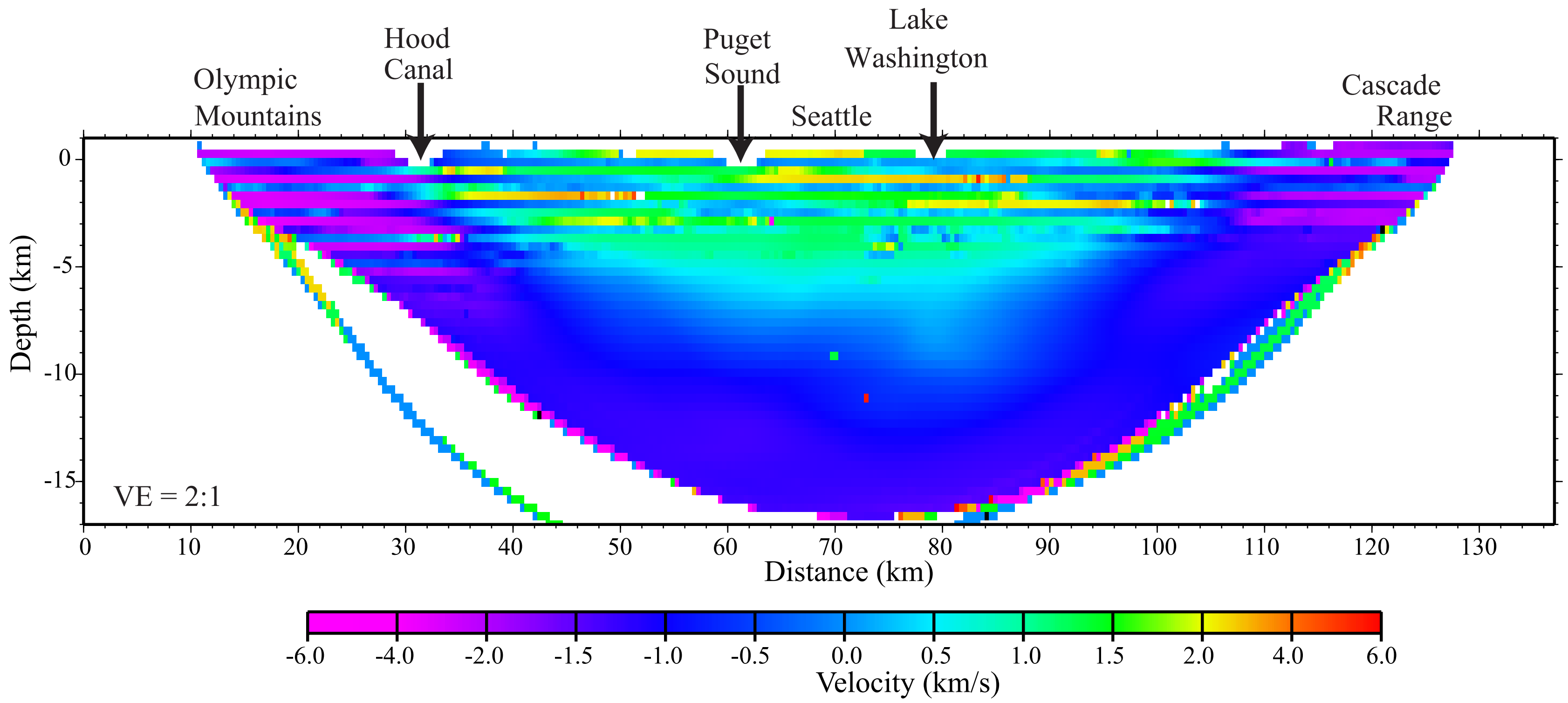

Figure 32. Resulting sensitivity model for the “Dry” SHIPS profile. Color represent the variation in velocity.

then below 5 km.

One cause of the lack of resolution is the lower portion of the model may be the small grid spacing. The grid spacing for the P-wave model was 400 m, which is fine for the upper 5 km but should have been larger for the lower portion of the model. The grid spacing based on the receiver spacing of 100 m, but in the center of the model where the signal to noise ratio is high, this spacing may have been too small. There are not enough crossing rays for the grid spacing that was chosen. It may be more reasonable to use a grid spacing of 800 m for this dataset, this large gird size will be tested in the future.

A comparison between the sensitivity test and checkerboard test show the result is very similar. They both show that the upper 5 km of the model is best resolved. The hit count, in this dataset, was not a reliable measure of the resolution. By looking at the hit count alone, one would assume that the model is well resolved to much greater depths than 5 km.

P-Wave Tomography Results

Overall the velocity field shows slower velocities (~1.7 to 4.5 km/s) near the surface which are associated with the Seattle basin (Figures 33 & 34). The base of the basin is indicated by the strong velocity gradient at 4.5 km/s (Figures 33 & 34). The velocity increases with depth with velocities reaching a maximum of ~ 7.2 km/s (Figures 33 & 34). The model shows the basin is ~ 6 to 7 km deep at its center (Figures 33 & 34). The length of the basin is ~ 70 km, which is indicative of the length of the Seattle fault (Figures 33 & 34).

The 4.5 km/s contour was chosen as the base of the basin for two reasons. First, where Siletz outcrops, the 4.5 km/s contour reaches the surface. This velocity is also

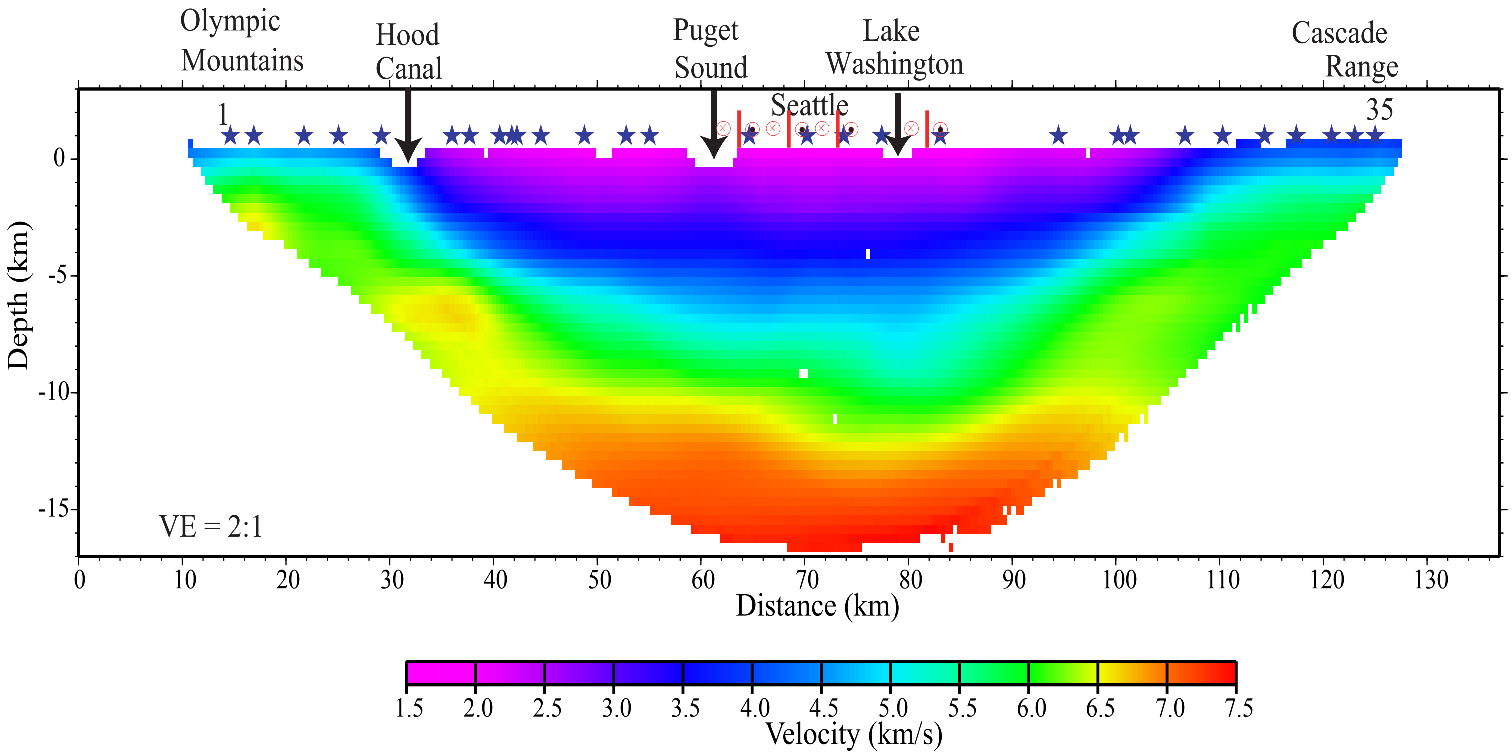

Figure 33. 2-D weighted slice of the final velocity model. Shotpoints are signified by the blue stars. Major waterways along the profile are annotated. The basin ranges in velocity from 1.7 km/s to 4.5 km/s. Mid-crustal velocities increase from 4.5 km.s to 6.5 km/s. Lower crustal velocities increase from 6.5 km/s to 7.2 km/s. The red lines at the top of the model are locations of postulated strike-slip faults with sense of motion (Johnson et al., 1999).

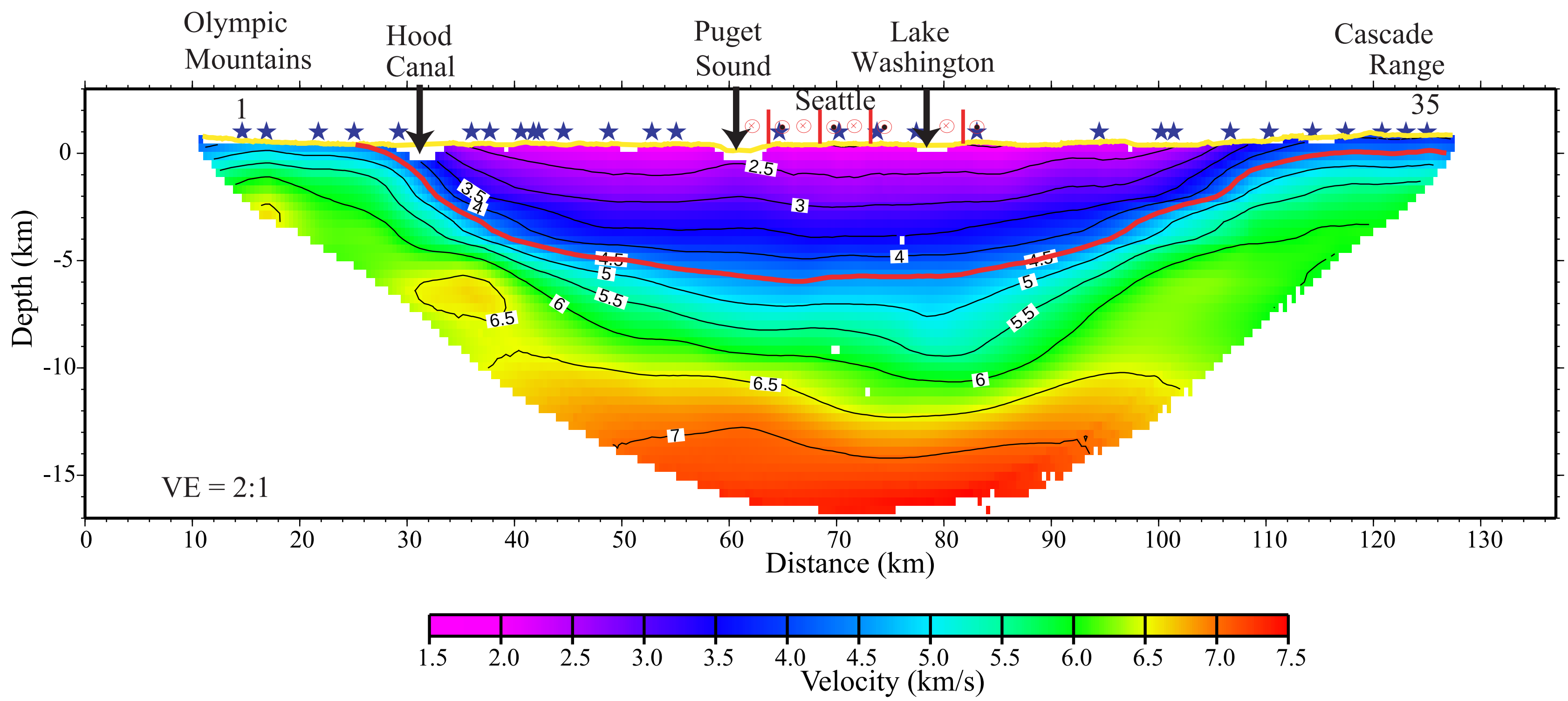

Figure 34. 2-D weighted slice of the final velocity model. Shotpoints are signified by the blue stars. Elevation is represented by the yellow line. Contour interval is 0.5 km/s. The 4.5 km/s contour chosen as the base of the Seattle basin is highlighted in red. Major waterways along the profile are annotated. The basin ranges in velocity from 1.7 km/s to 4.5 km/s. Mid-crustal velocities increase from 4.5 km.s to 6.5 km/s. Lower crustal velocities increase from 6.5 km/s to 7.2 km/s. The red lines at the top of the model are locations of postulated strike-slip faults with sense of motion (Johnson et al., 1999).

consistent with fractured and porous basalt (e.g., Mavko et al., 1998). The second reason comes from the Mobil-Kingston well that is stratigraphically tied to the “Dry” SHIPS profile by a north-south reflection line in the Puget Sound (ten Brink et al., in review, Figure 1). Mapping of the stratigraphy in the well to the velocity field for the section shows that the 4.5 km/s parallels the top of Siletz volcanic rocks.

By following the 4.5 km/s contour, one can see that the Siletz - basin contact dips smoothly at ~ 29E on the west-side of the profile. In the east, the Cascades - basin contact dips less steeply at ~ 20E. The increase in velocity just below the basin - bedrock contact, east of Puget Sound, could be pre-Tertiary basement rocks. An isolated high velocity anomaly (> 6.5 km/s) occurs on the west side of the model, this could be indicative of the Siletz terrane at depth. The model does not confirm whether or not the accretionary wedge is pushed under the Siletz terrane, as the model lacks ray coverage where the accretionary wedge rocks are expected. Velocities at the base of the model are not well resolved and therefore, the velocity estimates are probably only accurate to within 0.3 km/s. The maximum depth of ray penetration is about 14 km at the center of the model. Depth velocity slices through the model are shown in Figures 35 - 44. The first slice at the surface is used to show the extent of surficial coverage for the main line, the cross lines, and the Kingdome array (Figure 35). The other slices continue at 400 m intervals until the base of the basin is reached (Figures 36 - 43). Unfortunately, the southern two shots during the Kingdome experiment were not very strong and therefore we were not able to obtain additional raypaths crossing the Seattle fault (Figures 35 - 44). The crosslines added to the 3-D story in the upper 6 km (Figures 35 - 42). There is a low velocity zone at ~ 1.2 km depth along the easternmost cross line (Figure 38). This low velocity zone could

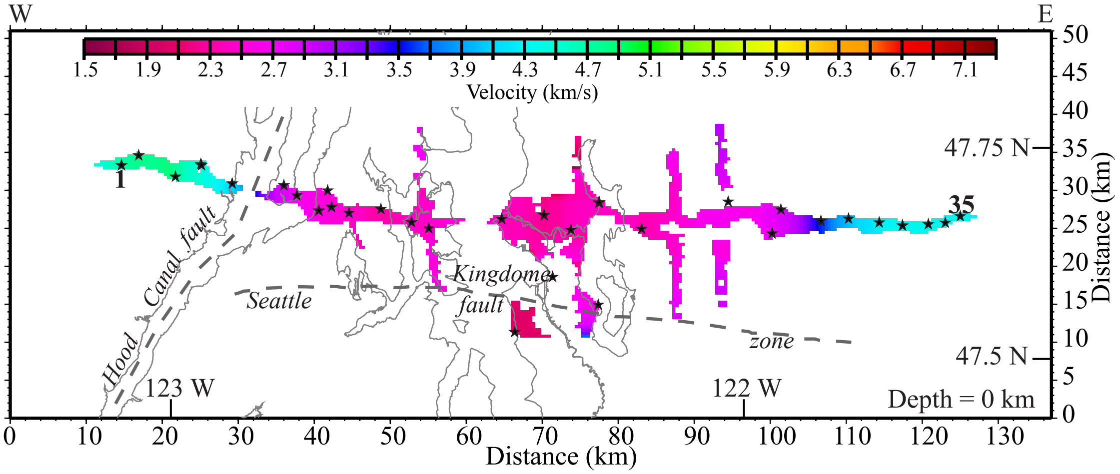

Figure 35. Masked velocity along the “Dry” SHIPS profile in map view at the surface. Small stars are shotpoint locations.

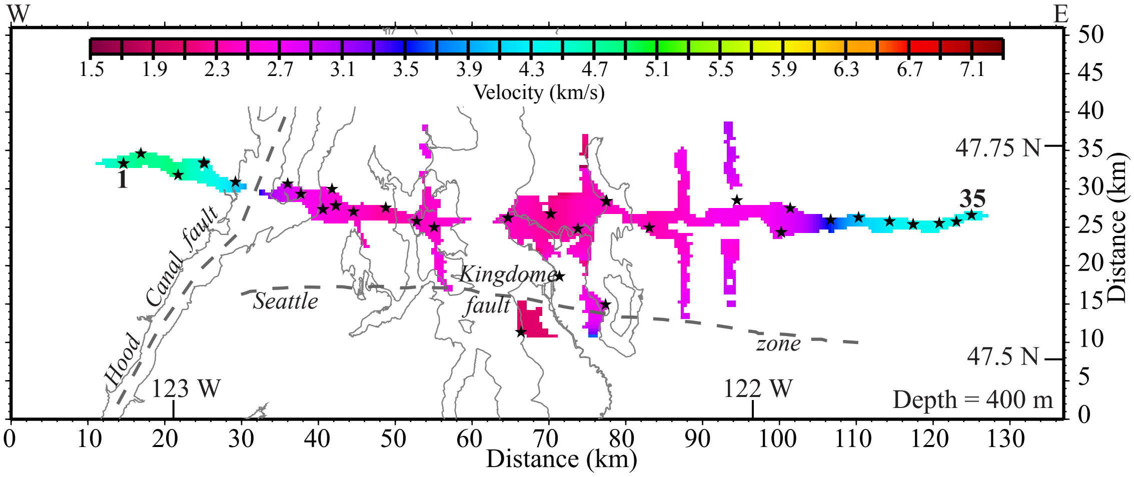

Figure 36. Masked velocity along the “Dry” SHIPS profile in map view at 400 m depth. Small stars are shotpoint locations.

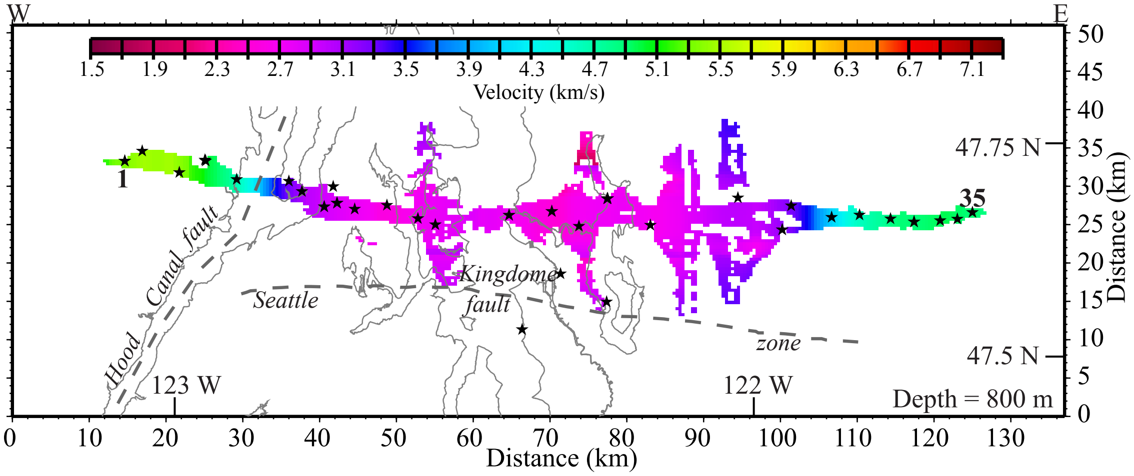

Figure 37. Masked velocity along the “Dry” SHIPS profile in map view at 800 m depth. Small stars are shotpoint locations.

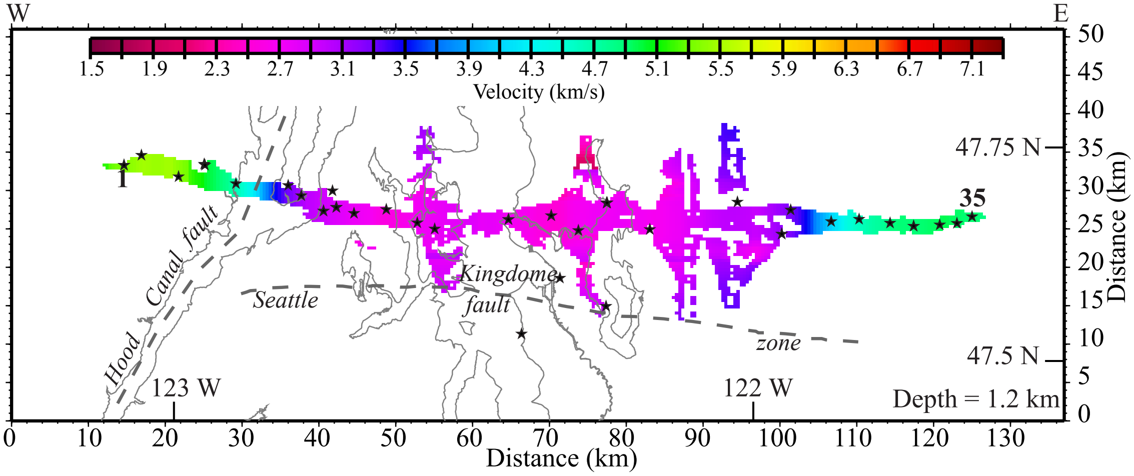

Figure 38. Masked velocity along the “Dry” SHIPS profile in map view at 1.2 km depth. Small stars are shotpoint locations.

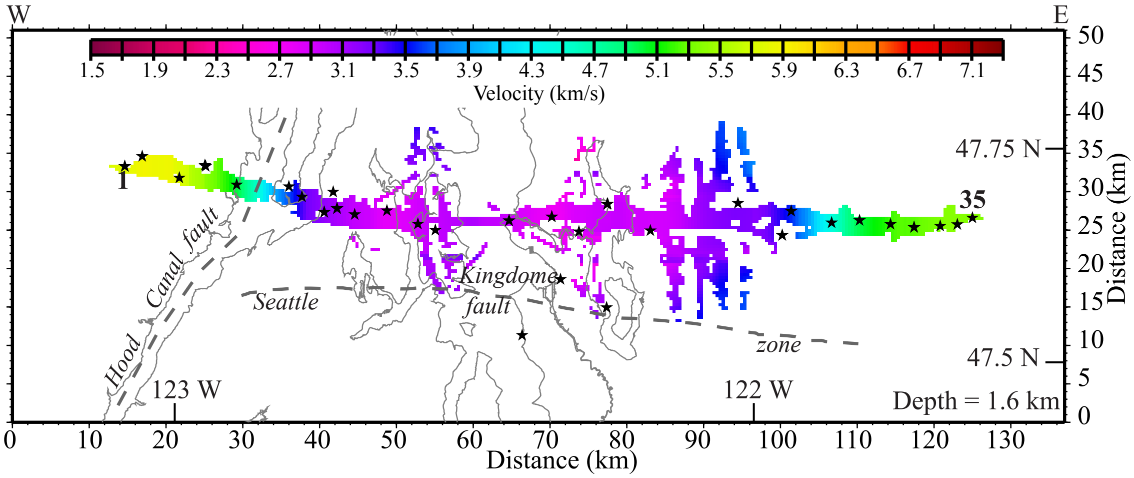

Figure 39. Masked velocity along the "Dry" SHIPS profile in map view at 1.6 km depth. Small stars are shotpoint locations.

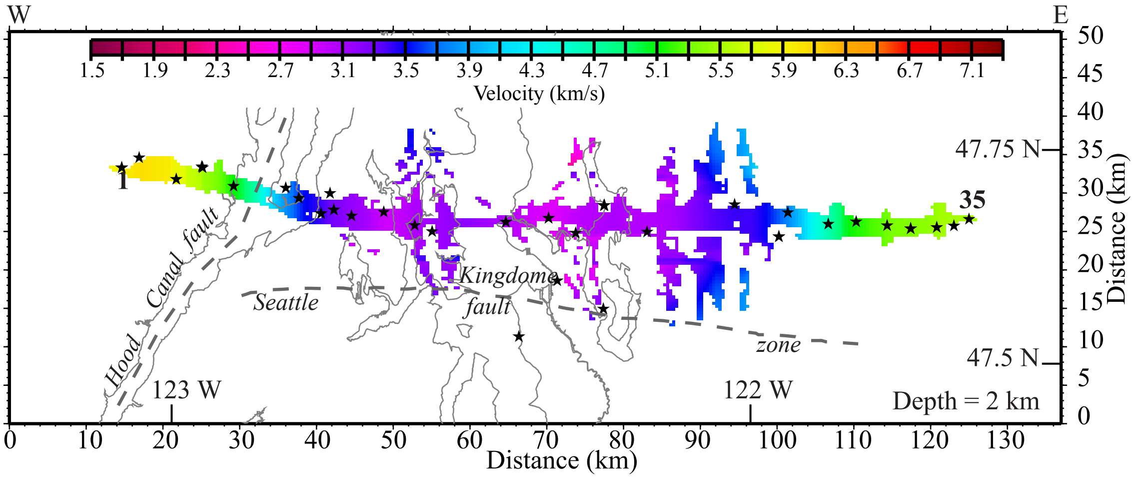

Figure 40. Masked velocity along the "Dry" SHIPS profile in map view at 2 km depth. Small stars are shotpoint locations.

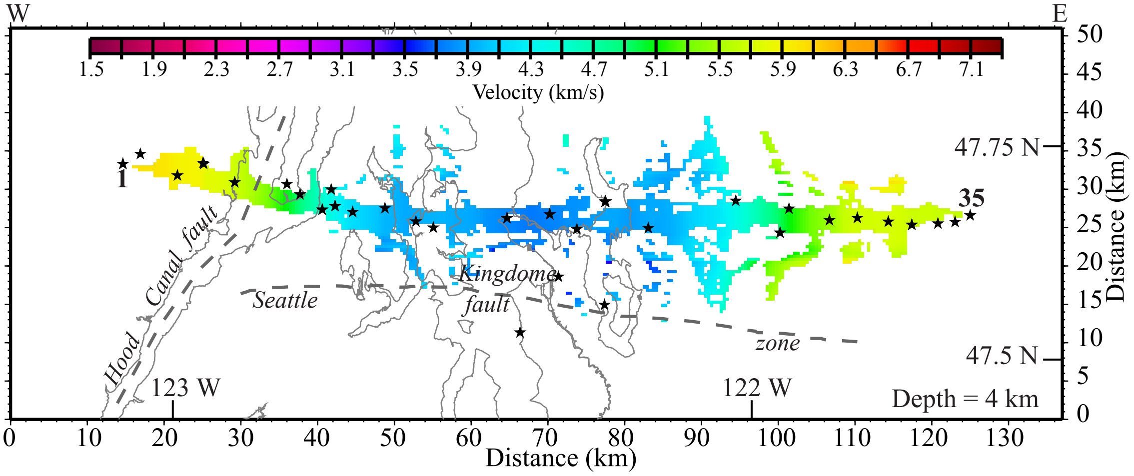

Figure 41. Masked velocity along the “Dry” SHIPS profile in map view at 4 km depth. Small stars are shotpoint locations.

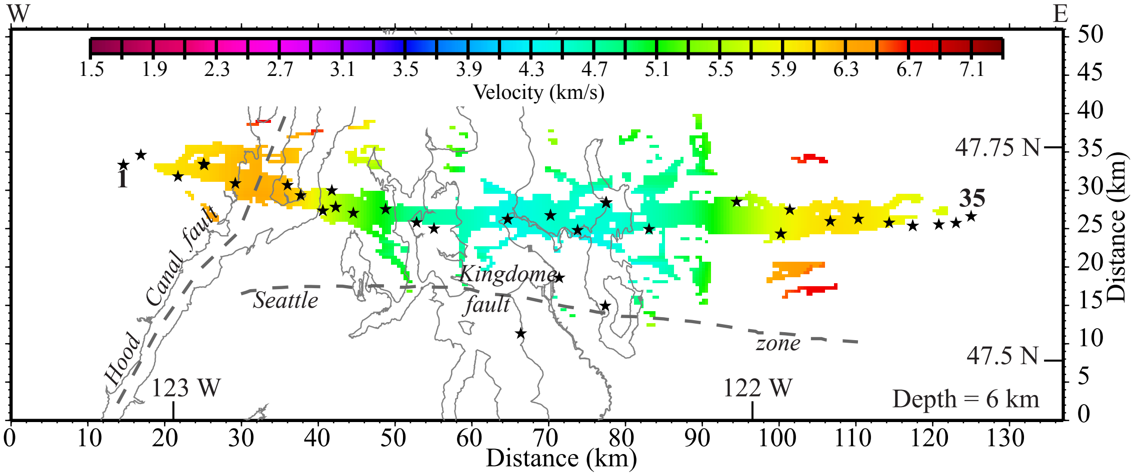

Figure 42. Masked velocity along the “Dry” SHIPS profile in map view at 6 km depth. Small stars are shotpoint locations.

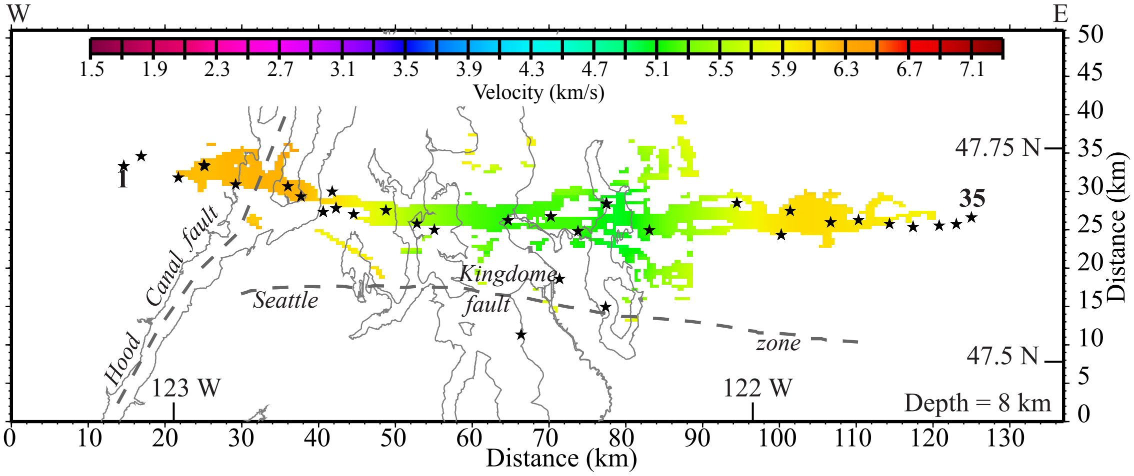

Figure 43. Masked velocity along the “Dry” SHIPS profile in map view at 8 km depth. Small stars are shotpoint locations.

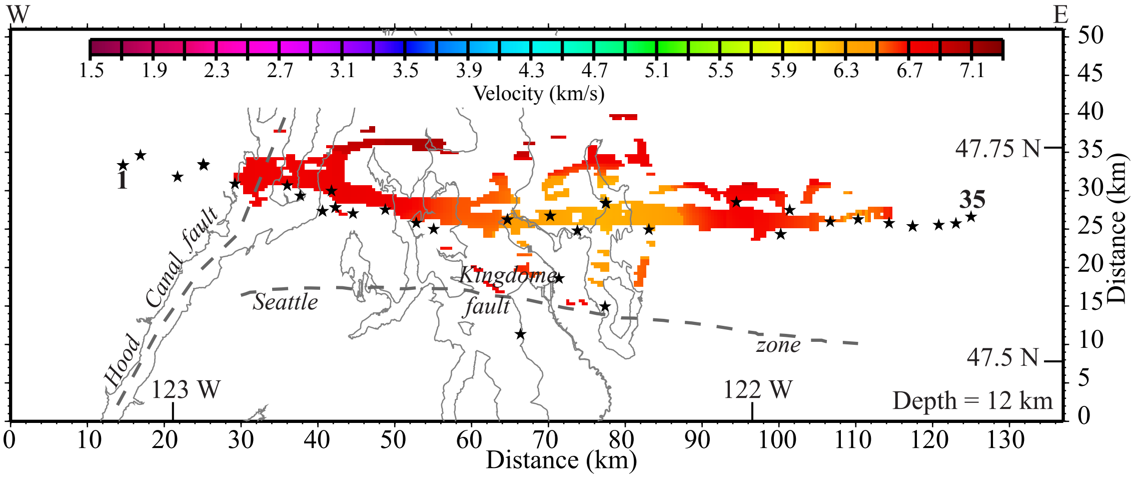

Figure 44. Ray coverage along the “Dry” SHIPS profile in map view at 12 km depth. Small stars are shotpoint locations.

be associated with a sub-basin within the larger Seattle basin, but this anomaly is not well resolved and requires further analysis.

Gravity

In order to see how the new “Dry” SHIPS velocity model fits into the existing gravity framework, a gravity model was constructed along the profile. In addition, the gravity model provided additional constraints to “Dry” SHIPS tomographic results. In the past, the gravity field has been a major source of information for understanding the structures within the Puget Lowland. First, a gravity map was constructed from data extracted from UTEP’s National database and merged with stations collected by the U. S. Geological Survey collected gravity along the “Dry” SHIPS profile (Figure 45) (Appendix A) (V. E. Langenheim, writ. comm., 2000). In order to look at the upper crustal contribution to the gravity field, a 2nd order polynomial fit was removed from the Bouguer anomaly. Gravity lows in this second order residual (Figure 46) shows the extent of the Seattle basin as well as several other basins within the Puget Lowland. The Olympic Mountains are represented by a large gravity low which is consistent with the lithologies within the exposed accretionary prism. A large gravity high between the Olympic complex and the Seattle basin is interpreted as the Siletz terrane (Figure 45).

Density Modeling

A gravity model was constructed along the “Dry” SHIPS transect (Appendix B) (Figure 45). Gravity values from stations within 1 km of the profile were extracted from the gravity database for use in a 2 ½ - D forward modeling program (Cady, 1980). The model was initially constructed using structures observed in the “Dry” SHIPS velocity model. Constraints on the east end of the model were provided from a gravity model

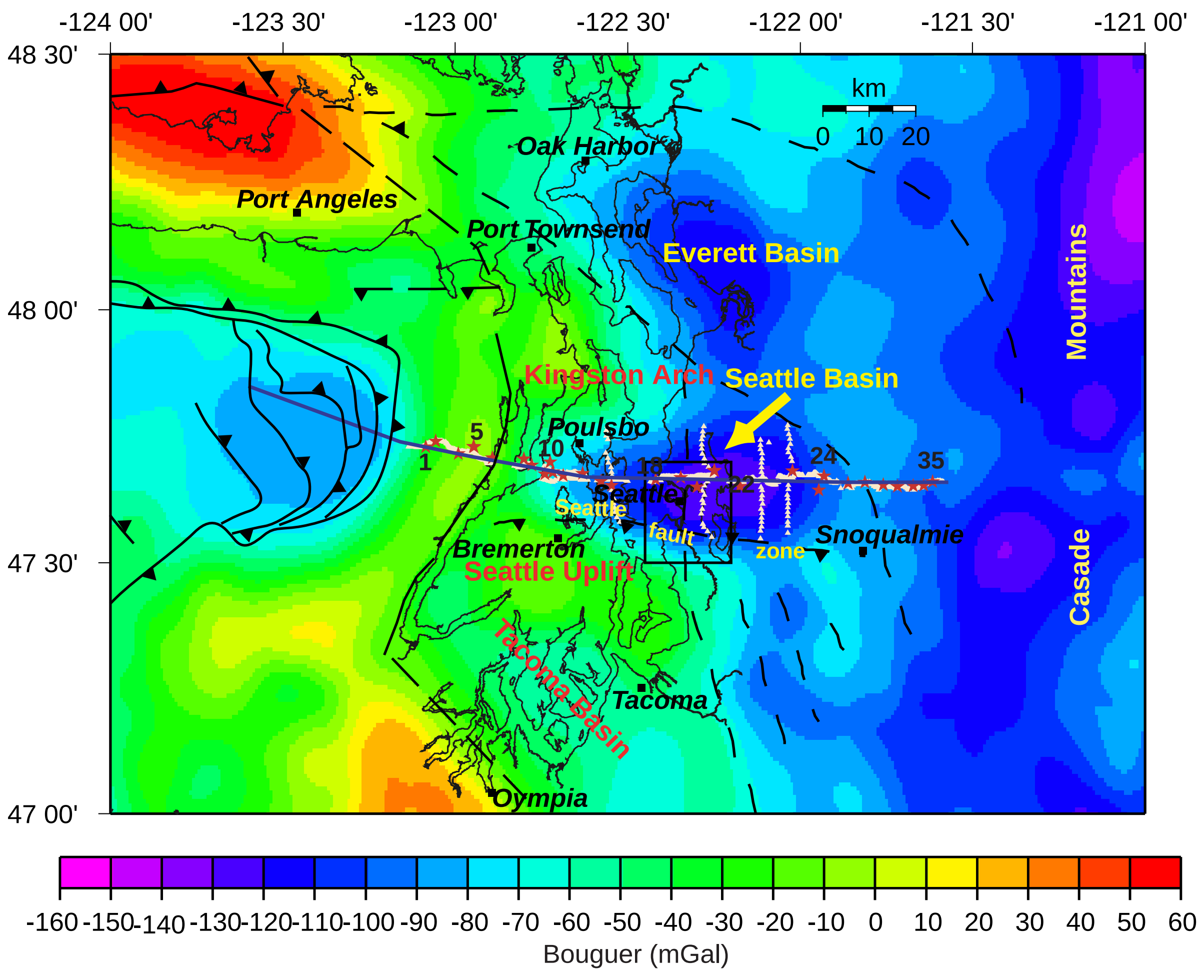

Figure 45. Bouguer gravity anomaly map. The “Dry” SHIPS profile is annotated in white with red stars for the shot points. The black square shows the Kingdome grid. The major basins and uplifts in the Puget Lowland are annotated. Faults are black lines and dashed where uncertain. The blue line is the profile used for gravity modeling.

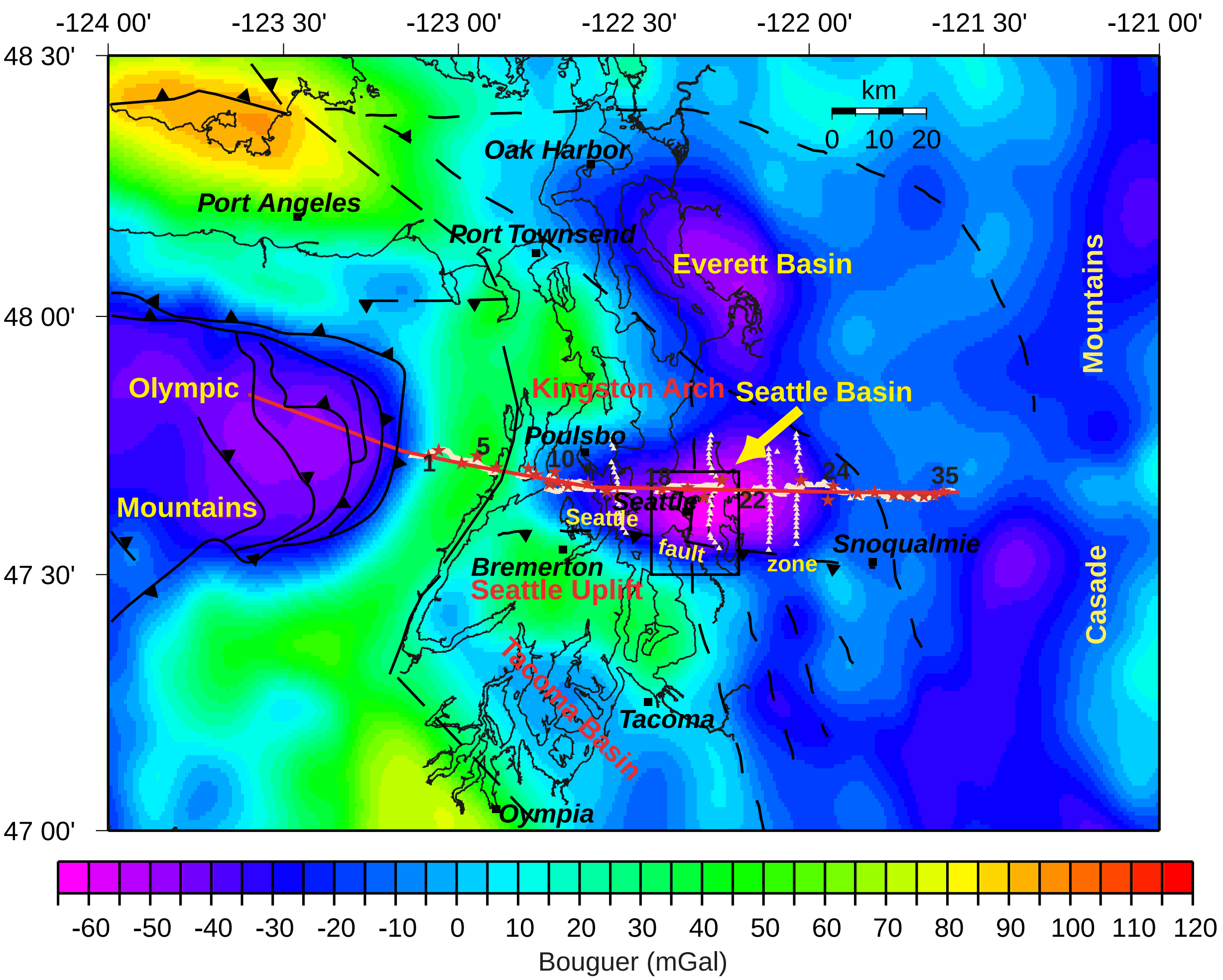

Figure 46. 2nd order residual of the Bouguer gravity anomaly. The “Dry” SHIPS profile is annotated in white with red stars for the shot points. The black square shows the Kingdome grid. The major basins and uplifts in the Puget Lowland are annotated. Faults are black lines and dashed where uncertain. The blue line is the profile used for gravity modeling.

constructed for PacNW ‘91 (Miller et al., 1997). The slab geometry was compiled from “Wet” SHIPS seismic studies of the Moho (Tréhu et al., 2001; Preston et al., 2001) and gravity models south of the study area (Finn, 1990; Parsons et al., 1998; Kilbride, 2000). A velocity model derived from a tomographic study of earthquake arrivals was also used as a guide for depths greater then 15 km (R. S. Crosson, person. comm., 2001). Near surface constraints were provided by existing geologic maps (e.g., Gower et al., 1985).

Initial densities were calculated using a typical velocity/density relationship (Christensen and Mooney, 1995) and from lab measurements of samples from local outcrops (Brocher and Christensen, 2001) (Figure 47). The accretionary wedge was assigned a density of 2560 kg/m^3 and the Siletz terrane has a density of 2890 kg/m^{3}on the basis of lab results obtained by Brocher and Christensen (2001). A pluton on the east end of the profile under the foothills of the Cascade Range was necessary to fit a small wavelength feature in the upper crust, which has a density contrast of 150 kg/m^3. The upper crustal rocks beneath the Cascades have a density of 2600 kg/m^3 which is consistent with PacNW ‘91 (Miller et al., 1997). The middle crust has a density of ~ 2800 kg/m^3, the lower crust has a density of 2900 kg/m^3, and the transitional layer has a density of 3150 kg/m^3 which is consistent with PacNW ‘91 (Miller et al., 1997). The oceanic crust has a density of 2900 kg/m^3, the upper mantle of the slab has a density of 3280 kg/m^3, and the downgoing crust and upper mantle of the slab has a density of 3300 kg/m^3, which is consistent with models south of the study area (Finn, 1990; Kilbride, 2000). The Cascade upper mantle wedge has a density of 3250 kg/m^3 (Miller et al., 1997) and the Juan de Fuca upper mantle has a density of 3280 kg/m^3 (Finn, 1990).

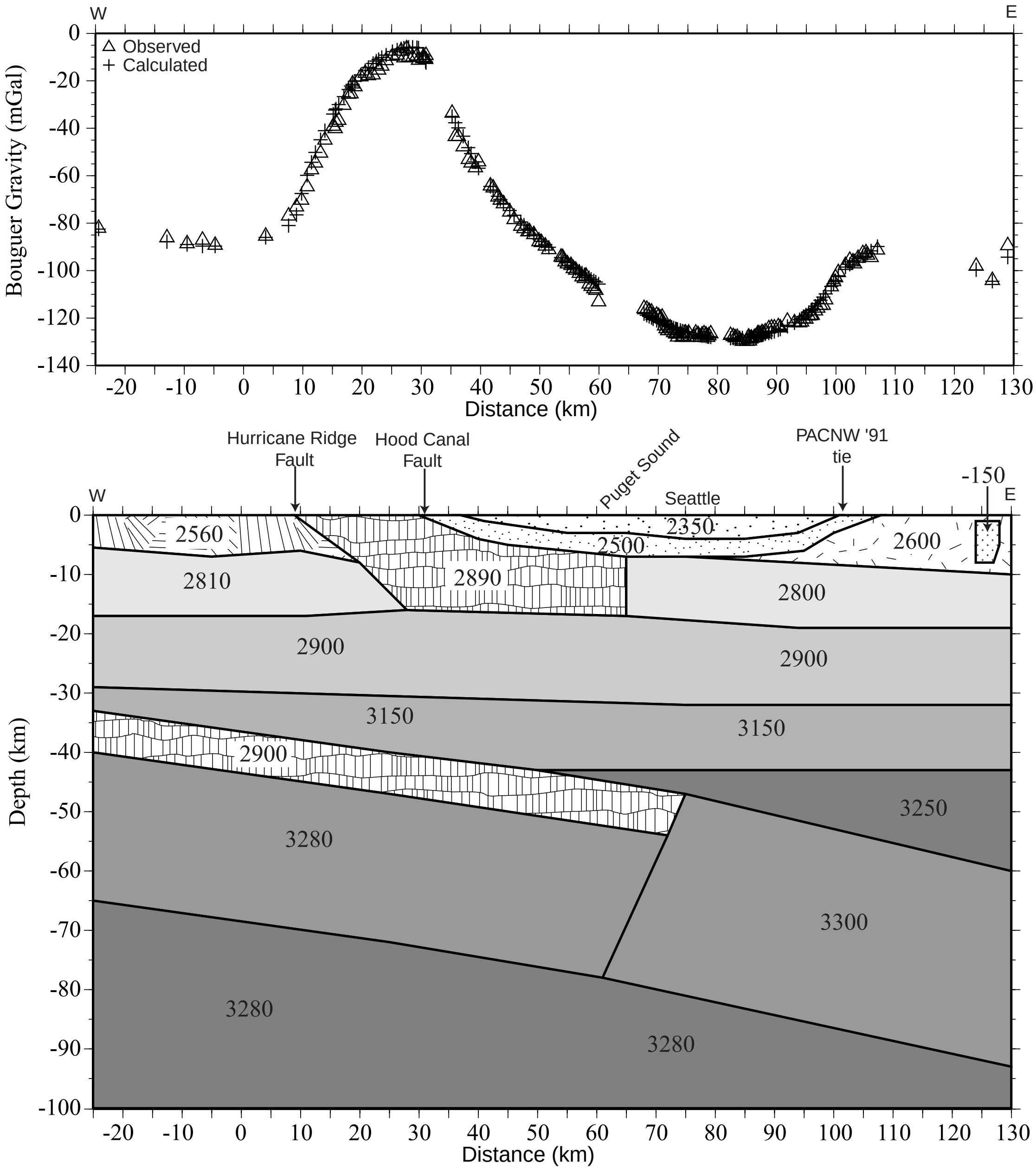

Figure 47. Preferred density model along the “Dry” SHIPS profile. Densities are in kg/m^3. Model coordinates are the same as used for the velocity model.

The large gravity signature is primarily produced by the contrast between the Olympic accretionary rocks, the Siletz terrane, and the Seattle basin. Deeper features such as the Juan de Fuca slab and upper mantle contribute little to the gravity signature. From west to east, the main features of the density model in the upper crust include the Hurricane Ridge fault, the Hood Canal fault and the Seattle basin (Figure 47). The Olympic accretionary wedge underthrusts the Siletz at the Hurricane Ridge fault and is underlain by denser material. The model (Figure 47) suggests that the Olympic accretionary complex is indistinguishable from the middle crust below 5 to 6 km depth. The Siletz terrane is distinguishable to a depth of 17 km and underlies the Seattle basin out to 65 km (Figure 47). Beneath the Seattle basin, the Siletz terrane is truncated near the location of the Coast Range Boundary fault. The Seattle basin is stratified with lower density, less consolidated material of about 4 km thickness and higher density, more consolidated material of about 3 km thickness. The oceanic plate is about 7 km thick and the slab dip about 7E out to a distance of 75 km where it increases its dip to 11E (Tréhu et al., 2001).

Two additional density models were created to test different geometries for the accretionary complex and the Siletz terrane. In both tests, the geometry of the Seattle basin was modified only slightly. The first model tests whether or not the Olympic accretionary complex can be extended to greater depth (Figure 48). To do this the accretionary rocks of the Olympics must be assigned a density of 2710 kg/m^3 which is significantly higher then lab results for these rocks (Brocher and Christensen, 2001). The Siletz terrane remains consistent with a density of 2910 kg/m^3 (Brocher and Christensen, 2001). This model also shows that the Olympic accretionary complex does not require a density contrast below 16 km.

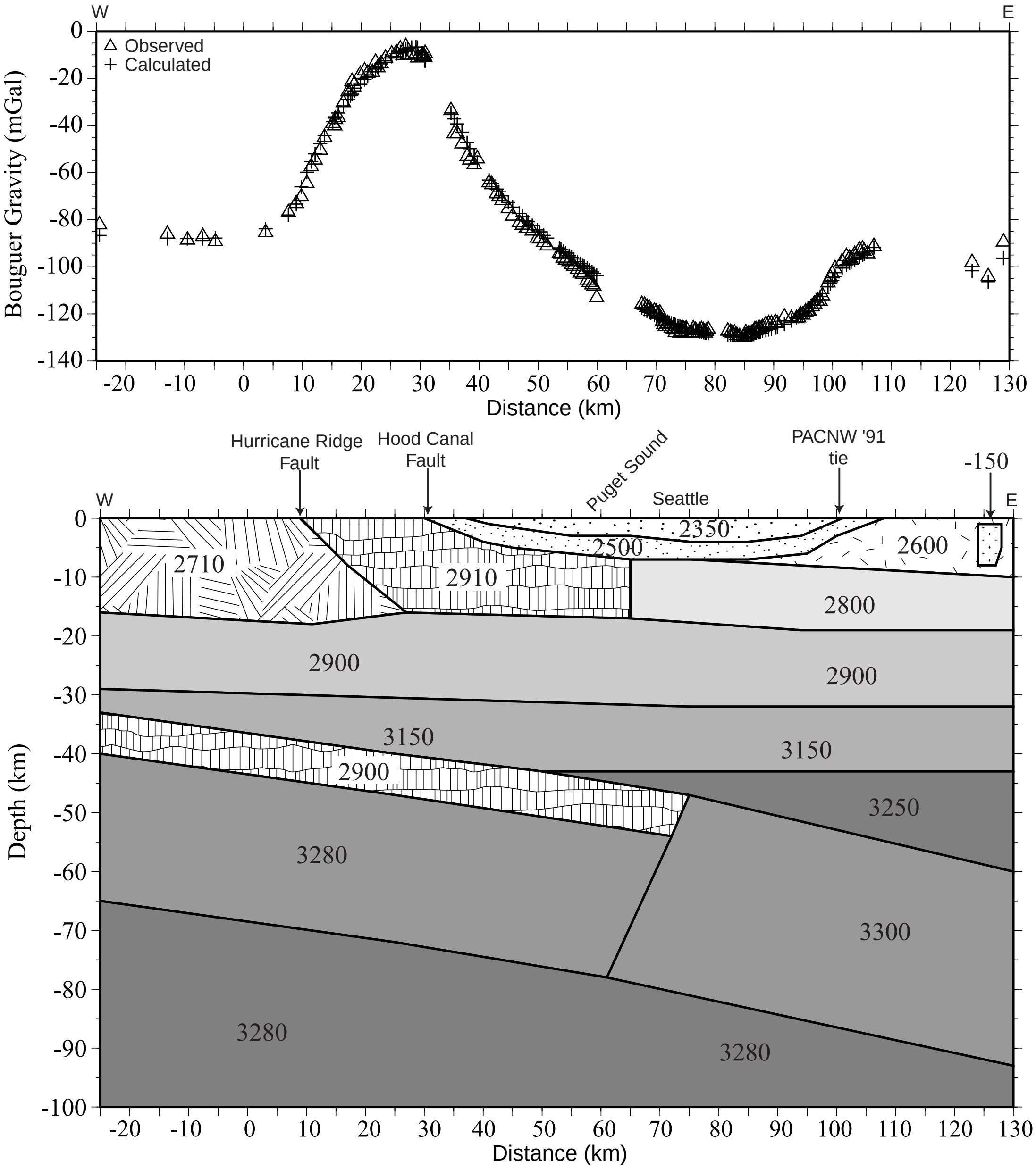

Figure 48. Alternative density model along the “Dry” SHIPS profile. Densities are in kg/m^3. Model coordinates are the same as used for the velocity model.

The second model tests whether or not the Siletz terrane extends to the middle of the Seattle basin (Figure 49). The only modification that was required for this model was a shallowing of the basin by 1 km. The densities for this model remain consistent with lab results and Figure 47. Therefore, the location of the Siletz/Cascade boundary cannot be determine with gravity alone.

The density model can be interpreted several different ways, but with the constraints of the seismic and other geologic data the upper 8 km of the model are well defined. The slab geometry is well defined by other studies (e.g., Tréhu et al., 2001), but the remainder of the model below 8 km becomes more speculative as to the true geologic structure. It cannot be determined where the Siletz terrane ends and the pre-Tertiary basement rocks begin, but the location of the eastern end of the Siletz terrane in the preferred density model is coincident with a change in the velocity field in the “Dry” SHIPS model (Figure 34).

Reflection Data Processing

The “Dry” SHIPS experiment was also designed to produce a low-fold stack by using close station spacing and relatively frequent shots. The processing and interpretation of the stack are still in the initial stages of analysis. Once the stack is completed, it will provide for further interpretation of the mid- to lower crust since the velocity models were only able to image the crust to 16 km depth.

Low Fold Stack

The first step in producing the stack was to define 2-D crooked line geometry (Figure 50). This step was accomplished first by setting the receivers and shots into the database and then defining a pattern. Once the pattern was established then a track through the

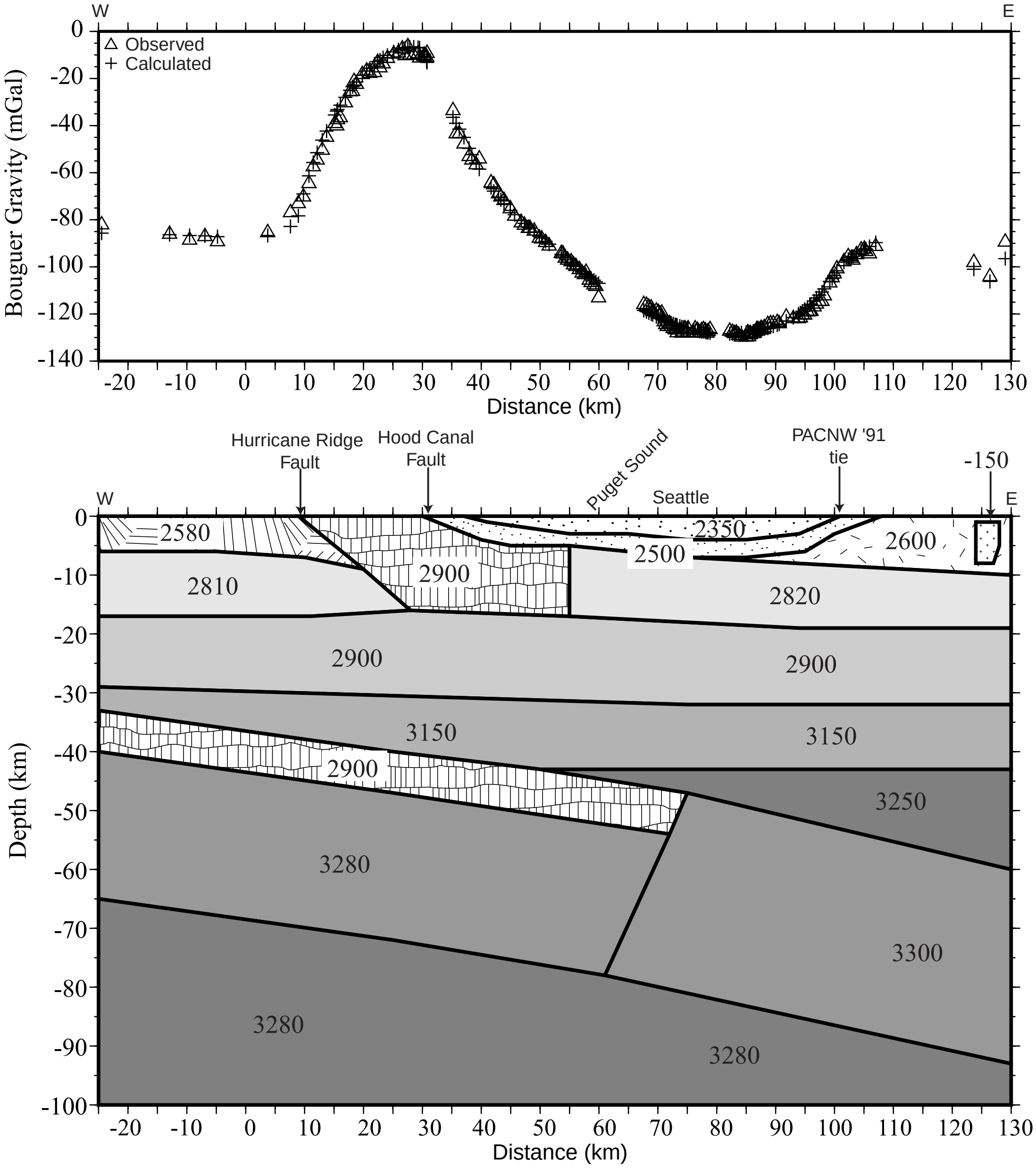

Figure 49. Alternative density model along the “Dry” SHIPS profile. Densities are in kg/m^3. Model coordinates are the same as used for the velocity model.

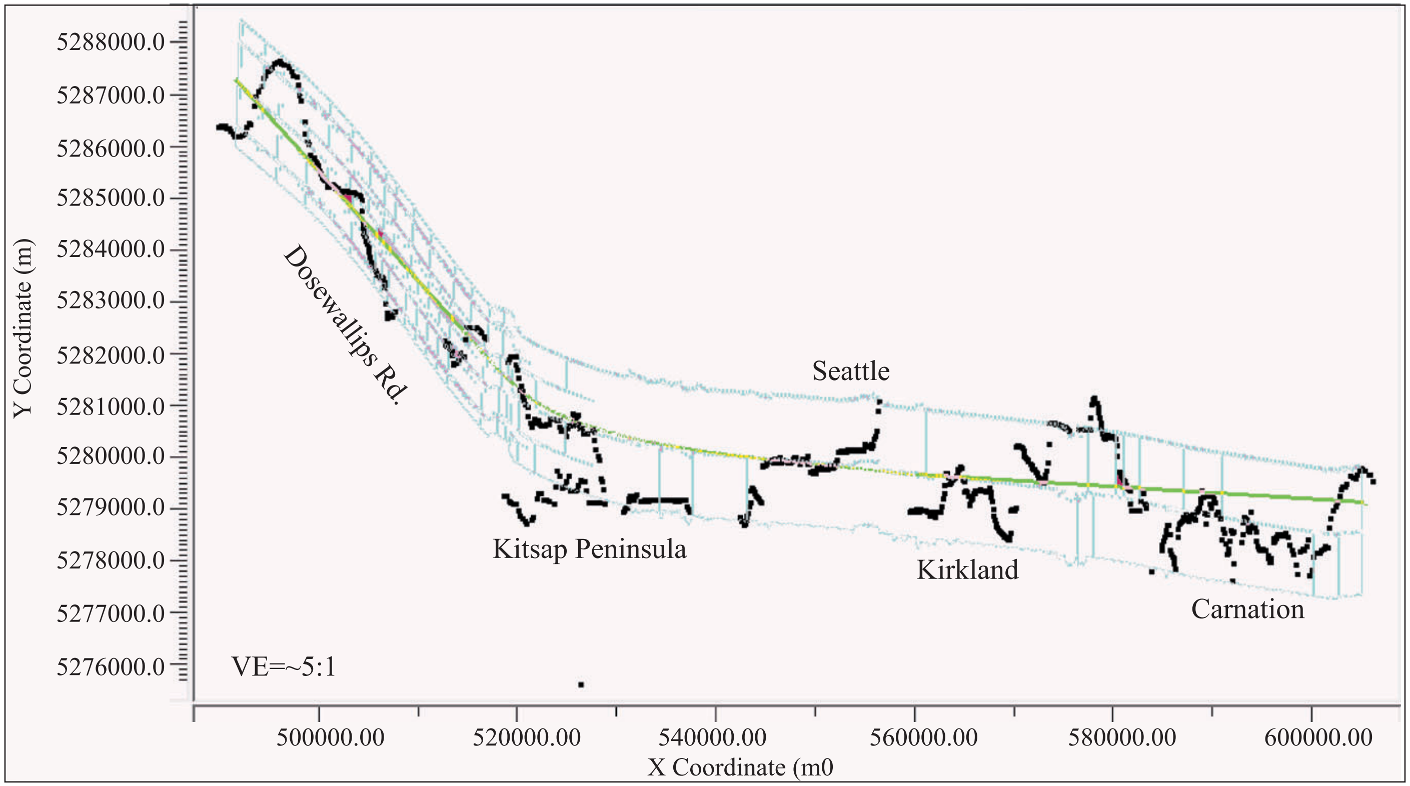

Figure 50. Map of the bin locations along the “Dry” SHIPS profile. Black dots are the stations. The green/yellow line is the track of the geometry. The light blue lines are the bins for the crooked line geometry.

receivers was chosen. From this track, a bin size of 200 m was assigned and adjusted for misfits. Finally, the mid-points were assigned to the bins.

The next steps in the processing were application of trace mutes and kills, elevation statics, true amplitude recovery, deconvoution, bandpass filter, and a sort to the CDP gathers. The final P-wave tomographic model was used for the interval velocity and converted to RMS stacking velocity. The converted velocity field provided a starting model for velocity analysis. Once the velocity analysis was completed then an AGC (amplitude gain control) of 2 s was applied, followed by NMO (normal moveout correction), ensemble balance, CDP (common depth point)/ensemble stack, bandpass filtering, coherency filtering, and finally a time to depth conversion using a lower resolution tomographic model was used to estimate the interval velocities. The nominal fold for the data is 25. The processing flows and parameters for the low-fold stack are in Table 1.

Initial Interpretation of Reflection Section

The low-fold reflection line provided an opportunity to analyze the data to greater depths compared to the “Dry” SHIPS tomography. The low-fold stack contains a series of reflectors which may line up with imaged structures in the sub-surface (Figure 51). In order to see these features more clearly the stack is overlain on a lower resolution tomographic result (Figure 52) (R. S. Crosson, person. comm., 2001). Reflections in the upper part of the stack appear to line up with the velocity field that represents the basin of velocities less then 4.5 km/s (Figure 52). There is a deeper reflector, which may line up with the top of the oceanic plate at a depth of ~ 30 km on the west side of the stack and dips to the east along a high velocity layer to a depth of 55 km at about CDP 600 (Figure 52).

Table 1: Data processing flows and parameters for the “Dry” SHIPS profile.

Processing	Parameters
Source Domain Processing	
Sort traces for main line	
Merge single shot gathers	
Crooked line geometry	
Trace Editing	
Top Muting	
Elevation Statics	0.0 m datum 1800 m/s replacement velocity
Amplitude correction	5000 ms operator length
Predictive deconvolution	300 ms prediction length 30 ms lag
Bandpass filter	2-8-20-30 Hz Butterworth
CMP Sorting	
CDP Domain Processing	
Import “Dry” SHIPS P-Wave velocity model	
Velocity analysis	
Normal moveout correction	
Ensemble balance	
CMP Stack	
Post-Stack Processing	
F-X deconvolution	8-50 Hz Wiener Levinson
Time-variant (TV) bandpass filter	2-8-50-60 Hz 0-7000 ms 2-8-30-40 Hz 8000-20000 ms
Coherency filter	1140 traces 1000 ms length
Time/Depth Conversion	Interval velocity in depth

I will be using alternative stacking methods in anticipation that there will be more reflections to interpret and match those with existing structures in both the low resolution tomographic image and the “Dry” SHIPS tomography.

Figure 51. Low-fold stack along the “Dry” SHIPS profile. Converted to depth.

Figure 52. Low-fold stack along the “Dry” SHIPS profile. Converted to depth with a low resolution tomographic image in the background (R. S. Crosson, person. comm., 2001).

Initial S-Wave Tomography

The horizontal component data was fair to good, several shots have shear wave arrivals across the length of the section (Figure 53). Many of the shot records for the horizontal components are highly reverberatory, which makes picking the S-wave arrivals difficult.

First arrival times for over 1500 S-wave arrivals were picked from the data to use in the tomographic code. Initially, the P-wave first arrival times were used as a guide for picking the S-wave arrival times. This worked as a first order approximation. The arrivals were inverted using the 3-D approach by Hole (1992) as described previously. The starting model for this inversion was converted from the final P-wave model. We converted the P-wave velocities to S-wave velocities using a Vp/Vs ratio of 1.8 which is consistent with the high velocity rocks in the region (Brocher and Christensen, 2001).

The initial model was set up with a 1 km grid cell spacing versus the 400 m grid cell spacing for the P-wave tomographic model. The RMS for the current model is ~ 500 ms. This RMS is rather high and I am in the process of evaluating the picks to reduce this to a more reasonable RMS of about 200 to 300 ms.

The initial S-wave model shows velocities in the basin ranging from 0.5 km/s up to 2.5 km/s (Figure 54). A gradient at 3.0 km/s likely indicates the basin/basement contact. The major difference from the P-wave model is the appearance of the basin to extent more gently towards the Cascades. Velocity increases with depth up to 5.0 km/s.

From the S-wave model a model of Vp/Vs was created using the P-wave model (Figure 55). These values can then be used to estimate the type of material within the Seattle basin. A typical Vp/Vs ratio for hard rock is ~ 1.8 is this region (e.g., Christensen,

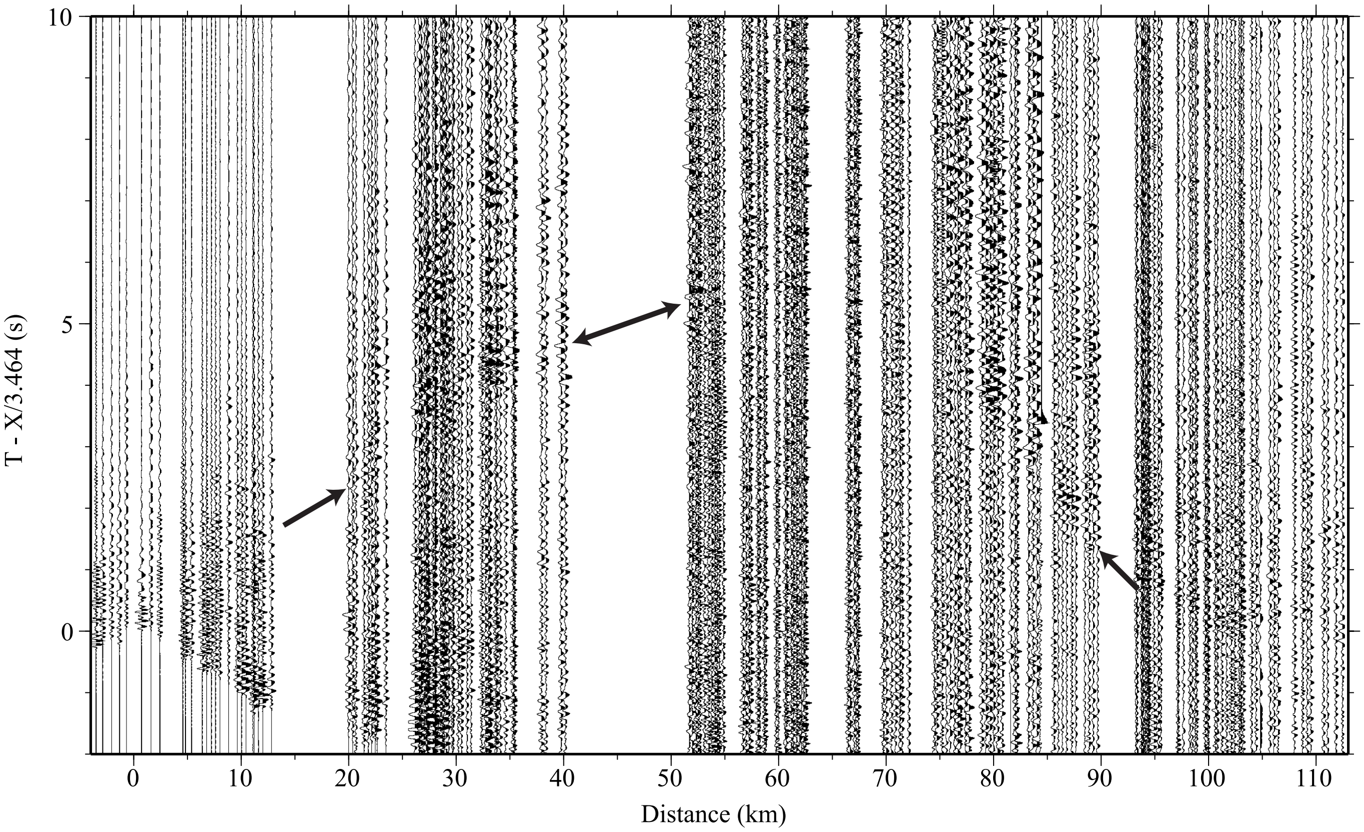

Figure 53. Seismic record section from the horizontal east - west component for shotpoint 1a. Arrows indicate S-wave arrivals. The data is reduced at 3.464 km/s.

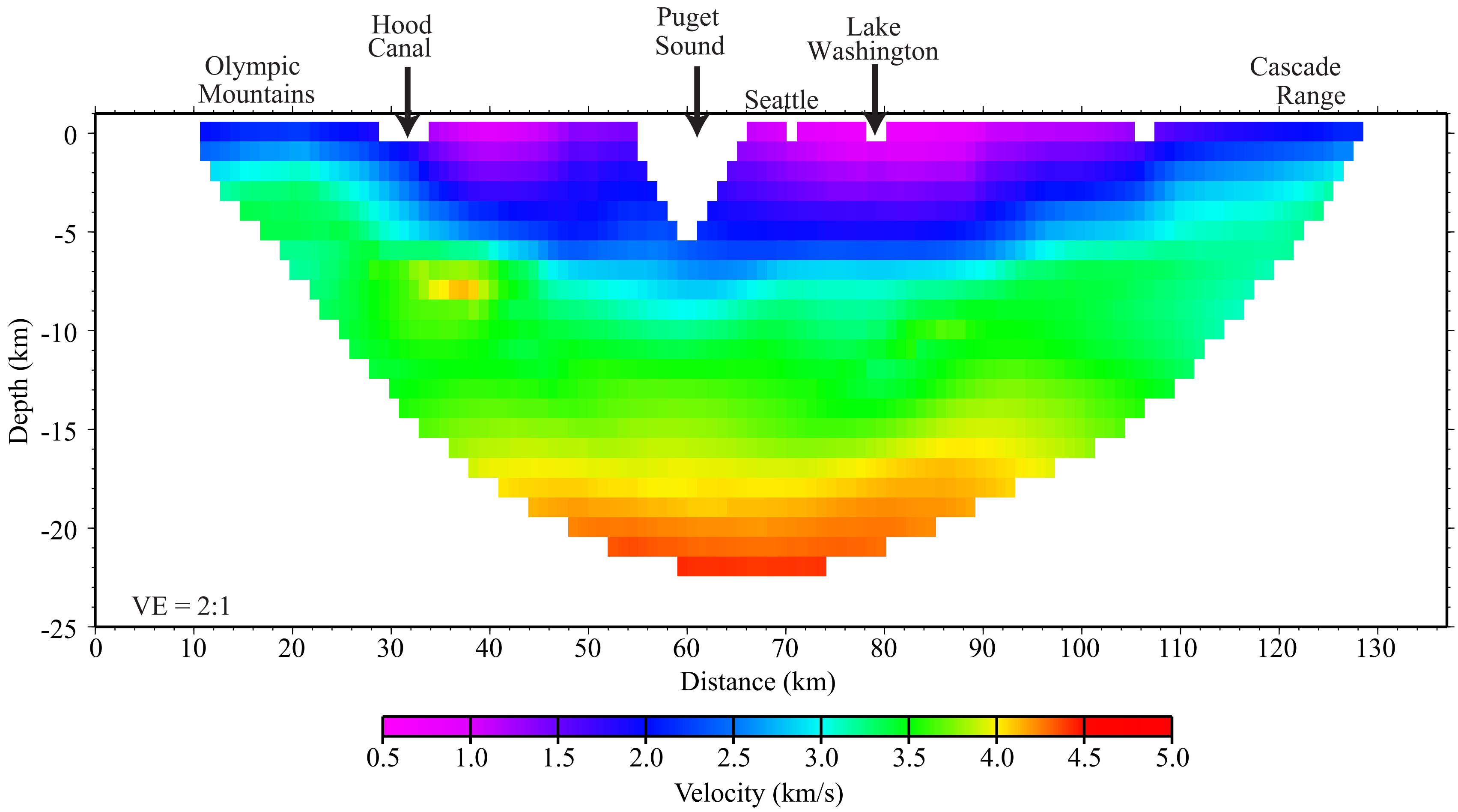

Figure 54. Shear-wave model along the “Dry” SHIPS profile.

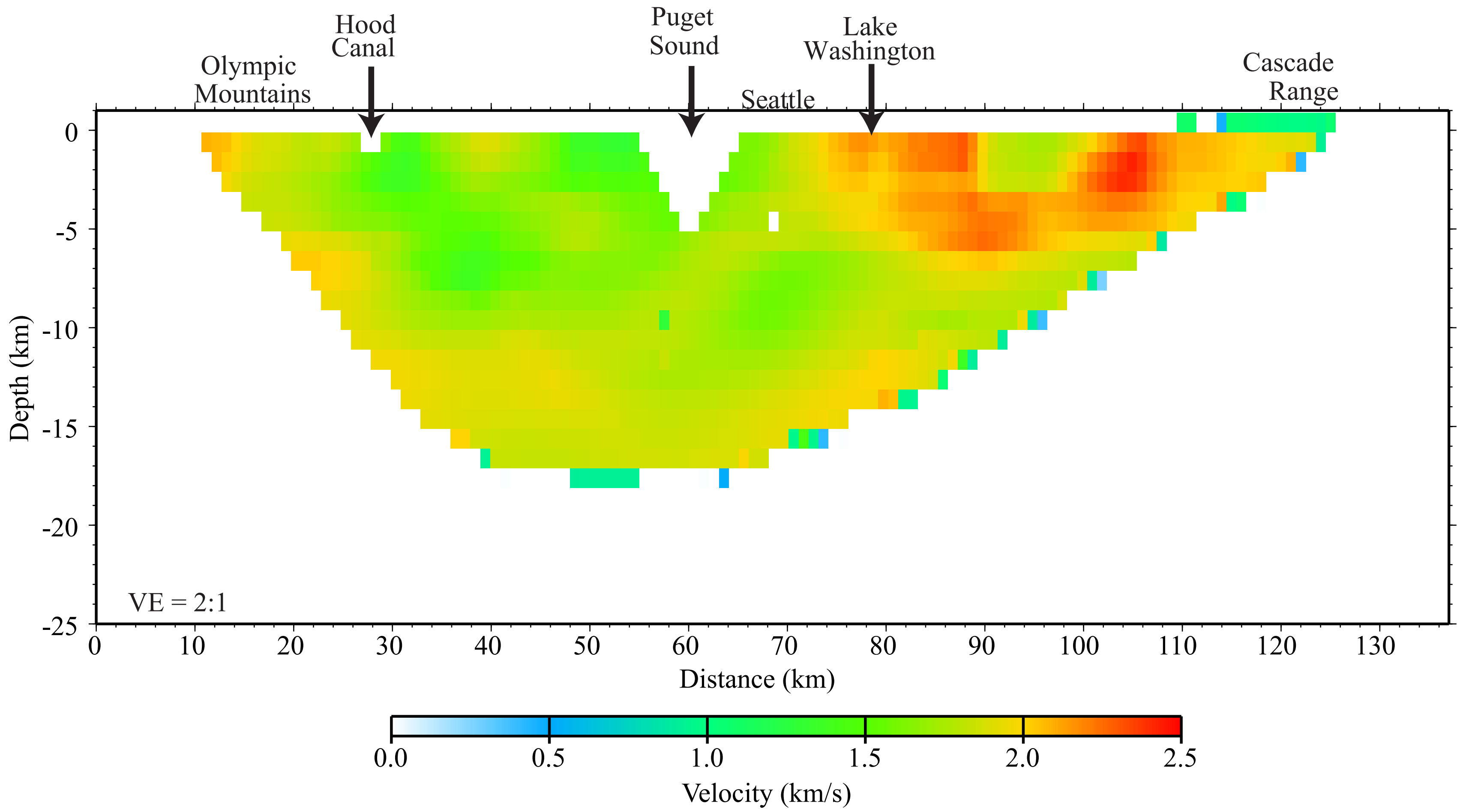

Figure 55. Vp/Vs along the “Dry” SHIPS Profile.

1982; Holbrook et al., 1992). A typical Vp/Vs ratio for clean sandstones is 1.6 to 1.7 (e.g., Winkler and Murphy, 1995). Poorly consolidated sandstones have a Vp/Vs ratio of ~ 2.0 (e.g., Mavko et al., 1998).

The “Dry” SHIPS ratio model shows low Vp/Vs ratios of 1.8 west of the Puget Sound which is consistent with estimates from experimental studies as well as published estimates (Christensen, 1982; Holbrook et al., 1992; Brocher and Christensen, 2001). The ratio is 2.0 or greater east of the Puget Sound which is consistent with a saturated material (e.g., Mavko et al., 1998).

The “Dry” SHIPS Poisson’s ratio model shows what has been expected for the Seattle basin. The basin under the city of Seattle contains primarily poorly unconsolidated saturated sedments in the upper km. The ends of the model are on hard rock. The areas of extremely high ratios will be likely candidate for large ground shaking when an earthquake occurs, which is consistent with a recent study of the Chi-Chi earthquake recorded during the “Dry” SHIPS experiment (Pratt et al., in review). As the modelling progresses these values will become more reliable.

Discussion

Seattle Basin Geometry - P-Wave Results

Results from “Wet” SHIPS suggest that the Seattle basin contains several sub-basins (Figure 56) (Brocher et al., 2001). In map view, the “Dry” SHIPS results suggest a sub-basin in only the eastern portion of the model (Figure 36), however, in cross section there is some evidence for four sub-basins in the velocity contours (Figure 57). The density model does not require a distinction of sub-basins (Figure 47). This can be explained by subtle changes within the basin in terms of the deposition of the sediments and does not

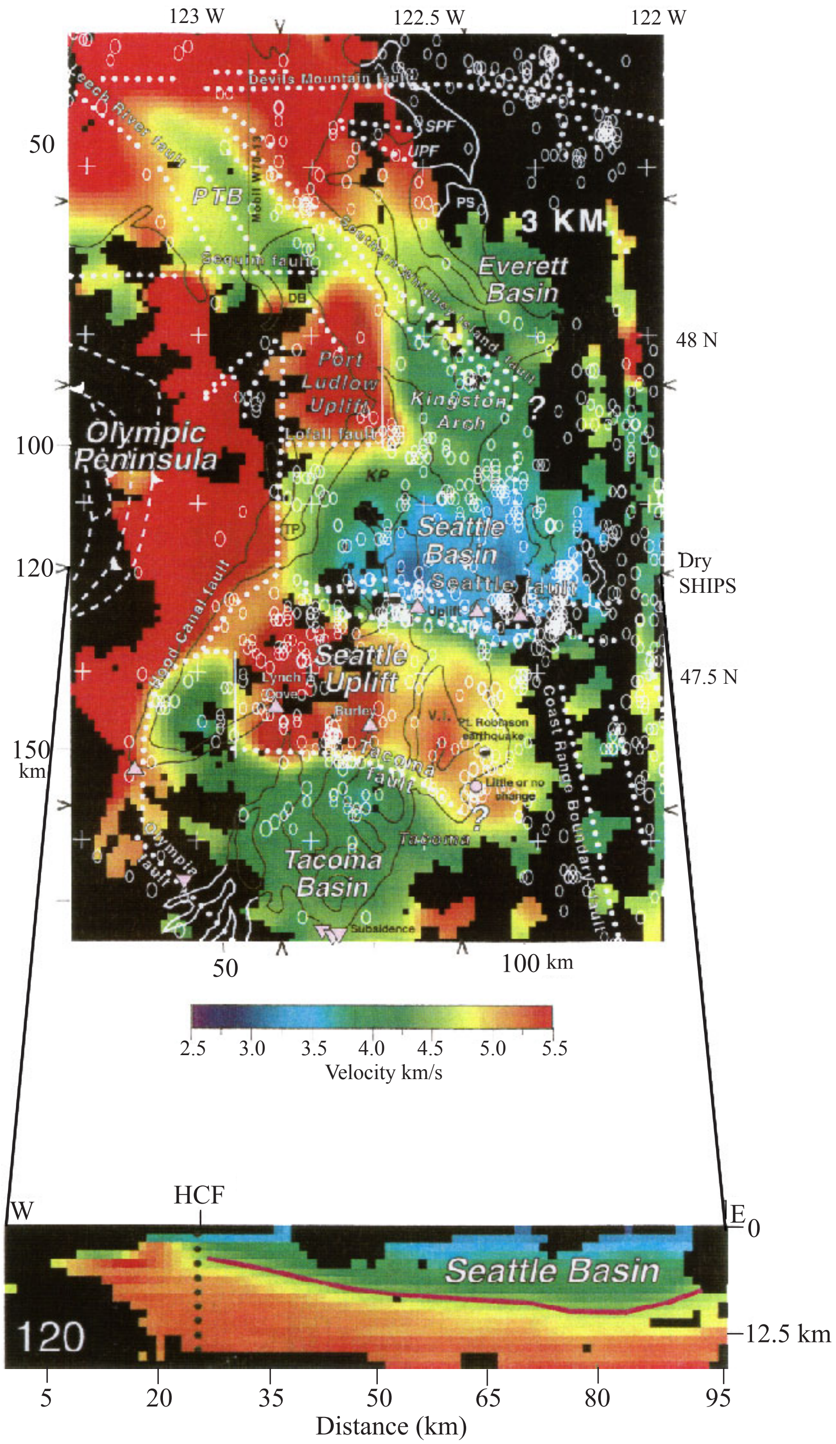

Figure 56. Tomographic profiles across the Seattle basin from Brocher et al. (2001). Profile 120 shows an estimated depth of the basin as well as the geometry of the basin, which is asymmetric. "Dry" SHIPS model coordinated are located along the base of the cross section.

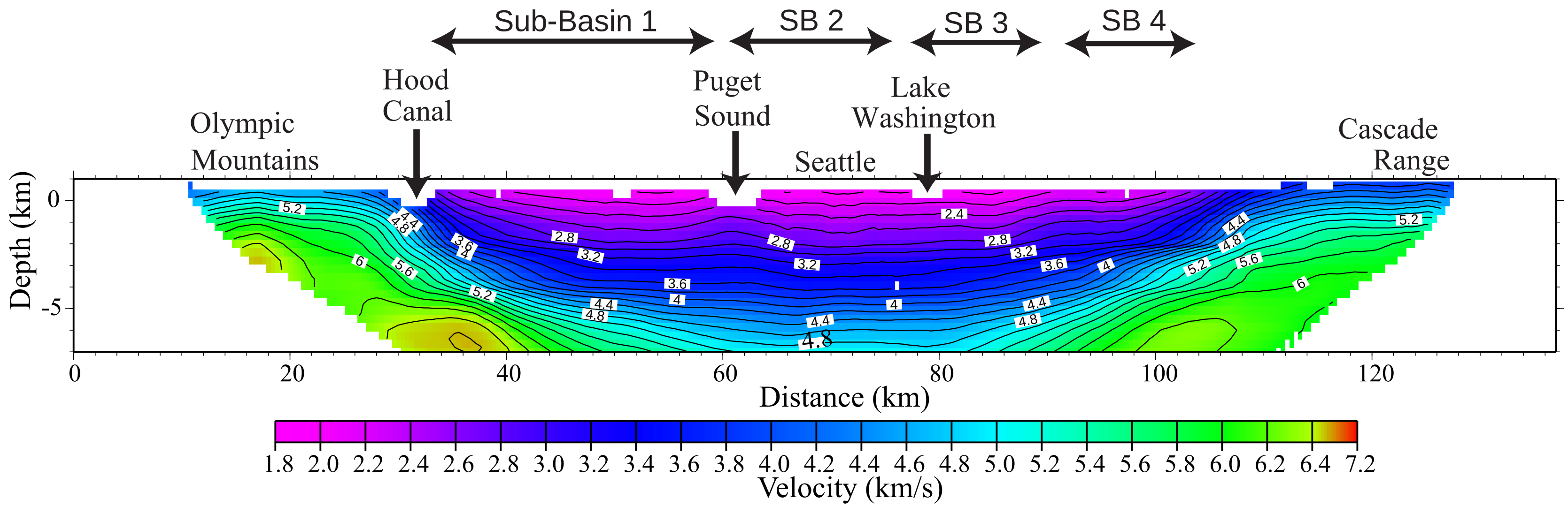

Figure 57. Zoomed portion of the “Dry” SHIPS model. Contour interval is 0.2 km/s. The 4 Sub-Basins (SB) are labeled at the top.

require distinct structural features. The “Dry” SHIPS profile extended further east than Brocher et al. (2001) and provides additional information for the entire basin (Figure 57). The length of the basin is about 70 km measured from Hood Canal to a step up in contours on the eastern portion of the model. The length of the Seattle basin can be used to determine the length of the Seattle fault. The Seattle basin is symmetric, therefore, either the bounding faults are active and moving at the same rate or that the Seattle fault is the source controlling the geometry of the Seattle basin.

A tie to a N-S reflection line within the Puget Sound from the “Wet” SHIPS '98 results confirms that the depth to the top of basement along the “Dry” SHIPS profile is 6 km (Figure 58) (ten Brink, in review). This reflection line is tied to the Mobil-Kingston well #1, where the stratigraphy is well defined. The velocity field from the N-S line also correlates well with the “Dry” SHIPS profile (Figure 59). On the N-S line, the 4.5 km/s contour correlates with the top of the Siletz as marked by from the Mobil-Kingston well where the top of Siletz is interpreted as basalt interbedded with siltstone, tuff, and conglomerate (Rau and Johnson, 1999). These results also show the basin is asymmetric in the north-south direction.

Industry seismic reflection data compiled by Pratt et al. (1997) have interpreted the top of the Siletz terrane to be much shallower than the “Dry” SHIPS result. Pratt et al. (1997) used interval velocities to make this interpretation and probably underestimated the depth to the top of Siletz terrane. Since, the north-south reflection line from “Wet” SHIPS data has a velocity model determined thru first arrival inversion that overlays the reflection profile (ten Brink et al., in review), the top of Siletz at the 4.5 km/s contour is probably more reliable in ten Brink et al. (in review) than in Pratt et al. (1997).

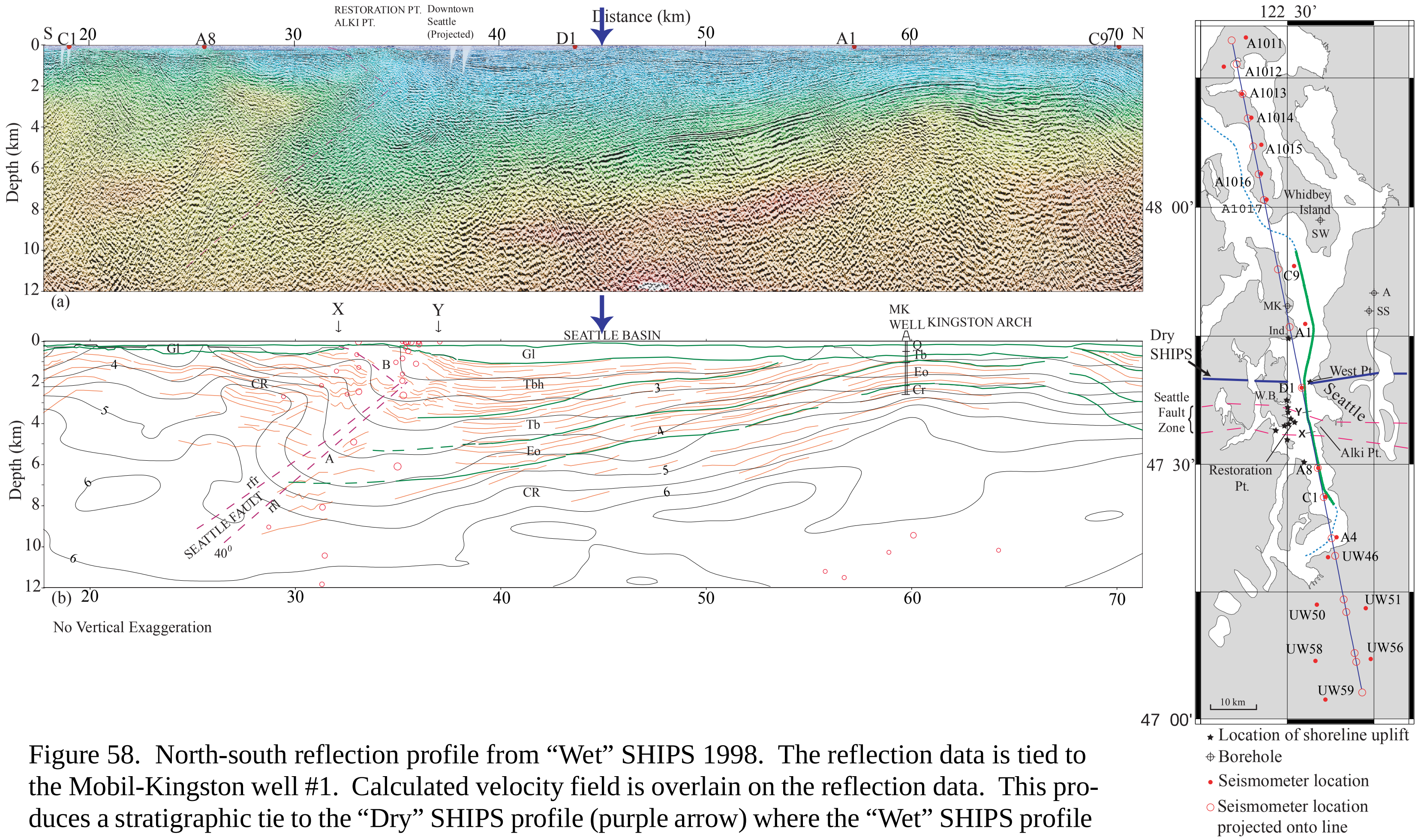

Figure 58. North-south reflection profile from "Wet" SHIPS 1998. The reflection data is tied to the Mobil-Kingston well #1. Calculated velocity field is overlain on the reflection data. This produces a stratigraphic tie to the "Dry" SHIPS profile (purple arrow) where the "Wet" SHIPS profile crosses (after ten Brink et al., in review).

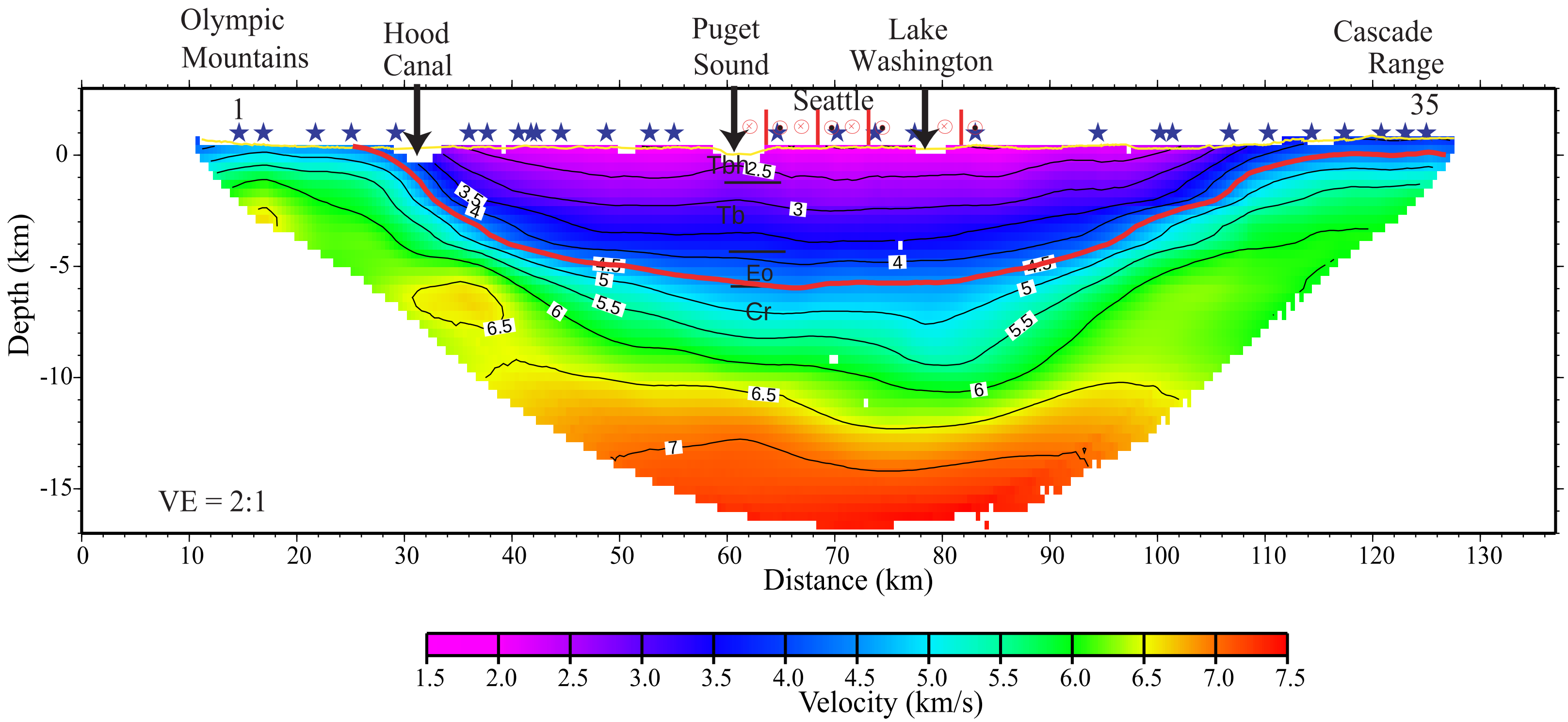

Figure 59. Final “Dry” SHIPS model. Contour interval is 0.5 km/s. The red contour represents the basin/basement contact. The stratigraphy from ten Brink et al. (in review) is overlain on the model.

Crustal Configuration - P-Wave Results

Deeper velocities in the “Dry” SHIPS model are consistent with other tomographic studies (Brocher et al., 2001; Van Wagoner et al., in review; R. S. Crosson, person. comm., 2001). East of the Puget Sound at about 70 km there is a decrease in velocity in the upper part of the crust (Figure 60). This is consistent with the density model as the edge of the Siletz terrane as found in the density model (Figure 47). This contact is also consistent with postulated strike-slip faults through the Puget Sound (Figure 60). These strike-slip faults are also coincident with seismicity in the upper 5 km (Figures 12 & 60). A lower resolution tomographic result shows the Olympic accretionary complex underthrusting the Siletz terrane (Figure 61, R. S. Crosson, person. comm., 2001), due to the ray coverage, the underthrusting is not imaged in the “Dry” SHIPS tomographic model. The density model is consistent with underthrusting at shallow depths (Figure 47).

One dilemma that remains unresolved is whether or not the deformation in the Puget Lowland is thin skinned or thick skinned. Pratt et al. (1997) argues that deformation beneath the Puget Lowland is thin skinned from the interpretation of industry seismic data where the décollement is at about 17 km depth. Our velocity model neither confirms nor rules out this interpretation. The density model on the other hand could be consistent with this interpretation, the base of the Siletz and/or pre-Tertiary rocks are at a depth of 17 km. The thick skinned interpretation (Wells and Weaver, 1993) requires the décollement at a depth of about 24 km which is below the region imaged by the velocity model.

Summary

The “Dry” SHIPS data has provided several new results that will help in further assessment of the seismic hazard for the Puget Lowland. The tomographic model shows

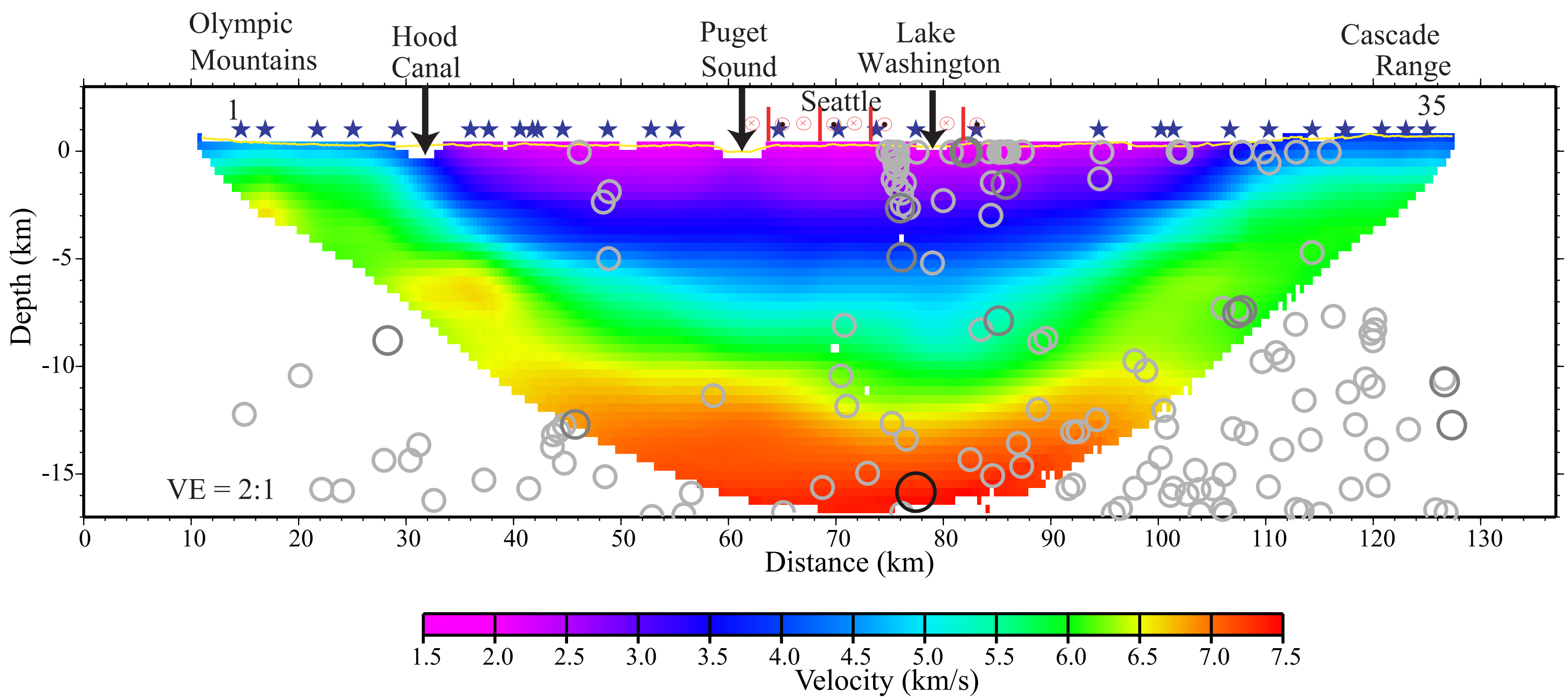

Figure 60. “Dry” SHIPS model with seismicity overlain. Magnitude scale is the same as Figure 13. The red lines are postulated strike-slip faults.

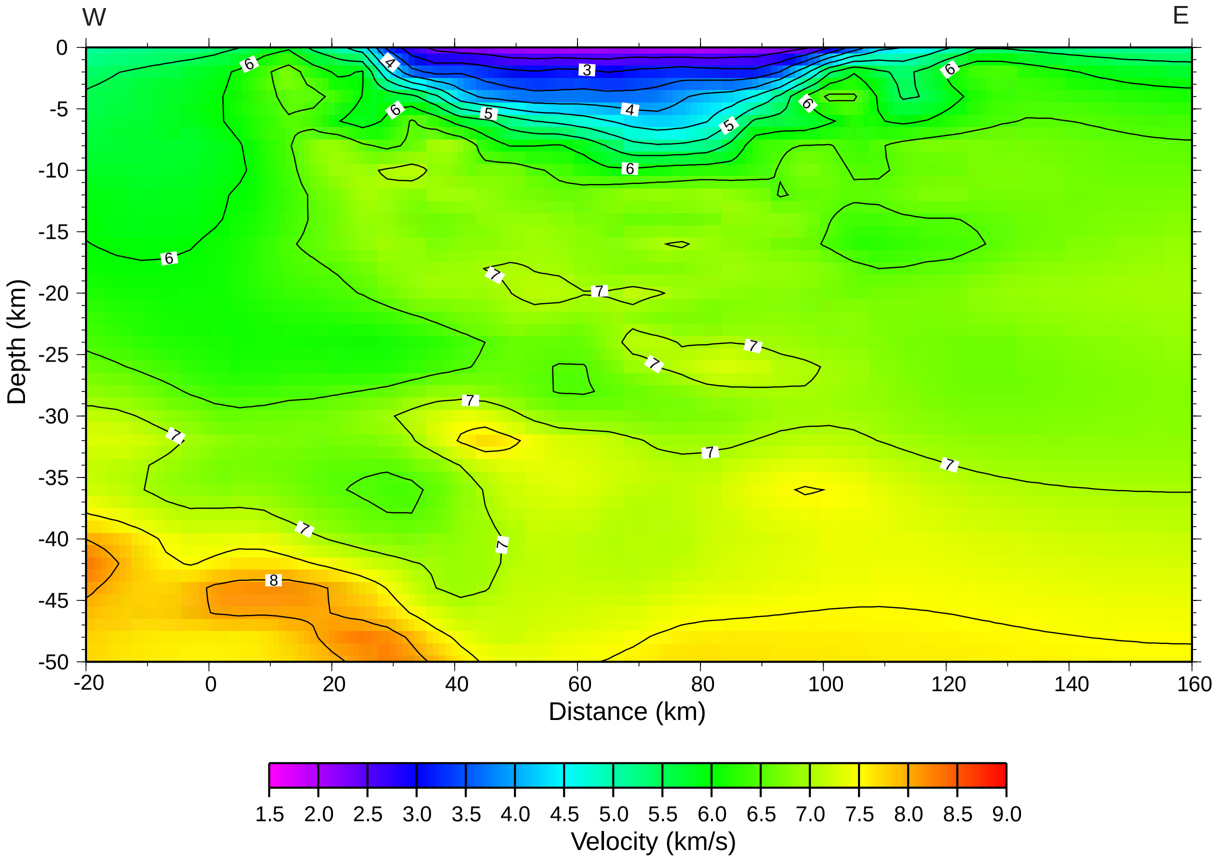

Figure 61. Tomographic image from a lower resolution study (R. S. Crosson, person. comm., 2001). Model coordinates are the same as the “Dry” SHIPS velocity model.

that the contact between the Siletz and the Seattle basin is well defined and can be mapped as the Hood Canal fault (Figure 35). The structure of the Seattle basin has been well defined from these data. The Seattle basin is symmetric and is ~ 6 to 7 km deep along the "Dry" SHIPS profile (Figure 35). The basin/basement contact is defined by the 4.5 km/s contour as tied to a N-S reflection line, which in turn is tied to the Mobil-Kingston well that drilled the top of Siletz. The Seattle basin has four sub-basins, which could be significant in determining the site response across the basin (Figure 35). The observation that the basin is 70 km in length is information that will further constrain the range of magnitudes of a future earthquake (Figure 35). Both sides of the basin have shallow dips where the basin sediments are in contact with the bedrock (Figure 35). A slower velocity field in the upper part of the basement near km 70 of the model probably marks a change in basement type to pre-Tertiary Cascade basement rocks from the Siletz terrane (Figure 35). Previously, this boundary has only been defined on the basis of gravity and magnetic maps. The seismicity along the profile lines up with the slowing of the velocity field and coincides at the surface with the location of proposed strike-slip faults (Figure 61) (Johnson et al., 1994; 1996).

The density model shows that the significant structures along the profile include the density contrast between the Olympic accretionary complex, the Siletz terrane, and the Seattle basin (Figure 48). The gravity model also shows that the slab and upper mantle have little effect on the gravity signature. The gravity model suggests that some underthrusting of the Olympic accretionary complex occurs. The location of the Hurricane Ridge fault and its geometry have been well defined by the gravity. The Siletz terrane has a distinct contrast with the Olympic accretionary complex in the density model. The gravity model agrees very well with the location of the contact between the Siletz terrane and the pre-Tertiary basement rocks defined by the P-wave tomography.

Further analysis of the S-wave data will aid in further assessing the seismic hazard. Also, additional testing of various stacking methods for the low-fold stack will provide mid- to lower crustal information along the profile.

CHAPTER 3: REGIONAL CRUSTAL STRUCTURE DERIVED FROM THE CD-ROM '99 SEISMIC REFRACTION/WIDE-ANGLE REFLECTION PROFILE

Introduction

Although the number of studies focusing on the crust and upper mantle have recently increased in the Rocky Mountains, there is still little detailed information on lithospheric structure in the western U. S. (e.g., Keller et al., 1998). The tectonic history of this region (Figure 62) begins with Precambrian accretionary events leading to the assembly of the North American craton (Laurentia). During the Proterozoic (1.4 Ga), extensive felsic magmatism spread across the southwestern portion of the North American craton (Laurentia). The volume and extent of this magmatic event was extensive (Anderson, 1989). Towards the end of the Proterozoic (1.0 - 1.1 Ga), the accretion of Laurentia was completed by the Grenville orogeny (Mosher, 1998) that was accompanied by widespread rifting (Adams and Keller, 1994). On a more global scale, the Grenville orogeny was part of the final assembly of the supercontinent Rodinia. However, Rodinia broke up near the end of the Proterozoic and passive continent margins formed along the rifted margins of Laurentia. Early Paleozoic tectonic stability was followed by late Paleozoic deformation (Ancestral Rockies), Late Cretaceous to early Tertiary shortening (Laramide orogeny), and Oligocene to Recent extension along the Rio Grande rift (Figure 62) (Karlstrom and Humphreys, 1998). Unraveling this tectonic history continues to be an ongoing challenge. The tremendous variety of tectonic activity from the Precambrian to present increases the difficulty of understanding the processes at work during Precambrian accretion.

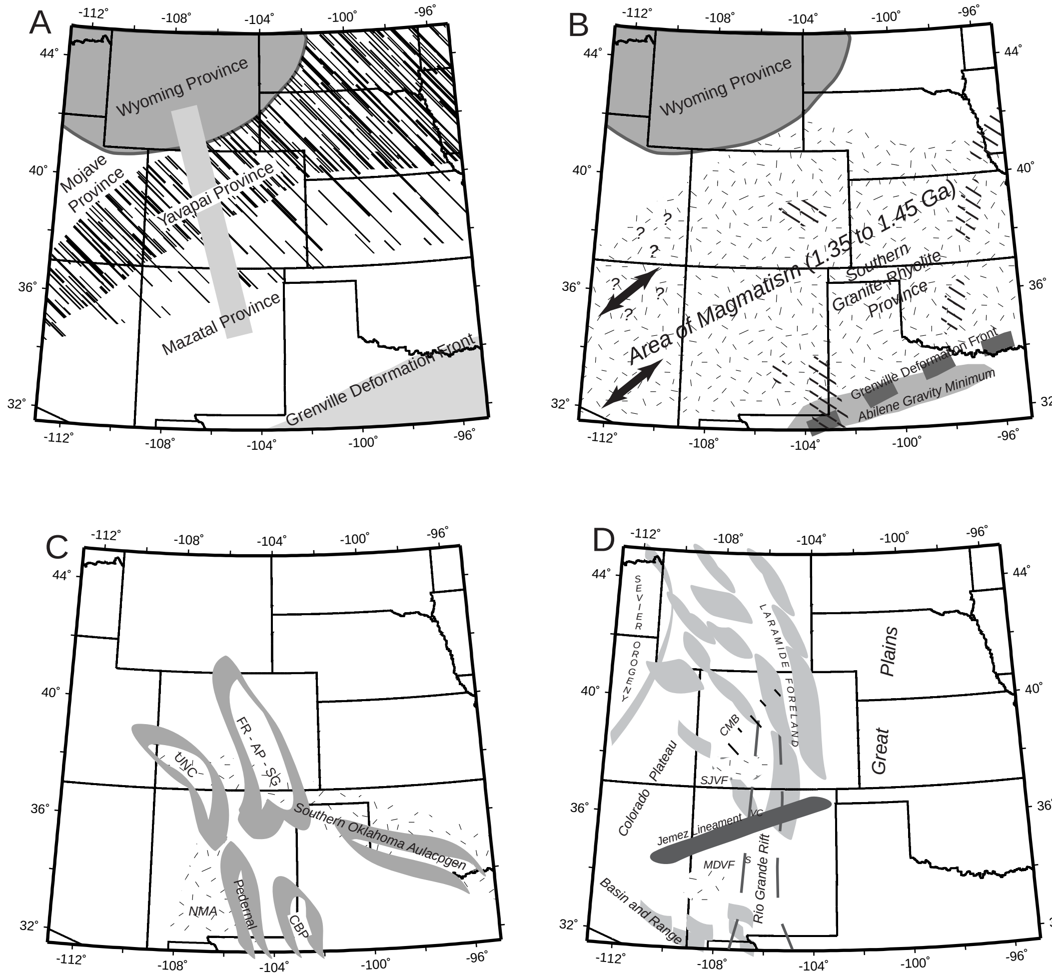

Figure 62. A: Map of the Southern Rocky Mountain region showing Precambrian terranes that formed southwestern Laurentia. The CD-RoM lithospheric transect is shown as the NW-trending gray line. B: Map showing the extent of 1.4 Ga (? ? Indicate where it cannot be confirmed) and 1.1 Ga magmatism (Midcontinent rift, Pecos mafic igneous suite - PMIC). Arrows indicate areas of localized Neoproterozoic extension, basin formation, and magmatism. The Abilene gravity minimum is very similar to the gravity low associated with the Sierra Nevada (Adams and Keller, 1994). C: Map of features associated with the break-up of Rodinia (Southern Oklahoma aulacogen; New Mexico aulacogen - NMA) and the Ancestral Rocky Mountains (Front Range- Apishapa-Sierra Grande uplift - FR-AP-SG; Uncompahgre uplift - UNC; Central basin platform - CBP). D: Regional map of Laramide structures (gray areas), the Colorado mineral belt (CMB), major mid-Tertiary volcanic centers (Mollogon-Datil volcanic field - MDVF; San Juan volcanic field - SJVF), and Rio Grande rift / Basin and Range. V - Valles caldera; S - Socorro magma chamber. (Compiled by G. R. Keller, 2001)

The Continental Dynamics - Rocky Mountains Project (CD-RoM '99) is a collaborative interdisciplinary study involving 14 American universities and the University of Karlsruhe, Germany and focuses on Precambrian features and their effects on Phanerozoic deformation. One of the major field efforts in the CD-RoM project took place during August 1999 and was the recording of a seismic refraction profile ~ 950 km in length (Figure 63). This seismic profile crossed several tectonic provinces including the Archean Wyoming province, the Proterozoic Yavapai and Mazatzal provinces, and the Great Plains. The primary targets for this experiment were determining the lithospheric structure along the CD-RoM transect with special emphasis on delineating the deep structure of the Cheyenne Belt suture zone, the Yavapai/Mazatzal terrane boundary, and the Jemez lineament using a line that was primarily perpendicular to these Precambrian structures (Figure 62). Deriving and analyzing a regional velocity model from the data collected during this experiment is the goal of this study.

Geologic Background

Precambrian

The core of the North American continent was formed during Archean time by suturing along mobile belts prior to 2.5 Ga (e.g., Hoffman, 1988). In southern Wyoming, rifting prior to 1.8 Ga formed a passive margin along the southern edge of the Archean craton (e.g., Karlstrom and Houston, 1984). Proterozoic lithosphere accreted to this passive margin from about 1.8 - 1.0 Ga, which continued the formation of North American craton, Laurentia (e.g., Hoffman, 1988). The first Proterozoic accretionary event at about 1.8 Ga collapsed the passive margin at the southwestern edge of the Wyoming craton (e.g., Chamberlain et al., 1993) and created the Cheyenne belt suture near the present Colorado/

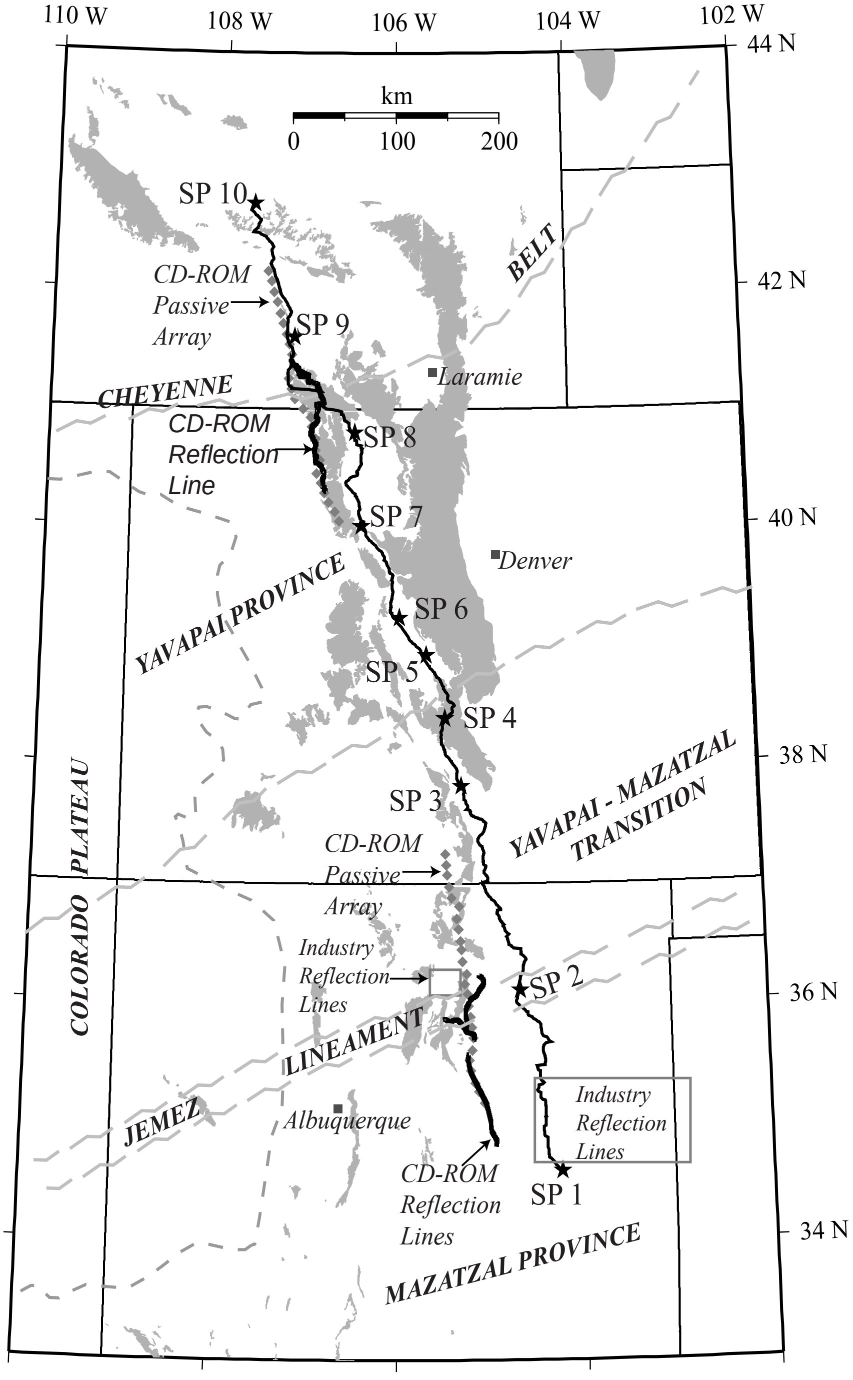

Figure 63. Basemap of CD-RoM seismic studies. CD-RoM seismic refraction stations are represented by the black line and shotpoints are the stars. CD-RoM seismic reflection lines are represented by the dark gray lines. CD-RoM passive source stations are the gray diamonds. Industry reflection lines are represented by the gray boxes. Precambrian outcrops are in medium gray. Various province and structural boundaries are in light gray.

Wyoming border (e.g., Karlstrom and Houston, 1984) (Figure 62). Subsequent accretion of island-arc terranes along NE-SW trending suture zones created the Proterozoic crust of Colorado and New Mexico (e.g., Karlstrom and Bowring, 1988).

A tectonic model for the evolution of the southern margin of the Wyoming province suggests that subduction ceased along a northwesterly dipping subduction zone and was followed by rifting in late Archean time (Figure 64) (e.g., Karlstrom and Houston, 1984). This led to the formation of a passive margin accompanied by deposition of marine sediments. Subduction resumed with a southward dip at the southern margin of the craton at about 1.8 Ga. This southern margin known as the Cheyenne belt (Figures 62A) is associated with a steeply dipping mylonitic shear zone (Duebendorfer and Houston, 1986). Subhorizontal lineations and subvertical foliations show strike-slip movement along the Cheyenne belt during a late period of deformation that overprints the earlier shear zone (Duebendorfer and Houston, 1986).

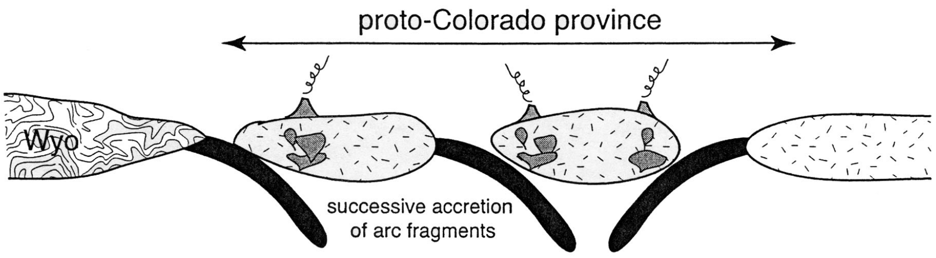

Figure 64. Schematic drawing of accretionary events onto the Archean craton (e.g., Condie, 1982; Karlstrom and Houston, 1984; Reed et al., 1987) (after Cavosie and Selverstone, in review).

From about 1.8 - 1.7 Ga, the Yavapai province formed from a series of accreted island-arc terranes along this southern margin (Figure 62A). This was followed by the addition of the Mazatzal province to the south of the Yavapai province from 1.7 - 1.6 Ga.

Both the Yavapai and Mazatzal provinces are dissected by major shear zones that are indicative of continuous deformation during Precambrian time. Juvenile crustal materials comprise the majority of the Yavapai province whereas supracrustal rocks comprise the majority of the Mazatzal province (e.g., Karlstrom and Bowring, 1988; 1993).

At about 1.4 Ga, anorogenic granitic plutons were emplaced throughout the southwest (Figure 62B). The 1.4 Ga event included regional deformation and metamorphism as interpreted by consistent shortening directions around 1.4 Ga plutons and reset cooling ages (e.g., Nyman et al., 1994). The 1.4 Ga event is poorly understood especially with respect to the amount of associated deformation in the older Proterozoic terranes. The North American craton was stabilized by the end of the Grenville orogeny at about 1.0 Ma (e.g., Hoffman, 1988). This event was part of the final stages of the formation of the supercontinent Rodinia (e.g., Karlstrom et al., 2001), which broke-up to form a passive continental margin that virtually encircled Laurentia (Figure 62B) (Stewart, 1976).

Phanerozoic

Cambrian to Devonian

The Rocky Mountain region from Cambrian to Devonian time, was primarily a shallow marine environment with few uplifts and deep basins (e.g., the Paradox basin). The main source of sediments for deposition in this shallow marine environment was from the Transcontinental arch to the east. Major tectonic events during this time were concentrated along the craton boundaries, which left the western mid-continent mainly unaffected (e.g., Sloss, 1988).

Mississippian to Pennsylvanian

During Mississippian time, the Rocky Mountain region was a shallow marine environment. Then during Pennsylvanian time, Precambrian rocks were uplifted to form the Ancestral Rocky Mountains in Colorado and New Mexico (Figures 62C and 65) (e.g., Mallory, 1958; Kluth and Coney, 1981). The Ancestral Rockies are commonly attributed to the Ouachita-Marathon orogeny (Kluth and Coney, 1981; Kluth, 1986), but Ye et al. (1986) attribute them to an Andean margin extending along the southwestern edge of Laurentia. In either case, the uplifts associated with the Ancestral Rockies are evidenced by unconformities, large sedimentary basins, and exposed fault zones. Although the maximum elevation of the Ancestral Rockies is thought to be significantly less than the present elevation of the modern Rocky Mountains, the structures, many of which were large, still have a significant influence on today's topography and subsurface structure (e.g., Kluth and Coney, 1981).

Permian to Jurassic

Permian to Jurassic time was another episode of minor tectonism in the western mid-continent. The Rocky Mountain region was a shallow marine environment again with a few uplifts remaining from the Ancestral Rockies orogeny (e.g, the Uncompahgre uplift) (e.g., Sloss, 1988).

Cretaceous to Recent

Late Mesozoic and early Tertiary shortening during the Laramide orogeny (Figure 62D) affected much of the southern Rocky Mountain region. Several models have been proposed to explain the Laramide orogeny (e.g., Bird, 1998). One model proposes that compression from the Laramide was parallel to North America plate motion (Gries, 1983).

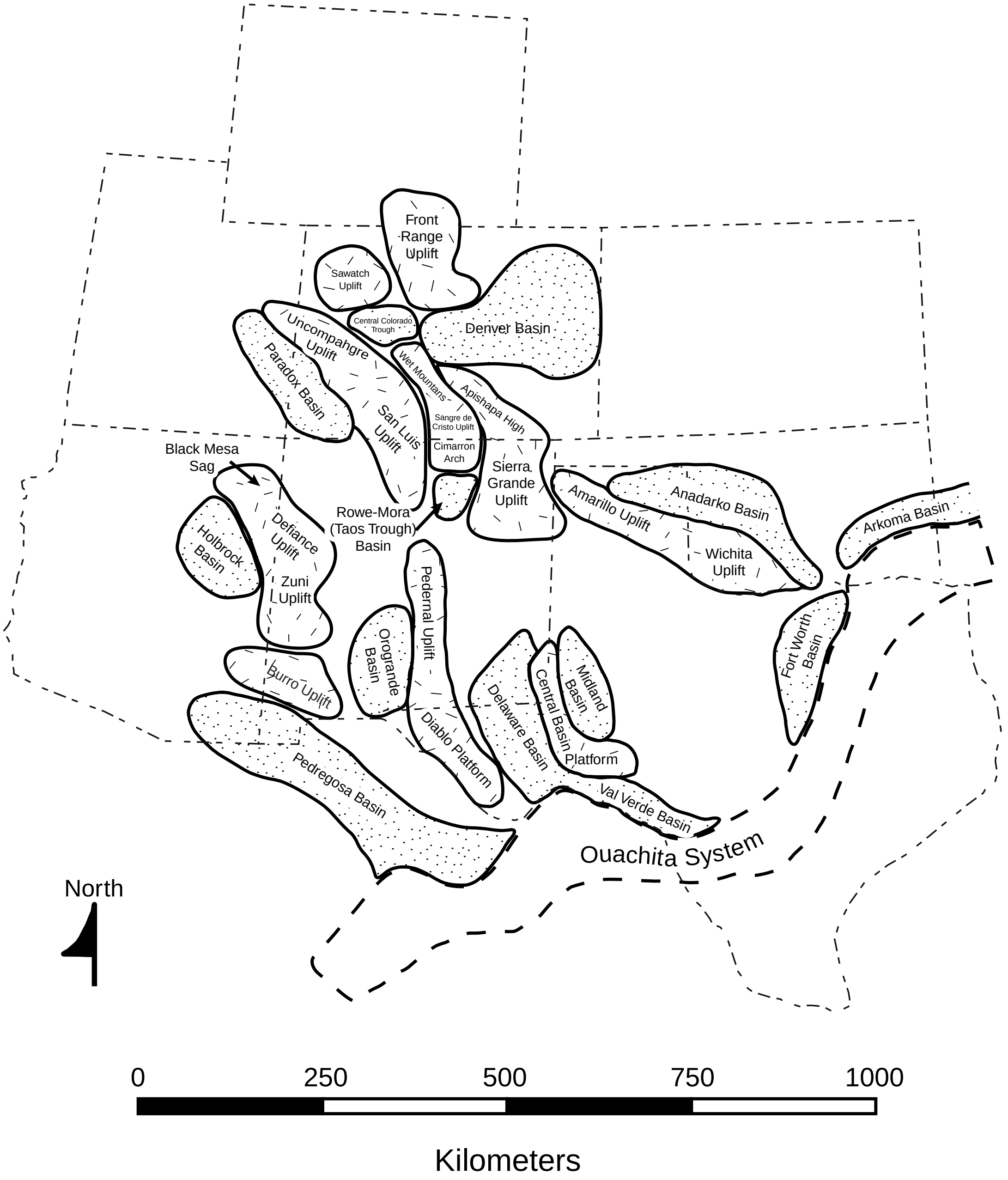

Figure 65. Schematic drawing of uplifts and basin during the Ancestral Rocky orogeny (modified from Dickinson, 1981; Peterson and Smith, 1986 by D. Smith).

Another model proposes that an oceanic plateau was subducted beneath the North American plate (e.g., Livaccari et al., 1981). The duration of the subduction of the oceanic plateau is not sufficient to explain for the duration of the Laramide orogeny therefore it cannot be the sole cause of the deformation (e.g., Bird, 1998). Additionally, another model proposes that the accretion and subsequent motion of “Baja British Columbia” produced the deformation inboard (Maxson and Tikoff, 1996). Livaccari and Perry (1993) suggest a strong horizontal component from the colliding Pacific and North American plates, which was transmitted through the Cordillera. This horizontal stress along with a low angle dip on the subducting plate, may have created strong coupling between the subducting plate and the overriding lithospheric mantle (e.g., Livaccari and Perry, 1993). The change in plate velocities required for this model do not coincide with the beginning and end of the Laramide, so again this cannot be the sole cause for the deformation (e.g., Bird, 1998). Bird (1998) presents a model stressing an increase in contact area between the subducting plate and the North American plate due to sub-horizontal subduction. This increase in contact area and a change in azimuth of the subducting plate led to the deformation that is evident today. A problem with this model is that it requires detachment of the lithospheric mantle, which disagrees with xenolith studies (Tikoff and Maxson, 2001). Isotopic studies from post-Laramide mantle xenoliths show that the mantle has been preserved throughout the Laramide and therefore suggests that the lithosphere could not have been detached (e.g., Ducea and Saleeby, 1998; Tikoff and Maxson, 2001).

Rocks in the southern Rocky Mountains were strongly deformed by basement-involved shortening during the Laramide orogeny (e.g., Hamilton, 1989). This deformation can be seen in seismic reflection studies, which show Precambrian rocks thrust over Phanerozoic sedimentary rocks in locations such as the Wind River Mountains of Wyoming (e.g., Gries, 1983; Smithson and Johnson, 1989).

Beginning at about 30 Ma, uplift and volcanism associated with extension along the Rio Grande rift began (Figure 62D). The rift is narrow at its head near the Colorado/ Wyoming border and widens to the south where it then merges with the Basin and Range province in northern Mexico. The Rio Grande rift has undergone at least two episodes of extension. The first episode was directed northwest-southeast and the second was followed by an episode of extension that was directed east-west and cut across Precambrian fabrics (e.g., Aldrich et al., 1986; Keller and Baldridge, 1999).

The modern Rocky Mountains were formed from a series of Laramide uplifts which, along with additional uplift and extension along the Rio Grande rift, created the present day topography. The relative importance of these events in terms of uplift is still hotly debated.

Geophysical Background

The CD-RoM seismic profile lies in an area with modest existing seismic constraints on crustal structure (Figure 66). Those seismic refraction profiles that do intersect the CD-RoM profile are mainly unreversed or do not have enough receivers and/or sources to strongly constrain crustal structure. Receiver function determinations also provide crustal thickness estimates in Colorado (Figure 66) (Sheehan et al., 1995).

Existing seismic studies provide estimates of both crustal velocity structure and thickness (Figure 67) (Appendix C & D). In Wyoming, average upper crustal velocities are estimated at 6.0 to 6.5 km/s. Lower crustal velocities are about 7.3 km/s, and Moho

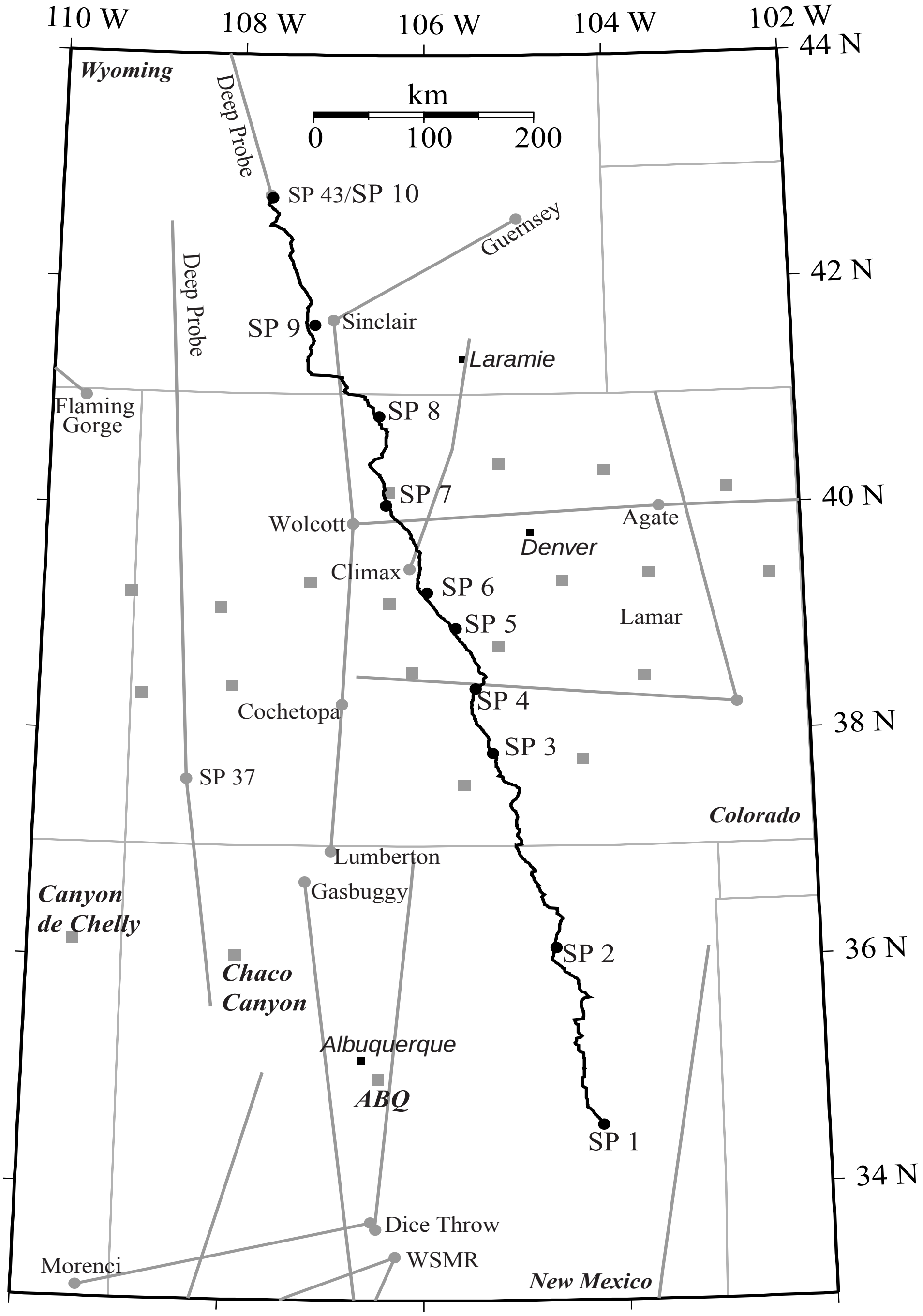

Figure 66. Basemap of previous geophysical work in the southern Rocky Mountains. Refraction lines are light gray lines and shotpoints are light gray circles (Appendix C). Passive source stacked receiver functions are light gray squares (Appendix D). CD-RoM refraction station is the black line and shotpoints are black circles.

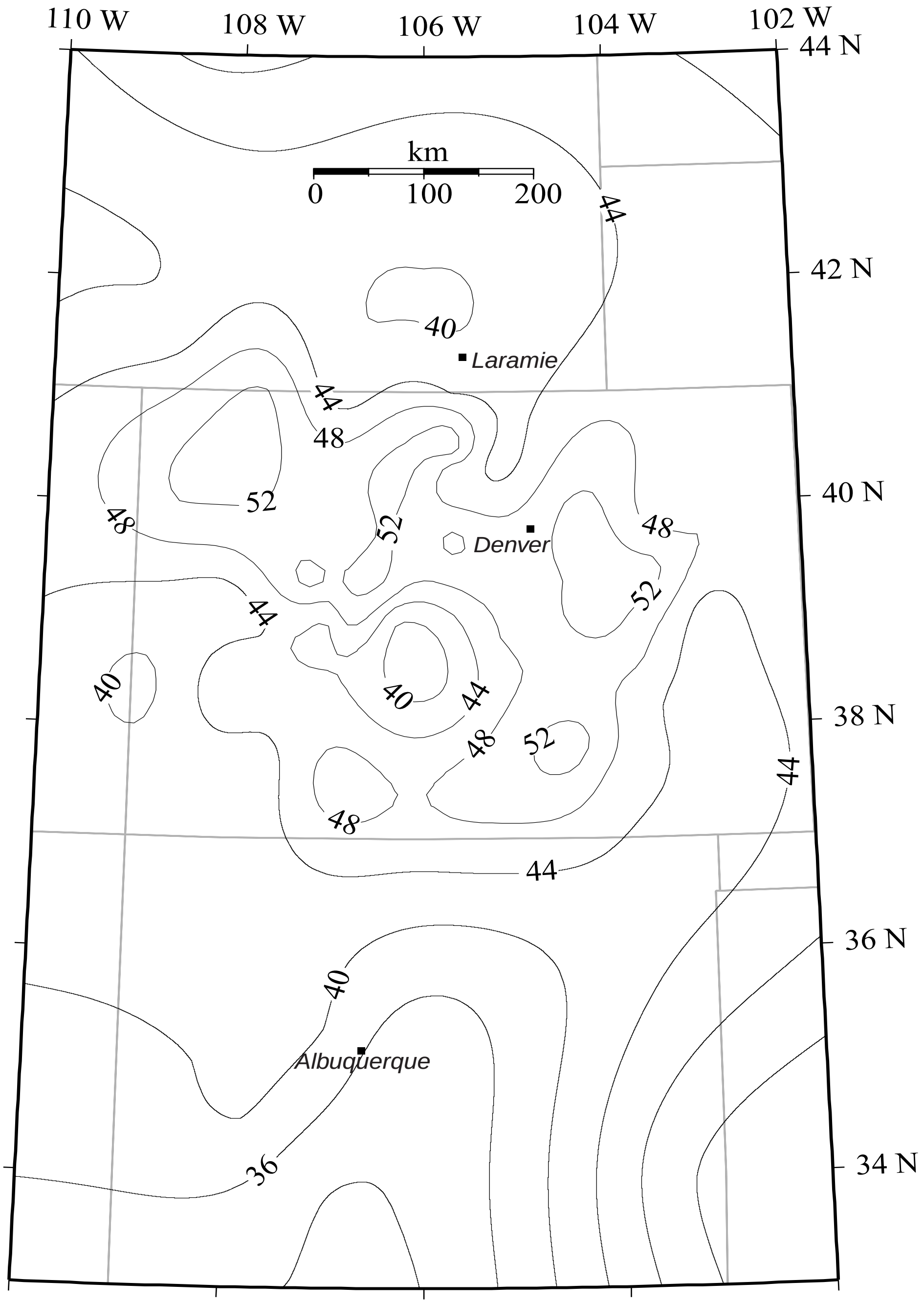

Figure 67. Crustal thickness (km) contour map of the southern Rocky Mountains. Values for this map were compiled from data on Figure 66. The values for these contours can be found in Appendix C & D. Contour interval is 4 km.

depth ranges between 40 to 55 km (Figures 67 & 68) (Allmendinger et al., 1982; Braile et al., 1974; 1989; Brewer et al., 1982; Prodehl, 1979; Prodehl and Lipman, 1989; Prodehl and Pakiser, 1980; Smith et al., 1982; Snelson et al., 1998; Wilden, 1965). A COCORP reflection line images the Wind River thrust (Smithson et al., 1979; Smithson and Johnson, 1989), but does not provide constraints on local crustal thickness and velocities.

A generalized crustal model for Colorado includes an average upper crustal velocity of 6.0 km/s, a lower crustal velocity of 6.6 km/s and a Moho depth ranging from 40 to 50 km (Braile et al., 1974; Jackson et al., 1963; Jackson and Pakiser, 1965; Keller et al., 1998; Krishna, 1988; Prodehl and Lipman, 1989; Prodehl and Pakiser, 1980; Roller, 1965; Snelson et al., 1998; Steeples and Miller, 1989). Receiver function studies show an average Moho depth of 45 km in northern Colorado and of about 40 km in southern Colorado (Sheehan et al., 1995). Compilations by Prodehl and Lipman (1989), Keller et al. (1998), and the Deep Probe results (Snelson et al., 1998) show an average upper crustal velocity of 6.2 km/s, lower crustal velocity of 6.9 km/s, and Moho depth of 40 km for New Mexico (Figure 68). The seismic lines that do not parallel the CD-RoM line (Figure 66) can be used to study lateral variations in crustal structure across New Mexico and Colorado (Cook et al., 1979; Jaksha, 1982; Olsen et al., 1979; Prodehl and Pakiser, 1980; Roberts et al., 1991; 1994; Schneider and Keller, 1994; Sinno et al., 1986; Snelson et al., 1998; Stewart and Pakiser, 1962; Toppozada and Sanford, 1976; Wolf and Cipar, 1993) and are integrated with the results of this study.

Data Acquisition & Analysis

The CD-RoM seismic dataset includes a refraction line, approximately 950 km long that was acquired in August of 1999 (Figure 63) in two deployments. About 600

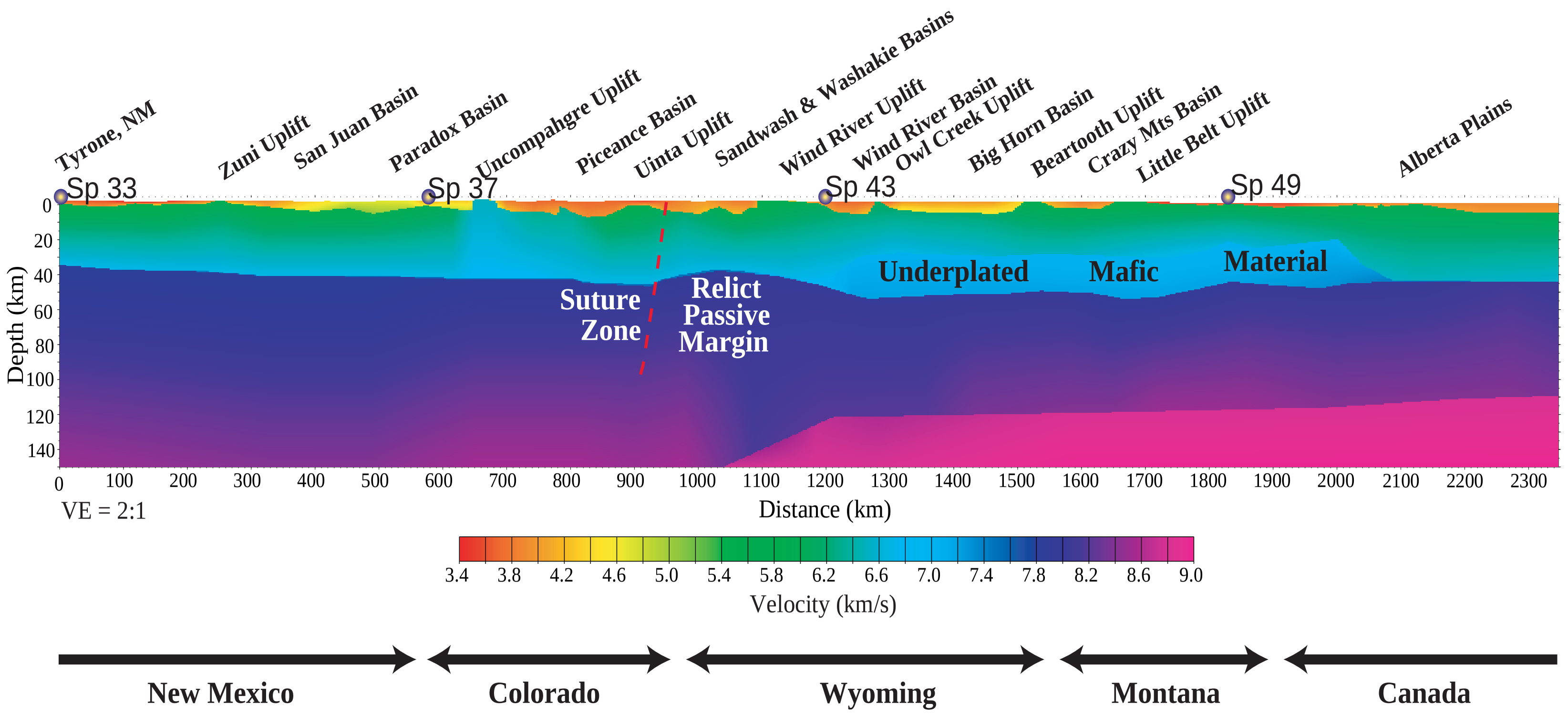

Figure 68. Deep Probe velocity model (Snelson et al., 1998). The CD-RoM profile intersects this model in a northwestward point at the Wyoming shotpoint (SP 43/SP 10).

instruments were used in each deployment (Appendix E). The shot points were placed strategically along the line to get the best depth penetration possible from the portable seismic recording systems (Appendix F). About 400 Texans (RefTek 125) and 225 RefTek (DAS) portable seismic recording systems were used during the experiment. These instruments were programmed to begin recording prior to the shot window and recorded for at least 240 s.

The first deployment occupied the southern two-thirds of the profile. The station interval for the southern third was 800 m and in the middle third was 1.6 km. For the second deployment, the northern third of the profile was occupied with stations every 800 m and the stations in the middle third were shifted by 800 m. Thus, the entire profile was covered by stations spaced nominally 800 m along the profile.

The refraction data were processed using the ProMAX® system at UTEP. Ellipsoidal offsets were calculated using coordinates of the stations and shot points in latitude and longitude. Latitude and longitude of the receivers and shot points were preserved in arc-seconds within ProMAX®. There were 15 successful shots during the experiment. Shot-points Gardner (SP 3), Canon City (SP 4), Hartsel (SP 5), Kremmling (SP 7), and Day Loma (SP 10) (Figure 62) were shot twice and merged to increase the data density. Dead or noisy traces were edited out of the data and a Butterworth bandpass filter (2-8-30-40 hz) was applied to enhance the data. First and secondary arrival times were picked and exported from ProMAX® and formatted for ray tracing modelling and inversion. Gaps in the seismic record sections are as a result of canyons or rivers and/or instrument failure.

Overall the recorded data quality was high, providing clear arrivals to offsets of > 200 km for most record sections. The main first arrival phases that were used in the analysis were Pg (upper and middle crust), Pl (lowermost crust), and Pn (upper mantle). The main reflected phases used were PcP (mid-crustal), PlP (lowermost crust) and PmP (Moho). It should be noted that there is a tremendous amount of reflectivity within the upper and middle crust that is being analyzed by our colleagues at the University of Karlsruhe, Germany.

First arrival energy for Pg was strong on all of the record sections. This phase mirrors the large changes in topography that are observed along most of the record sections. The Ft. Sumner, New Mexico (SP 1) source shows some of the best energy of all of the shots. Pg arrivals were observed to offsets of ~ 180 km (Figures 69 & 70). The source near Wagon Mound, New Mexico (SP 2) produced Pg arrivals to offsets of ~ 150 km to the south and ~ 180 km to the north (Figures 71 - 74). The source near Gardner, Colorado (SP 3) produced Pg arrivals to offsets of ~ 190 km to the south and ~ 180 km to the north (Figures 75 - 78). The source near Canon City, Colorado (SP 4) produced Pg arrivals to offsets of ~ 150 km to the south and ~ 180 km to the north (Figures 79 - 82). Similarly, the source near Hartsel, Colorado (SP 5) produced Pg arrivals to offsets of ~ 180 km to the south and ~ 135 km to the north (Figures 83 - 86). The source near Fairplay, Colorado (SP 6) produced Pg arrivals to offsets of ~ 90 km to the south and ~ 160 km to the north (Figures 87 & 88). The source near Kremmling, Colorado (SP 7) produced Pg arrivals of offsets to ~ 180 km to the south and ~ 180 km to the north (Figures 89 - 92). The source near Walden, Colorado (SP 8) produced Pg arrivals to offsets of ~ 180 km to the south and ~ 165 km to the north (Figures 93 - 96). The source south of Rawlins,

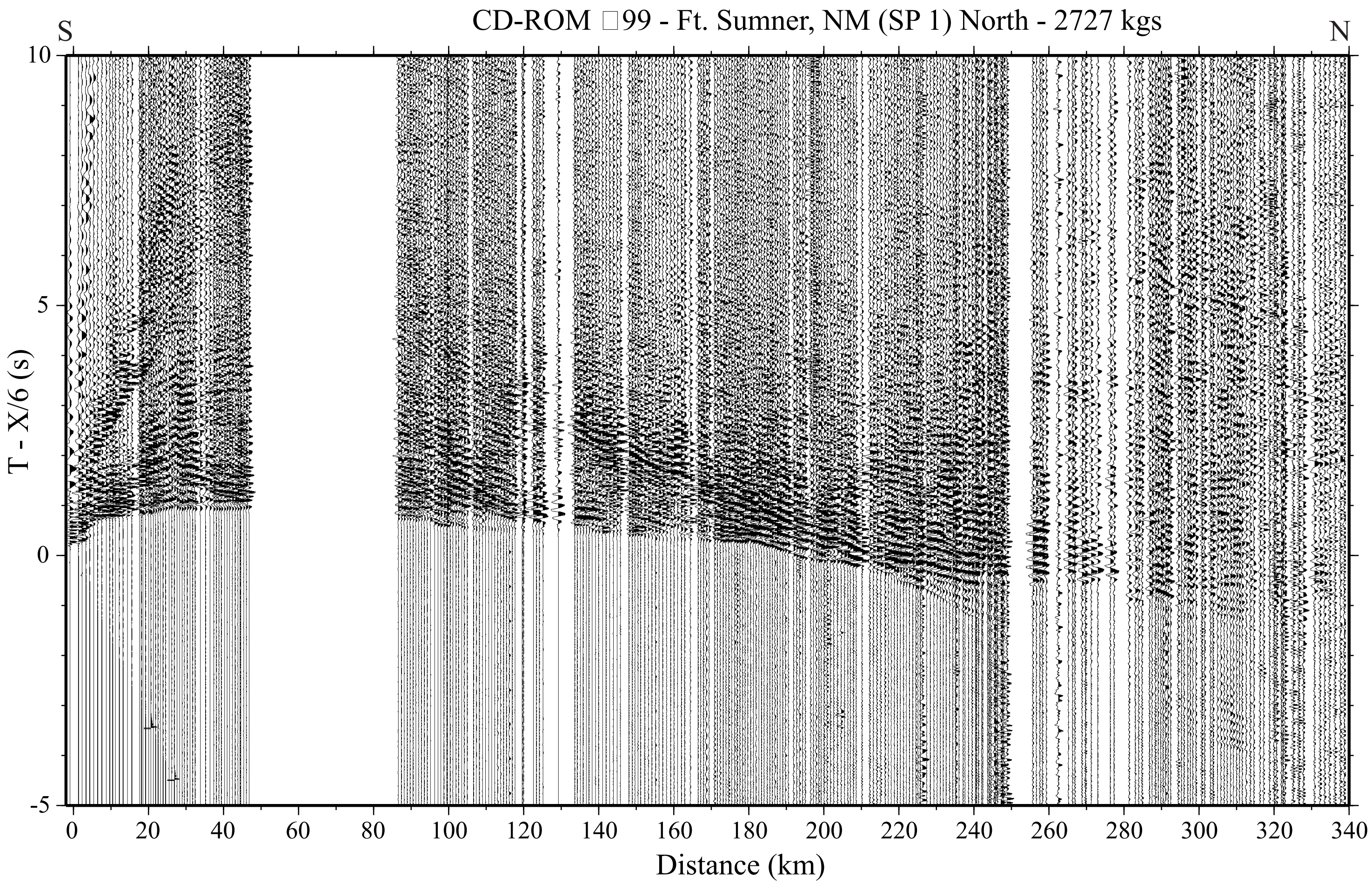

Figure 69. Seismic record section from the Ft. Sumner shotpoint (SP 1).

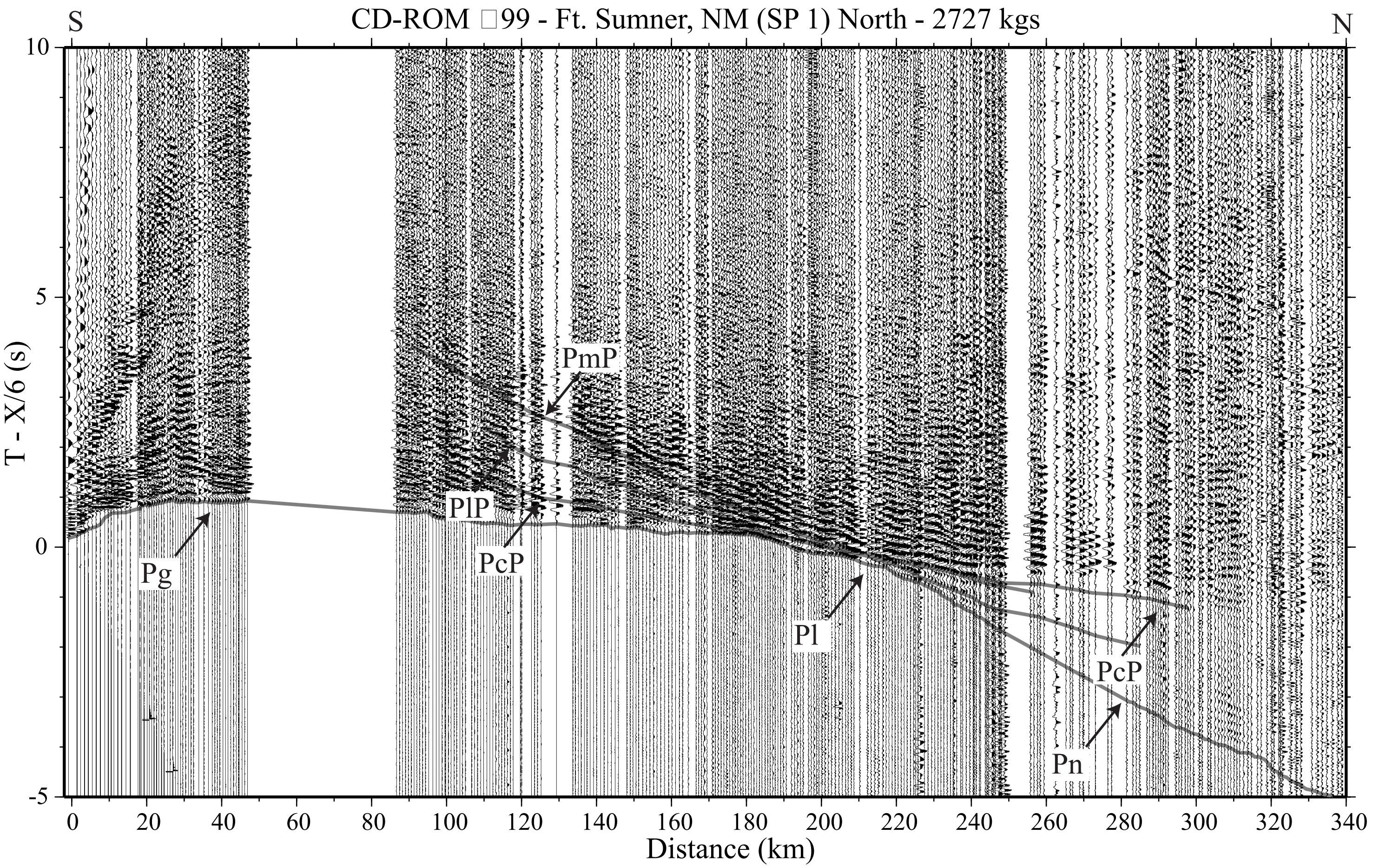

Figure 70. Seismic record section from the Ft. Sumner shotpoint (SP 1). Pg, Pl, Pn, PcP, PlP, and PmP are visible throughout the record. Observed traveltimes are overlain on record.

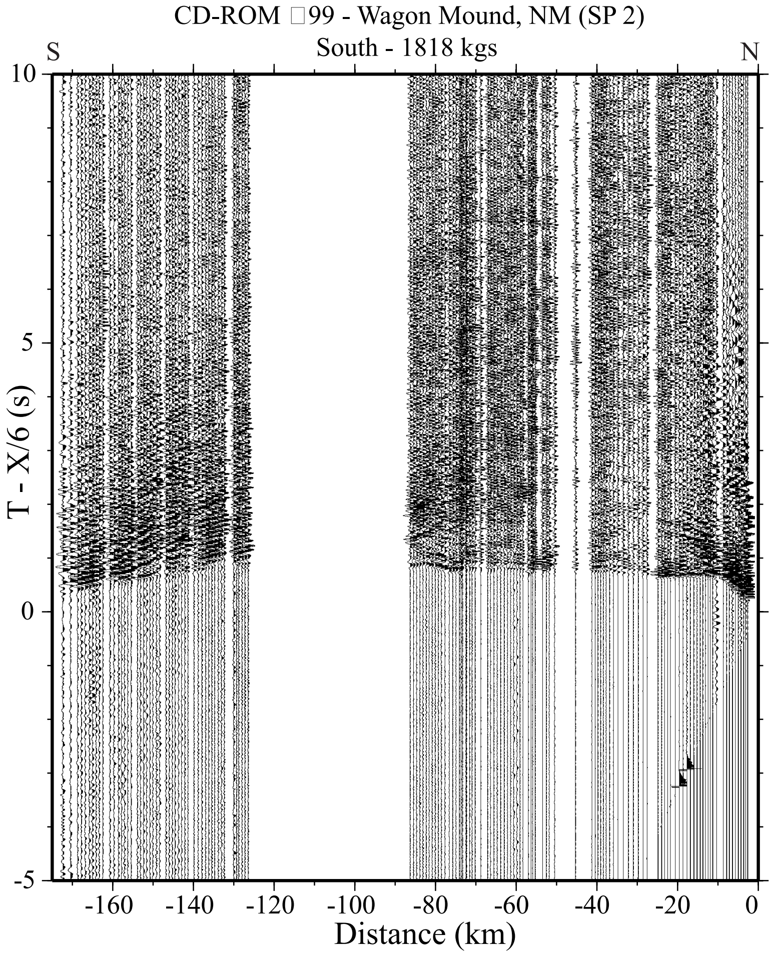

Figure 71. Seismic record section from the Wagon Mound shotpoint (SP 2) to the south.

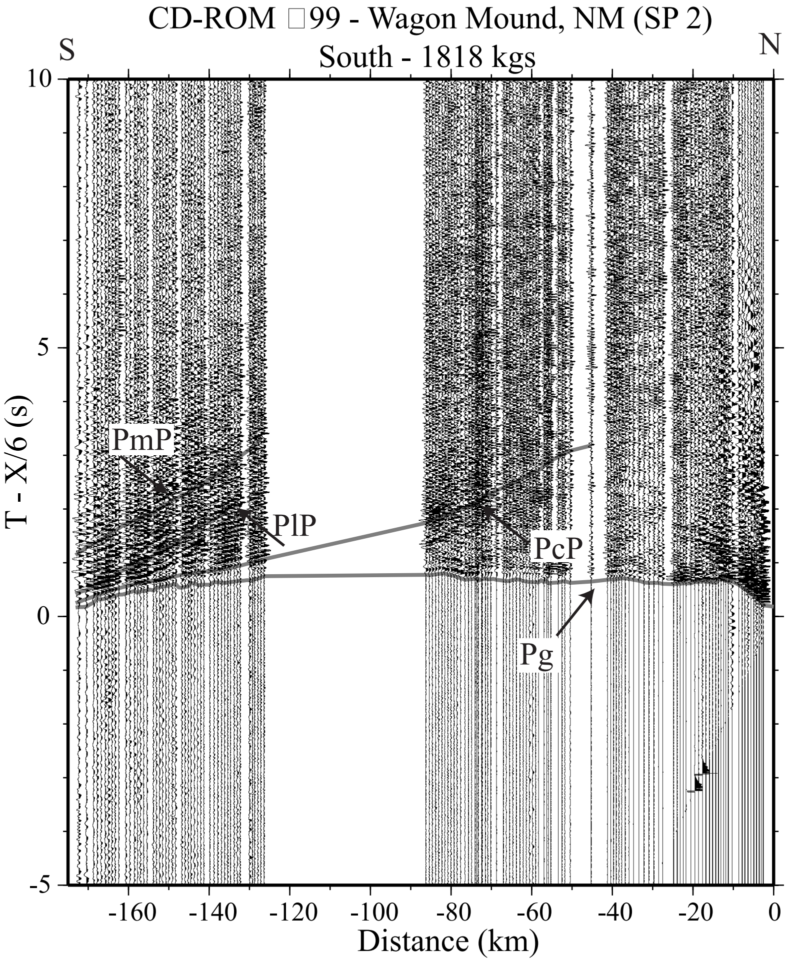

Figure 72. Seismic record section from the Wagon Mound shotpoint (SP 2) to the south. Pg, Pl, PcP, PlP, and PmP are visible for the length of this section. Observed traveltimes are overlain on record.

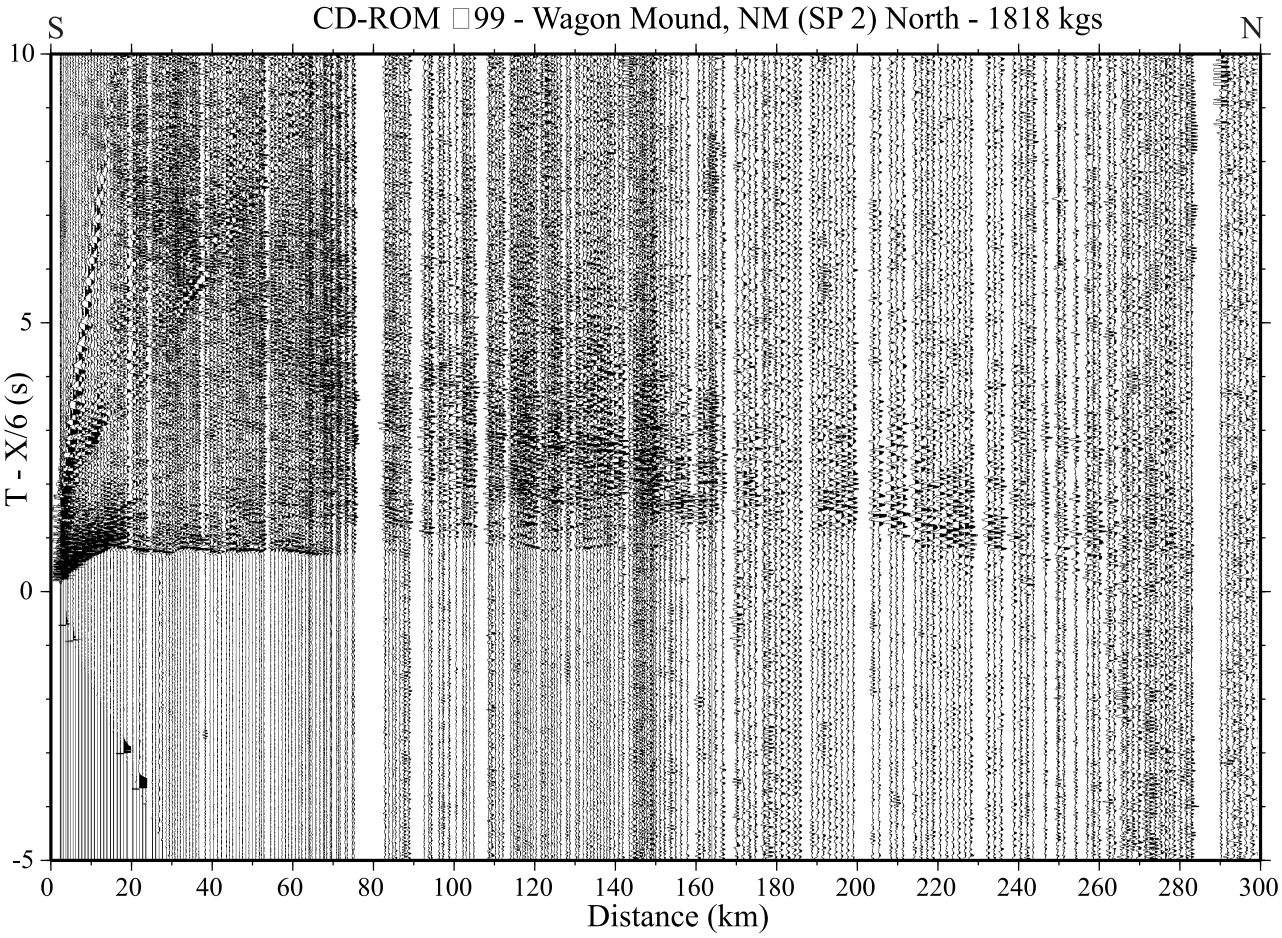

Figure 73. Seismic record section from the Wagon Mound shotpoint (SP 2) to the north.

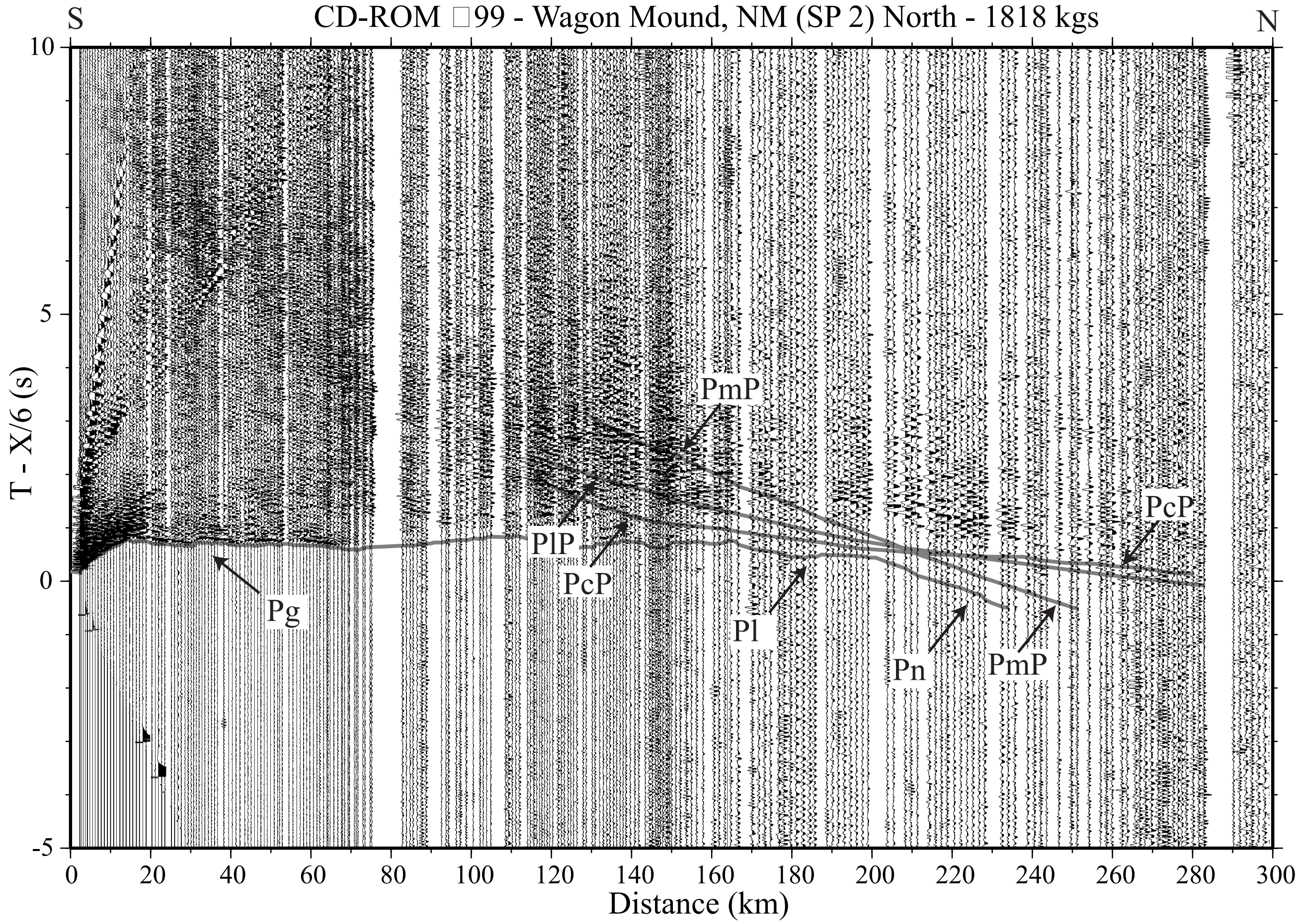

Figure 74. Seismic record section from the Wagon Mound shotpoint (SP 2) to the north. Pg, Pl, Pn, PcP, PlP, and PmP are visible for the length of this section. Observed traveltimes are overlain on record.

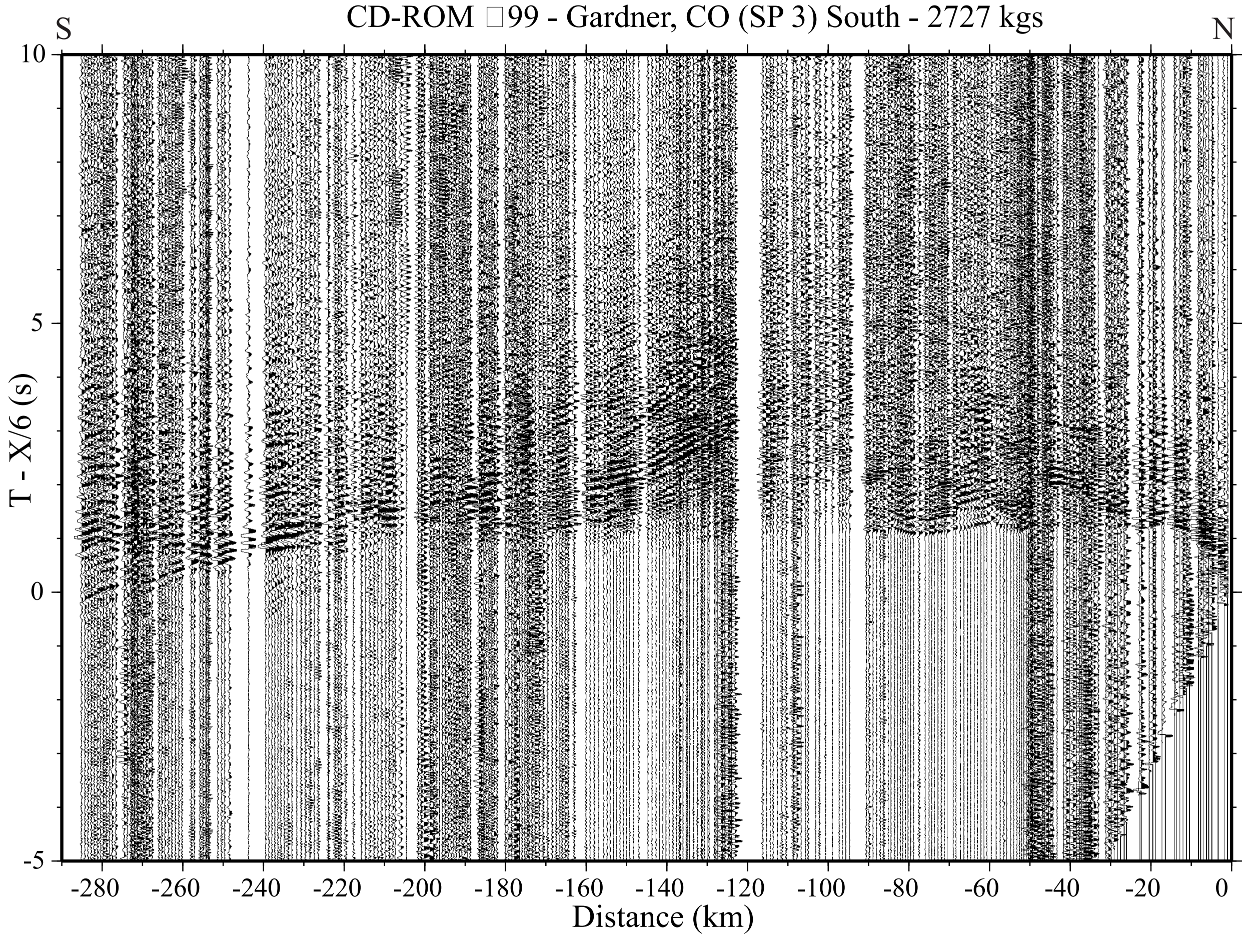

Figure 75. Seismic record section from the Gardner shotpoint (SP 3) to the south.

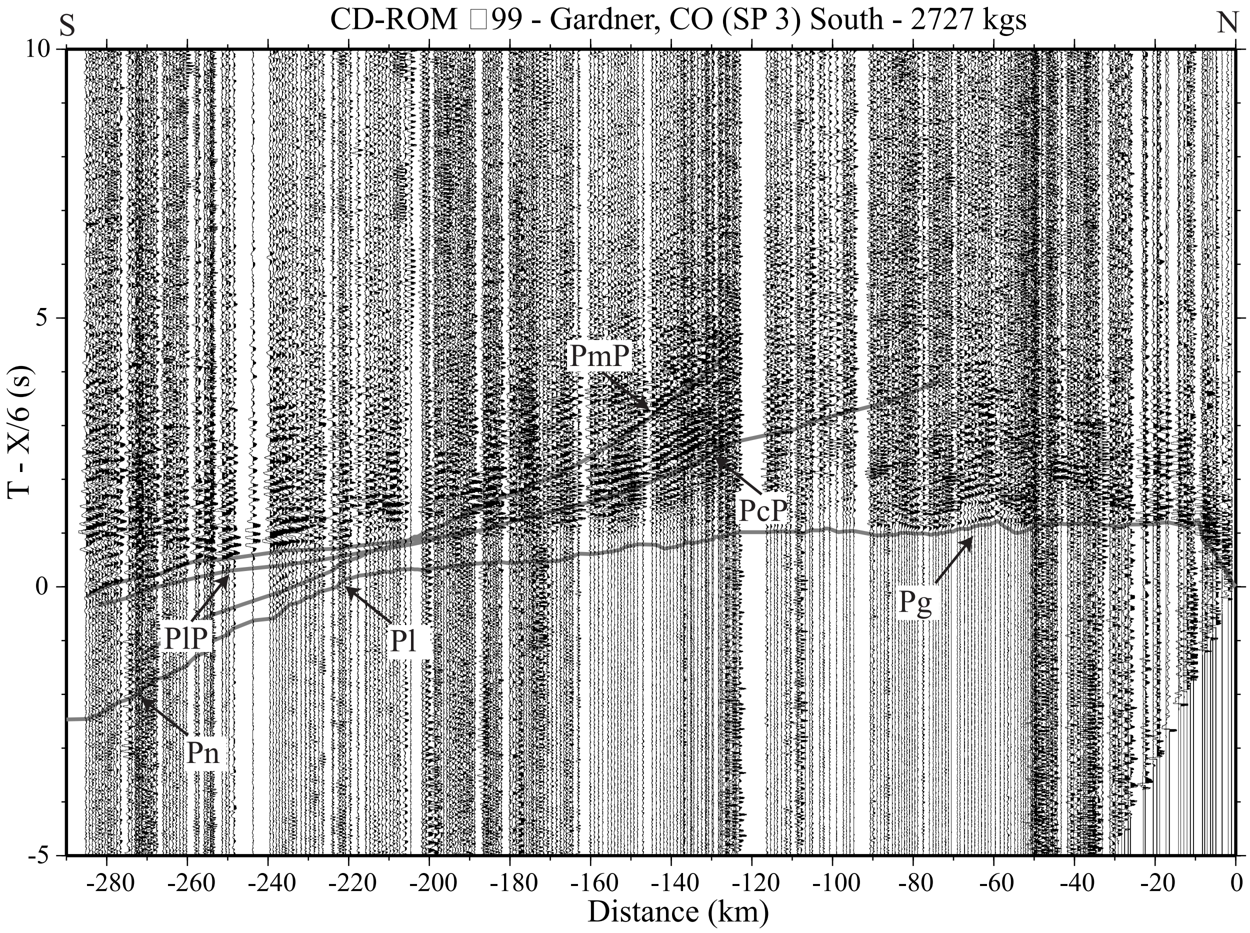

Figure 76. Seismic record section from the Gardner shotpoint (SP 3) to the south. Pg, Pl, Pn, PcP, PlP, and PmP are visible for the length of this section. Observed traveltimes are overlain on record.

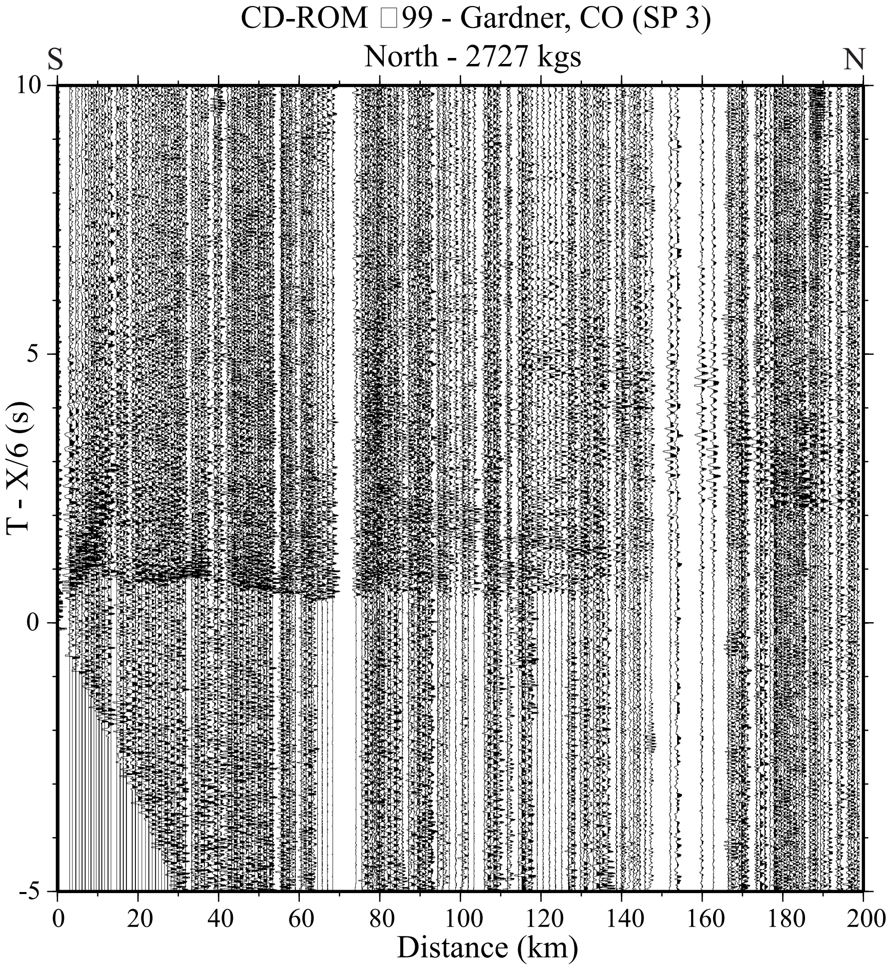

Figure 77. Seismic record section from the Gardner shotpoint (SP 3) to the north.

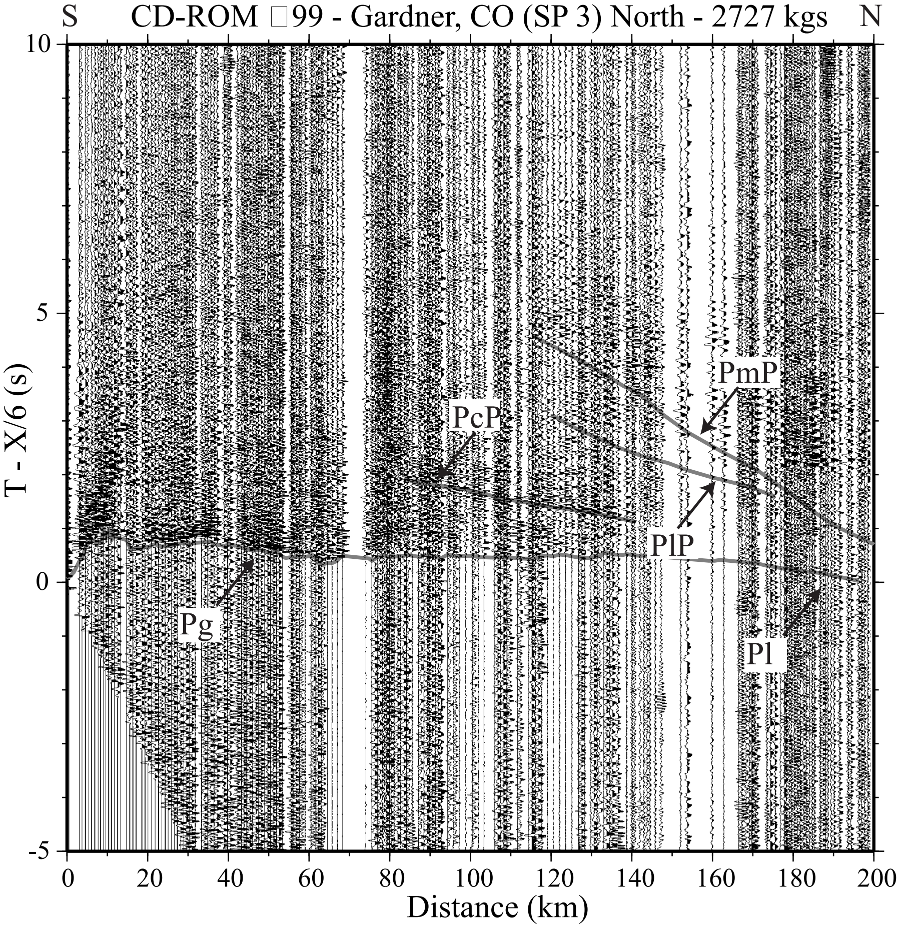

Figure 78. Seismic record section from the Gardner shotpoint (SP 3) to the north. Pg, Pl, PcP, PlP, and PmP are visible for the entire length of the section. Observed traveltimes are overlain on record.

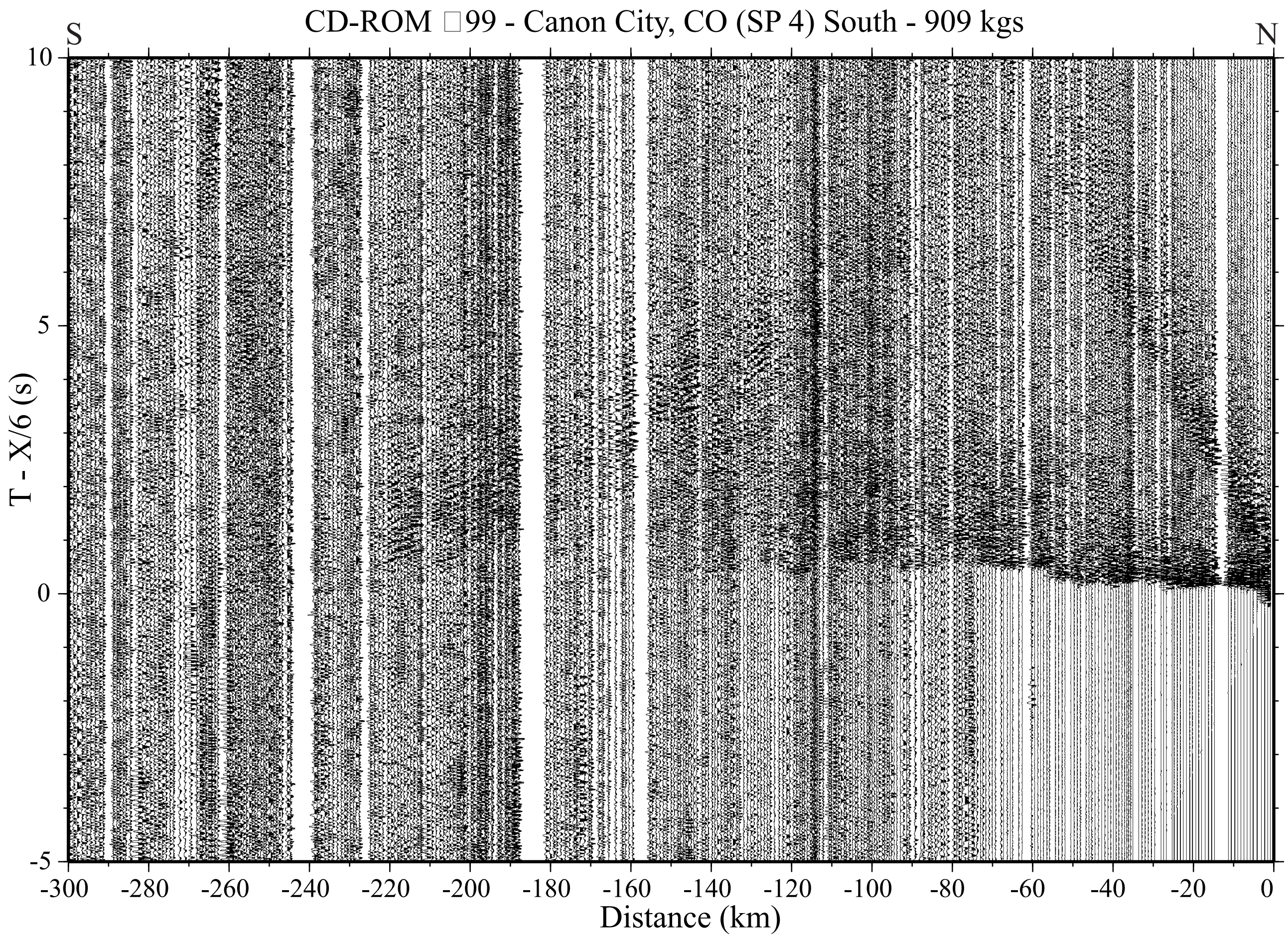

Figure 79.Seismic record section from the Canon City shotpoint (SP 4) to the south.

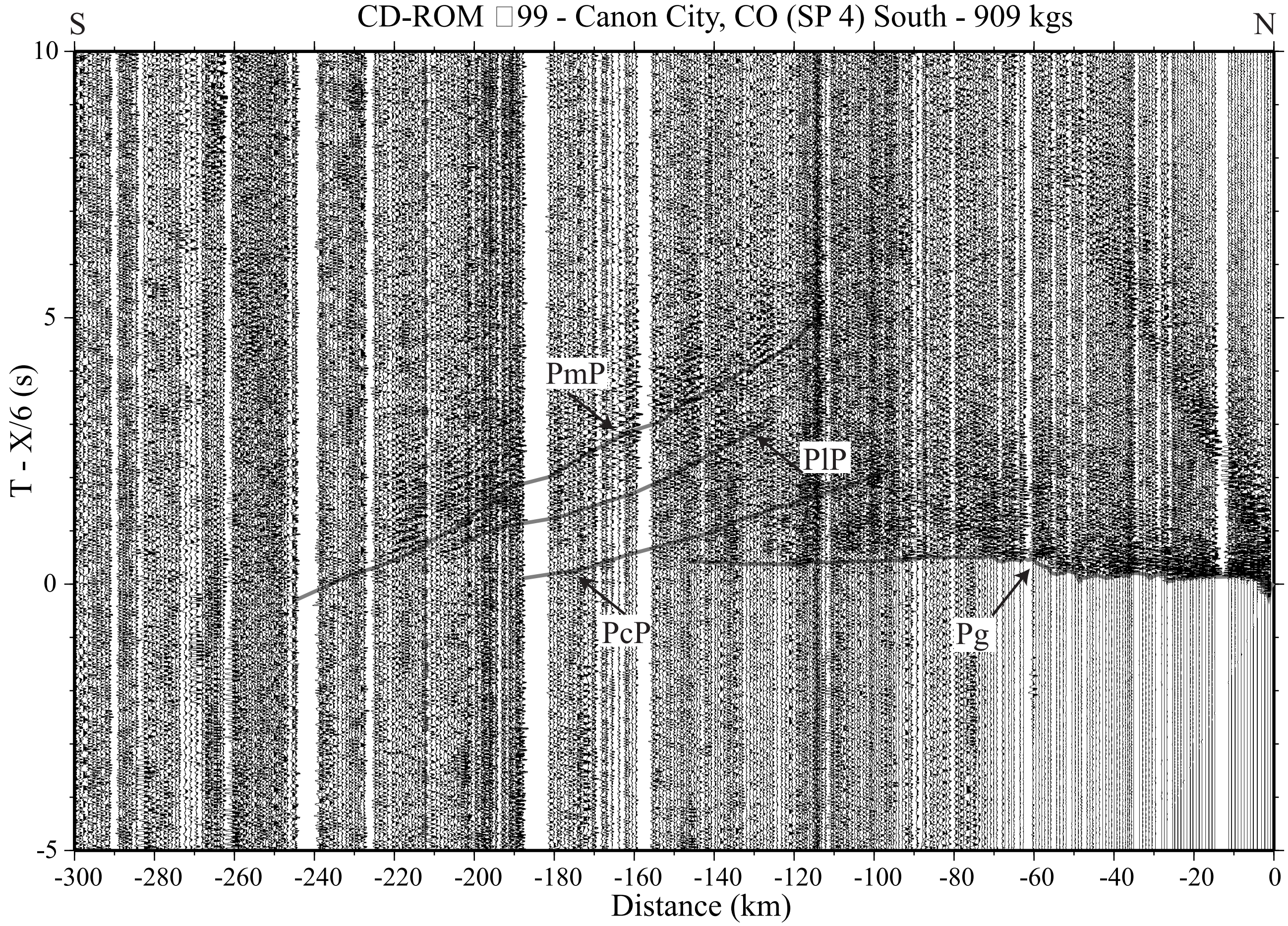

Figure 80. Seismic record section from the Canon City shotpoint (SP 4) to the south. Pg, PcP, PlP, and PmP are visible for the entire length of the section. Observed traveltimes are overlain on record.

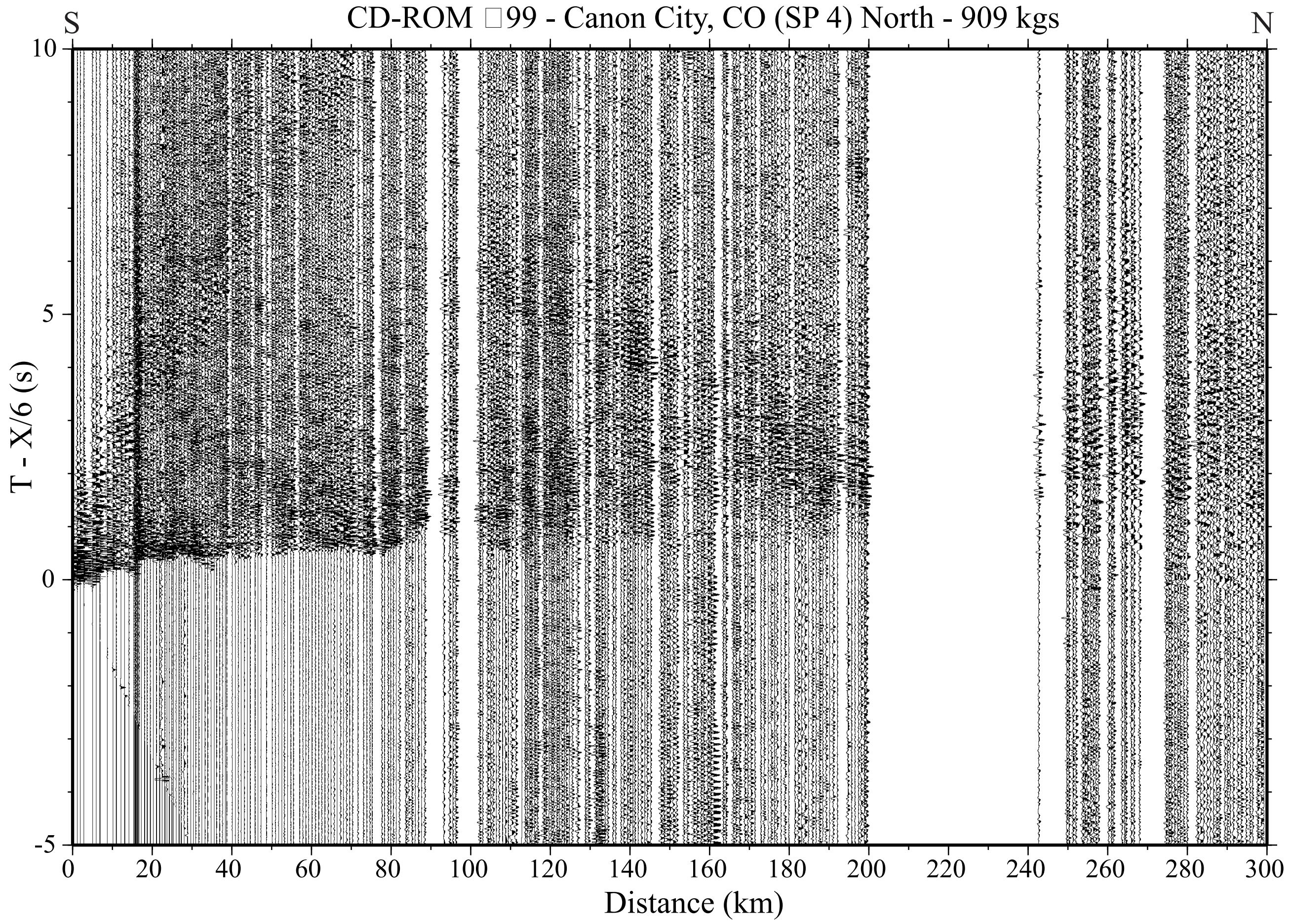

Figure 81. Seismic record section from the Canon City shotpoint (SP 4) to the north.

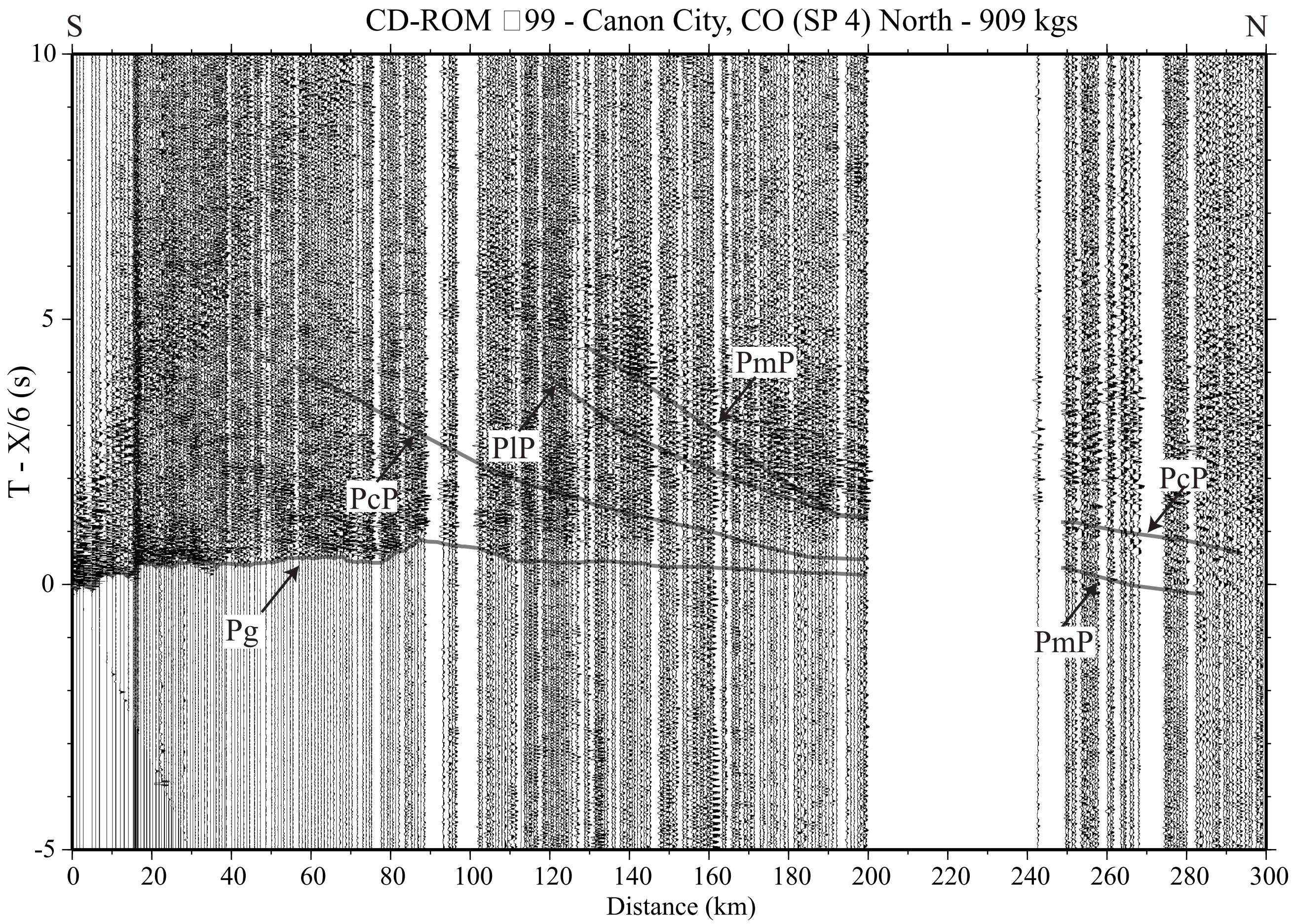

Figure 82. Seismic record section from the Canon City shotpoint (SP 4) to the north. Pg, PcP, PlP, and PmP are visible for most of the section. Observed traveltimes are overlain on record.

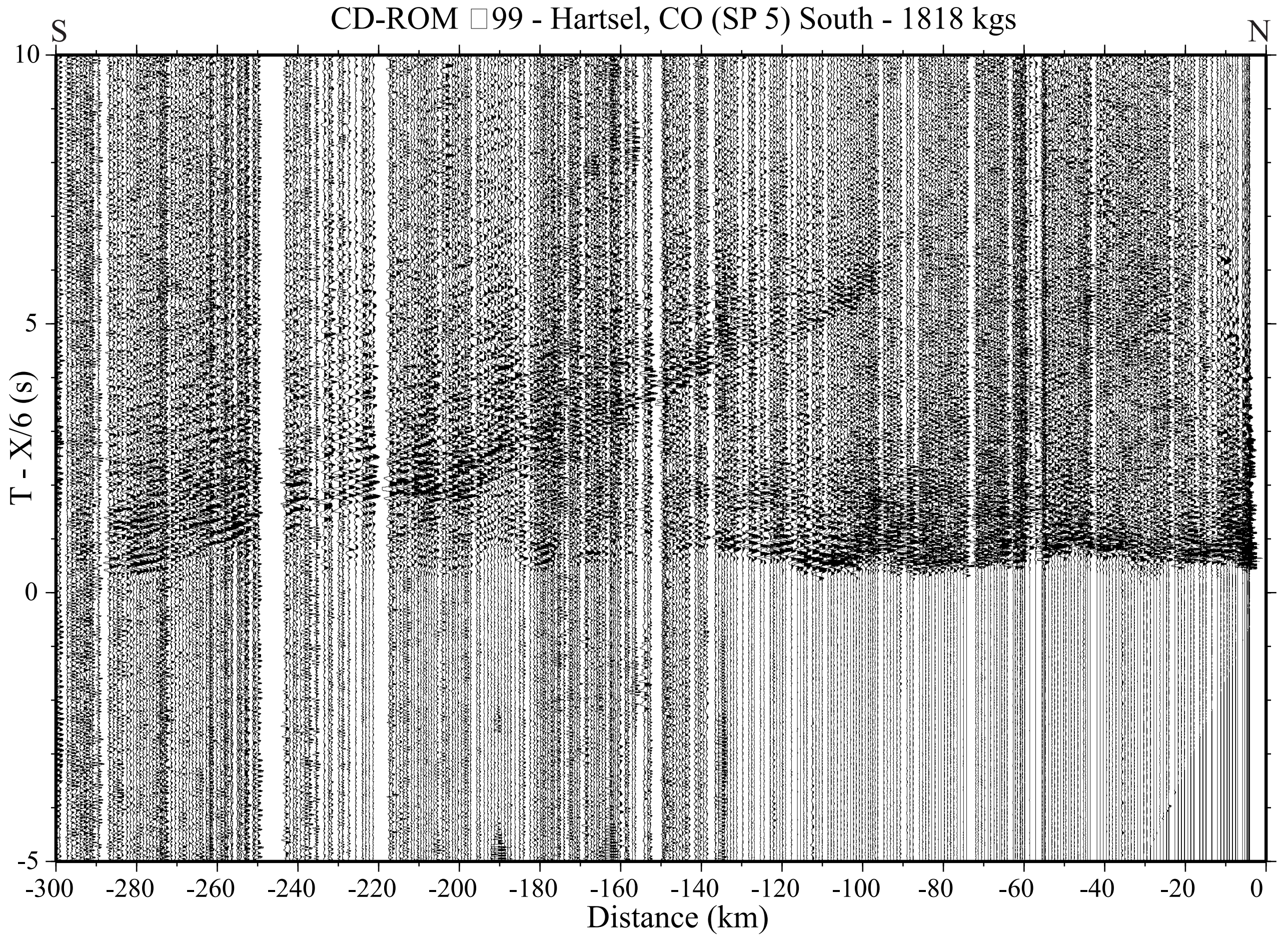

Figure 83. Seismic record section from the Hartsel shotpoint (SP 5) to the south.

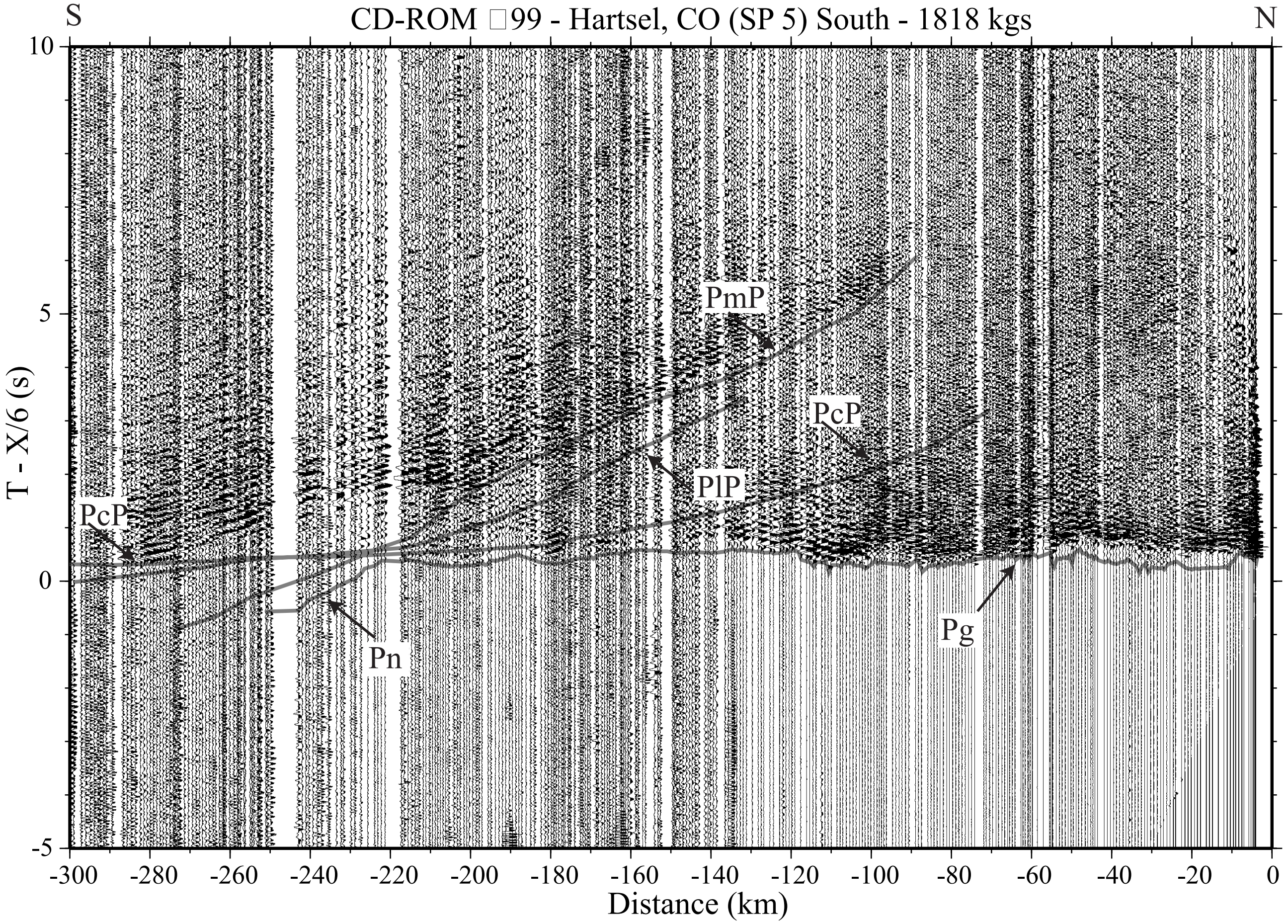

Figure 84. Seismic record section from the Hartsel shotpoint (SP 5) to the south. Pg, Pn, PcP, PlP, and PmP are visible for the entire length of the section. Observed traveltimes are overlain on record.

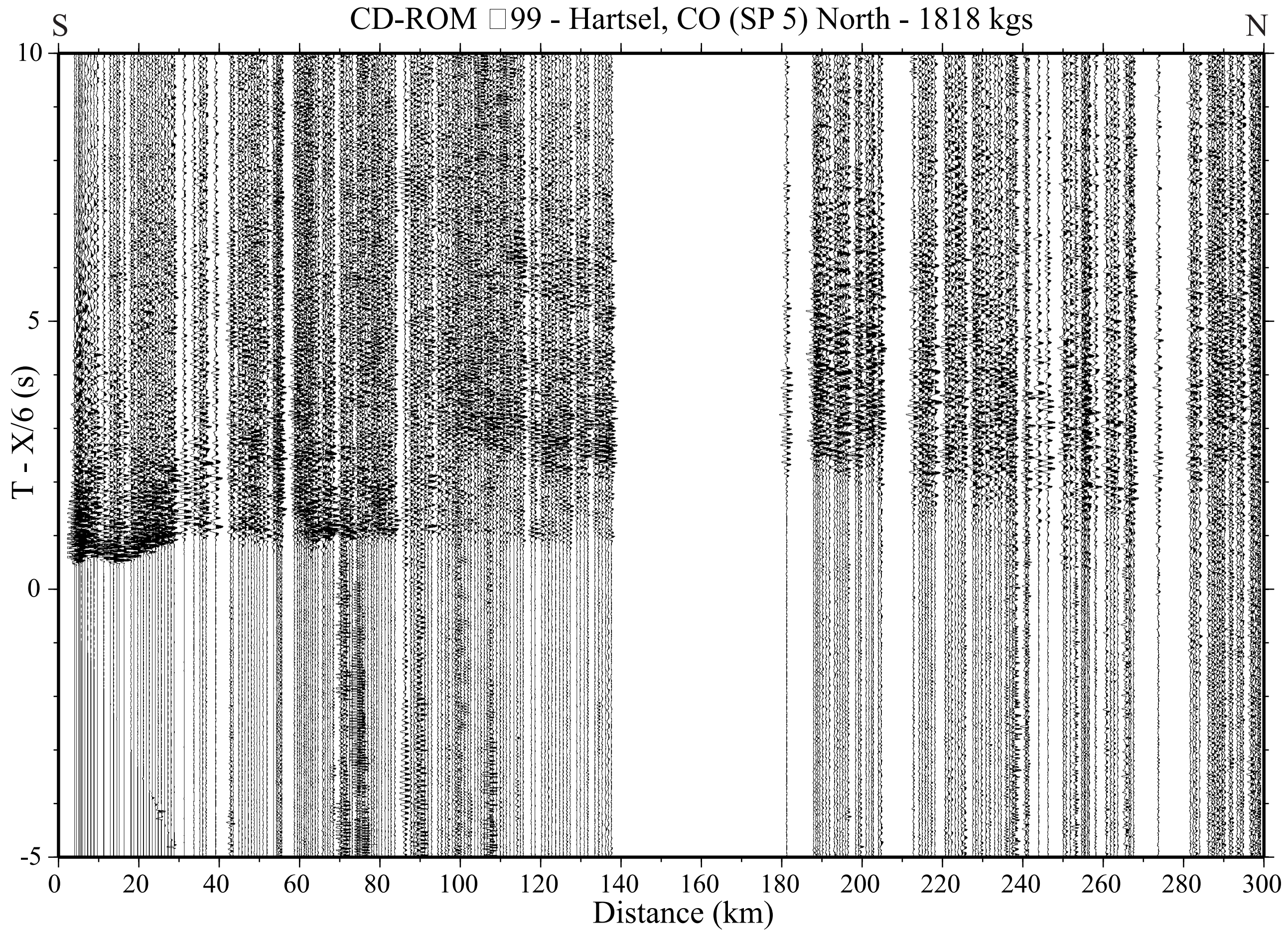

Figure 85. Seismic record section from the Hartsel shotpoint (SP 5) to the north.

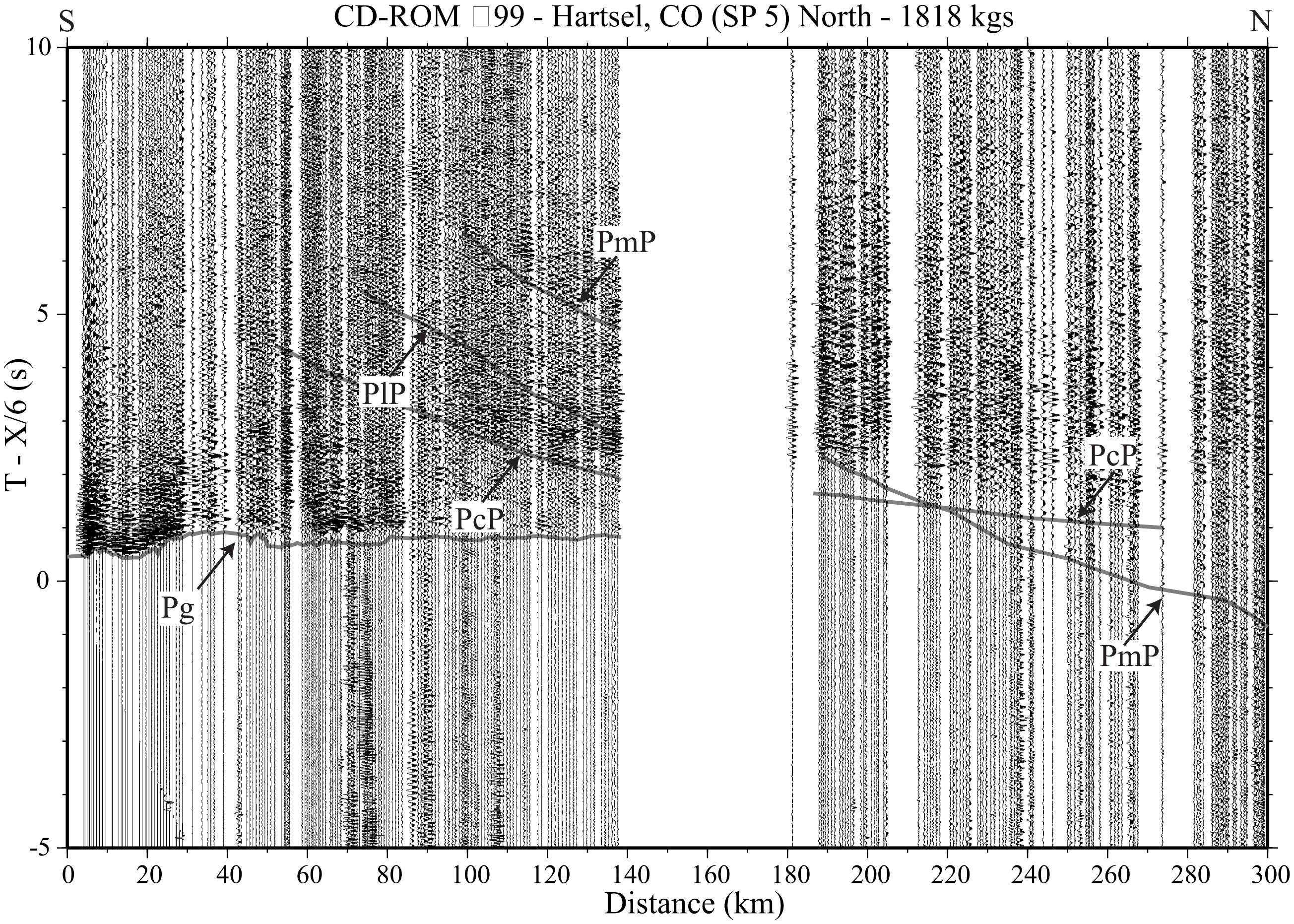

Figure 86. Seismic record section from the Hartsel shotpoint (SP 5) to the north. Pg, PcP, PlP, and PmP are visible on the section. Observed traveltimes are overlain on record.

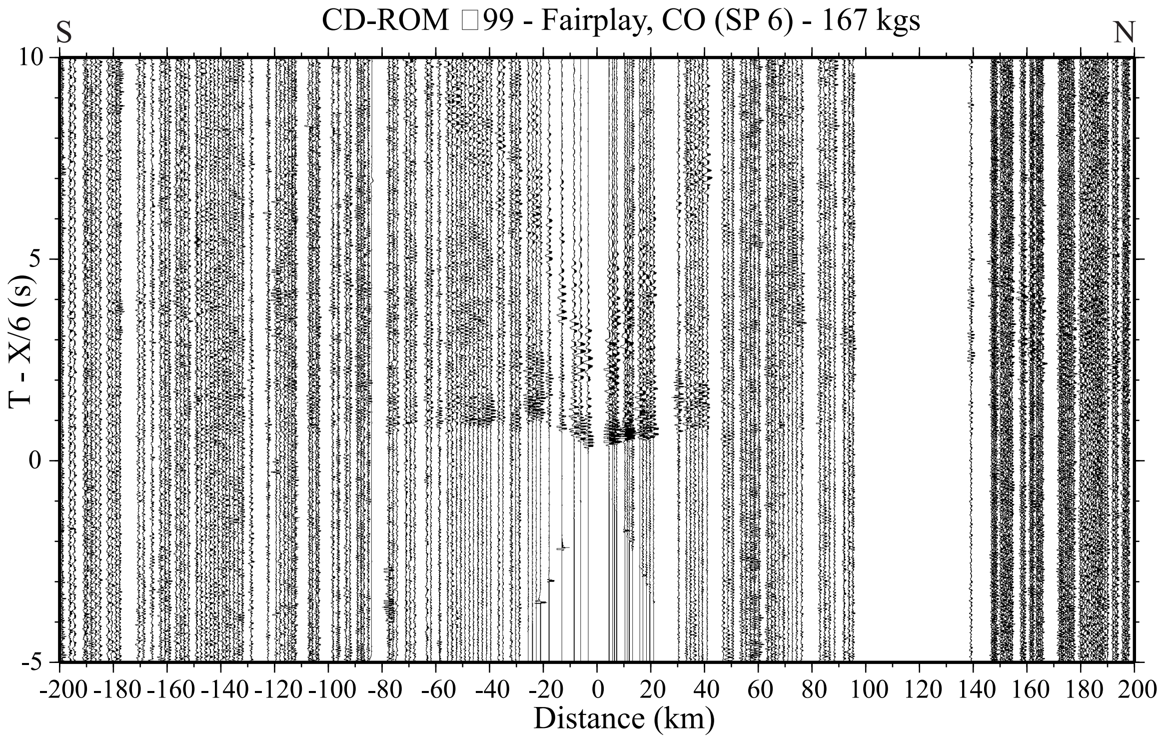

Figure 87. Seismic record section from the Fairplay shotpoint (SP 6).

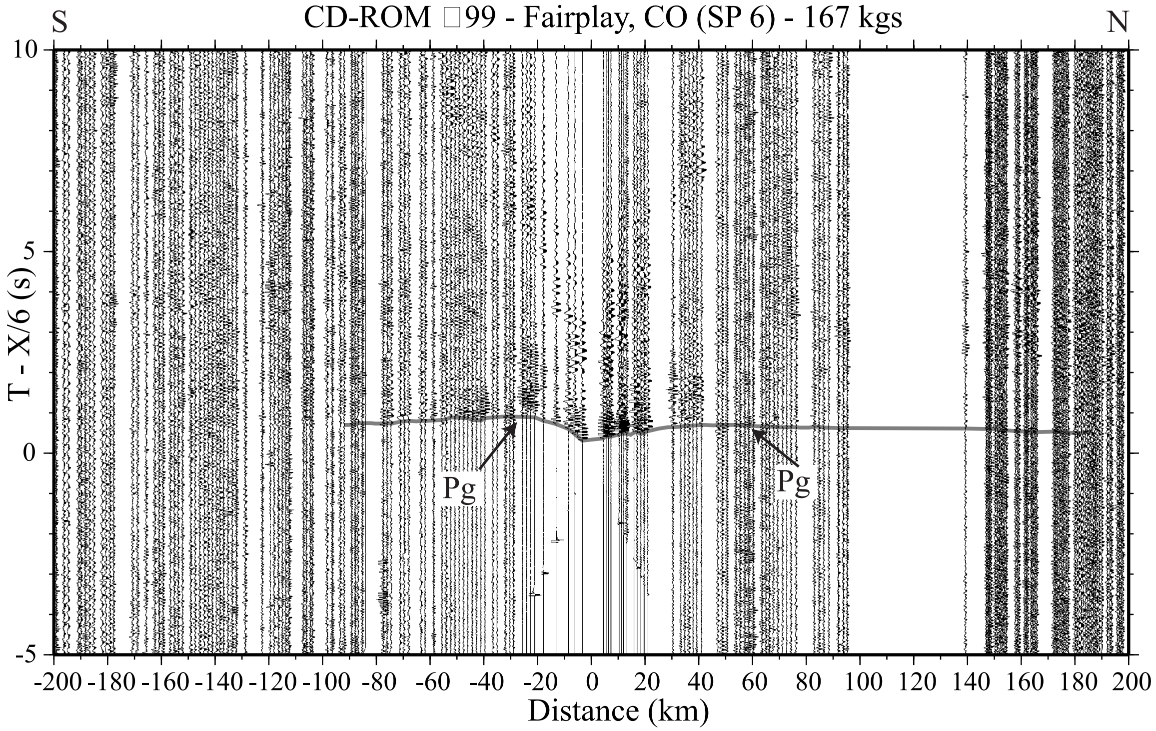

Figure 88. Seismic record section from the Fairplay shotpoint (SP 6). Pg is the only visible phase on this section. Observed traveltimes are overlain on record.

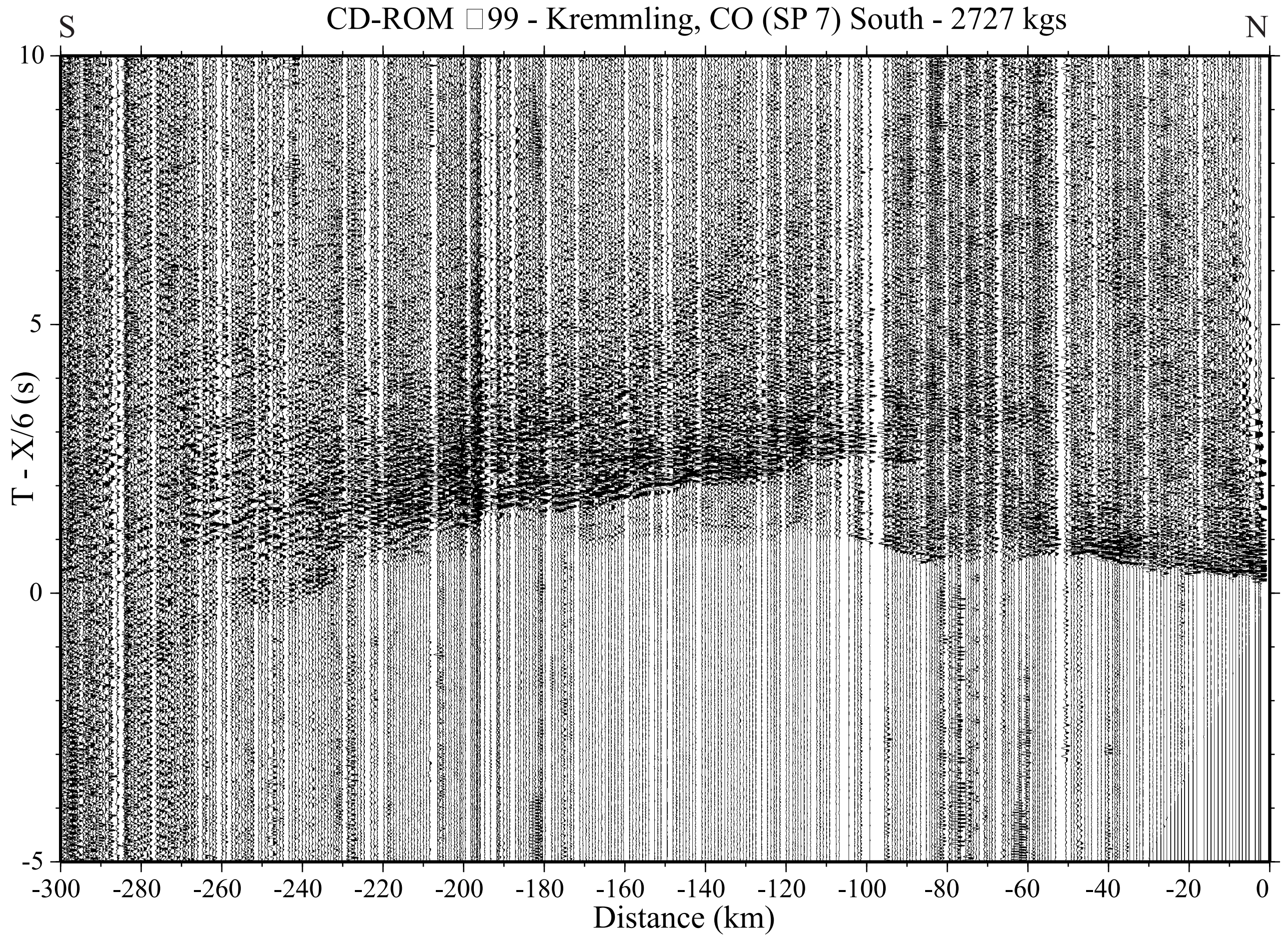

Figure 89. Seismic record section from the Kremmling shotpoint (SP 7) to the south.

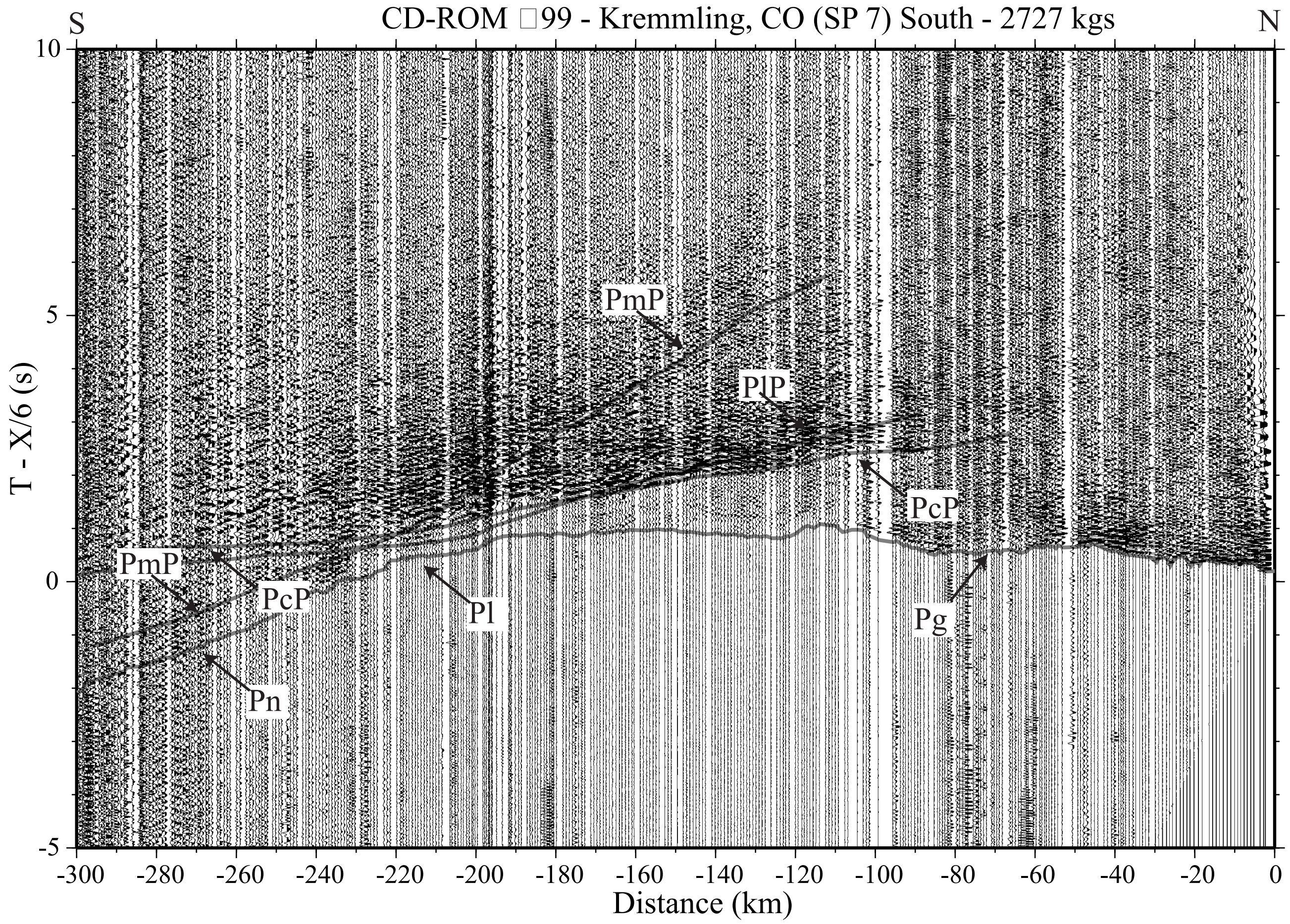

Figure 90. Seismic record section from the Kremmling shotpoint (SP 7) to the south. Pg, Pl, Pn, PcP, PlP, and PmP are visible for the entire length of the section. Observed traveltimes are overlain on

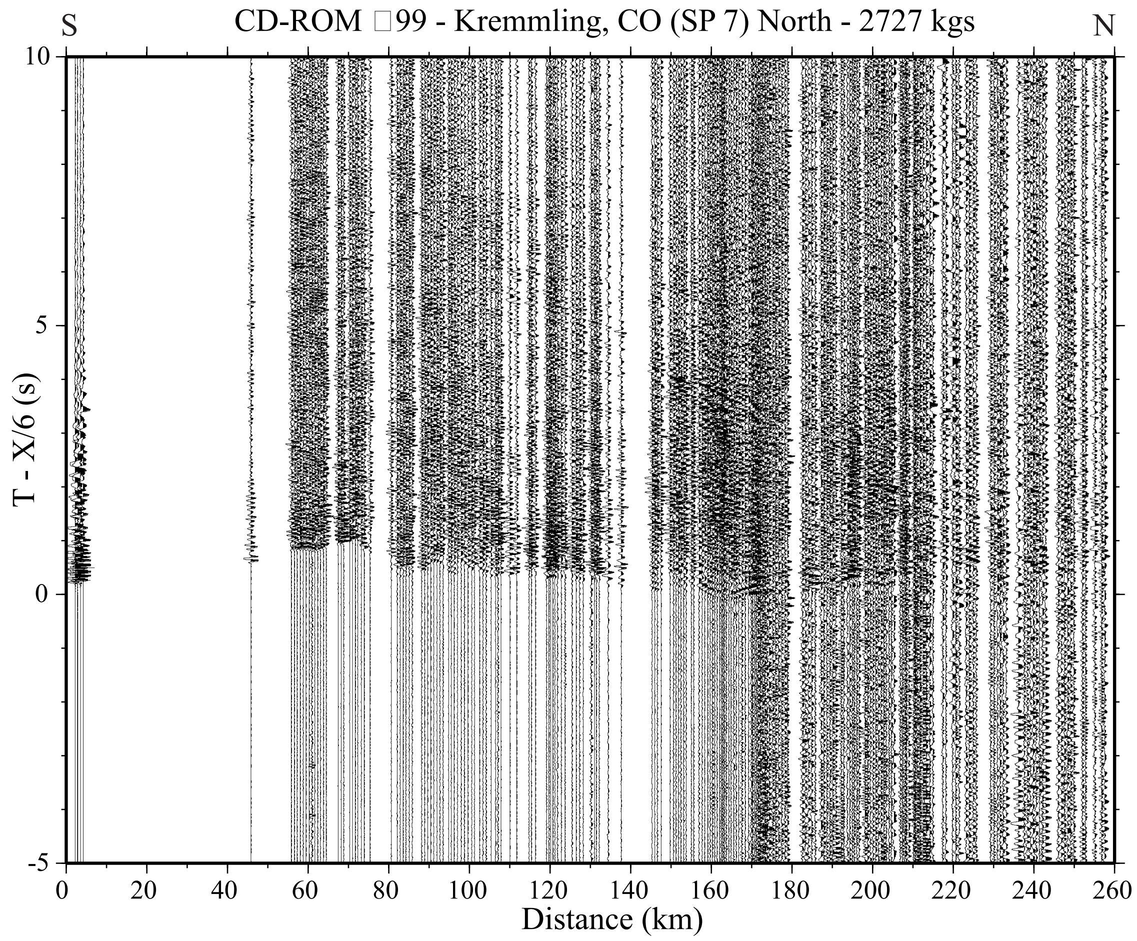

Figure 91. Seismic record section from the Kremmling shotpoint (SP 7) to the north.

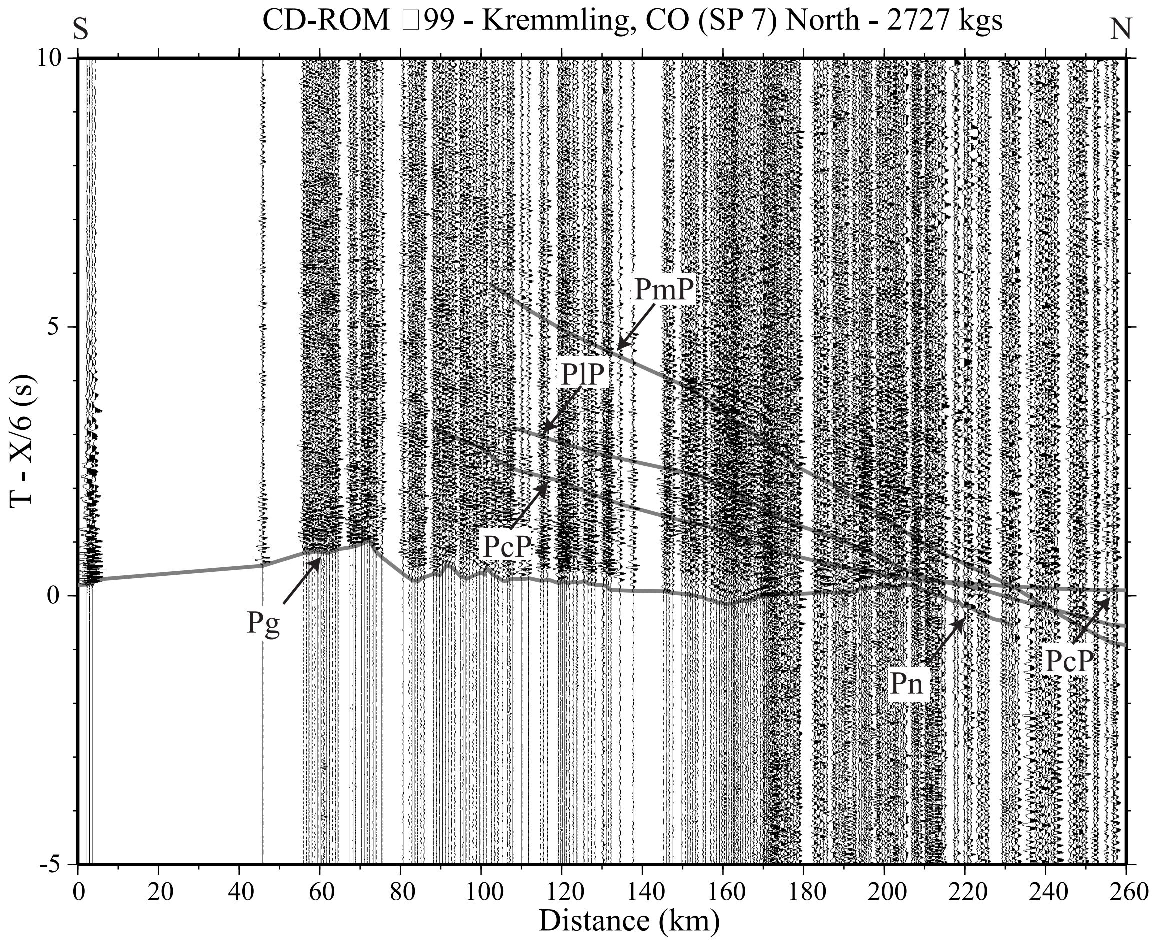

Figure 92. Seismic record section from the Kremmling shotpoint (SP 7) to the north. Pg, Pn, PcP, PlP, and PmP are visible on this section. Observed traveltimes are overlain on record.

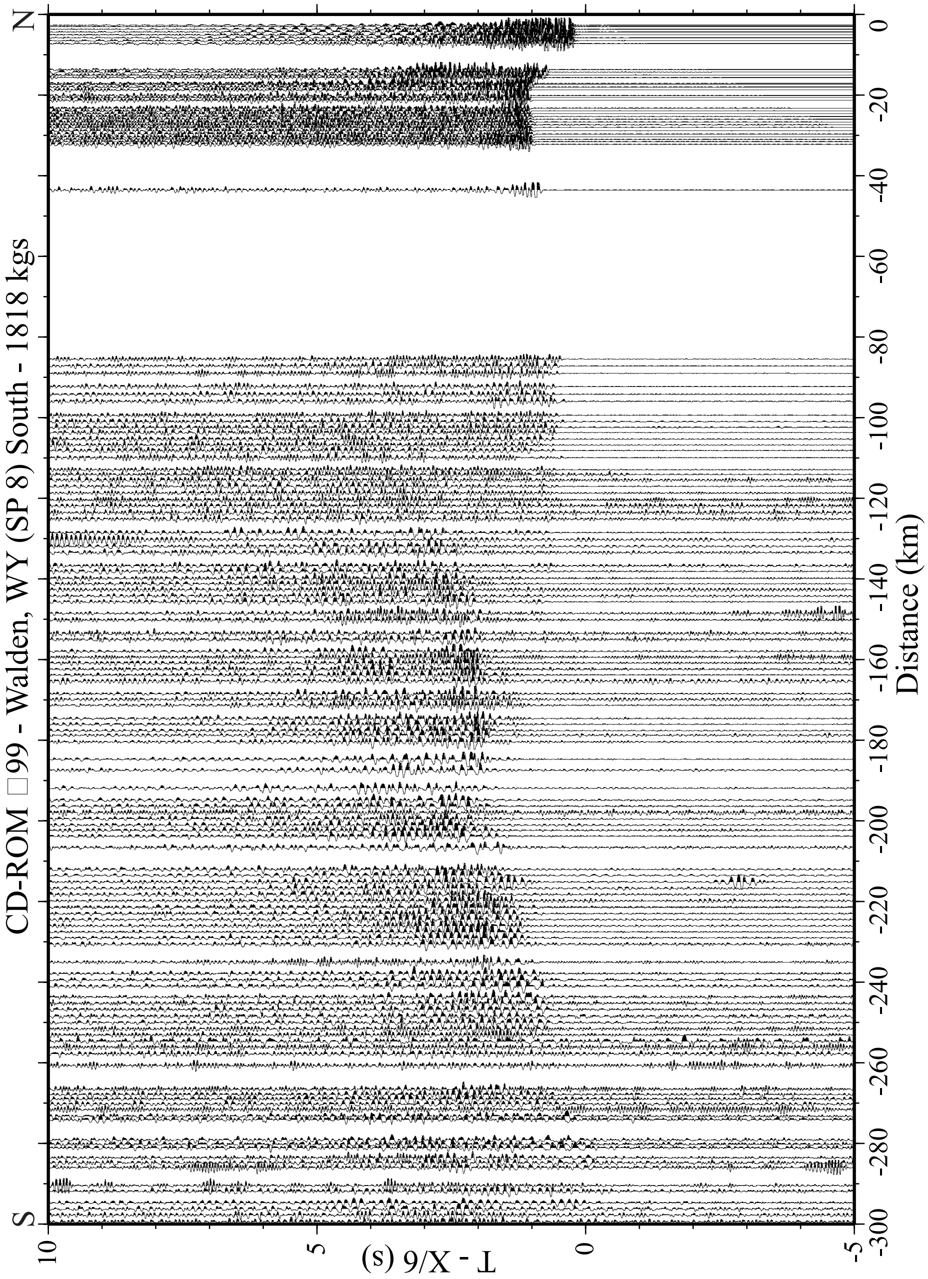

Figure 93. Seismic record section from the Walden shotpoint (SP 8) to the south.

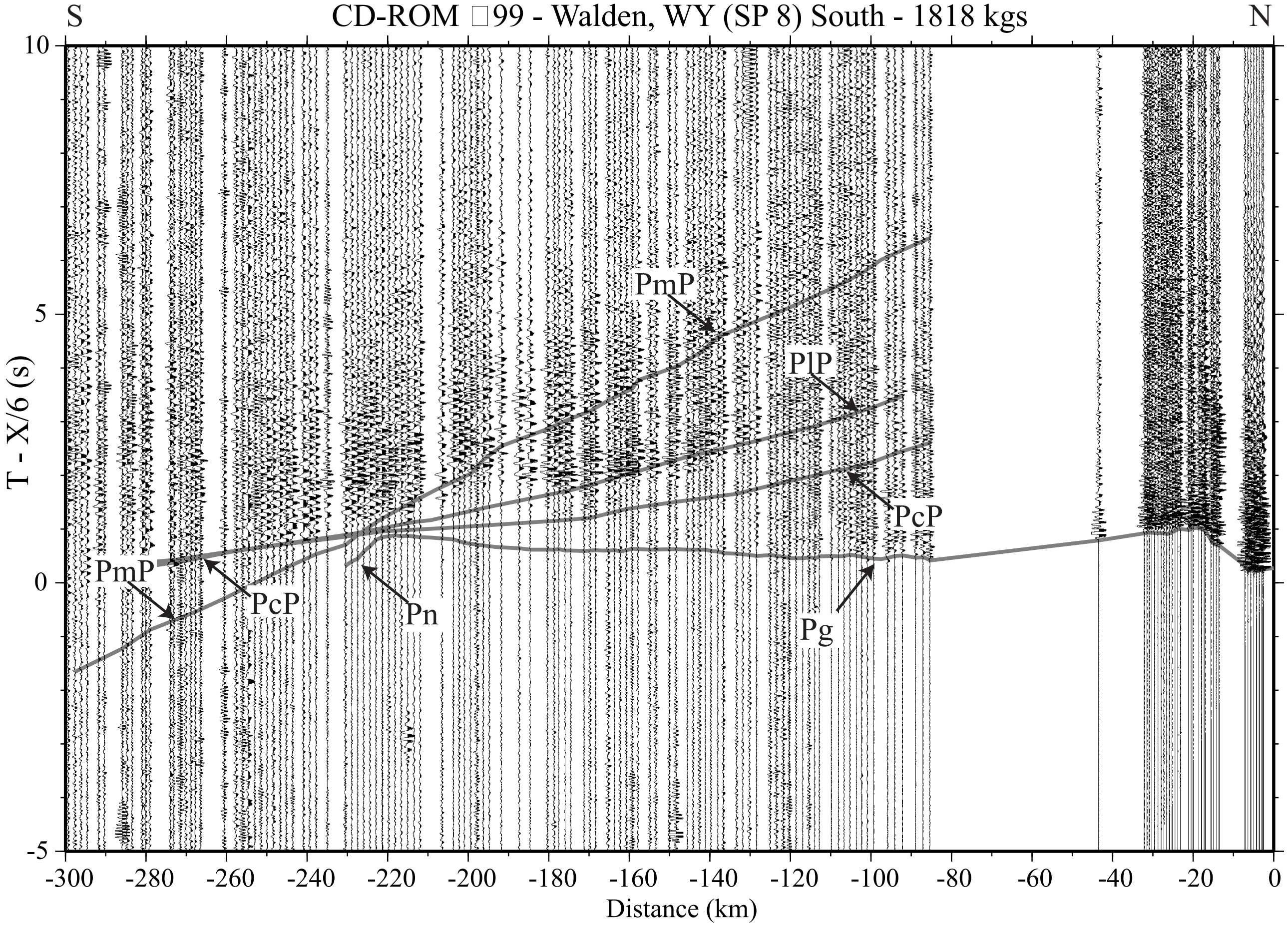

Figure 94. Seismic record section from the Walden shotpoint (SP 8) to the south. Pg, Pn, PcP, PlP, and PmP are visible on this section. Observed traveltimes are overlain on record.

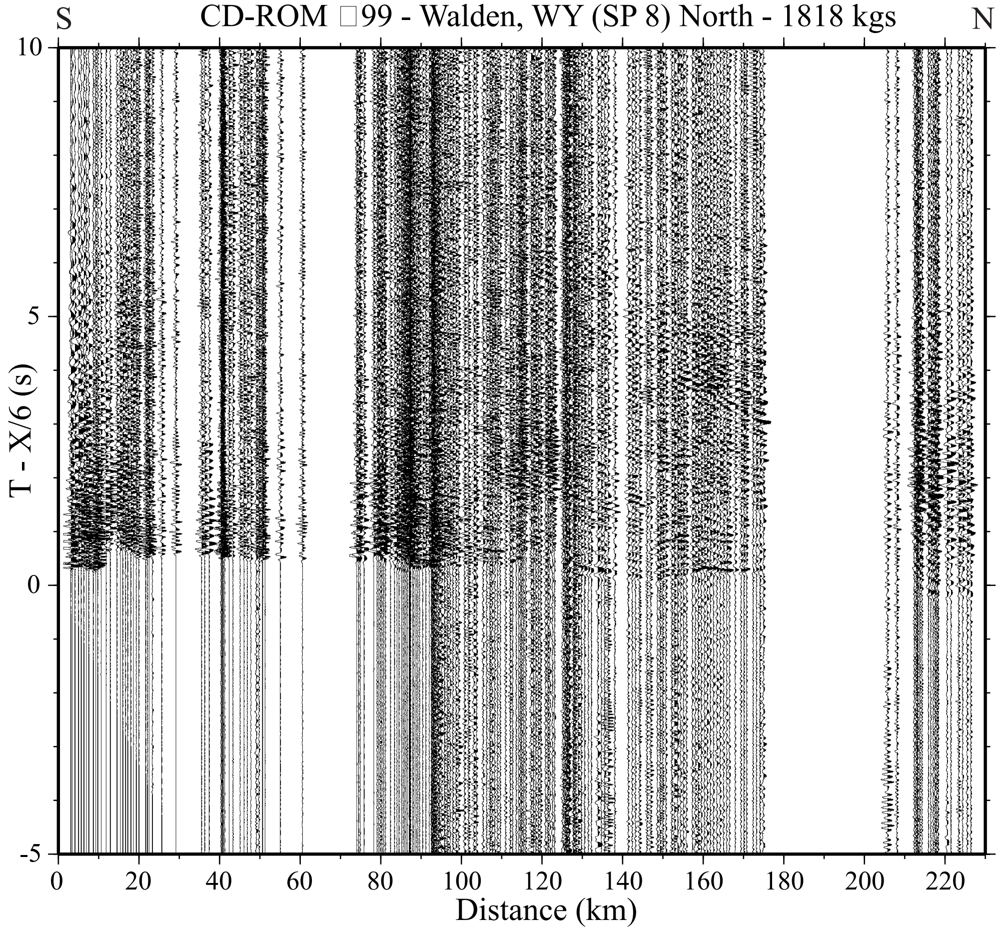

Figure 95. Seismic record section from the Walden shotpoint (SP 8) to the north.

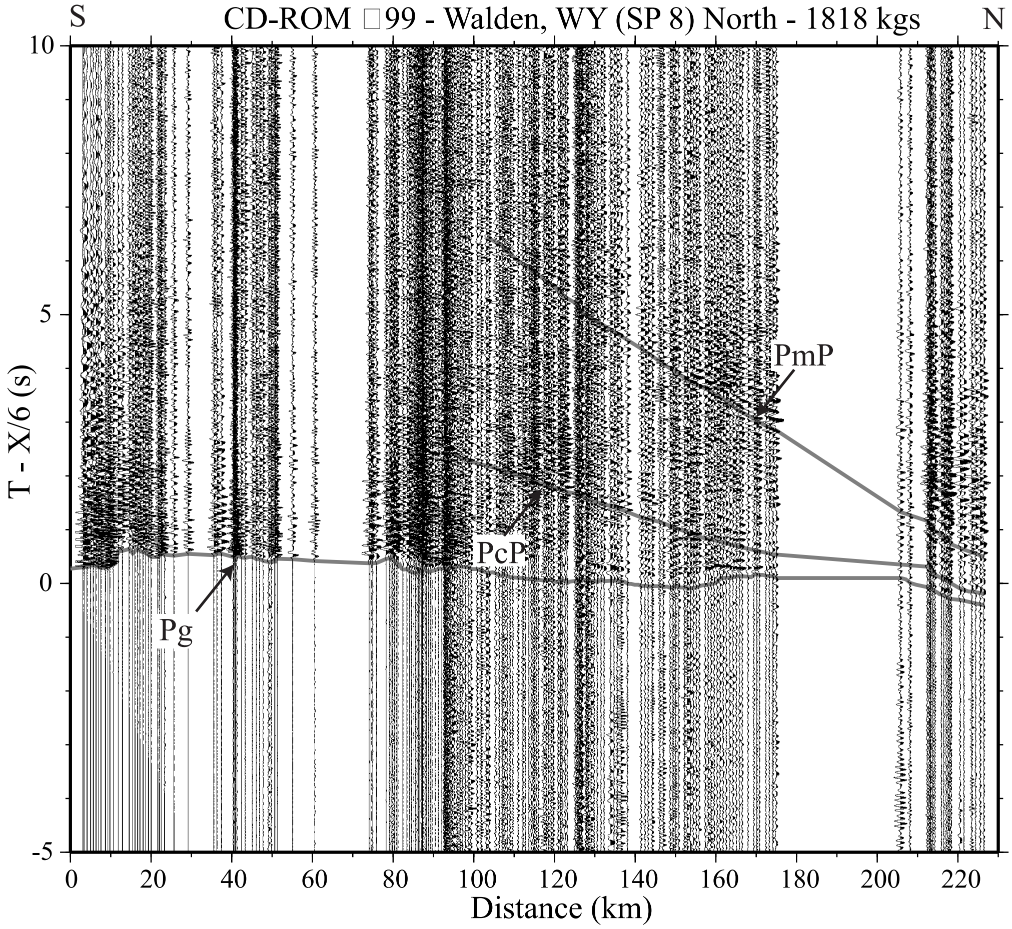

Figure 96. Seismic record section from the Walden shotpoint (SP 8) to the north. Pg, PcP, and PmP are visible on this section. Observed traveltimes are overlain on record.

Wyoming (SP 9) produced Pg arrivals to offsets of ~ 135 km to the south and ~ 120 km to the north (Figures 97 & 98). The source located at the Day Loma pit, Wyoming (SP 10) produced Pg arrivals to offsets of ~ 160 km to the south (Figures 99 & 100).

The lowermost crustal first arrival (Pl) was sometimes hard to identify on record sections, but it was visible on 7 record sections from the CD-RoM effort. The difficulty in identifying this phase is due in part from the low signal to noise ratio but is also due to the changing thickness of this layer along the profile. For this phase to be a first arrival, the velocity contrasts in the lowermost crust must be large and the thickness of the lowermost crustal layer must be on the order of 10 km. SP 1 produced Pl arrivals from ~ 180 to 220 km from the shotpoint (Figures 69 & 70). SP 2 produced Pl arrivals from about ~ 150 to 170 km south of the shotpoint and ~ 180 to 200 km north of the shotpoint (Figures 71 - 74). SP 3 produced Pl arrivals from ~ 190 to 220 km south of the shotpoint and ~ 180 to 200 km north of the shotpoint (Figures 75 - 78). SP 7 produced Pl arrivals from ~ 180 to 220 km south of the shotpoint (Figures 89 - 92). SP 10 produced Pl arrivals from ~ 160 to 190 km south of the shotpoint (Figures 99 & 100).

Generation of the upper mantle refraction (Pn) requires a particularly energetic source in areas with thick crust and was present on 6 record sections. SP 1 produced a Pn arrivals from ~ 220 to 340 km from the shotpoint (Figures 69 & 70). SP 2 produced Pn arrivals from about ~ 200 to 250 km north of the shotpoint, there were no visible Pn arrivals to the south of the shotpoint (Figures 71 - 74). SP 3 produced Pn arrivals from ~ 220 to 280 km south of the shotpoint, there were no visible Pn arrivals north of the shotpoint (Figures 75 - 78). SP 5 produced Pn arrivals from ~ 220 to 270 km south of the shotpoint; there were no visible Pn arrivals north of the shotpoint (Figures 83 - 86). SP 7

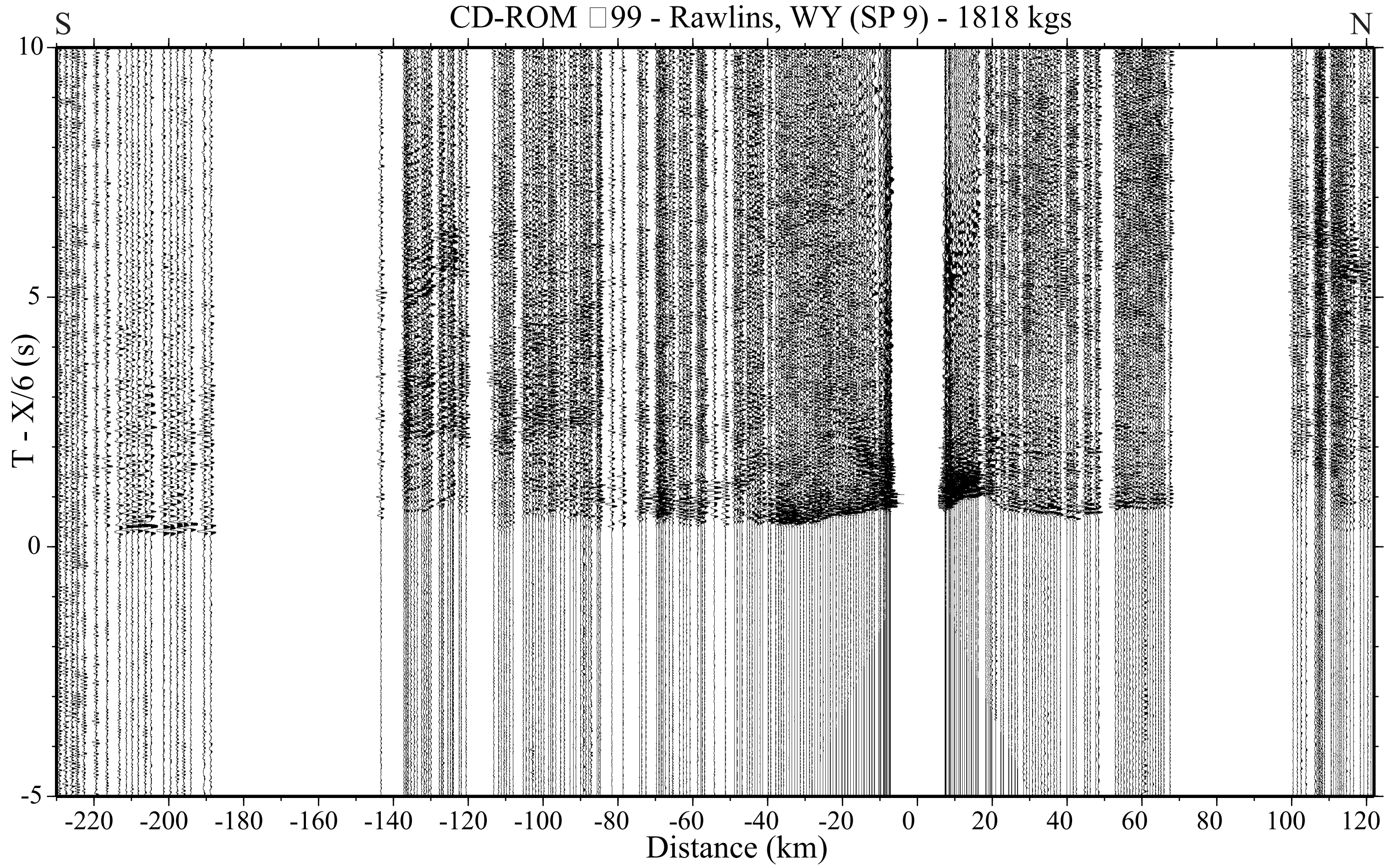

Figure 97. Seismic record section from the Rawlins shotpoint (SP 9).

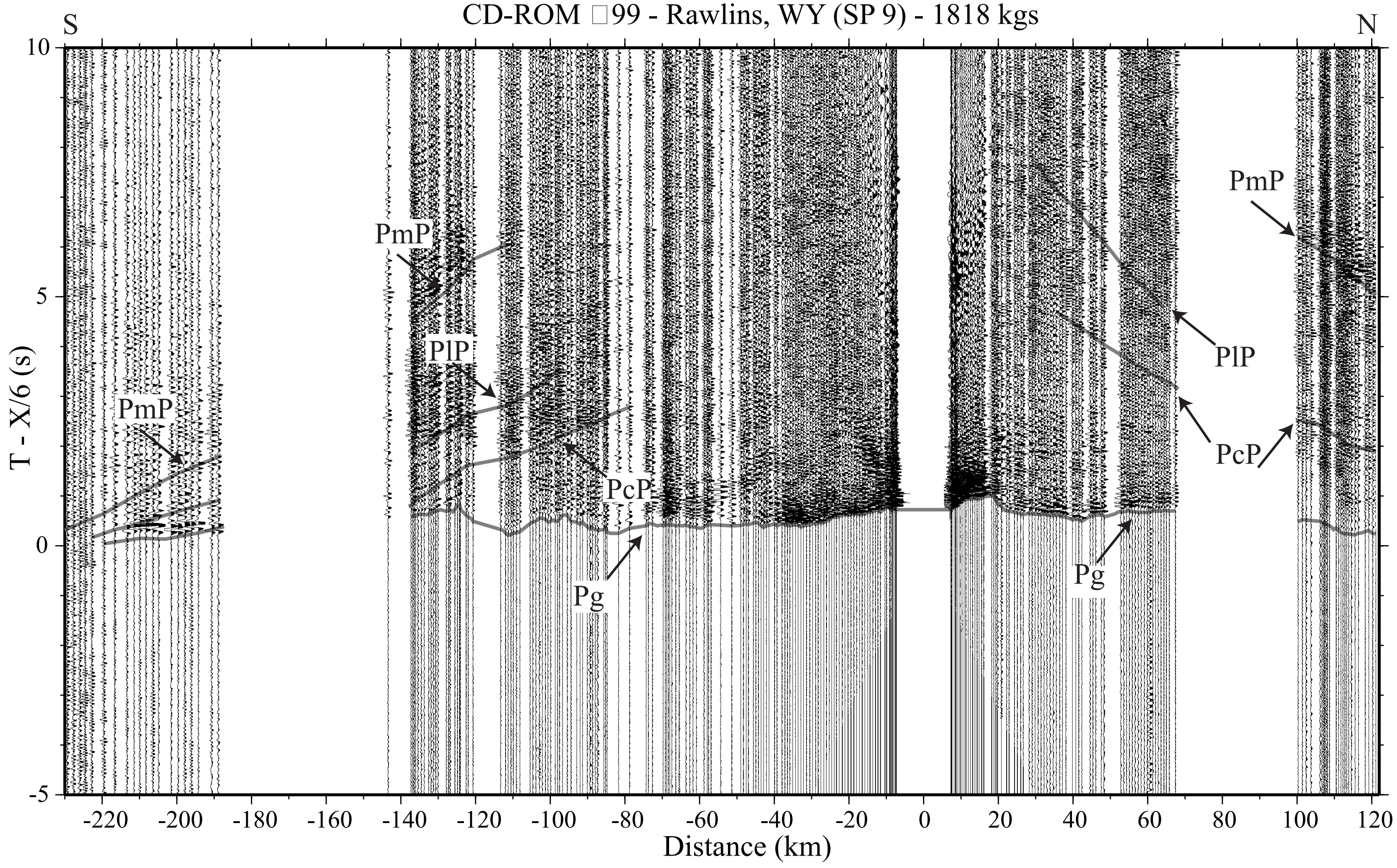

Figure 98. Seismic record section from the Rawlins shotpoint (SP 9). Pg, PcP, PlP and PmP are visible on this section. Observed traveltimes are overlain on record.

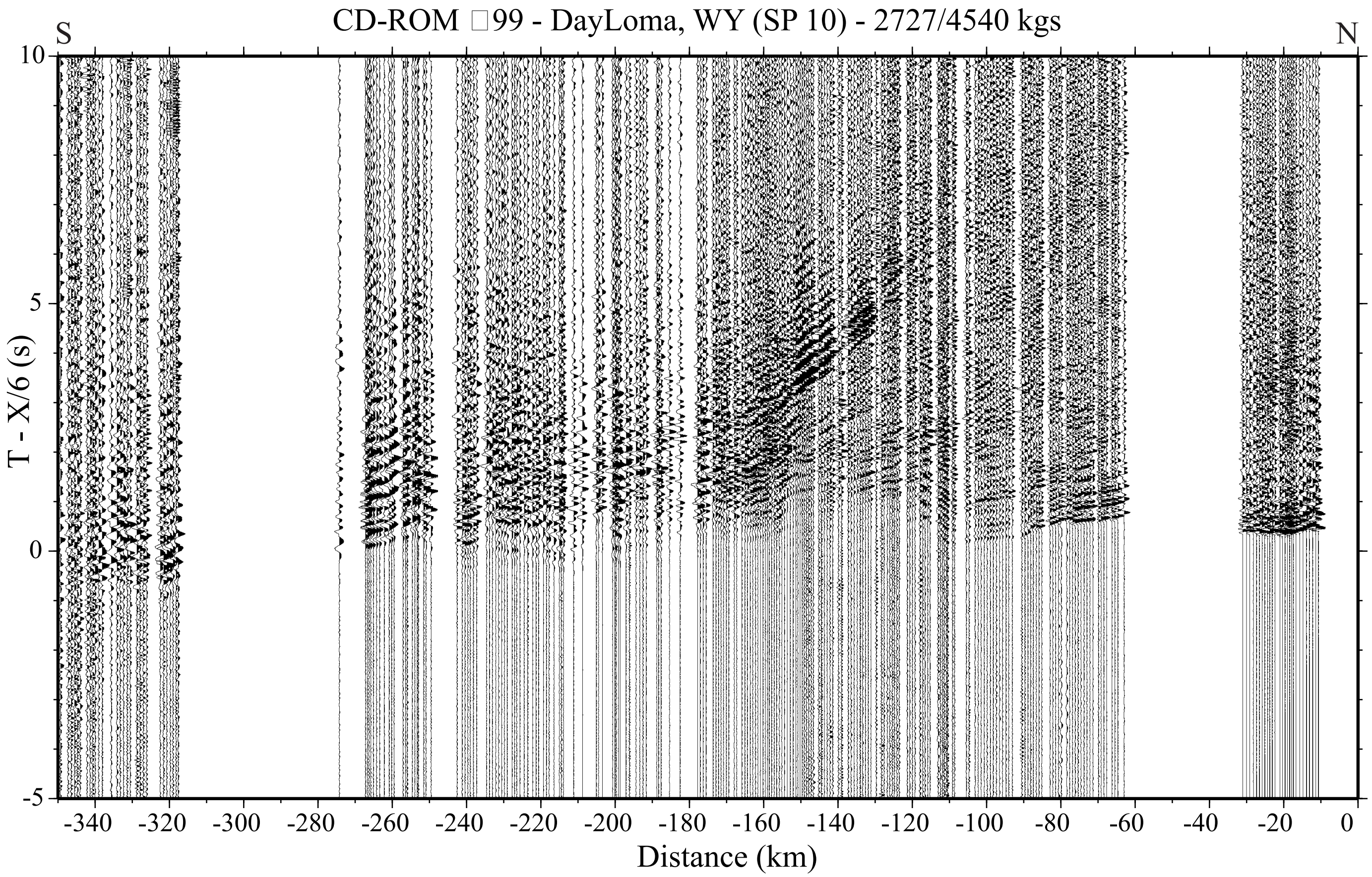

Figure 99. Seismic record section from the Day Loma shotpoint (SP 10).

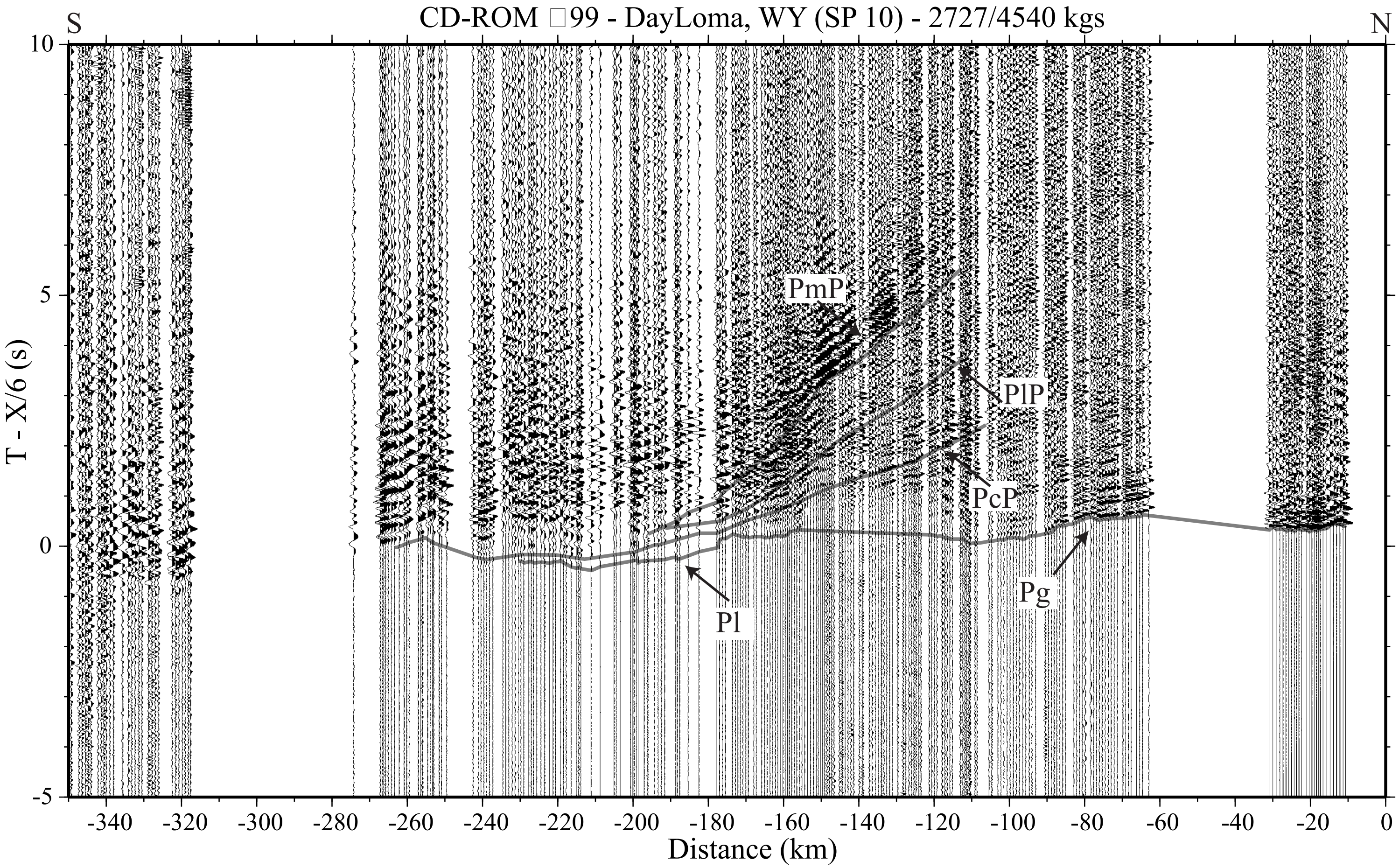

Figure 100. Seismic record section from the Day Loma shotpoint (SP 10). Pg, Pl, PcP, PlP, and PmP are visible on this section. Observed traveltimes are overlain on record.

produced Pn arrivals from ~ 220 to 290 km south of the shotpoint and from 210 to 240 km to the north of the shotpoint (Figures 89 - 92). SP 8 produced Pn arrivals from ~ 220 to 230 km to the south of the shotpoint; there were no visible Pn arrivals north of the shotpoint (Figures 93 - 96).

The mid-crustal reflector (PcP), generally has high amplitudes and post-critically over takes the Moho reflector (PmP) in terms of amplitude and travel time making picking the post-critical PmP difficult (Figures 101 - 104). This energy pattern seems to be common among most of the record sections. At first glance one might pick the higher amplitude energy as PmP, but when looking at the move-out for that arrival, it becomes clear that the low apparent velocity indicates the wave is sampling the upper/middle crust and not the lower crust (Figures 101 - 104). Therefore, the PmP phase must arrive earlier as it has an apparent velocity that is approaches the average velocity of the entire crust. The lowermost crustal reflector (PlP) often has high amplitudes as well, but its amplitude is exceeded by the mid-crustal reflector (PcP) on some sections (Figures 101 - 104). The Moho reflection (PmP) is present on all record sections except for that from SP 6. As stated above, the post-critical reflection is difficult to pick due the moderate amplitude that suggests the velocity contrast across the Moho is gradational (Figures 101 - 104).

Reflectivity Modeling

The large amplitudes associated with the post-critical portion of several record sections were enigmatic (e.g., Figure 70). The move-out of the energy was about 6 km/s which indicated that this wide-angle reflection could not be associated with the Moho, but originated in the mid-crust (PcP). Synthetic seismograms were created to better understand the reflectivity seen within the seismic record sections (Fuchs and Müller,

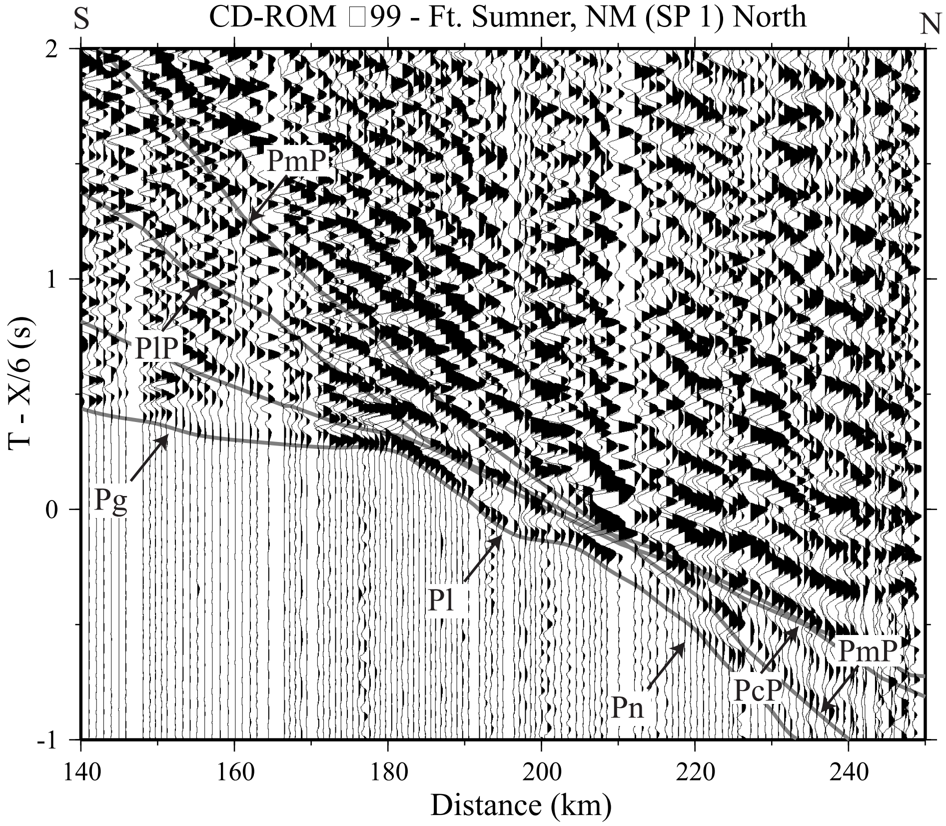

Figure 101. Close-up view of a portion of the Ft. Sumner record section. The PcP phase has a high amplitude and has a move out of about 6 km/s.

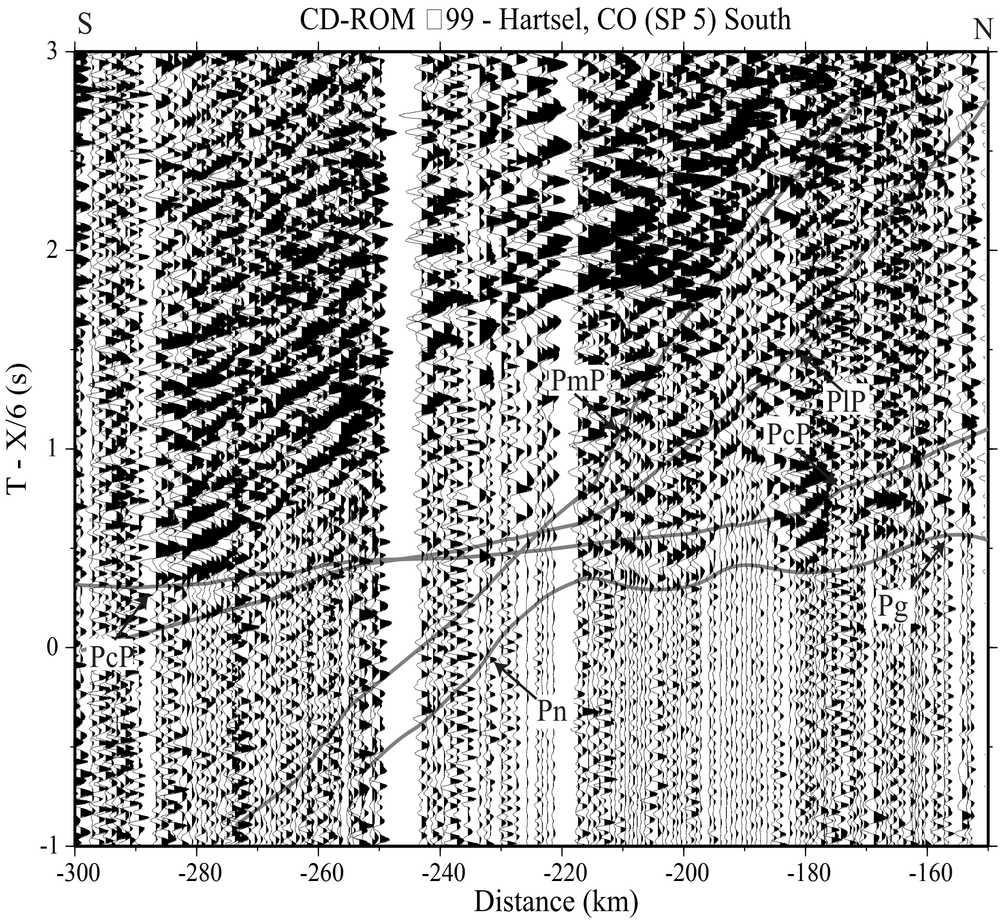

Figure 102. Close-up view of a portion of the Harstel record section. Showing that the PcP phase is high amplitude and has a move out to that of the crust not the high velocity lower crustal layer.

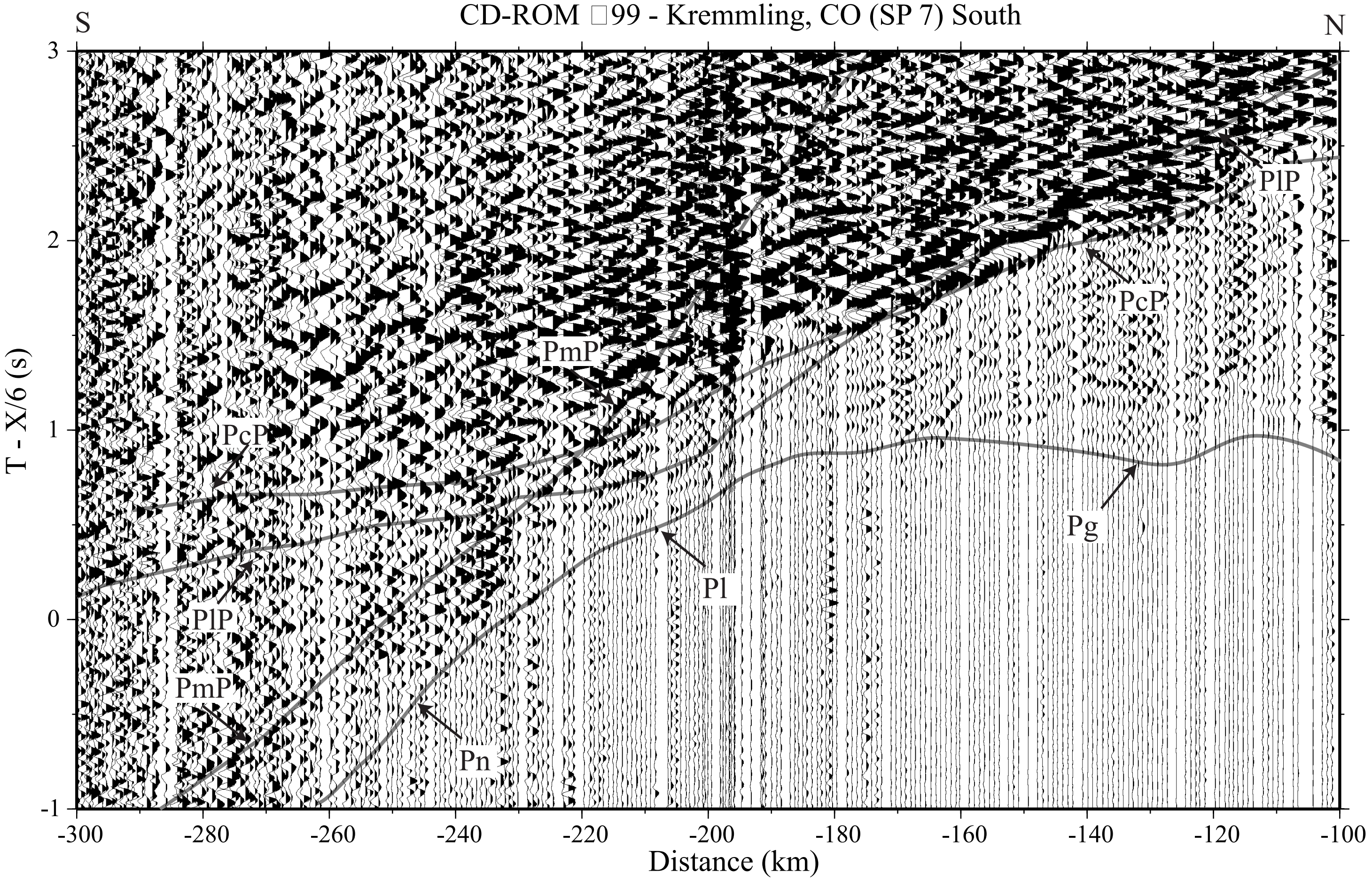

Figure 103. Close-up view of a portion of the Kremmling record section. Showing that the PcP phase is high amplitude and has a move out to that of the crust not the high velocity lower crustal layer.

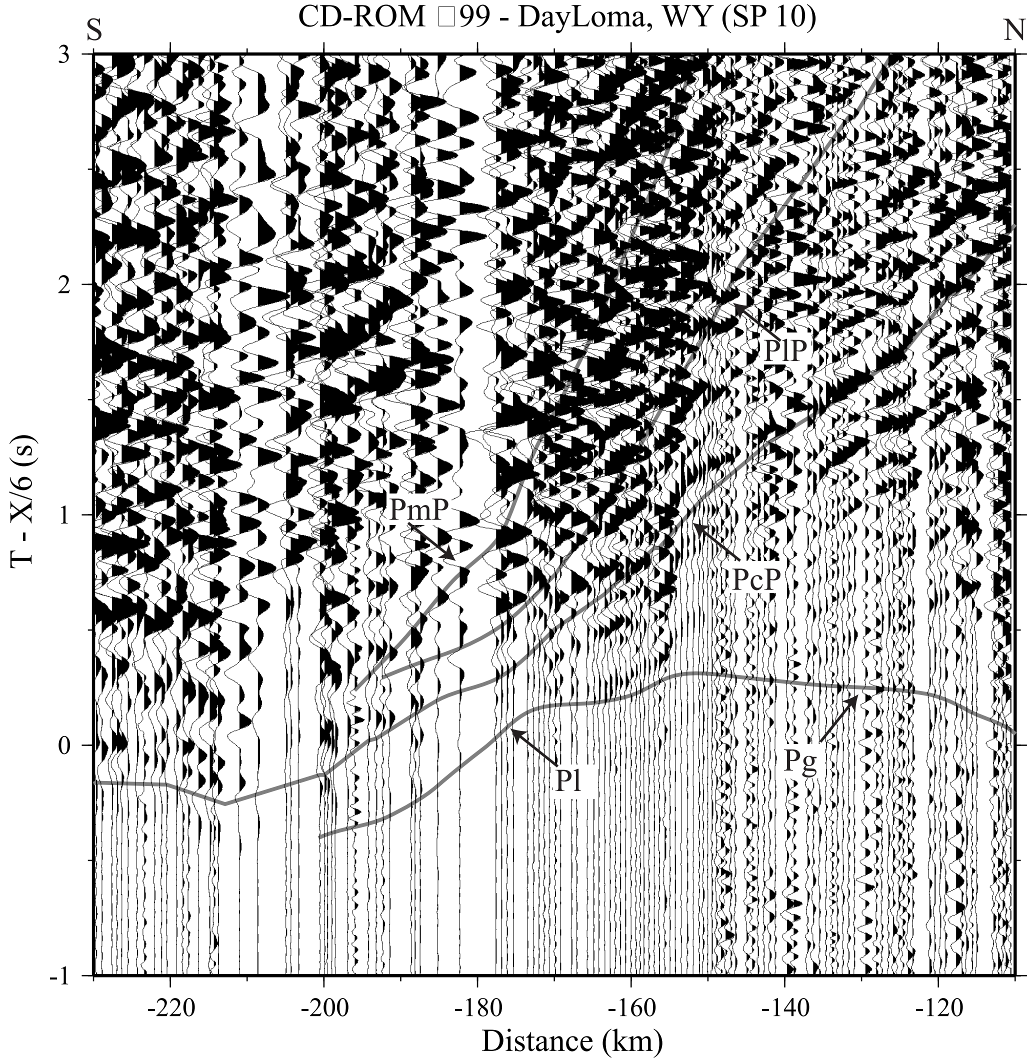

Figure 104. Close-up view of a portion of the Day Loma record section. Showing that the PcP phase is high amplitude.

1971). The technique uses a 1-D model through the earth from the shotpoint location and calculates waveforms for a defined set offsets and time. Only the P-wave energy was calculated for the synthetic.

The Ft. Sumner (Sp 1) record section was chosen as the best candidate for this calculation because the data quality was very high (Figure 105). The 1-D model that was created using the final tomographic model. The 1-D had a sharp boundary at ~ 22 km depth, then another sharp boundary at ~ 29 km depth, and then the high-velocity lowermost crust was a zone of gradational velocity increase to depth from 46 - 49 km these values (Figure 106). The synthetic produced from this 1-D model shows similar waveforms compared to the original data (Figure 107). The amplitudes of the PcP phases from the mid-crustal interface are comparable as is the moveout of this wide-angle reflection.

Initial Modeling

Too gain an initial understanding of the main phases, initial modeling was undertaken using the forward modeling software MacRay (Luetgert, 1992). The Deep Probe model (Figure 68) was used as a reference and then modified to account for the local geology along the CD-RoM profile. The upper 5 km of the model was constrained by known geology using various maps and the literature (Figure 108) (e.g., MacLachlan et al., 1972; Cordell et al., 1982; Woodward, 1988; Sloss, 1988; Blackstone, 1993). Several iterations of forward modeling were undertaken to insure the quality of the picks and phase identifications before proceeding into the inversion. The main phases picks are the same between this modeling and the modeling our German colleagues are undertaking.

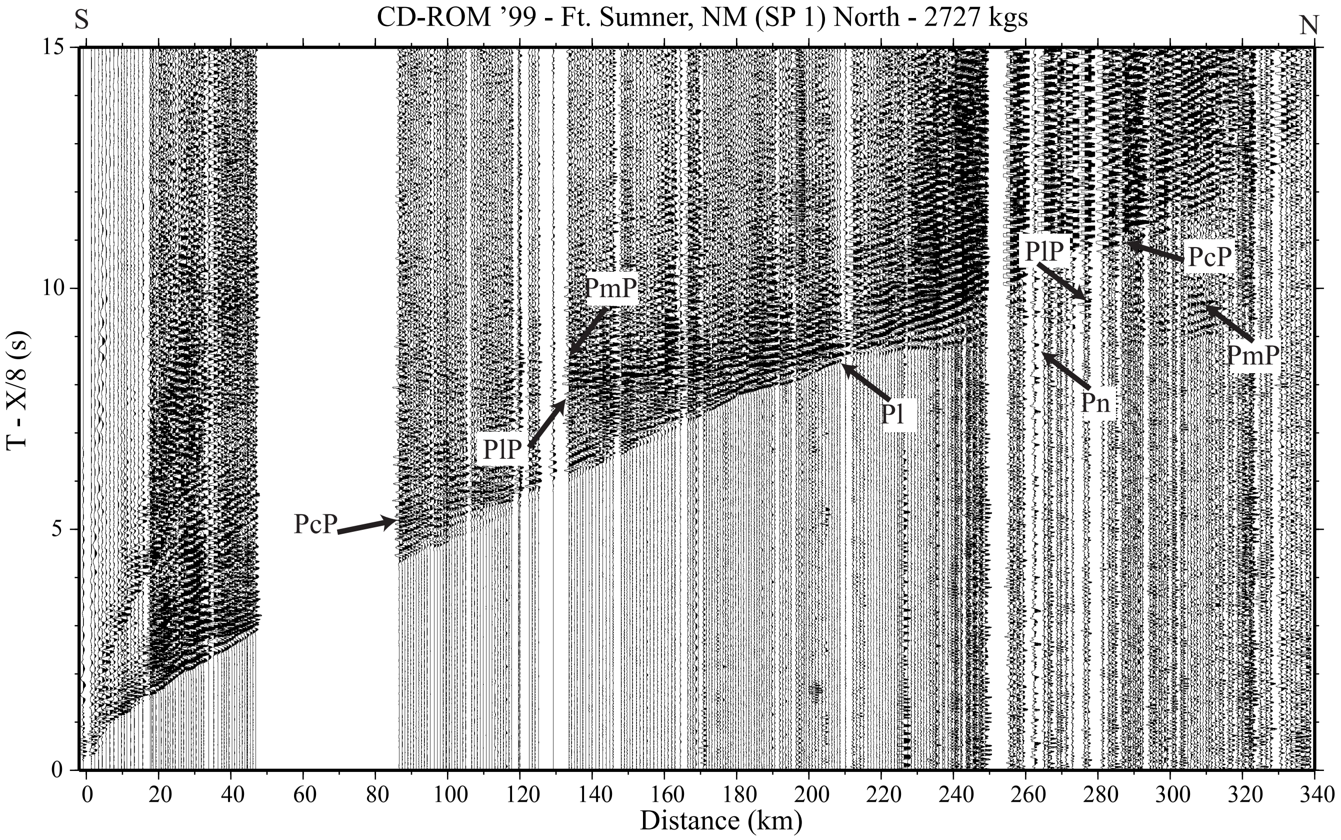

Figure 105. Seismic record section from the Ft. Sumner shotpoint (SP 1) reduced at 8 km./s for a one to one comparison with the synthetic seismograms in Figure 107.

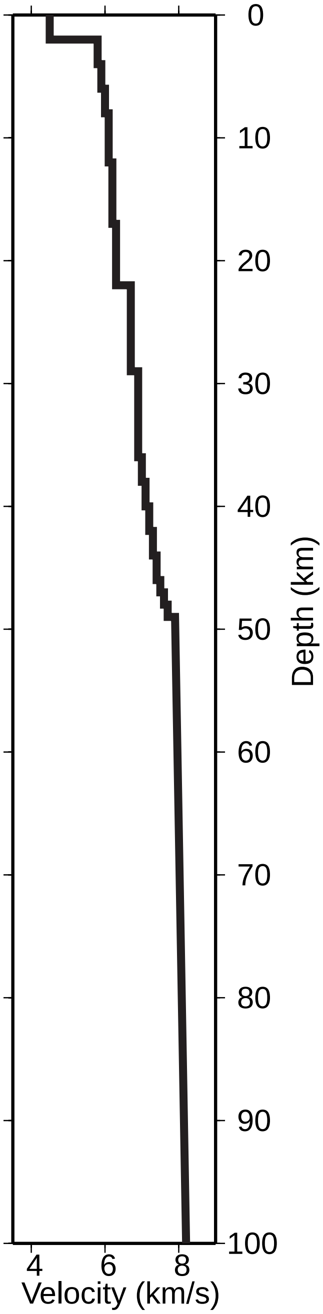

Figure 106. 1-D model used to create synthetic seismograms in Figure 107.

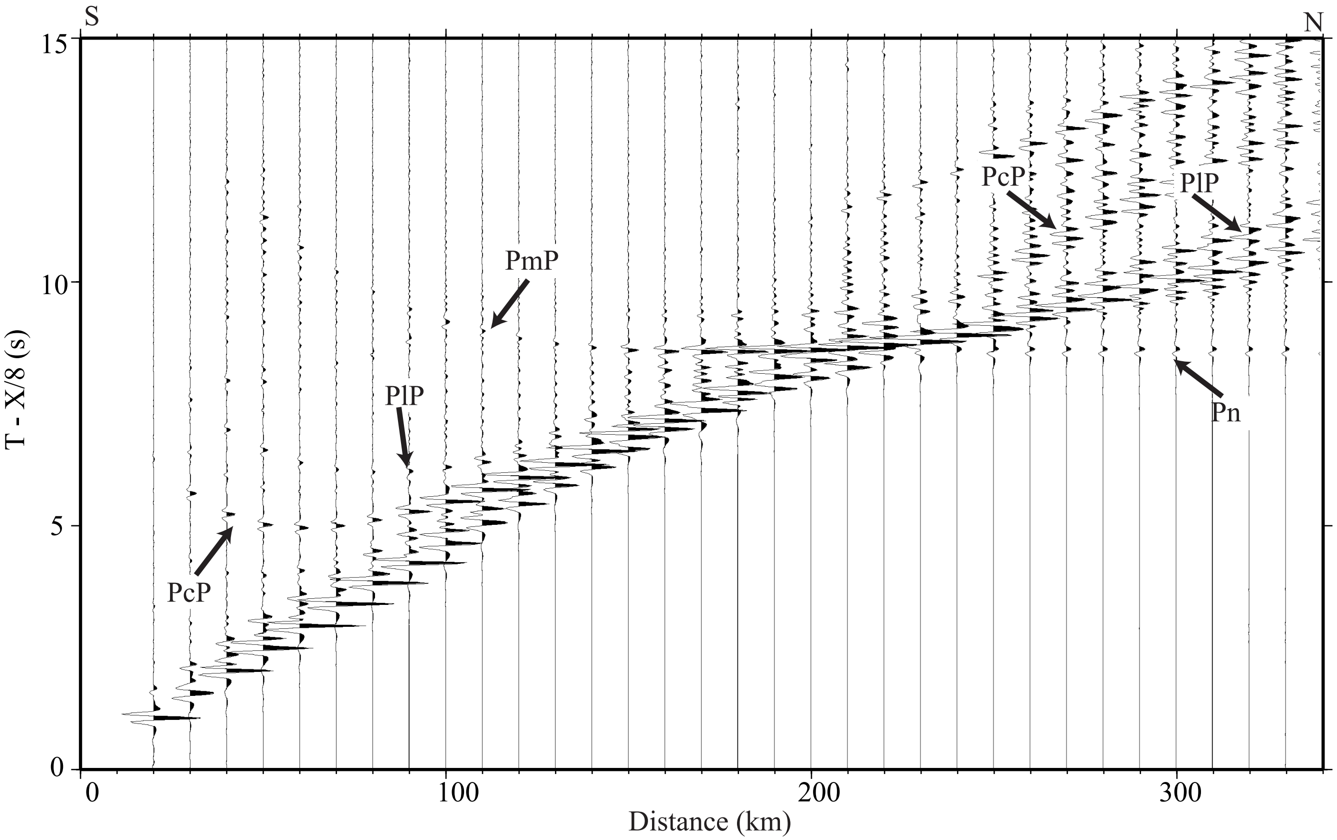

Figure 107. Synthetic seismograms of the Ft. Sumner (Sp 1) record section. Phases of interest are labeled.

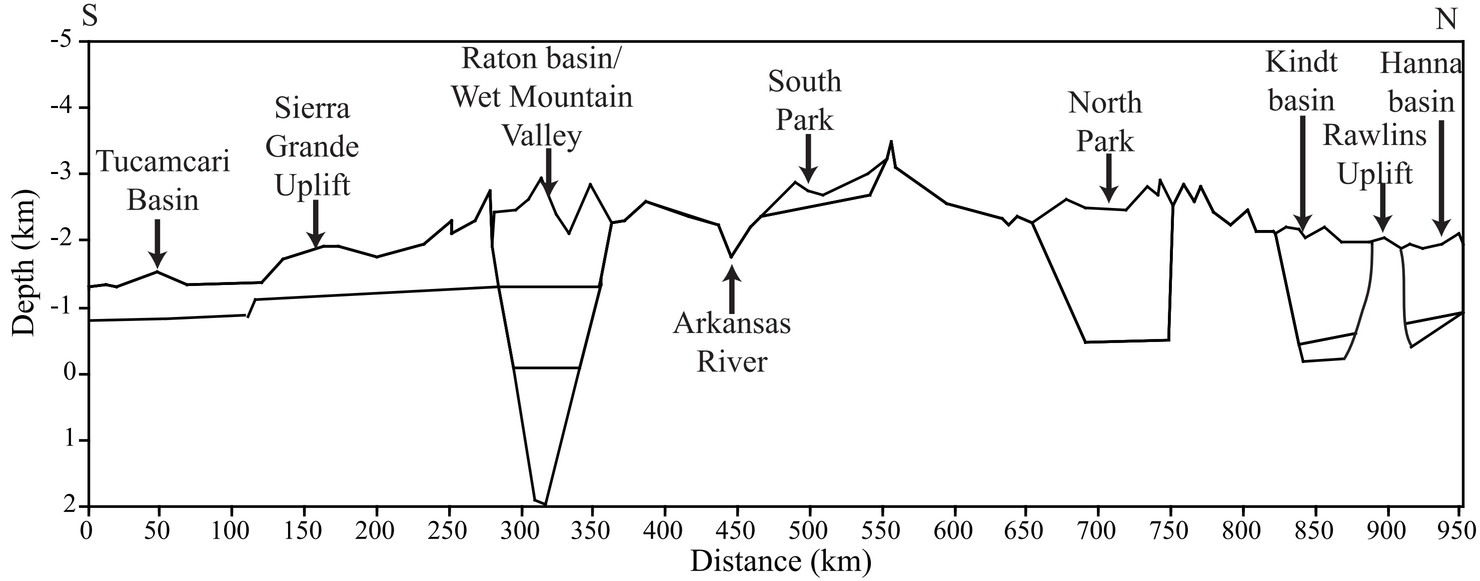

Figure 108. Upper 2 km of the model as derived by the literature (e.g., MacLachlan et al., 1972; Cordell et al., 1982; Woodward, 1988; Sloss, 1988; Blackstone, 1993 provided by L. Treviño)

Tomography

Over 2600 P-wave first arrivals from the data were used in a traveltime tomography code. The picking error for the first arrivals is ~ 100 ms and the reflections are ~ 200 ms or more. We used a 3-D approach for this problem because of the crooked-line geometry of the profile (Figure 63). This approach solves any geometrical artifacts that would have occurred in 2-D modeling. We chose the Hole (1992) code, which is a non-linear high resolution tomographic technique. It is computationally efficient and handles large velocity contrasts (Hole, 1992). The code uses a finite difference approximation to the eikonal equation to calculate traveltimes (Vidale, 1988;1990). The model space consists of a 3-D velocity model defined on a uniformly spaced grid. Initial traveltimes are calculated to all grid points by a finite difference operator which uses the average slowness across each cell (Hole, 1992). Ray paths are back-projected through the array of calculated traveltimes to obtain the traveltime at any given receiver for a source in the model space.

The inversion requires a linearization of the eikonal equation with a Taylor series expansion that ignores higher order terms (Hole, 1992). The eikonal equation is solved iteratively for perturbations to the velocity model until the RMS residual no longer changes or reaches the picking error of the dataset. The technique is non-linear because traveltimes are re-calculated through an updated model after each inversion.

Procedures for running the inversion were as follows. First, an initial 1-D model is expanded into a 3-D volume and used to calculate initial ray paths. Second, traveltime residuals are calculated. Third, a slowness perturbation model is found in the inversion, which minimizes the differences between calculated and observed traveltimes. Next, the initial model is updated and smoothed using a moving average filter. Finally, the new model is input to the next iteration and traveltimes are recalculated. The smoothing factor or moving average filter is reduced, by almost half, for every iteration until the size of the smoother is equal to that of the receiver spacing. This continues until the change in RMS becomes insignificant.

Since the PcP, PlP, and PmP phases were so prominent, we used the forward modeling of these reflections in the Hole code (Hole and Zelt, 1995) to further constrain the model. The reflections are calculated by first propagating waves to a defined surface in depth and then the rays are turned around and re-calculated back to the source (Hole and Zelt, 1995). Using the 3-D first arrival model as a reference, a depth is chosen first for the first interface. This layer is then defined in terms of depth nodes within the 3-D space and iterated on until the observed and calculated traveltimes fit. Once the interface is resolved then the 3-D first arrival model is updated with the new interface. This procedure is used for calculating the location of the top of the mid-crustal interface (PcP), the top of the lowermost crustal layer (PlP), and the top of the Moho (PmP).

The model space used in this study has corners at -107.30^{o}, 43.00^{o} at the origin and -104.30^{o}, 34.00^{o} for the opposite corner. The stations and shot locations were transformed from latitude and longitude to X and Y with an oblique Mercator projection. The size of the model is 1022 km in x (south-north) by 87 km in y (west-east) by 70 km in depth and has a 1 km grid spacing (Figure 109). The sides of the model have ~ 10 km of padding in x and y and 4 km in z to prevent rays escaping from the model. All the 2-D figures were calculated based on weighted averages in the 3-D volume using the hit count.

The initial model was created using a 1-D average from the forward modeling with MacRay and the Deep Probe '95 model (Snelson et al., 1998). The 1-D model was constructed with a gentle velocity gradient though the crust (Figure 106). At the base of the model a low velocity was assigned, which prevents rays from getting trapped or guided at the bottom of the model (Hole, 1992). An initial model that produced and RMS of less than 1.5 s was chosen for the inversion (Figure 109). The inversion is very sensitive to the starting model. For example, a slower model than the one used for the inversion would not calculate all ray paths after a couple of iterations. A model that was faster than the one chosen, produced a large starting RMS which was difficult to reduce to a reasonable RMS.

We carried out 4 runs of the code to produce the final model. The first run used a smoothing factor of 200 km x 60 km x 40 km in grid nodes for 10 iterations (Figure 110). The starting RMS was 1.22 s for iteration 1. Iteration 3 from this run, which had a RMS of 0.66 s, was input to the 2nd run. The second run used a smoothing factor of 100 km x 40 km x 20 km in grid nodes for 10 iterations. Iteration 4 from the 2nd run, which had a RMS of 0.44 s, was input to the 3rd run. The third run used a smoothing factor of 60 km x 30 km x 10 km grid nodes for 10 iterations. Iteration 4 from the 3rd run, which had a RMS of 0.30 s, was input to the 4th run. The final run used a smoothing factor of 30 km x 30 km x 10 km in grid nodes for 10 iterations. The final RMS for the model is ~ 0.160 s.

Overall the traveltime fits are excellent although there are places where the misfit is as much as 300 ms (Figure 111). This misfit appears to be a systematic error within the inversion. If two rock types share the same cell then the slower material will prevail and

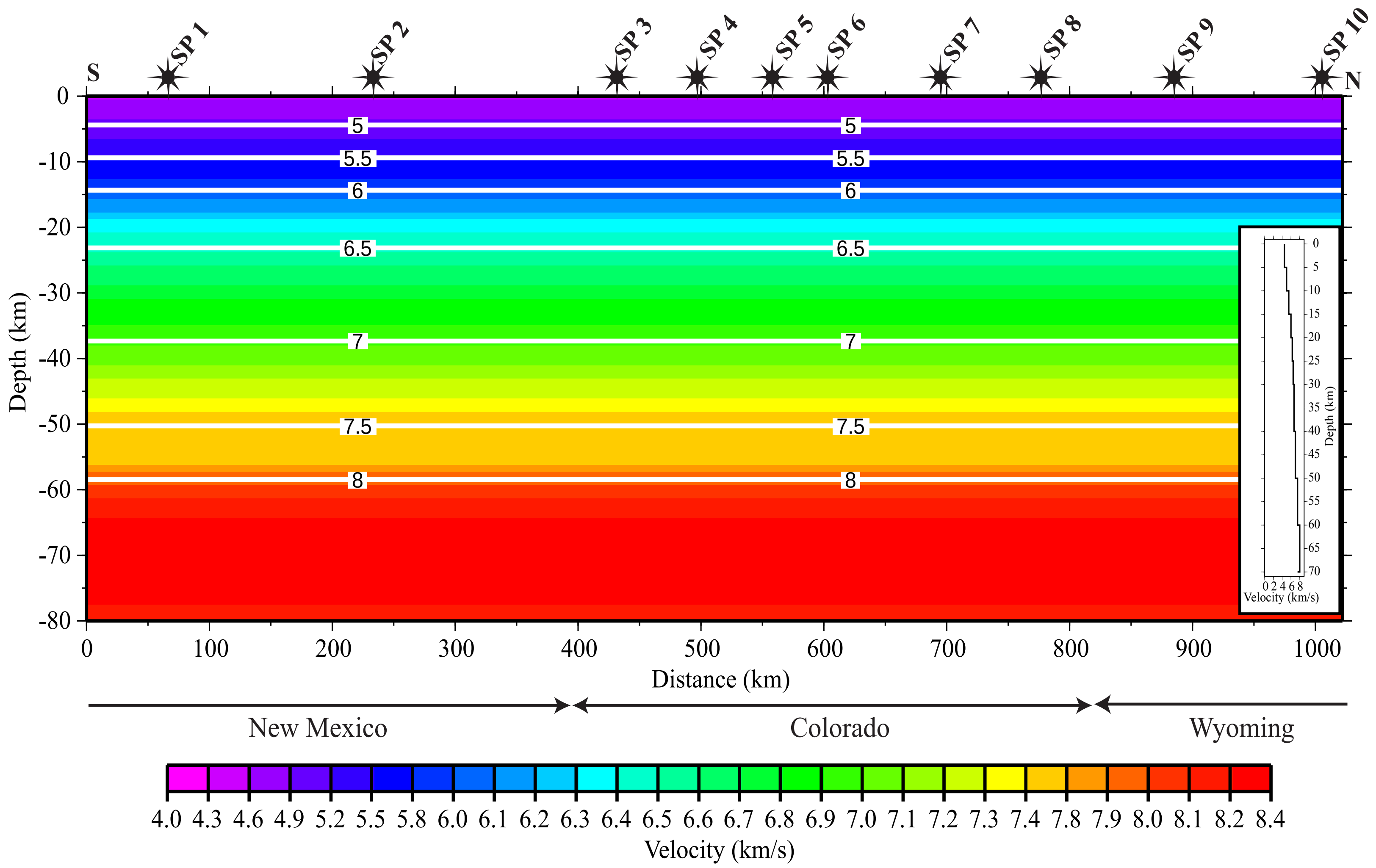

Figure 109. Starting model for tomographic inversion.

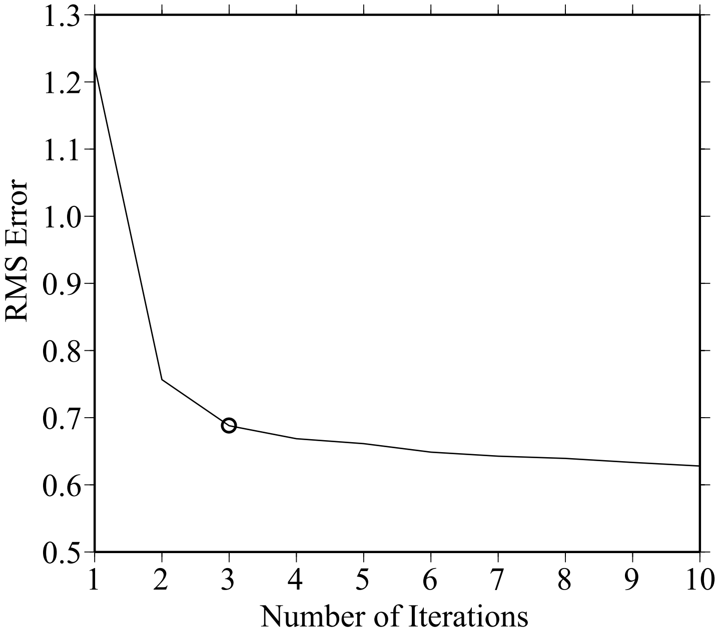

Figure 110. RMS curve of starting model. Circle shows the iteration that was chosen for the next run.

the calculated traveltime will reflect a large misfit (Zelt et al., 1996).

Measures of Resolution

A sense for the resolution of the model can be gained by evaluating the RMS error, traveltime fits, ray coverage, and the resolution matrix. Unfortunately with this technique, the resolution matrix is not created because the technique is non-linear (Hole, 1992). We have been able to provide RMS error, traveltime fits, and ray coverage for the velocity model. In an effort to further evaluate the resolution of the model, checkerboard tests were carried out.

Ray Coverage

The ray coverage or hit count represents the number of rays hitting a particular cell. The more hits for any given cell the better resolved that cell will be. Considering the

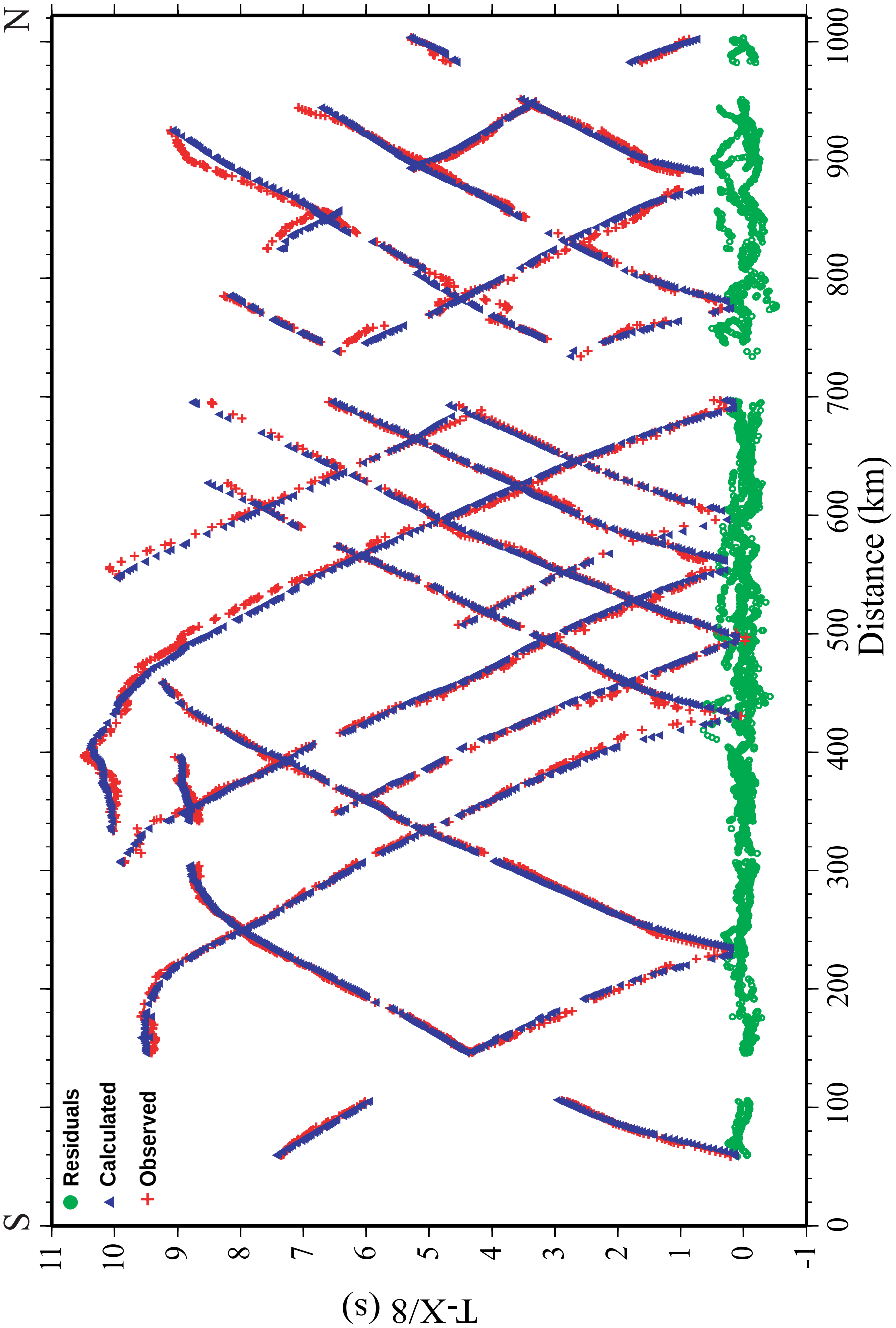

Figure 111. Traveltime fit for CD-RoM 99.

modest number of shots in the experiment, the ray coverage is adequate except for the deep portion of the northern third of the profile (Figure 112). The inclusion of the reflected phases greatly increases the ray coverage. However, these rays cannot be shown.

Checkerboard Tests

Following the technique of Zelt (1998), 40 km x 20 km sinusoidal checkers with amplitudes of +/- 5% were added to a smoothed 1-D version of the final velocity model. Traveltimes times for this model were calculated input to the inversion as the “observed” traveltimes along with the smoothed 1-D model. The inversion was then allowed to run for five iterations. Unfortunately, these tests failed and will be the subject of future investigation.

Estimated Resolution

Based on forward and inversion modeling, in collaboration with our German colleagues and the tomographic inversion of the first arrivals (Figure 115) and reflections (Figures 116), I feel that the resolution of the depth for the deep interfaces (Figure 116) is +/- 2 km if the velocity structure is assumed to be completely accurate. However if one considers the uncertainty of the velocity, then the uncertainty could be as much as +/- 3 km. The estimated uncertainty related to the upper crustal velocity field is +/- 0.1 km/s down to about 25 km and then increases with depth up to +/- 0.2 km/s.

Tomographic Results

First Arrival Model

The final first arrival model shows modest variations in the crustal structure from south to north as well as from the surface to depth (Figure 115). The upper crust has an average velocity of ~ 6.1 km/s and the middle crust has an average velocity of ~ 6.7 km/s.

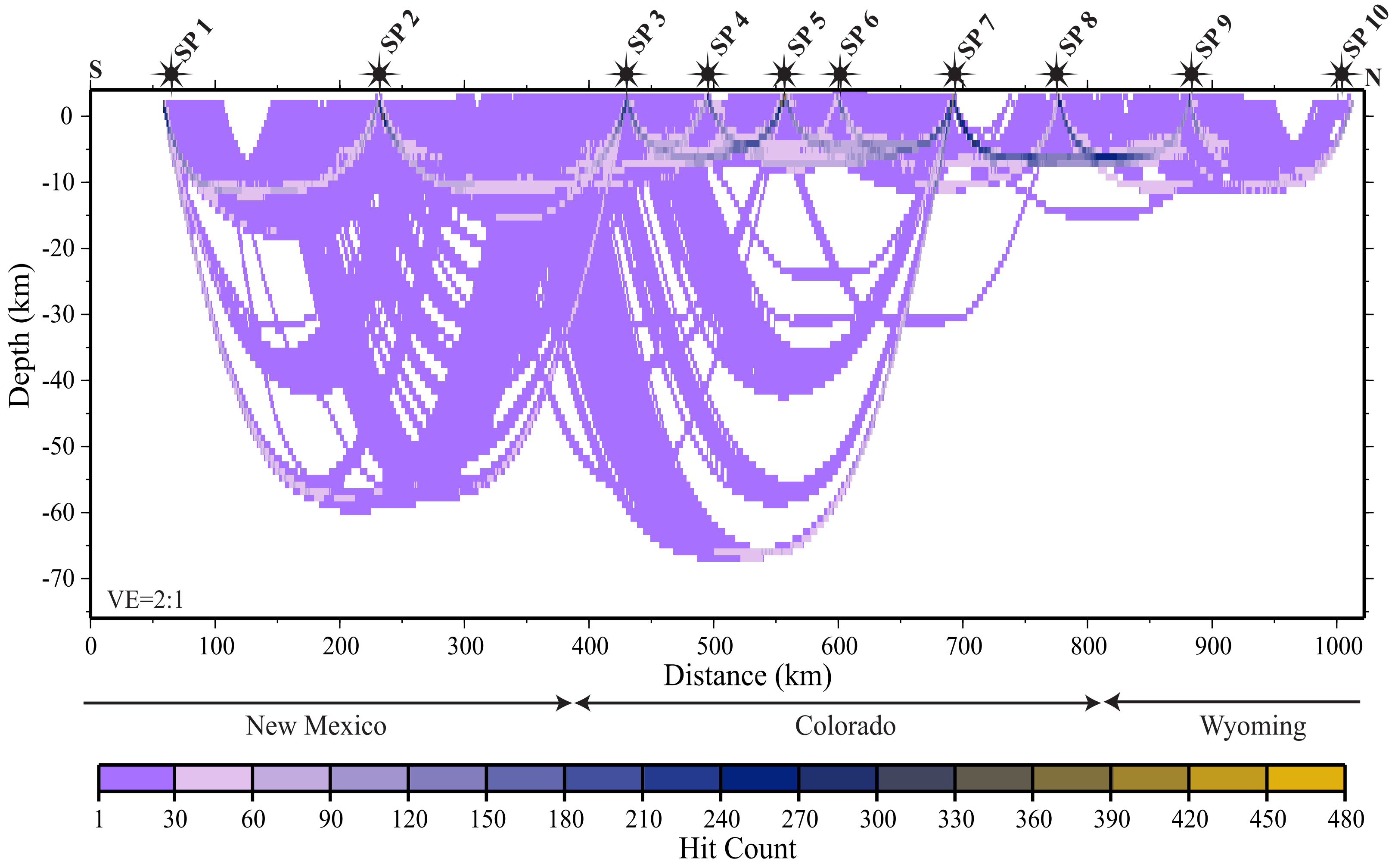

Figure 112. Hit count for CD-RoM velocity model.

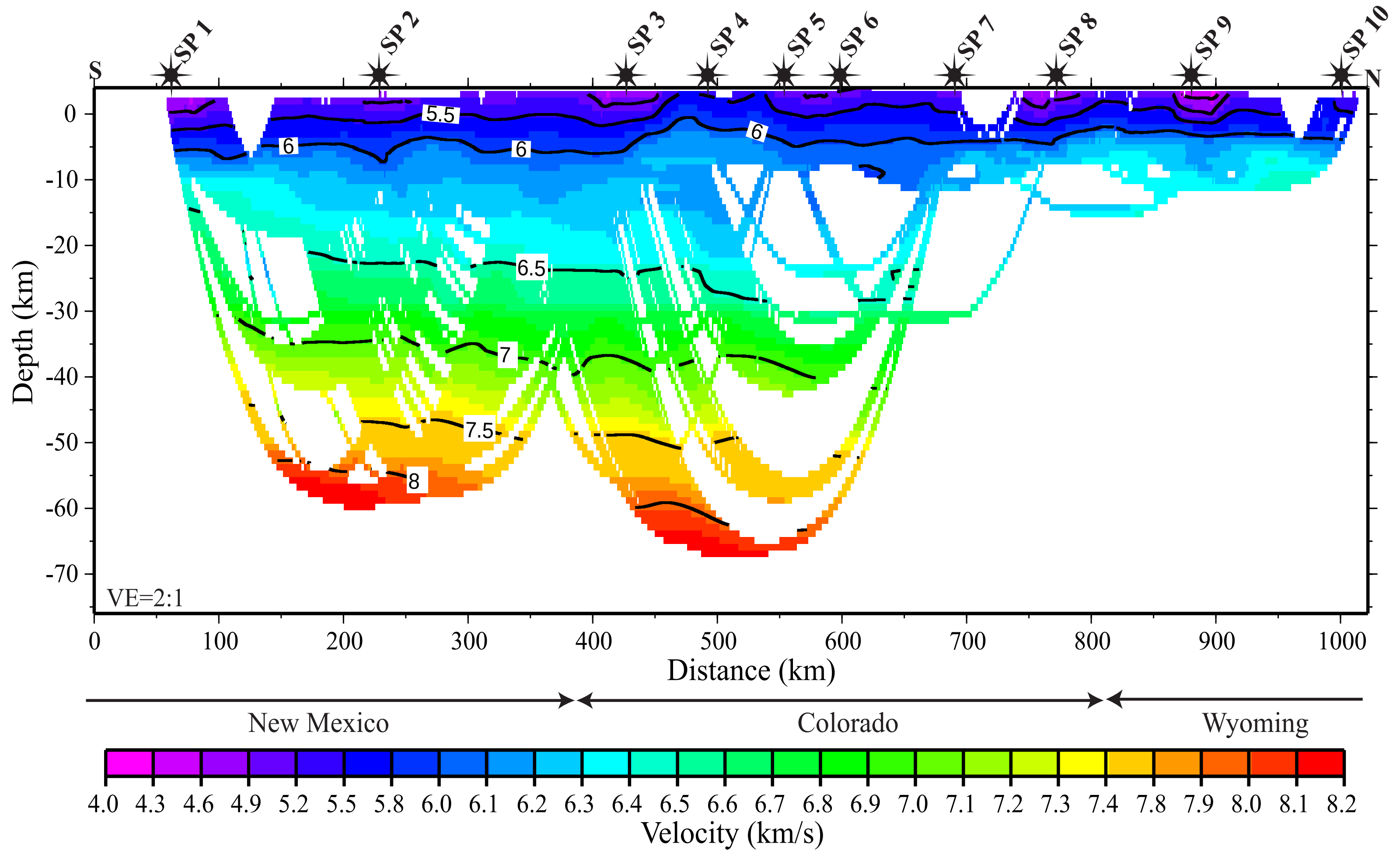

Figure 115. Final first arrival velocity model of CD-RoM. Contour interval is 0.5 km/s.

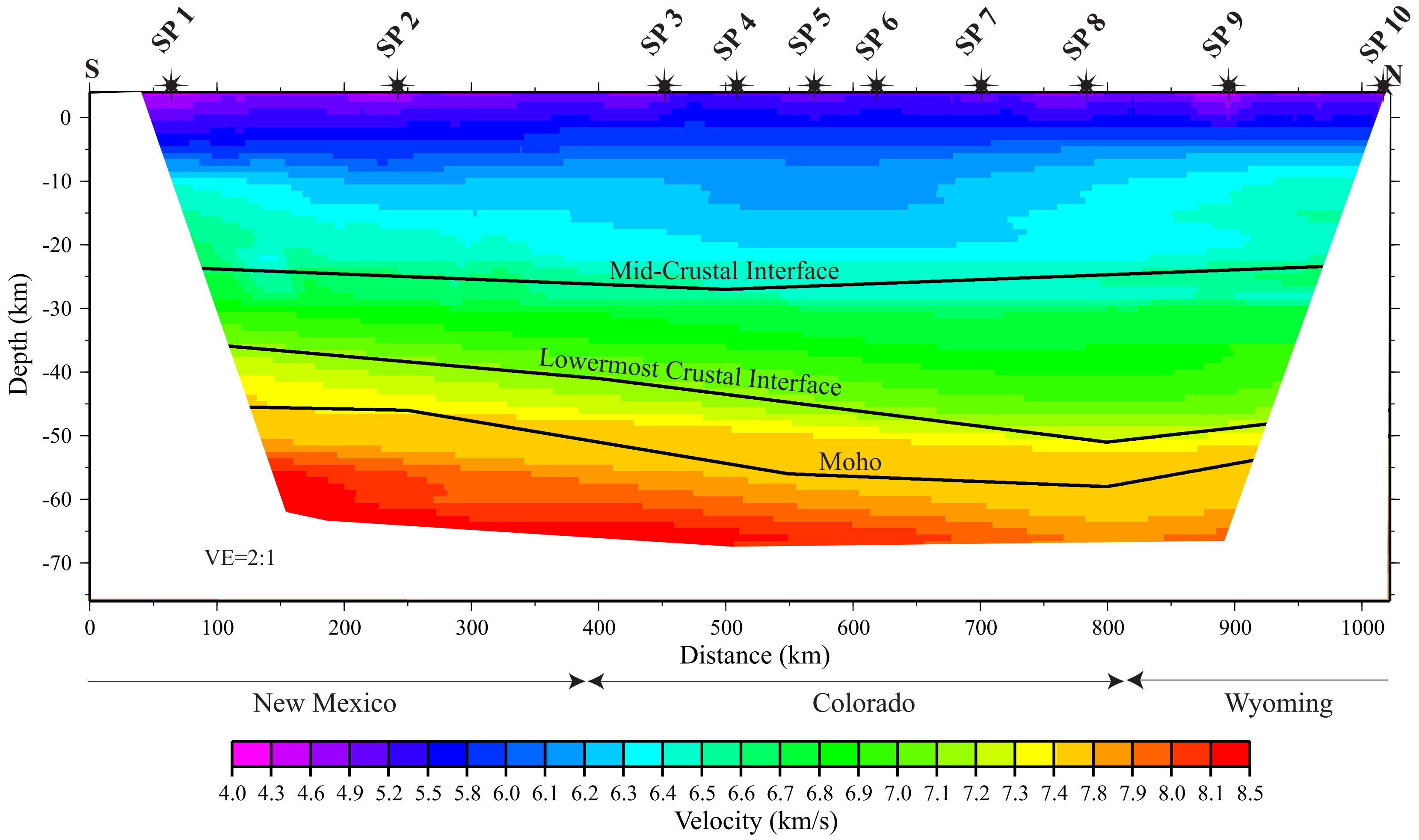

Figure 116. Final velocity model of CD-RoM. Prominent interfaces are labeled.

The high velocity lowermost crust has an average velocity of 7.2 km/s. The upper mantle velocity is ~ 7.8 to 7.9 km/s. A number of upper crustal structures such as the Wet Mountains and the Park basins are represented in the model and are consistent with the detailed upper crustal analysis being conducted by our colleagues at the University of Karlsruhe, Germany. The most notable feature of the model is the high velocity lower crustal layer (~ 7.2 km/s), which ranges in thickness from 10 to 5 km throughout the model. There is also a significant (~ 5 km) increase in the depth of the Moho in central Colorado.

Wide-Angle Reflection Model

The addition of the wide-angle reflections as additional constraints to the first arrival model provides the depths to critical interfaces within the model. The final model (Figure 116) shows that the mid-crustal interface is at a depth of about 25 km at the southern end of the model and increases in depth to about 30 km before rising to about 25 km at the northern of the profile. The top lowermost crustal interface is at about 35 km depth at the southern end of the profile and deepens under central Colorado to about 45 km before thinning at the northern end of the profile at about 40 km. The Moho depth at the southern end of the profile is about 45 km. The Moho deepens to about 55 km under central Colorado and rises at the northern end of the profile to about 45 km. Previous studies at the northern end of the profile (Johnson et al., 1984; Prodehl and Lipman, 1989) show that the crust thins to about 40 km at the north of the CD-RoM profile.

Gravity

Sheehan et al. (1995) showed that there was a lack of correlation between the topography and the crustal thickness in Colorado. Therefore, only the regional (long wavelength) portion of the gravity field was of interest in the modeling in this study. The details of the upper crustal (short wavelength) features will be further delineated by other members of the CD-RoM team. Gravity data were extracted from National Geodetic Survey database using the GRAV program. A Bouguer anomaly map was created (Figure 117) using a smoothing filter to eliminate noise and make the map readable. A profile was created along the seismic profile for density modeling (Appendix G). Only values that within 5 km of the seismic profile were used in the density modeling so that the gravity and seismic models correlate (Appendix H).

Density Modeling

The extracted gravity values were used in a forward modeling program based on the 2 ½ - D approach of Cady (1980). The density and velocity models were jointly iterated to obtain an integrated result (Figure 118). The density values were calculated based on a typical velocity/density relationship using the final tomographic model for CD-RoM (e.g., Christensen and Mooney, 1995). The upper crust has a density value of 2700 kg/m^3 and the middle crust has a value of 2900 kg/m^3. The lowermost crust has a value of 3050 kg/m^3 and the standard mantle density value was 3330 kg/m^3.

When the mantle is homogeneous then the overall shape of the calculated gravity profile is similar to the observed profile, but the calculated anomaly is greater than the observed anomaly by ~ 50 mGal. As shown on Figure 117, the profile crosses a large gravity low in Colorado at an oblique angle. Cordell et al. (1991) analyzed the gravity field in the southern Rocky Mountain region and concluded that this anomaly was largely due to thinning of the lithosphere. Dueker and Sheehan (1998) show that this area is associated with low velocities in the upper mantle. Thus the upper mantle does play a role

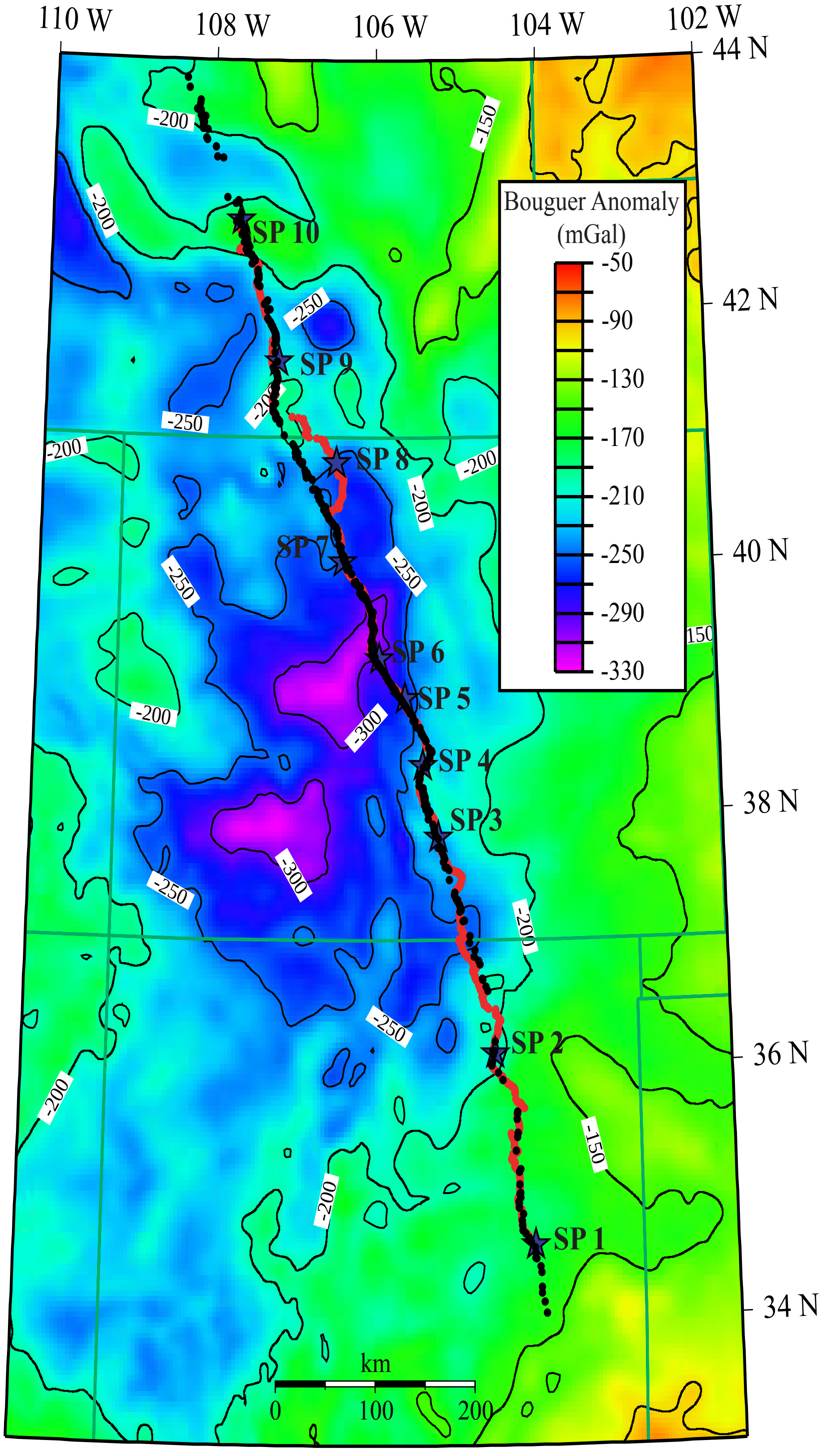

Figure 117. Bouguer anomaly map. Refraction profile shown in red, shot location are stars and the density profile is shown in black.

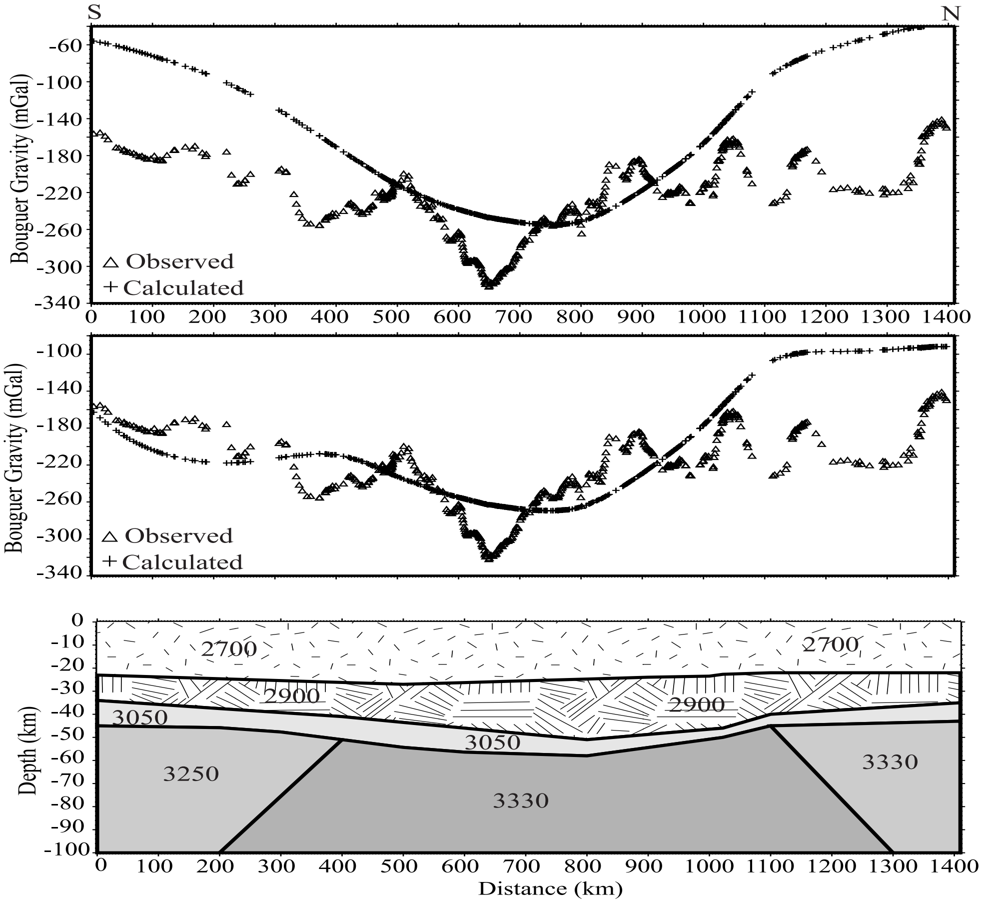

Figure 118. Density model for CD-RoM. A. Bouguer fit with a homogenous mantle. B. Bouguer fit with varied mantle. C. The density model with density values in kg/m^3.

regional in the attainment of isostatic balance. has a value of 3330 kg/m^3. The

Discussion

Mid-Crust

The CD-RoM velocity model contains a number of interesting features (Figure 116). The reflection from the mid-crustal interface (PcP) (~ 20 km) is very prominent within the data and, at wide angles, is represented multiple reflected energy within the upper crust which manifests itself as a long coda (Figure 105) (e.g., Lay and Wallace, 1995). This interface lies at a depth of about 25 km depth and seems to be consistent to what is typically thought of as the Conrad discontinuity (e.g., Sheriff, 1994). The Conrad discontinuity is traditional defined as a compositional boundary at the base of the felsic upper crust (e.g., Lay and Wallace, 1995). In tectonically active regimes, modern seismic refraction/wide-angle reflection experiments usually produce complex velocity models in which it is hard to identify an interface that represents the classical Conrad discontinuity (e.g., Miller et al., 1997). Although the crust is the Basin and Range is significantly thinner than that of the Rocky Mountains, the seismic record sections from the region are strikingly similar in terms of amplitude and apparent velocity when one compares the PmP reflector in the Basin and Range (Figure 119) (Hicks, 2001) to the PcP reflector in the Rocky Mountain area (Figure 105). The PcP reflector seems to be common in the Proterozoic terranes of the mid-continent as well (Figure 120B) (Braile et al., 1989). This observation suggests that the Basin and Range crust is similar to that of the Proterozoic terranes except that the mafic lower crust is absent.

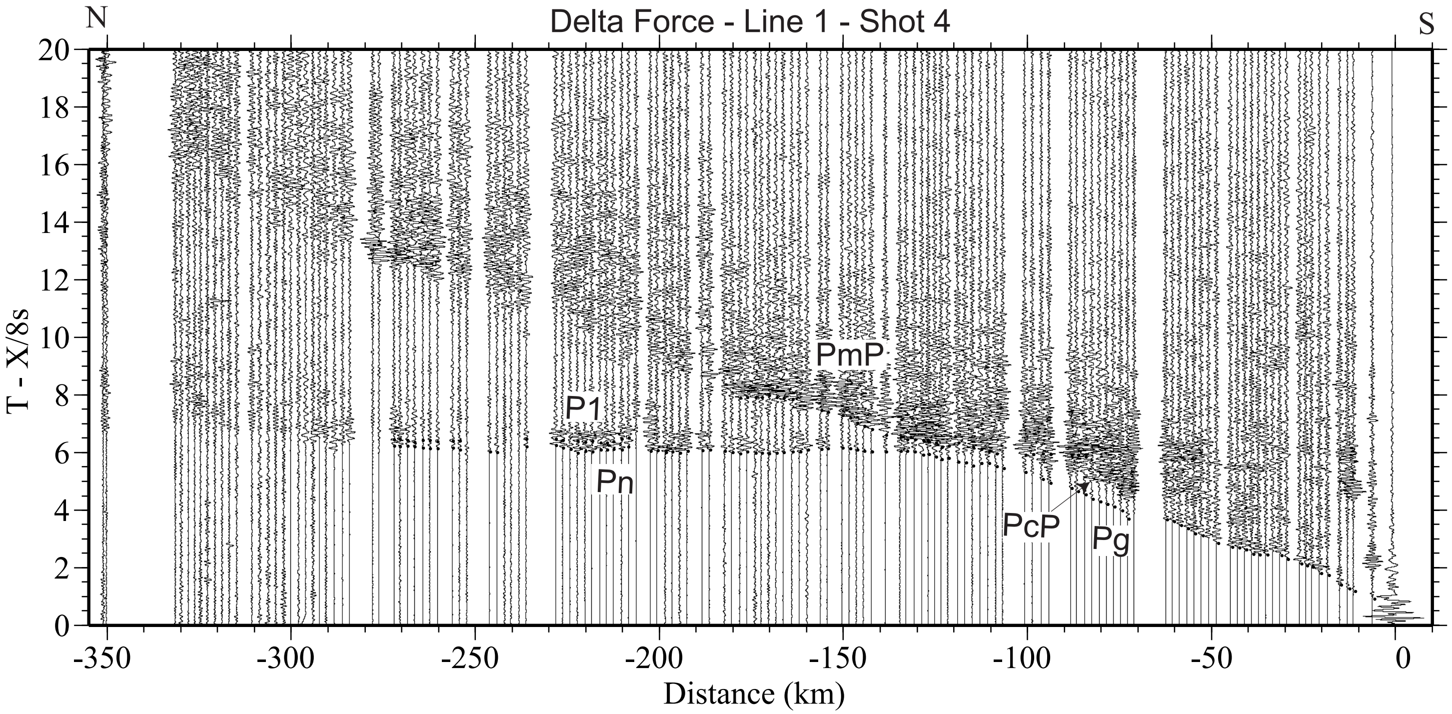

Figure 119. Seismic record section from Delta Force. This line trends N-NW from Bylthe, CA to Death Valley. Although the crust is much thinner here the reflectivity is strikingly similar (After Hicks, 2001).

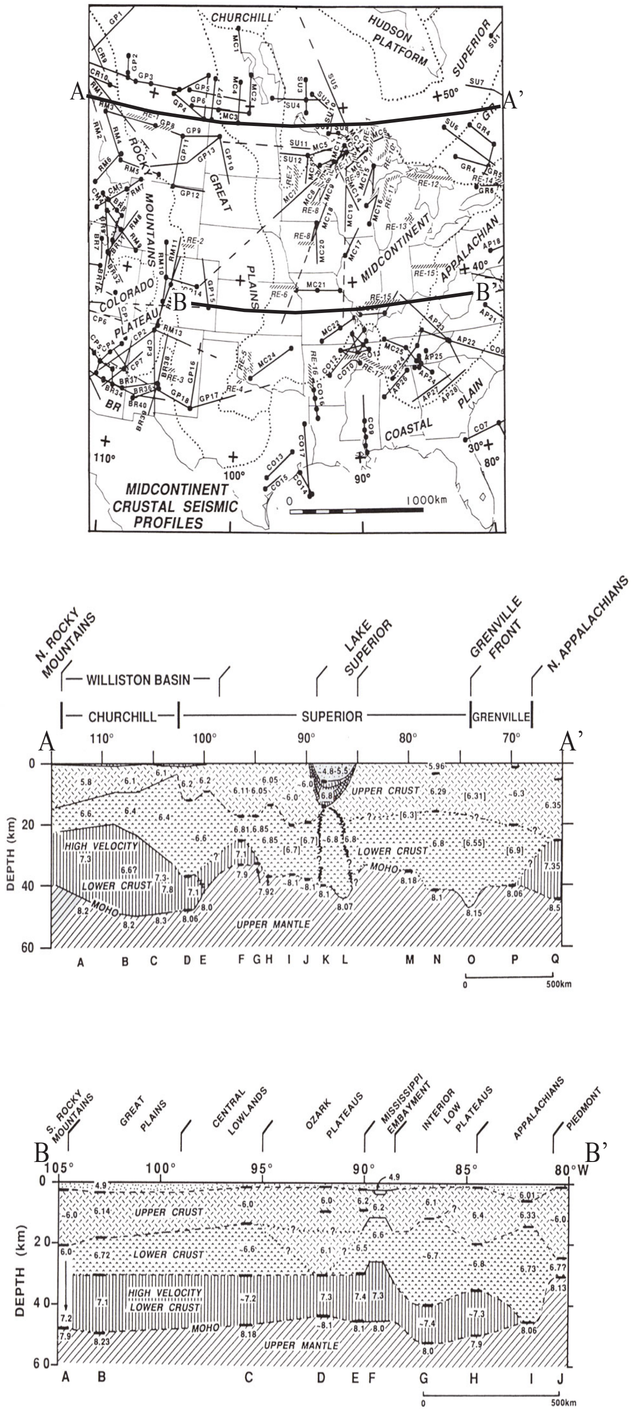

Figure 120. Velocity model compiled across the United States (after Braile et al., 1989). A: Northern cross section across the Archean craton. B: Southern cross section across the Colorado Plateau and Mid-continent.

Lowermost Crust and Moho

The seismic refraction data clearly show a first arrival from the lower crust on several of the record sections indicating the presence of a thick, high-velocity layer. This arrival is from a layer which has a velocity of ~ 7.2 km/s indicating that its composition is strongly mafic (Figure 116). We cannot, at present, be sure of the full extent of this layer beyond the CD-RoM transect, but it is observed in many areas of the mid-continent region east of the Rocky Mountains (Figure 120) (Braile et al., 1989) and the Colorado Plateau (Wolf and Cipar, 1993). Using the word "underplating" to refer to an array of processes whereby mantle material or its derivatives are added to lowermost portion of the crust, this layer seems best interpreted as representing underplated material. However, given the complex geologic history of the region (e.g., Karlstrom et al., 2001; Oldow et al., 1989) the question of the timing of the events that formed it quickly arises. In addition, geologic data (e.g., Anderson, 1989) and several large gravity anomalies in the region clearly document the addition of both mafic and felsic material to what is now the upper crust (e.g., Plouff and Pakiser, 1972; Schneider and Keller, 1994; Adams and Keller, 1996) over the past 1.6 Ga. These events have all effected the Rocky Mountain region to some degree, and separating their influence on crustal structure from that of older structures and understanding their interactions with old structures is a major goal of the CD-RoM project.

The velocity models derived from recent seismic studies in the Aleutian arc (Holbrook et al., 1999; Fliedner and Klemperer, 2000) and Pacific Northwest region of North America (Miller et al., 1997) provide examples of what the crust of the Rocky Mountain region may have looked like as it formed during the period of ~ 1.8 to 1.6 Ga. The crust in the Aleutian arc is ~ 30 thick but has a velocity structure that suggests a much more mafic composition than typical continental crust. This observation suggests that continental crust cannot be formed from island arc material alone. In a more continental setting along the western flank of the Cascade Range, the crust is about 45 km thick and has a rather high average P- wave velocity (~ 6.5 km/s) (Miller et al., 1997) compared the value typical value for continents (~ 6.3 km/s; Smithson et al., 1981; Christensen and Mooney, 1995). In both cases, the seismic velocities observed are even more impressive given the heat flow regimes present that lower seismic velocities relative to levels they will achieve after the tectonic activity has ceased.

Locally, magmatism was significant during several tectonic events and crustal scale thickening by buckling and faulting (Erslev, 1993; Tikoff and Maxson, 2001) could have occurred during the during events such as the Ancestral Rocky Mountain and Laramide orogenies. However, a distinctive regional attribute of the crust is its thickness and the high velocities at its base. Studies of modern arcs show that we could expect the original crust to be high velocity, but the only constraint concerning its thickness is the fact that Proterozoic rocks exposed today were buried at depths of 10-20 km from 1.6 to 1.45 Ga. This would suggest that the original crust was not overthickened and subject to collapse. The best time for regional underplating to produce or thicken the high velocity lower crust under the southern Rockies and Great Plains was at 1.4 Ga. However, preserving this layer through all of the subsequent tectonic events is problematic. We do not mean to imply that other events did not add to this layer or otherwise modify it, but 1.4 Ga is the only time that magmatism of the geographic extent and intensity needed to produce it occurred. Although outcrops of mafic rocks of this age are very rare, enclaves of dioritic rocks found in the some granites suggest that large volumes of mafic rocks where probably present at depth (Frost and Frost, 1997; Karlstrom and Humphreys, 1998).

If a major phase of underplating occurred at 1.4 Ga and is present in the form of a widespread high velocity lower crustal layer today, how could this ~45km thick crust be near sea level during the Cretaceous and at an elevation of 1-1.8 km today? Thick crust with an elevation near sea level has recently observed along EUOROBRIDGE seismic profile in Lithuania and Belarus crosses the East European craton where the crust is ~50 km thick and at an elevation of ~100m (EUROBRIDGE Working Group, 1999). This observation reminds us that elevation is a function of the buoyancy of the entire lithosphere. O'Reilly et al. (2001) show that Proterozoic lithospheric mantle is dense and resistive to delamination, and these observations suggest that the crust of the Southern Rocky Mountain region and adjacent Great Plains could have remained thick and relatively near sea level during most of the time from 1.4 Ga to the Laramide when thermal effects began to effect the mantle and increase its buoyancy.

I do not mean to minimize the complex effects of Neoproterozoic and Phanerozoic events on crustal structure. For example in New Mexico and Colorado, the amount of felsic magmatic activity during the Cenozoic was enough to thicken the upper crust substantially (5 - 10 km) by emplacement of batholiths and offset some of the thinning due to erosion. However, this analysis suggests that the original continental crust was stabilized early (~ 1.6 Ga) and thickened by underplating at ~ 1.4 Ga. Since that time, local modification has sometimes been significant, but the Mesoproterozic crust and lithospheric mantle appears to have remained largely intact over a broad region.

REFERENCES

Adams, D. C., and G. R. Keller, 1994, Possible extension of the Midcontinent Rift in west Texas and eastern New Mexico: Canadian Journal of Earth Science, v. 31, p. 709-720.

Aldrich, M. J., Chapin, C. E., and Laughlin, A. W., 1986, Stress history and tectonic development of the Rio Grande Rift, New Mexico: Journal of Geophysical Research, v. 91, n. B6, p. 6199-6211.

Allmendinger R., Brewer, J. A., Brown, L. D., Kaufman, S. K., Oliver, J. E., and Houston, R. S., 1982, COCORP profiling across the Rocky Mountain Front in southern Wyoming, part2: Precambrian basement structure and its influence on Laramide deformation: Geological Society of America Bulletin, v. 93, p. 1253-1263.

Anderson, J. L., 1989, Proterozoic anorogenic granites of the southwestern U. S., in, J. P. Jenny and S. J. Reynolds (eds.): Arizona Geological Digest, v. 19, p. 211-238.

Asada, T., and Aldrich, L. T., 1966, Seismic observations of explosions in Montana, in J. S. Steinhart and T. J. Smith, eds., The Earth Beneath the Continents: Washington, D.C., American Geophysical Union Monograph 10, p. 382-390.

Atwater, T., 1989, Plate tectonic history of the northeast Pacific and western North America, *in* Winterer, E. L., Hussong, D. M., and Decker, R. W., eds., The Eastern Pacific Ocean and Hawaii: Boulder, Colorado, Geological Society of America, The Geology of North America, v. N, p. 21-72.

Atwater, B.F., and Hemphill-Haley, E., 1997, Recurrence intervals for great earthquakes of the past 3,500 years at northeastern Willapa Bay, Washington: U.S. Geological Survey Professional Paper 1576, 108 p.

Babcock, R. S., Burmester, R. F., Engbretson, D. C., and Warnock, A., 1992, A rifted margin origin for the Crescent basalts and related rocks in the northern Coast Range volcanic province, Washington and British Columbia: Journal of Geophysical Research, v. 97, no. B5, p. 6799-6821.

Beck, M.E., 1989, Paleomagnetism of continental North America; implications for displacement of crustal blocks within the Western Cordillera, Baja California to British Columbia, in Geophysical Framework of the Continental United States, edited by L.C. Pakiser and W.D. Mooney: Mem. Geol. Soc. Am., v. 172, p. 471-492.

Beck, M. E., Jr., and Engebretson, D. C., 1982, Paleomagnetism of small basalt exposures in the west Puget Sound area, Washington, and speculations on the accretionary origin of the Olympic Mountains: Journal of Geophysical Research, v. 87, no B5., p. 3755-3760.

Bird, P., 1998, Kinematic history of the Laramide orogeny in latitudes 35^{o} - 49^{o} N, western United States, Tectonics, v. 17, no. 5, p. 780-801.

Blackstone, D. L., Jr., 1993, Precambrian basement map of Wyoming; outcrop and structural configuration, in Schmidt, Christopher J; Chase, Ronald B; Erslev, Eric A: Laramide basement deformation in the Rocky Mountain foreland of the Western United States, Special Paper - Geological Society of America, vol.280, pp.335-337, Boulder, CO, United States (USA).

Blakely, R.J., R.E. Wells, and C.S. Weaver, Puget Sound aeromagnetic maps and data: U.S. Geological Survey Open-File Report 99-514, 1999.

Blakely, R.J., Wells, R.E., Tolan, T.L., Beeson, M.H., Trehu, A.M., and Liberty, L.M., 2000, New aeromagnetic data reveal large strike-slip (?) faults in the northern Willamette Valley, Oregon: Geological Society of America Bulletin, v. 112, p. 1225-1233.

Blakely, R.J., Wells, R.E., Weaver, C.S., and Johnson, S.Y., 2001, Location, structure, and seismicity of the Seattle fault, Washington: Geological Society of America Bulletin, in revision after journal review.

Borchert, C. A., and Roller, J. C., 1967, Preliminary interpretation of a seismic-refraction profile across the Large Aperture Seismic Array, Montana: U. S. Geological Survey, Technical Letter NCER, 53p.

Braile, L. W., Smith, R. B., Keller, G. R., Welch, R. M., and Meyer, R. P., 1974, Crustal structure across the Wasatch Front from detailed seismic refraction studies: Journal of Geophysical Research, v. 79, p. 2669-2766.

Braile, L. W., Hinze, W. J., von Frese, R. R. B., and Keller, G. R., 1989, Seismic properties of the crust and upper most mantle of the conterminous United States and adjacent Canada, *in* Pakiser, L.C., and Mooney, W. D., eds., Geophysical Framework of the continental United States: Boulder, Colorado, Geological Society of America Memoir 172, p. 655-680.

Brandon, M. T., and Calderwood, A. R., 1990, High-pressure metamorphism and uplift of the Olympic subduction complex: Geology, v. 18, p. 1252-1255.

Brandon, M. T., and Vance, J. A., 1992, Tectonic evolution of the Cenozoic Olympic subduction complex, Washington State, as deduced from fission track ages for detrital Zircons: American Journal of Science, v. 292, p. 565-636.

Brandon, M. T., Roden-Tice, M. K., and Garver, J. I., 1998, Late Cenozoic exhumation of the Cascadia accretionary wedge in the Olympic Mountains, northwest Washington State: Geological Society of America Bulletin, v. 110, no. 8, p. 985-1009.

Brewer, J. A., Allmendinger, R. W., Brown, L. D., Oliver, J. E., and Kaufman, S., 1982, COCORP profiling across the Rocky Mountains from in southern Wyoming; part 1, Laramide structure: Geological Society of America Bulletin, v. 93, p. 1242-1252.

Brocher, T.M., and N.I. Christensen, 2001, Density and velocity relationships for digital sonic and density logs from coastal Washington and laboratory measurements of Olympic Peninsula mafic rocks and greywackes, U.S. Geological Survey Open-File Report 01-264, 39 p.

Brocher, T.M., T. Parsons, R.A. Blakely, N.I. Christensen, M.A. Fisher, R.E. Wells, and the SHIPS Working Group, 2001, Upper crustal structure in Puget Lowland, Washington: Results from 1998 Seismic Hazards Investigation in Puget Sound, J. Geophy. Res., 106, 13,541-13,564.

Brocher, T.M., Pratt, T. L., Miller, K. C., Trehu, A. M., Snelson, C. M., Weaver, C. S., Creager, K. C., Crosson, R. S., ten Brink, U. S., Alvarez, M. G., Harder, S. H., and Asudeh, I., 2000, Report for explosion and earthquake data acquired in the 1999 Seismic Hazards Investigation in Puget Sound (SHIPS), Washington: U.S. Geological Survey Open-File Report 00-318, 85 p.

Brocher, T.M. and Ruebel, A.L., 1998, Compilation of 29 sonic and density logs from 23 oil test wells in western Washington State, U.S. Geological Survey Open-File Report 98-249, 41 p.

Bucknam, R. C., Hemphill-Haley, E., and Leopold, E. B., 1992, Abrupt uplift within the past 1700 years at southern Puget Sound, Washington: Science, v. 258, p. 1611-1614.

Burchfiel, B. C., Cowan, D. S., and Davis, G. A., 1992, Tectonic overview of the Cordilleran orogen in the western United States, *in* Burchfiel, B.C., Lipman, P.W., and Zoback, M. L., eds., The Cordilleran Orogen: Conterminous U.S.: Boulder, Colorado, Geological Society of America, The Geology of North America, v. G-3, p. 407-479.

Calvert, A.J., M.A. Fisher, and SHIPS Working Group, 2001, Imaging the Seattle fault zone with high-resolution seismic tomography, Geophys. Res. Lett., 28, 2337-2340.

Cady, J. W., 1980, Calculation of gravity and magnetic anomalies of finite-length right polygonal prisms: Geophysics, v. 45, p. 1507-1512.

Cavosie, A., and Selverstone, J., in review, Early Proterozoic oceanic crust in the northern Colorado Front Range: Implications for crustal growth and initiation of basement faults, Tectonics.

Chamberlain, K. R., Pael, S. C., Frost, B. R., and Snyder, G., 1993, Thick-skinned deformation of the Archean Wyoming province during Proterozoic arc-continent collision: Geology, v. 21, p. 1035-1038.

Christensen, N. I., 1982, Seismic velocities, in, R. S. Carmichael, ed., Handbook of physical properties of rocks: CRC PRess, Boca Raton, Florida, v. 2, p. 1-228.

Christensen, N. I., and Mooney, W. D., 1995, Seismic velocity structure and composition of the continental crust: A global review, Journ. Geophys. Res, 100, 9761-9788.

Clague, J. J., 1997, Evidence for large earthquakes at the Cascadia subduction zone: Reviews of Geophysics, v. 35, no. 4, p. 439-460.

Clowes, R.M., Yorath, C.J., and Hyndman, R.D., 1987, Reflection mapping across the convergent margin of western Canada, Geophys. J. Roy. Astron. Soc., 89, 79-84.

Condie, K. C., Plate-tectonics model for Proterozoic continental accretion in the southwestern United States, Geology, 10, 37-42, 1982.

Cook, F. A., McCullar, D. B., Decker, E. R., and Smithson, S. B., 1979, Crustal structure and evolution of the southern Rio grande rift, *in* Riecker, R. E., eds., Rio Grande Rift; Tectonics and Magmatism: Washington, D. C., American Geophysical Union, p. 195-208.

Cordell, L, 1982, Extension in the Rio Grande rift: Journal of Geophysical Research, v. 87, p. 8561-8569.

Cordell, L., Y. A. Zorin, and G. R. Keller, 1991, The decompensative anomaly and deep structure of the Rio Grande rift: Journal of Geophysical Research, v. 96, p. 6557-6558.

Crosson, R. S., 1972, Small earthquakes, structure, and tectonics of the Puget Sound region: Bulletin of the Seismological Society of America, v. 62, no. 5., p. 1133-1171.

Curray, J. R., Moore, D. G., Lawver, L. A., Emmel, F. J., Raitt, R. W., Henry, M., and Kieckhefer, R., 1979, Tectonics of the Andaman Sea and Burman, American Association of Petroleum Geologists, Memoir 29, p. 189-198.

Danes, Z.F., 1985, Sedimentary thickness in the Puget Sound area, Washington derived from aeromagnetic data, Washington (State), Dept. Natural Resources, Div. of Geology and Earth Resources, Open-file Report 85-5.

Dewberry, S. R., and Crosson, R. S., 1996, The MD 5.0 earthquake of 29 January 1995 in the Puget Lowland of western Washington: An event of the Seattle fault?: Bulletin of the Seismological Society of America, v. 86, no. 4, p. 1167-1172.

Dickinson, W. R., 1981, Plate tectonic evolution of the southern Cordillera, in, Relations of tectonics to ore deposits in the southern Cordillera, Dickinson, William R; Payne, William D., eds., Univ. Ariz., Lab. Geotectonics, Tucson, AZ, United States (USA), Arizona Geological Society Digest, vol.14, pp.113-135, 1981

Doser, D. I., Crain, K. D., Baker, M. R., Kreinovich, V., and Gertenberger, M. C., 1998, Estimating uncertainties for geophysical tomography, Journ. Reliable Computing, 4, 241-268.

Duebendorfer, E. M., and Houston, R. S., 1986, Kinematic history of the Cheyenne belt: A Proterozoic suture in southeastern Wyoming: Geology, v. 14, p. 171-174.

Ducea, M. N., and Saleeby, J. B., 1998, The age and origin of a thick ultramafic keel from beneath the Sierra Nevada batholith, Contributions to Mineralogy and Petrology, v. 133, p. 169-185

Dueker, K. G., and A. F. Sheehan, 1998, Mantle discontinuity structure beneath the Colorado Rocky Mountains and High Plains, J. Geophys. Res., v. 103, 7153-7169.

Duncan, R. A., 1982, A captured island chain in the coast range of Oregon and Washington: Journal of Geophysical Research, v. 87, no. B13, p. 10,827-10,837.

Engebretson, D.C., Gordon, R.G., and Cox, A., 1985, Relative motions between oceanic and continental plates in the Pacific basin, Geol. Soc. Amer., Special Paper 206, 64 p.

Erslev, E. A., 1993, Thrusts, back-thrusts, and detachment of Rocky Mountain foreland arches, in C. J. Schmidt, R. B. Chase, and E. A. Erslev (eds.), Laramide basement deformation in the Rocky Mountain foreland of the western United States: Geological Society of America, Special paper 280, p. 339-358.

EUROBRIDGE Seismic Working Group, 1999, Seismic velocity structure across the Fennoscandia-Sarmatia suture of the East European Craton beneath the EUROBRIDGE profile through Lithuania and Belarus, Tectonophysics, v. 314, p. 193-217.

Finn, C., 1990, Geophysical constraints on Washington convergent margin structure: Journal of Geophysical Research, v. 95, no. B12, p. 19,533-19,546.

Fisher, M. A., Calvert, A. J., Parsons, Tom, Wells, R. E., Brocher, T., M., Weaver, C. S., and the SHIPS Working Group, 2000, Crustal structure from SHIPS seismic reflection data along a transect from the southern Puget Lowland north to the San Juan Islands: Supplement to EOS, Transactions of the American Geophysical Union, v. 81, p. 878.

Fliedner, M. M., and S. L. Klemperer, 2000, Crustal structure transition from oceanic arc to continental arc, eastern Aleutian Islands and Alaska Peninsula: Earth and Planetary Science Letters, v. 179, p. 567-579.

Frankel, A., Carver, D., Cranswick, E., Meremonte, M., Bice, T., and Overturf, D., 1999, Site response for Seattle and source parameters of earthquakes in the Puget Sound region: Bulletin of the Seismological Society of America, v. 89, no. 2., p. 468-483.

Frost, C. D., and Frost, B. R., 1997, Reduced rapakivi-type granites: The tholeiite connection, Geology, v. 25, p. 647-650.

Fuchs, K., and Müller, G., 1971, Computation of synthetic seismograms with the reflectivity method and comparison with observations, Geophys. J. R. astr. Soc, 23, 417-433.

Goldfinger, C., and C.H. Nelson, 2001, Holocene recurrence of Cascadia great earthquakes based on the turbidite event record, Nature, in review.

Gower, H. D., Yount, J. C., and Crosson, R. S., 1985, Seismotectonic map of the Puget Sound region, Washington: U.S. Geological Survey Miscellaneous Investigation Ser. Map, I-1613.

Gries, R., 1983, North-south compression of Rocky Mountain foreland structures, *in* Lowell, J. D., ed., Rocky Mountains Foreland Basins and Uplifts: Rocky Mountain Association of Geologists Symposium, p. 9-32.

Guffanti, M., and Weaver, C.S., 1988, Distribution of late Cenozoic volcanic vents in the Cascade Range: Volcanic arc segmentation and regional tectonic considerations: J. Geophys. Res., v. 93, p. 6513-6529.

Hamilton, W. B., 1989, Crustal geologic processes of the United States, *in* Pakiser, L.C., and Mooney, W. D., eds., Geophysical Framework of the continental United States: Boulder, Colorado, Geological Society of America Memoir 172, p. 743-781.

Hauser, E. C., and Lundy, J., 1989, COCORP deep reflections: Moho at 50 km (16 s) beneath the Colorado Plateau: Journal of Geophysical Research, v. 94, p. 7071 - 7081.

Hiett, B. J., 2000, 3D geometry and velocity structure of the Tacoma basin, western Washington, [MS Thesis], University of Texas at El Paso, 115 p.

Hicks, N. O., 2001, Crustal Structure of the Basin and Range Province: Southern Nevada, Southeastern California, and Western Arizona, [M. S. Thesis], University of Texas at El Paso.

Hoffman, P. F., 1988, United Plates of America, birth of a craton: Early Proterozoic assembly and growth of Laurentia: Annual Reviews of Earth and Planetary Sciences, v. 16, p. 543-603.

Holbrook, W. S., D. Lizarralde, S, McGeary, N. Bangs, and J. Diebold, 1999, Structure and composition of the Aleutian arc and implications for continental crustal growth: Geology, v.27, p. 31-34.

Holbrook, W. S., Mooney, W. D., and Christensen, N. I., 1992, The seismic velocity structure of the deep continental crust, in, Fountain, D. M., Arculus, R., and Kay, R. W., eds., Continental lower crust, p. 1-43, Elsevier, Amsterdam, The Netherlands.

Hole, J. A., 1992, Nonlinear high-resolution three-dimensional seismic travel time tomography: Journal of Geophysical Research, v. 97, no. B5, p. 6553-6562.

Hole, J. A., and Zelt, B. C., 1995, 3-D finite-difference reflection travel times, Geophy. J. Int., 121, 427-434.

Irving, E., Paleopoles and paleolatitudes of North America and speculations about displaced terranes, Can. J. Earth Sci., 16, 669-694, 1979

Jackson, W. H., Stewart, S. W., and Pakiser, L.C., 1963, Crustal structure in eastern Colorado from seismic-refraction measurements: Journal of Geophysical Research, v. 68, p. 5767-5776.

Jackson, W. H., and Pakiser, L. C., 1965, Seismic study of crustal structure in the southern Rocky Mountains: U. S., Geological Survey Professional Paper 525-D, p. D-85-D-92.

Jaksha, L. H., 1982, Reconnaissance seismic refraction-reflection surveys in southwestern New Mexico: Geological Society of America Bulletin, v. 93, p. 1030-1037.

Johnson, R. A., K. E. Karlstrom, S. B. Smithson, R. S. Houston, 1984, Gravity profiles across the Cheyenne belt: A Precambrian crustal suture in southeastern Wyoming: Journal of Geodynamics, v. 1, p. 445-472.

Johnson, S.Y., 1984, Evidence for a margin-truncating transcurrent fault (pre-Late Eocene) in western Washington, Geology, v. 12, p. 538-541.

Johnson, S. Y., Dadisman, S. V., Childs, J. R., and Stanley, W. D., 1999, Active tectonics of the Seattle fault and central Puget Sound, Washington - Implications for earthquake hazards: Geological Society of America Bulletin, v. 111, no. 7, p. 1042-1053.

Johnson, S. Y., Potter, C. J., and Armentrout, J. M., 1994, Origin and evolution of the Seattle fault and Seattle basin, Washington: Geology, v. 22, p. 71-74.

Johnson, S. Y., Potter, C. J., Armentrout, J. M., Miller, J. J., Finn, C., and Weaver, C. S., 1996, The southern Whidbey Island fault: An active structure in the Puget Lowland, Washington: Geological Society of America Bulletin, v. 108, no. 3,p. 334-354.

Jones, M.A., 1996, Thickness of unconsolidated deposits in the Puget Sound Lowland, Washington and British Columbia, U.S. Geological Survey, Water Resources Investigations Report (WRIR) 94-4133.

Karlstrom, K. E., and Bowring, S. A., 1988, Early Proterozoic assembly of tectonostratigraphic terranes in southwestern North America: Journal of Geology, v. 96, p. 561-576.

Karlstrom, K. E., and Bowring, S. A., 1993, Proterozoic orogenic history of Arizona, Transcontinental Proterozoic provinces, *in* Reed, J. C., Jr., Bickford, M. E., Houston, R. S., Link, P. K., Rankin, D. W., Sims, P. K., and Van Schmus, W. R., eds., Precambrian: Conterminous U. S.: Boulder, Colorado, Geological Society of America, The Geology of North America, v. C-2, p. 188-211.

Karlstrom, K. E., and Houston, R. S., 1984, The Cheyenne Belt: analysis of a Proterozoic suture in southern Wyoming: Precambrian Research, v. 25, p. 415-446.

Karlstrom, K. E., and E. D. Humphreys, 1998, Persistent influence of Proterozoic accretionary boundaries in the tectonic evolution of southwestern North America: Interaction of cratonic grain and mantle modification events: Rocky Mountain Geology, v. 33, p. 161-180.

Karlstrom, K. E., Karl-Inge Ahall, Stephen S. Harlan, M. L. Williams, J. McLelland, and G. W. Geissman, 2001, Long-lived (1.8-1.0 Ga) convergent orogen in southern Laurentia, its extensions to Australia and Baltica, and implications for refining Rodinia: Precambrian Research, v. 111, p. 5-30.

Keller, G. R., and Baldridge, W. S., 1999, The Rio Grande rift: A geological and geophysical review: Rocky Mountain Geology, v. 34, 131-148.

Keller, G. R., Braile, L. W., and Schlue, J. W.,1979a, Regional crustal structure of the Rio Grande rift from surface wave dispersion measurements, in R. E. Riecker, ed, Rio Grande Rift; Tectonics and Magmatism: Washington, D. C., American Geophysical Union, p.115-126.

Keller, G. R., Braile, L. W., and Morgan, P., 1979b, Crustal structure, geophysical models, and contemporary tectonism of the Colorado Plateau: Tectonophysics, v. 61, p. 131-147.

Keller, G. R., Snelson, C. M., Sheehan, A. F., and Dueker, K. G., 1998, Geophysical studies of crustal structure in the Rocky Mountain region: A review: Rocky Mountain Geology, v. 33, no. 2, p. 217-228.

Kilbride, F. E. A., 2000, Receiver function studies in the southwestern United States and correlation between stratigraphy and Poisson’s ratio southwestern Washington State, [Ph. D. Dissertation], University of Texas at El Paso, 194 p.

Kluth, C. F., 1986, Plate tectonics of the Ancestral Rocky Mountains: Tulsa, Oklahoma, American Association of Petroleum Geologists Memoir 41, p. 353-369.

Kluth, C. F., and Coney, P. J., 1981, Plate tectonics of the Ancestral Rocky Mountains: Geology, v. 9, p. 10-15.

Krishna, V. G., 1988, Crustal velocity models in the western United States from travel times and amplitudes of seismic refraction data: Bulletin of the Seismological Society of America, v. 78, p. 816-837.

Lay, T., and Wallace, T. C., 1995, Modern global seismology, Academic Press Inc., San

Diego, California, p. 86.

Lees, J. M., and Crosson, R. S., 1990, Tomographic imaging of local earthquake delay time for three-dimensional velocity variation in western Washington: Journal of Geophysical Research, v. 95, no. B4, 4763-4776.

Livaccari, R. F., Burke, K., and Sengor, A. M. C., 1981, Was the Laramide orogeny related to the subduction of an oceanic plateau?, Nature, 289, 276-278.

Livaccari, R. F., and Perry, F. V., 1993, Isotopic evidence for preservation of Cordilleran lithospheric mantle during the Sevier - Laramide orogeny, western United States: Geology, v. 21, p. 719-722.

Ludwin, R. S., Weaver, C. S., and Crosson, R. S., 1991, Seismicity of Washington and Oregon, *in* Slemmons, D. B., Engdahl, E. R., Zoback, M. D., and Blackwell, D. D., eds., Neotectonics of North America: Boulder, Colorado, Geological Society of America, Decade Map Volume 1.

Luetgert, J. H., 1992, MacRay: interactive two-dimensional seismic raytracing for the Macintosh: U. S. Geological Survey Open-File Report 92-356, p. 1-2.

MacLachlan, J. C., Bemis, H. C., Bryson, R. S., Holt, R. D., Lewis, C. J., and Wilde, D. E., 1972, Configuration of the Precambrian rock surface, in, Geologic Atlas of the Rocky Mountain region: Rocky Mt. Assoc. Geol., Denver, CO., p. 53.

Magill, J. R., Wells, R. E., Simpson, R. W., and Cox, A. V., 1982, Post 12 m.y. rotation of southwest Washington: Journal of Geophysical Research, v. 87, no. B5, p. 3761-3776.

Mallory, W. W., 1958, Pennsylvanian coarse arkosic redbeds and associated mountains in Colorado, in, Symposium on Pennsylvanian rocks of Colorado and adjacent areas: Rocky Mtn. Assoc. Geologists, Denver, CO, United States (USA), pp.17-20.

Malone, S. D., Crosson, R. S., Creager, K. C., Qamar, A., Thomas, G. C., Ludwin, R., Troost, K. G., Booth, D. B., and Haugerud, 2001, Preliminary report on the MW=6.8 Nisqually, Washington earthquake of 28 February 2001, Seismol. Res. Lett., 72, p. 353-362.

Mavko, G., Mukerji, T., Dvorkin, J., 1998, The rock physics handbook: tools for seismic analysis in porous media: Cambridge University Press, Cambridge, UK, 329 p.

Maxson, J., and Tikoff, B., 1996, Hit-and-run collision model for the Laramide orogeny, western United States, Geology, v. 24, p. 968-972.

McCamy, K., and Meyer, R. P., 1964, A correlation method of apparent velocity measurement: Journal of Geophysical Research, v. 69, p. 691-699.

Miller, K. C., Keller, G. R., Gridley, J. M., Luetgert, J. H., Mooney, W. D., and Thybo, H., 1997, Crustal structure along the west flank of the Cascades, western Washington: Journal of Geophysical Research, v. 102, no. B8, p. 17,857-17,873.

Monger, J. W. H., and Nokleberg, W. J., 1996, Evolution of the northern North American Cordillera: generation, fragmentation, displacement, and accretion of successive North American plate-margin arcs, *in* Coyner, A. R., and Fahey, P. L., eds., Geology and ore deposits of the American Cordillera: Reno, NV, Geological Society of Nevada, p. 1133-1152.

Mosher, S., 1998, Tectonic evolution of, the southern Laurentian Grenville orogenic belt: Geological Society of America Bulletin, v. 110, no. 11, p. 1357-1375.

Nyman, M. W., Karlstrom, K. E., Kirby, E., and Graubard, C. M., 1994, Mesoproterozoic contractional orogeny in western North America: Evidence from ca. 1.4 Ga plutons: Geology, v. 22, p. 901-904.

Oldow, J. S., A. W. Bally, H. G. Ave Lallemant, and W. P. Leeman, 1989, Phanerozoic evolution of North America Cordillera, United States and Canada, in Bally, A. W., and Palmer, A. R. (eds.), The Geology of North America: An Overview: Boulder, CO, Geological Society of America, Geology of North America, v. A, p. 139-232.

Olsen, K. H., Stewart, J. N., and Keller, G. R., 1979, Crustal structure along the Rio Grande rift from seismic refraction profiles, *in* Riecker, R. E., eds., Rio Grande Rift; Tectonics and Magmatism: Washington, D. C., American Geophysical union, p. 127-143.

O'Reilly, S. Y., W. L. Griffin, Y. H. Poudjom Djomani, and P. Morgan, 2001, Are lithospheres forever? Tracking changes in the subcontinental lithospheric mantle through time: GSA Today, v. 11, p. 4 - 10.

Parsons, T., McCarthy, J., Kohler, W. M., Ammon, C. J., Benz, H. M., Hole, J. A., and Criley, E. E., 1996, Crustal structure of the Colorado Plateau, Arizona: Application of new long-offset seismic data analysis techniques: Journal of Geophysical Research, v. 101, p. 11,173-11,194.

Parsons, T., Wells, R. E., Fisher, M. A., Flueh, E., and ten Brink, U. S., 1999, three-dimensional velocity structure of Siletzia and other accreted terranes in the Cascadia forearc of Washington: Journal of Geophysical Research, v. 104, no. B8, p. 18,015-18,039.

Peterson, J.A., and Smith, D. L., 1986, Rocky Mountain paleogeography through geologic time, in Peterson, J. A., eds., Paleotectonics & Sedimentation: Tulsa, Oklahoma, The American Association of Petroleum Geologists Memoir 41, p. 3-19.

Plouff, D., and L. C. Pakiser, 1972, Gravity study of the San Juan Mountains, Colorado: U.S. Geological Survey, Professional Paper 800-B, p. B183-B190.

Pratt, T.L., T. M. Brocher, C. S. Weaver, K. C. Miller, A. M. Trehu, K. C. Creager, R. S. Crosson, C. M. Snelson, 2002, Amplification of seismic waves by the Seattle basin, northwestern U.S., BSSA, in review.

Pratt, T. L., Johnson, S., Potter, C., Stephenson, W., and Finn, C., 1997, Seismic reflection images beneath Puget Sound, western Washington State: The Puget Lowland thrust sheet hypothesis: Journal of Geophysical Research, v. 102, no., B12, p. 27,469-27,489.

Preston, LA., K.C. Creager, R.S. Crosson, T. Van Wagoner, A.M. Trehu, T.M. Brocher, and M.A. Fisher, 2001, Cascadia slab structure and deep earthquakes, Seismol. Res. Lett., 72, 237.

Prodehl, C. P., 1979, Crustal structure of the western United States: U. S. Geological Survey Professional Paper 1034, 74 p.

Prodehl, C. P., and Pakiser, L. C., 1980, Crustal structure of the southern Rocky Mountains from seismic measurements: Geological Society of America Bulletin, v. 91, p. 147-155.

Prodehl, C. P., and Lipman, P., 1989, Crustal structure of the Rocky Mountain region, in Pakiser, L. C., and Mooney, W. D., eds., Geophysical framework of the continental United States: Boulder, Colorado, Geological Society of America Memoir 172, p. 249-284.

Rau, W.W., and S.Y. Johnson, 1999, Well stratigraphy and correlations, western Washington and northwestern Oregon, U.S. Geological Survey, Geologic Investigations Series Map I-2621, 31 pages, 3 foldouts.

Reed, J. C. Jr., Bickford, M. E., Premo, W. R., Aleinikoff, J. N., and Pallister, J. S., Evolution of the early Proterozoic Colorado province: Constraints from U-Pb geochronology, geology, 15, 861-865, 1987.

Riddihough, R. P., 1984, Recent movements of the Juan de Fuca plate system: Journal of Geophysical Research, v. 89, p. 6980-6994.

Roberts, D. G., Adams, D. C., and Keller, G. R., 1991, A geophysical analysis of crustal structure in the Ruidoso area: New Mexico Geological Society, 42nd Field Conference Guidebook, p. 191-197.

Roberts, D. G., Adams, D. C., and Keller, G. R., 1994, Crustal structure of west-central New Mexico: A preliminary seismic interpretation: New Mexico Geological Society, 45th Field Conference Guidebook, p. 143-145.

Roller, J. C., 1965, Crustal structure in the eastern Colorado Plateau province from seismic-refraction measurements: Bulletin of the Seismological Society of America, v. 55, p. 107-119.

Satake, K., Shimazaki, K., Tsuji, Y., and Ueda, K., 1996, Time and size of a giant earthquake in Cascadia inferred from Japanese tsunami records of January 1700, Nature, 379, p. 246-249.

Schneider, R. V., and Keller, G. R., 1994, Crustal structure of the western margin of the Rio Grande rift and Mogoloon-Datil, volcanic field, southwestern New Mexico and southeastern Arizona, in Keller G. R., and Cather, S. M., eds. Basins of the Rio grande Rift: Structure, Stratigraphy, and Tectonic Setting: Boulder, Colorado, Geological Society of America Special Paper 291, p. 207-226.

Schultz, A.P., and Crosson, R.S., 1996, Seismic velocity structure across the central Washington Cascade range from refraction interpretation with earthquake sources, J. Geophys. Res., 101, 27,899-27,915.

Sheriff, R. E., 1991, Encyclopedic dictionary of exploration geophysics: Society of Exploration Geophysicists, Tulsa, Oklahoma, p. 50.

Simpson, R. W., and Cox, A., 1977, Paleomagnetic evidence for tectonic rotation of the Oregon Coast range: Geology, v. 5, p. 585-589.

Sinno, Y. A., Daggett, P. H., Keller, G. R., Morgan, P., and Harder, S. H., 1986, Crustal structure of the southern Rio grande rift determined from seismic refraction profiles: Journal of Geophysical Research, v. 87, p. 2583-2596.

Sheehan, A. F., Abers, G. A., Jones, C. H., and Lerner-Lam, A. L., 1995, Crustal thickness variations across the Colorado Rocky Mountains from teleseismic receiver functions: Journal of Geophysical Research, v. 100, p. 20,391-20,404.

Sloss, L. L., 1988, Tectonic evolution of the craton in Phanerozoic time, *in* Sloss, L. L., ed., Sedimentary Cover - North America Craton; U. S.: Boulder, Colorado, Geological Society of America, The Geology of North America, v. D-2.

Smith, R. B., and 9 others, 1982, The Yellowstone-Snake River plain seismic profiling experiment; Crustal structure of the Yellowstone region and experiment design: Journal of Geophysical Research, v. 87, p. 2583-2596.

Smithson, S. B., Brewer, J. A., Kaufman, S., Oliver, J. E., and Hurich, C. A., 1979, Structure of the Laramide Wind River uplift, Wyoming, from COCORP deep reflection data and from gravity data: Journal of Geophysical Research, v. 84, p. 5955-5972.

Smithson, S. B., Johnson, R. A., and Wong, Y. K., 1981, Mean crustal velocity: a critical parameter for interpreting crustal structure and crustal growth: Earth and Planetary Science Letters, v. 53, p. 323-332.

Smithson, S. B., and Johnson, R. A., 1989, Crustal structure of the western U. S. based on reflection seismology, *in* Pakiser, L.C., and Mooney, W. D., eds., Geophysical framework of the continental United States: Boulder, Colorado, geological Society of America Memoir 172, p. 577-612,

Snavely, Jr., P. D., MacLeod, N. S., and Wagner, H. C., 1968, Tholeiitic and alkalic basalts of the Eocene Siletz river volcanics, Oregon Coast range: American Journal of Science, v. 266, p. 454-481.

Snelson, C. M., Henstock, T. J., Keller, G. R., Miller, K. C., and Levander, A., 1998, Crustal and uppermost mantle structure along the Deep Probe seismic profile: Rocky Mountain Geology, v. 33, no. 2, p. 181-198.

Steeples, D. W., and Miller, R. D., 1989, Kansas refraction profiles: Kansas Geological Survey, Bulletin 226, p. 129-164.

Steinhart, J. S., and Meyer, R. P., 1961, Explosion Studies of Continental Structure: Carnegie Institution of Washington, Publication 622, 409 pp.

Stewart, J. H., 1976, Late Precambrian evolution of North America: Plate tectonics implication, Geology, v. 4, p. 11-15.

Stewart, S. W., and Pakiser, L. C., 1962, Crustal structure in eastern new Mexico interpreted from the GNOME explosion: Bulletin of the Seismological Society of America, v. 52, p. 1017-1030.

Symons, N. P., and Crosson, R. S., 1997, Seismic velocity structure of the Puget Sound region from 3-D non-linear tomography: Geophysical Research Letters, v. 24, no.21, p. 2593-2596.

Taber, J. J. and Smith, S. W., 1985, Seismicity and focal mechanisms associated with the subduction of the Juan de Fuca plate beneath the Olympic Peninsula, Washington: Bulletin of the Seismological Society of America, v. 75, no. 1, p. 237-249.

Tabor, J. J., and Cady, W. M., 1978, The structure of the Olympic Mountains, Washington-analysis of a subduction zone: U. S. Geological Survey Professional Paper 1033, 38 p.

ten Brink, U.S., P.C. Molzer, M.A. Fisher, R.J. Blakely, R. Bucknam, and the SHIPS Working Group, 2002, Structure and evolution of the Seattle fault and basin, Washington, J. Geophys. Res., in review.

Toppozada, T. R., and Sanford, A. R., 1976, Crustal structure in central New Mexico interpretated from the Gasbuggy explosion: Bulletin of the Seismological Society of America, v. 6, p. 877-886.

Tréhu, A. M., T. M. Brocher, M. A. Fisher, K. C. Creager, L. Preston, and SHIPS98 Working Group, 2001, Geometry of the subducting Juan de Fuca plate: New constraints from SHIPS98, in Joint USGS/GSC Open File Report: International Workshop on Cascadia Intraslab Earthquakes - Science and Hazard, in press.

Tikoff, B. and J. Maxson, 2001, Lithospheric buckling of the Laramide foreland during Late Cretaceous and Paleogene, western United States: Rocky Mountain Geology, v. 36, p. 13-35.

Van Wagoner, T., R.S. Crosson, N.P. Symons, G.F. Medema, K.C. Creager, and L.A. Preston, 2001, High resolution seismic tomography and earthquake relocation in the Puget Lowland, Washington, J. Geophys. Res., in review.

Vidale, J., 1988, Finite-difference calculation for travel times, Bull. Seis. Soc. Am., 78, 2062-2076, 1988.

Vidale, J. E., 1990, Finite-difference calculation of traveltimes in three dimensions: Geophysics, v. 55, p. 521-526.

Weaver, C. S., and Baker, G. E., 1988, Geometry of the Juan de Fuca plate beneath Washington and northern Oregon from seismicity: Bulletin of the Seismological Society of America, v. 78, no. 1, p. 264-275.

Weaver, C. S., and Smith, S. W., 1983, Regional tectonic and earthquake hazard implications of a crustal fault zone in southwestern Washington: Journal of Geophysical Research, v. 88, no. B12, p. 10,371-10,383.

Wells, R. E., Engebretson, D. C., Snavely, Jr., P. D., and Coe, R. S., 1984, Cenozoic plate motions and the volcano-tectonic evolution of western Oregon and Washington: Tectonics, v. 3, no. 2, p. 275-294.

Wells, R. E., and Heller, P. L., 1988, The relative contribution of accretion, shear, and extension to Cenozoic tectonic rotation in the Pacific Northwest: Geological Society of America Bulletin, v. 100, p. 325-338.

Well. R. E., and Simpson, R. W., 2001, Microplate motion of the Cascadia forearc and implications for subduction deformation, Earth, Planets, and Space, v. 53, no. 4, p. 275-283.

Wells, R.E., and C.S. Weaver, Block deformation in Puget Lowland, in V.E. Frizzel, ed., Proceedings of the National Earthquake Prediction Evaluation Council, U.S. Geological Survey, p. 14-16, Open File Report 93-333, 1993.

Wells, R.E., Weaver, C.S., and Blakely, R.J., 1998, Fore-arc migration in Cascadia and its neotectonic significance, Geology, 26, 759-762.

Wilden, R. 1965, Seismic-refraction measurements of crustal structure beneath American Falls Reservoir, Idaho, and Flaming Gorge Reservoir, Utah: U. S. Geological Survey Professional Paper 525-C, p. C-44-C-50.

Winkler, K. W., and Murphey, W. F., III, 1995, Acoustic velocity and attenuation in porous rocks, in, Rock physics & phase relations: A handbook of physical constants, Ahrens, T. J., eds, American Geophysical Union, Washington, DC, p. 20-34.

Wolf, L. W., and Cipar, J. J., 1993, Through thick and thin: A new model for the Colorado Plateau from seismic refraction data from Pacific to Arizona crustal experiment: Journal of Geophysical Research, v. 98, p. 19,881-19,894.

Woodward, L. A., 1988, Tectonic map of the Rocky Mountain region of the United States, in Sloss, L. L., ed., Sedimentary Cover - North American Craton: U. S.: Boulder, Colorado, Geological Society of AMerica, the Geology of North America, v. D-2, plate 2.

Ye, H. Royden, L., Burchfiel, C., and Schuepbach, M., 1996, Late Paleozoic deformation of interior North America: The greater Ancestral Rocky Mountains: American Association of Petroleum Geologists Bulletin, v. 80, p. 1397-1432.

Yount, J. C., and Gower, H. D., 1991, Bedrock geologic map of the Seattle 30' by 60' quadrangle, Washington: U. S. Geological Survey Open-File Report 91-147, 37 p, 4 pl., scale 1:100 000.

Zelt, B. C., Ellis, R. M., Clowes, R. M., and Hole, J. A., 1996, Inversion of three-dimensional wide-angle seismic data from the southwestern Canadian Cordillera, Journal of Geophysical Research, v. 101, no. B4, p. 8503-8529.

Zelt, C. A., 1998, Lateral velocity resolution from three-dimensional seismic refraction data, Geophys. J. Int., 135, 1101-1112.

APPENDIX A

Strike Lines along SHIPS ‘99 Profile for Density Modeling

Latitude	Longitude
47.85	-123.60
47.74	-123.16
47.71	-122.95
47.67	-122.62
47.66	-121.87
47.66	-121.57

APPENDIX B

Gravity Points along SHIPS '99 Profile for Density Modeling

Distance at Start (km)	Distance From Profile (km)	Gravity Value (mGal)	Latitude	Longitude
0.51	0.12	-82.08	47.847	-123.594
12.05	0.48	-86.11	47.808	-123.451
15.46	0.58	-88.65	47.807	-123.403
18.04	0.24	-87.13	47.792	-123.374
20.18	0.53	-89.35	47.782	-123.349
28.75	0.00	-85.44	47.760	-123.239
32.61	0.52	-76.98	47.743	-123.193
33.94	0.22	-73.11	47.742	-123.175
34.80	0.41	-70.23	47.737	-123.165
35.73	0.65	-64.59	47.733	-123.153
36.49	0.91	-57.43	47.729	-123.144
37.13	0.73	-54.57	47.730	-123.135
38.01	0.43	-50.45	47.731	-123.122
38.71	0.37	-44.92	47.730	-123.113
40.11	0.25	-39.05	47.728	-123.094
40.48	0.15	-40.08	47.731	-123.089
40.61	0.54	-37.45	47.734	-123.086
41.05	0.91	-36.58	47.737	-123.079
41.90	1.47	-30.20	47.740	-123.066
42.70	1.83	-25.53	47.742	-123.055
43.16	1.81	-25.49	47.741	-123.049
43.39	1.95	-21.30	47.742	-123.045
43.83	2.05	-22.37	47.742	-123.039
44.78	1.99	-18.24	47.739	-123.027
45.50	1.48	-16.77	47.734	-123.019
46.05	0.99	-17.81	47.728	-123.013
46.88	0.82	-17.44	47.725	-123.003
47.40	0.67	-13.16	47.723	-122.996
47.77	0.65	-15.48	47.722	-122.992
48.35	0.59	-13.75	47.720	-122.984
49.05	0.74	-11.50	47.720	-122.975
50.15	0.90	-9.59	47.720	-122.960
50.95	1.01	-9.10	47.719	-122.949
51.57	1.06	-7.45	47.719	-122.941
52.06	0.40	-10.28	47.712	-122.936
52.51	0.18	-6.47	47.709	-122.931
52.85	0.01	-9.90	47.707	-122.927
53.56	0.16	-10.12	47.705	-122.918
54.28	0.22	-9.47	47.703	-122.909
54.56	0.68	-11.19	47.699	-122.906

Distance at Start (km)	Distance From Profile (km)	Gravity Value (mGal)	Latitude	Longitude
55.24	0.62	-10.59	47.698	-122.897
55.36	0.45	-10.08	47.699	-122.895
55.72	1.06	-10.92	47.693	-122.892
55.79	1.30	-9.32	47.714	-122.885
60.17	0.34	-33.66	47.693	-122.831
60.74	0.20	-43.44	47.693	-122.824
61.26	0.50	-43.49	47.690	-122.817
62.05	0.55	-47.84	47.697	-122.804
62.90	0.51	-53.09	47.696	-122.793
63.40	0.58	-54.54	47.696	-122.787
64.11	0.54	-56.58	47.694	-122.777
64.69	0.53	-54.12	47.693	-122.770
66.66	0.55	-64.24	47.690	-122.744
67.12	0.67	-65.05	47.691	-122.738
67.90	0.18	-69.01	47.685	-122.728
68.30	0.07	-70.23	47.682	-122.724
68.86	1.34	-71.76	47.670	-122.719
69.93	0.06	-75.35	47.680	-122.702
70.68	0.09	-78.45	47.680	-122.692
71.77	0.25	-81.20	47.679	-122.677
72.31	0.16	-82.23	47.678	-122.670
73.03	0.29	-83.68	47.678	-122.661
73.26	0.64	-83.63	47.680	-122.657
74.00	0.04	-84.78	47.674	-122.648
74.87	0.37	-87.80	47.669	-122.638
75.27	0.71	-88.18	47.665	-122.634
75.93	0.61	-89.60	47.665	-122.625
76.50	0.57	-91.17	47.665	-122.616
78.57	0.83	-94.35	47.662	-122.588
78.88	0.63	-94.50	47.664	-122.584
79.29	0.27	-96.23	47.667	-122.578
79.67	0.22	-97.11	47.668	-122.573
80.26	0.49	-97.82	47.665	-122.566
80.67	0.51	-99.07	47.665	-122.560
81.06	0.46	-99.71	47.665	-122.555
81.65	0.45	-101.14	47.665	-122.547
82.15	0.46	-102.60	47.665	-122.540
82.55	0.46	-103.31	47.665	-122.535
82.83	0.34	-102.21	47.672	-122.531
83.30	0.52	-105.56	47.664	-122.525
83.69	0.48	-106.52	47.665	-122.520
84.11	0.43	-107.65	47.665	-122.514
84.48	0.47	-108.22	47.665	-122.509
84.91	0.42	-113.05	47.665	-122.503

Distance at Start (km)	Distance From Profile (km)	Gravity Value (mGal)	Latitude	Longitude
92.63	0.33	-115.95	47.671	-122.400
93.07	0.41	-116.32	47.671	-122.394
93.45	0.40	-117.15	47.671	-122.389
93.86	0.40	-117.49	47.671	-122.384
94.13	0.41	-118.87	47.671	-122.380
94.72	0.42	-118.77	47.671	-122.372
95.09	0.42	-119.32	47.671	-122.367
95.41	0.43	-120.18	47.671	-122.363
95.67	0.45	-119.54	47.671	-122.359
96.07	0.48	-123.24	47.671	-122.354
96.34	0.56	-124.46	47.672	-122.350
96.57	0.56	-125.22	47.672	-122.347
97.01	0.42	-124.05	47.671	-122.342
97.27	0.24	-125.34	47.669	-122.338
97.60	0.23	-126.06	47.669	-122.334
97.92	0.31	-126.62	47.670	-122.329
98.10	0.18	-126.58	47.665	-122.327
98.28	0.32	-127.97	47.670	-122.325
98.73	0.34	-126.79	47.670	-122.319
99.05	0.37	-128.18	47.670	-122.314
99.32	0.17	-127.58	47.665	-122.311
99.63	0.39	-126.32	47.663	-122.307
99.93	0.39	-128.09	47.670	-122.303
100.15	0.00	-126.25	47.666	-122.300
101.01	0.68	-127.99	47.672	-122.288
101.34	0.69	-126.22	47.672	-122.284
101.73	0.70	-126.98	47.672	-122.278
102.04	0.65	-128.03	47.672	-122.274
102.38	0.73	-127.13	47.673	-122.270
102.74	0.72	-126.60	47.672	-122.265
103.04	0.70	-127.17	47.672	-122.261
103.32	0.71	-128.04	47.672	-122.257
103.53	0.83	-127.49	47.673	-122.254
103.88	1.11	-126.60	47.676	-122.250
107.20	0.40	-127.20	47.662	-122.206
107.64	0.43	-127.85	47.661	-122.200
108.00	0.42	-128.19	47.661	-122.195
108.35	0.41	-128.08	47.661	-122.190
108.74	0.40	-129.15	47.661	-122.185
109.18	0.38	-129.82	47.661	-122.179
109.97	0.41	-129.69	47.661	-122.169
110.26	0.59	-128.01	47.659	-122.165
110.38	0.41	-129.56	47.661	-122.163
110.63	0.27	-128.70	47.667	-122.160

Distance at Start (km)	Distance From Profile (km)	Gravity Value (mGal)	Latitude	Longitude
110.73	0.18	-128.50	47.663	-122.158
111.17	0.24	-128.32	47.667	-122.152
111.36	0.19	-128.02	47.666	-122.150
111.77	0.29	-126.59	47.667	-122.144
111.91	0.44	-127.02	47.668	-122.142
111.97	0.40	-126.66	47.668	-122.142
112.30	0.45	-126.74	47.668	-122.137
112.54	0.23	-126.17	47.666	-122.134
112.74	0.01	-126.60	47.664	-122.131
113.06	0.00	-125.72	47.664	-122.127
113.67	0.11	-124.48	47.665	-122.119
114.14	0.06	-124.15	47.664	-122.113
114.59	0.00	-124.12	47.664	-122.107
115.24	0.10	-123.68	47.665	-122.098
115.63	0.43	-124.10	47.660	-122.093
116.80	0.82	-121.21	47.656	-122.077
117.98	0.29	-121.94	47.666	-122.061
118.89	0.72	-121.95	47.669	-122.049
119.17	0.67	-121.59	47.669	-122.045
119.56	0.55	-120.35	47.668	-122.040
119.95	0.47	-120.37	47.667	-122.035
120.38	0.35	-119.16	47.666	-122.029
120.77	0.26	-118.87	47.665	-122.024
120.97	0.45	-118.79	47.667	-122.021
121.51	1.41	-116.89	47.675	-122.014
121.96	1.42	-115.85	47.675	-122.008
122.42	1.38	-114.65	47.675	-122.002
122.84	1.33	-114.65	47.674	-121.996
123.27	1.30	-112.35	47.674	-121.990
124.22	1.31	-106.75	47.674	-121.978
124.57	1.33	-104.61	47.674	-121.973
124.94	1.34	-102.93	47.674	-121.968
125.43	1.34	-100.80	47.674	-121.962
126.60	1.27	-97.85	47.673	-121.946
127.30	1.21	-95.54	47.672	-121.937
127.85	1.21	-96.29	47.672	-121.929
128.16	0.60	-97.13	47.666	-121.925
128.70	0.39	-94.73	47.664	-121.918
129.55	0.78	-92.78	47.668	-121.907
130.05	0.17	-92.44	47.659	-121.900
130.30	0.18	-93.37	47.659	-121.897
130.91	0.11	-94.51	47.659	-121.889
132.02	0.12	-91.28	47.659	-121.874
148.69	0.26	-98.15	47.662	-121.651

Distance at Start (km)	Distance From Profile (km)	Gravity Value (mGal)	Latitude	Longitude
151.40	0.38	-104.03	47.657	-121.615
153.97	0.12	-89.42	47.659	-121.581

APPENDIX C

Refraction Profiles in the Rocky Mountain Region

Shotpoint	Coordinates	Ave. Crustal Velocity	Ave. Station Spacing	Ref.	R F Thickness	Crustal Thickness	Location
DP-37-North	37.85N 108.44W	N/A	1.25km	1	N/A	43 km	38.5N 108.5W
DP-43-South	42.75N 107.69W	N/A	1.25km	1	N/A	54 km	40.0N 108.9W
		N/A	1.25km	1	N/A	43 km	41.5N 108.7W
DP-37-South	37.85N 108.44W	N/A	1.25km	1	N/A	41 km	35.0N 108.3W
DP-43-North	42.75N 107.69W	N/A	1.25km	1	N/A	54 km	44.5N 108.5W
		N/A	1.25km	1	N/A	52 km	47.5N 110.0W
Lumberton	36.95N 106.94W	6.25 km/s	7 km	2	N/A	50 km	37.5N 106.9W
Cochetopa-S	38.35N 106.73W	6.25 km/s	7 km	2	N/A	50 km	37.5N 106.9W
Cochetopa-N	38.35N 106.73W	6.25 km/s	7 km	2	44	50 km	39.0N 106.8W
Wolcott-S	39.85N 106.68W	6.25 km/s	7 km	2	44	50 km	39.0N 106.8W
Wolcott-N	39.74N 106.75W	6.2 km/s	7 km	2	N/A	42 km	41.0N 106.9W
Sinclair-S	41.70N 106.98W	6.2 km/s	7 km	2	N/A	42 km	41.0N 106.9W
Climax-N	39.37N 106.17W	6.4 km/s	15 km	3,2, 4	46	54 km	40.5N 105.7W
Sinclair-E	41.65N 106.98W	6.5 km/s	8 km	4	N/A	40 km	42.1N 106.0W
Guernsey-W	42.55N 104.98W	6.5 km/s	8 km	4	N/A	40 km	42.1N 106.0W
Lamar-N	38.25N 102.75W	6.35 km/s	1 km	5	49	48 km	39.7N 103.2W

Shotpoint	Coordinates	Ave. Crustal Velocity	Ave. Station Spacing	Ref.	R F Thickness	Crustal Thickness	Location
Wolcott-E	39.85N 106.75W	6.3 km/s	15 km	4,6	53	50 km	39.8N 106.0W
Agate-W	39.57N 103.75W	6.6 km/s	15 km	4,6	54	52 km	40.0N 104.5W
Agate-E	39.57N 103.75W	N/A	1 km	7	49	46 km	40.0N 103.5W
Concordia-W	39.52N 97.91W	N/A	1 km	7	N/A	36 km	39.5N 97.91W
American Falls	42.84N 112.81W	6.5 km/s	10 km	8,4	N/A	40 km	41.5N 110.5W
Flaming Gorge	40.95N 109.64W						
Bingham-NE	40.53N 112.16W	N/A	6 km	9	N/A	40 km	41.8N 111.0W
Gasbuggy	36.68N 107.21W	N/A	30 km	10	N/A	40 km	35.3N 107.0W
Dice Throw-N	33.68N 106.52W	6.15 km/s	9 km	11	N/A	34 km	35.0N 106.4W
Dice Throw-W	33.68N 106.52W	6.25 km/s	15 km	12,15	N/A	34 km	33.4N 108.0W
Morenci-E	33.10N 109.37W	6.25 km/s	15 km	12,15	N/A	34 km	33.4N 108.0W
Tyrone-NE	32.65N 108.39W	6.3 km/s	5 km	13,14	N/A	32 km	33.1N 107.3W
WSMR-SW	33.38N 106.28W	6.3 km/s	5 km	13,14	N/A	32 km	33.1N 107.3W
WSMR-S	33.62N 106.47W	6.25 km/s	7 km	13	N/A	30 km	32.5N 106.6W
Tyrone-SE	32.65N 108.39W	6.25 km/s	7 km	13	N/A	30 km	32.2N 106.8W
Tyrone-N	32.65N 108.39W	6.25 km/s	8 km	15, 1	N/A	34 km	33.4N 108.0W
					N/A	40 km	34.5N 107.8W
WSMR-W	33.62N 106.47W	N/A		16	N/A	33 km	34.0N 107.1W

Shotpoint	Coordinates	Ave. Crustal Velocity	Ave. Station Spacing	Ref.	R F Thickness	Crustal Thickness	Location
Gnome	32.26N 103.87W	6.7 km/s	40 km	18	N/A	51 km	34.0N 103.5W
Montana		N/A		19-22	N/A	45-50 km	
Hanksville	38.37N 110.93W	N/A		23-26	N/A	45 km	37.6N 110.5W
Chinle	35.93N 109.57W	N/A		23-26	N/A	45 km	
PACE profiles		N/A		26,27	N/A	45 km	

References and notes for Appendix C

1 - DEEP PROBE Working Group (Snelson et al., 1998)

2 - Prodehl and Pakiser (1980) - employed a series of shots extending across Colorado. Climax North includes evidence for crustal tinning beneath the Laramie Range.

3 - Jackson and Pakiser (1965) - unreversed.

4 - Prodehl and Lipman (1989) - a summary of existing profiles with original interpretations of several USGS profiles.

5 - Jackson et al. (1963) - unreversed.

6 - Krishna (1988) - unreversed.

Lamar West shows evidence of large offsets in the Moho via PmP phase arrival variations. Derived a thin 42 km crust for Agate-Wolcott which seems incompatible with other results.

7 - Steeples and Miller (1989)

8 - Wilden (1965) - reversed with shot in the middle of the profile.

9 - Braile et al. (1974) - unreversed but tied to American Falls - Flaming Gorge.

10 - Toppozada and Sanford (1976) - unreversed.

11 - Olsen et al. (1979) - unreversed but tied to COCORP and teleseismic measurements at Albuquerque.

12 - Jaksha (1982) -partly reversed using the Morenci mine in Arizona.

13 - Sinno et al. (1986) - 3 interlocking lines with one reversed.

14 - Cook et al. (1979) - unreversed.

Used the Santa Rita mine near Silver City, NM instead of the nearby Tyrone mine.

References and notes for Appendix C

15 - Schneider and Keller (1994) - unreversed but tied to Dice Throw - Morenci. Reinterpreted the data from Jaksha (1982) to produce 2-D models.

16 - Roberts et al. (1994) - short, unreversed. Helps constrain regional crustal model of Adams and Keller (1994).

17 - Roberts et al. (1991) - short, unreversed. Helps constrain regional crustal model of Adams and Keller (1994).

18 - Stewart and Pakiser (1962) - unreversed.

19 - Steinhart and Meyer (1961) - a series of profiles covering most of Montana.

20 - McCamy and Meyer (1964) - a series of profiles covering most of Montana.

21 - Asada and Aldrich (1966) - a series of profiles covering most of Montana.

22 - Borcherdt and Roller (1967) - A profile across the LASA array.

References 19-22 present a series of profiles which were recorded across Montana. These data are not well documented in that few seismograms are presented and many of the profiles were unreversed. The crustal models presented indicate that the crust is 45-50 km thick in the area.

23 - Roller (1965) - reversed.

24 - Prodehl (1979) - reinterpretation of Hanksville - Chinle.

25 - Hauser and Lundy (1989) - COCORP interpretation of thick crust.

26 - Wolf and Cipar (1993) - thick crust interpretation.

27 - Parsons et al. (1996) - complex and locally thin crust interpretation.

References and notes for Appendix C

References 23-27 present conflicting views about crustal thickness in the southern Colorado Plateau. The main point is that the existing data are ambiguous in regard to the presence of a layer with a P-wave velocity of about 7.3 km/s in the lowermost crust. If it is included, crustal thicknesses are 45 - 50km, if not they are 40 - 45 km. Thus an average value of 45 km was used here (Keller et al., 1979).

APPENDIX D

Receiver Functions in the Rocky Mountain Region

Coordinates	Receiver Function Thickness
36.97N 102.97W	43 km*
36.97N 103.65W	43 km*
37.54N 105.58W	49 km
37.65N 102.97W	43 km*
37.65N 103.65W	45 km*
37.65N 104.32W	50 km*
37.65N 107.70W	42 km*
37.77N 104.36W	54 km
38.32N 103.65W	45 km*
38.32N 105.68W	41 km*
38.32N 106.35W	40 km*
38.32N 107.03W	45 km*
38.32N 107.70W	46 km*
38.32N 108.38W	52 km*
38.33N 108.93W	39 km
38.41N 107.99W	48 km
38.50N 103.70W	47 km
38.54N 106.12W	50 km
38.77N 105.22W	48 km
39.00N 101.62W	47 km*
39.00N 102.30W	47 km*
39.00N 102.97W	42 km*
39.00N 103.65W	50 km*
39.00N 104.32W	54 km*
39.00N 105.00W	49 km*
39.00N 105.68W	44 km*
39.00N 106.35W	42 km*
39.00N 107.03W	44 km*
39.00N 107.70W	44 km*
39.10N 108.13W	42 km
39.15N 106.36W	49 km
39.23N 109.08W	44 km
39.25N 99.53W	43 km
39.33N 107.19W	54 km
39.35N 104.54W	52 km
39.38N 101.05W	45 km
39.38N 102.35W	47 km
39.41N 103.62W	54 km
39.68N 101.62W	47 km*
39.68N 102.30W	47 km*
39.68N 102.97W	48 km*

Coordinates	Receiver Function Thickness
39.68N 103.65W	49 km*
39.68N 104.32W	54 km*
39.68N 105.00W	50 km*
39.68N 105.68W	53 km*
39.68N 106.35W	52 km*
39.68N 107.03W	48 km*
40.13N 106.37W	53 km
40.15N 102.77W	46 km
40.32N 104.07W	51 km
40.35N 102.97W	47 km*
40.35N 105.00W	44 km*
40.35N 105.68W	46 km*
40.35N 106.35W	53 km*
40.35N 107.70W	53 km*
40.38N 105.20W	43 km
41.03N 105.00W	43 km*
41.03N 105.68W	43 km*
41.03N 107.70W	52 km*

* Stacked Receiver Functions

APPENDIX E

Station Locations for CD-RoM '99

Station Number	Latitude	Longitude	Elevation (m)
5001	34.577	-104.249	1283.1
5002	34.584	-104.256	1290.2
5003	34.591	-104.264	1298.4
5004	34.598	-104.272	1303.6
5005	34.605	-104.279	1305.2
5006	34.612	-104.287	1305.9
5007	34.619	-104.295	1309.3
5008	34.627	-104.303	1320.3
5009	34.634	-104.312	1324.9
5010	34.641	-104.319	1330.4
5011	34.648	-104.322	1329.8
5012	34.655	-104.325	1336.2
5013	34.662	-104.333	1328.6
5014	34.668	-104.340	1317.4
5015	34.676	-104.349	1309.8
5016	34.683	-104.358	1312.5
5017	34.691	-104.381	1299.7
5018	34.697	-104.381	1303.7
5019	34.704	-104.378	1297.5
5020	34.712	-104.380	1303.4
5021	34.719	-104.384	1318.7
5022	34.726	-104.384	1314.8
5023	34.733	-104.384	1319.0
5024	34.740	-104.384	1318.6
5025	34.747	-104.384	1326.5
5026	34.754	-104.384	1331.1
5027	34.761	-104.386	1339.0
5028	34.767	-104.388	1350.6
5029	34.775	-104.391	1372.1
5030	34.782	-104.393	1377.3
5031	34.789	-104.393	1377.3
5032	34.797	-104.393	1379.3
5033	34.804	-104.393	1375.2
5034	34.811	-104.393	1371.3
5035	34.817	-104.393	1378.0
5036	34.825	-104.393	1391.1
5037	34.832	-104.393	1394.0
5038	34.839	-104.393	1384.2
5039	34.846	-104.393	1400.4
5040	34.853	-104.389	1409.0
5041	34.860	-104.392	1409.5

Station Number	Latitude	Longitude	Elevation (m)
5042	34.867	-104.410	1426.1
5043	34.874	-104.420	1440.5
5044	34.881	-104.428	1450.2
5045	34.888	-104.428	1460.1
5046	34.896	-104.428	1469.9
5047	34.902	-104.428	1493.4
5048	34.910	-104.428	1486.6
5049	34.917	-104.428	1502.7
5050	34.924	-104.428	1504.9
5051	34.931	-104.428	1509.4
5052	34.938	-104.428	1510.0
5053	34.945	-104.428	1513.9
5054	34.951	-104.428	1524.0
5055	34.959	-104.409	1502.6
5056	34.967	-104.409	1510.5
5057	34.973	-104.409	1531.2
5058	34.981	-104.409	1539.9
5059	34.987	-104.409	1523.8
5060	34.995	-104.409	1499.9
5061	35.002	-104.409	1497.8
5062	35.009	-104.409	1509.3
5063	35.016	-104.408	1487.2
5064	35.023	-104.409	1484.5
5065	35.031	-104.412	1455.9
5066	35.037	-104.405	1441.8
5067	35.044	-104.408	1422.3
5068	35.051	-104.408	1416.6
5069	35.059	-104.408	1414.8
5070	35.065	-104.408	1409.5
5071	35.072	-104.408	1405.1
5072	35.080	-104.408	1401.0
5073	35.087	-104.408	1413.4
5074	35.094	-104.408	1419.4
5075	35.101	-104.408	1422.6
5076	35.108	-104.408	1424.1
5077	35.115	-104.408	1417.0
5078	35.122	-104.408	1403.5
5079	35.129	-104.409	1400.4
5080	35.137	-104.409	1400.2
5081	35.144	-104.409	1393.0
5082	35.150	-104.409	1385.1
5083	35.158	-104.409	1378.0
5084	35.165	-104.412	1369.4
5085	35.172	-104.415	1353.9
5086	35.177	-104.438	1354.0

Station Number	Latitude	Longitude	Elevation (m)
5087	35.186	-104.449	1354.0
5088	35.194	-104.458	1354.1
5089	35.202	-104.459	1354.1
5090	35.208	-104.458	1354.1
5091	35.215	-104.458	1354.1
5092	35.222	-104.459	1354.1
5093	35.229	-104.460	1354.2
5094	35.238	-104.461	1364.2
5095	35.245	-104.483	1374.3
5096	35.250	-104.488	1382.8
5097	35.257	-104.494	1391.1
5098	35.264	-104.490	1380.3
5099	35.270	-104.486	1374.6
5100	35.278	-104.481	1370.7
5101	35.285	-104.478	1375.0
5102	35.292	-104.478	1388.4
5103	35.299	-104.479	1395.4
5104	35.306	-104.438	1362.3
5105	35.314	-104.432	1356.5
5106	35.321	-104.424	1350.3
5107	35.327	-104.433	1349.8
5108	35.334	-104.442	1352.9
5109	35.342	-104.454	1373.8
5110	35.349	-104.458	1367.4
5111	35.356	-104.460	1375.6
5112	35.363	-104.461	1384.1
5113	35.370	-104.462	1375.2
5114	35.378	-104.462	1352.5
5115	35.384	-104.461	1341.9
5116	35.391	-104.461	1329.1
5117	35.398	-104.460	1333.3
5118	35.406	-104.460	1341.6
5119	35.413	-104.459	1362.3
5120	35.420	-104.463	1401.2
5121	35.427	-104.480	1435.6
5122	35.434	-104.484	1433.9
5123	35.441	-104.487	1446.1
5124	35.448	-104.490	1466.7
5125	35.455	-104.492	1467.3
5126	35.462	-104.495	1471.1
5127	35.470	-104.410	1400.0
5128	35.476	-104.407	1425.4
5129	35.483	-104.407	1425.2
5130	35.491	-104.406	1424.7
5131	35.497	-104.403	1422.1

Station Number	Latitude	Longitude	Elevation (m)
5132	35.505	-104.401	1408.7
5133	35.512	-104.400	1394.3
5134	35.519	-104.401	1401.5
5135	35.526	-104.407	1423.4
5136	35.533	-104.407	1419.6
5137	35.540	-104.407	1417.3
5138	35.547	-104.409	1419.2
5139	35.554	-104.412	1424.0
5140	35.561	-104.416	1425.6
5141	35.569	-104.420	1423.9
5142	35.575	-104.424	1421.9
5143	35.582	-104.425	1423.2
5144	35.590	-104.426	1423.6
5145	35.597	-104.427	1423.6
5146	35.604	-104.428	1421.1
5147	35.611	-104.427	1417.7
5148	35.618	-104.426	1405.7
5149	35.626	-104.423	1394.5
5150	35.632	-104.422	1392.1
5151	35.638	-104.416	1387.8
5152	35.646	-104.404	1377.0
5153	35.653	-104.393	1395.0
5154	35.660	-104.345	1457.5
5155	35.667	-104.354	1462.4
5156	35.675	-104.364	1476.7
5157	35.682	-104.370	1488.4
5158	35.689	-104.375	1502.9
5159	35.696	-104.376	1510.5
5160	35.703	-104.390	1424.5
5161	35.710	-104.411	1361.2
5162	35.714	-104.426	1372.1
5165	35.735	-104.438	1725.7
5170	35.775	-104.441	1730.1
5171	35.781	-104.447	1728.1
5172	35.788	-104.447	1708.6
5173	35.795	-104.447	1705.8
5174	35.802	-104.447	1694.6
5175	35.809	-104.447	1693.2
5176	35.816	-104.451	1698.7
5177	35.824	-104.456	1698.7
5178	35.830	-104.466	1695.4
5179	35.837	-104.481	1683.6
5180	35.844	-104.494	1682.5
5181	35.851	-104.508	1700.7
5182	35.858	-104.521	1727.6

Station Number	**Latitude**	**Longitude**	**Elevation (m)**
5183	35.866	-104.531	1755.5
5184	35.873	-104.540	1733.7
5185	35.880	-104.553	1744.7
5186	35.887	-104.580	1764.8
5187	35.895	-104.584	1761.0
5188	35.901	-104.584	1767.1
5189	35.909	-104.584	1770.2
5190	35.915	-104.584	1779.7
5191	35.922	-104.602	1768.7
5192	35.930	-104.611	1791.7
5193	35.937	-104.619	1798.6
5194	35.944	-104.628	1804.2
5195	35.951	-104.638	1814.0
5196	35.958	-104.649	1827.2
5197	35.965	-104.661	1849.4
5198	35.972	-104.673	1876.2
5199	35.979	-104.682	1884.4
5200	35.986	-104.690	1879.6
5201	35.994	-104.698	1899.7
5202	36.000	-104.705	1900.1
5203	36.008	-104.708	1871.1
5204	36.015	-104.703	1871.9
5205	36.022	-104.697	1866.2
5206	36.029	-104.695	1862.2
5207	36.036	-104.694	1860.3
5208	36.043	-104.693	1860.0
5209	36.050	-104.692	1862.4
5210	36.057	-104.691	1868.6
5211	36.064	-104.690	1877.9
5212	36.071	-104.689	1877.0
5213	36.078	-104.688	1884.0
5214	36.085	-104.688	1888.5
5215	36.092	-104.687	1894.8
5216	36.100	-104.687	1906.6
5217	36.106	-104.687	1915.5
5218	36.114	-104.687	1900.8
5219	36.121	-104.687	1885.0
5220	36.128	-104.686	1870.9
5221	36.135	-104.683	1857.4
5222	36.142	-104.679	1849.5
5223	36.150	-104.676	1841.2
5224	36.156	-104.674	1830.2
5225	36.163	-104.672	1833.3
5226	36.171	-104.669	1825.0
5227	36.178	-104.667	1817.0

Station Number	Latitude	Longitude	Elevation (m)
5228	36.185	-104.665	1812.2
5229	36.192	-104.663	1806.2
5230	36.199	-104.660	1801.8
5231	36.206	-104.659	1796.6
5232	36.213	-104.659	1788.8
5233	36.220	-104.657	1803.7
5234	36.227	-104.652	1804.0
5235	36.234	-104.645	1808.0
5236	36.241	-104.639	1794.9
5237	36.249	-104.635	1799.3
5238	36.256	-104.633	1804.7
5239	36.263	-104.630	1805.9
5240	36.270	-104.628	1815.7
5241	36.277	-104.627	1804.6
5242	36.283	-104.627	1801.0
5243	36.291	-104.627	1799.0
5244	36.298	-104.626	1786.9
5245	36.305	-104.626	1797.3
5246	36.312	-104.624	1766.7
5247	36.319	-104.621	1771.2
5248	36.326	-104.617	1760.2
5249	36.333	-104.614	1762.3
5250	36.341	-104.611	1762.1
5251	36.347	-104.608	1757.1
5252	36.355	-104.597	1739.0
5253	36.362	-104.597	1747.6
5254	36.369	-104.599	1757.4
5255	36.376	-104.608	1760.7
5256	36.383	-104.616	1761.0
5257	36.390	-104.628	1776.0
5258	36.397	-104.640	1777.8
5259	36.404	-104.649	1793.3
5260	36.412	-104.649	1790.6
5261	36.419	-104.646	1788.1
5262	36.426	-104.649	1798.1
5263	36.433	-104.649	1797.7
5264	36.440	-104.649	1811.2
5265	36.447	-104.649	1810.3
5266	36.454	-104.726	1840.4
5267	36.461	-104.736	1852.4
5268	36.468	-104.747	1853.9
5269	36.475	-104.756	1852.3
5270	36.482	-104.779	1863.5
5271	36.489	-104.780	1868.6
5272	36.496	-104.781	1877.2

Station Number	Latitude	Longitude	Elevation (m)
5273	36.503	-104.784	1879.6
5274	36.511	-104.785	1883.8
5275	36.518	-104.789	1898.5
5276	36.525	-104.790	1902.4
5277	36.532	-104.792	1909.5
5278	36.539	-104.794	1902.9
5279	36.546	-104.799	1919.6
5280	36.553	-104.804	1931.8
5281	36.560	-104.795	1919.5
5282	36.567	-104.785	1908.7
5283	36.574	-104.777	1900.5
5284	36.582	-104.794	1919.9
5285	36.588	-104.805	1929.8
5286	36.596	-104.813	1936.1
5287	36.603	-104.818	1946.0
5288	36.610	-104.821	1948.4
5289	36.617	-104.823	1980.7
5290	36.624	-104.825	1974.5
5291	36.631	-104.831	1984.7
5292	36.638	-104.837	1993.4
5293	36.645	-104.835	2001.4
1008	36.647	-104.836	2182.3
5294	36.652	-104.840	2020.4
5295	36.660	-104.843	2031.4
1007	36.663	-104.841	2182.3
5296	36.666	-104.846	2043.4
5297	36.673	-104.855	2061.9
1006	36.678	-104.854	2182.4
5298	36.681	-104.863	2079.7
5299	36.688	-104.870	2095.1
1005	36.690	-104.869	2182.5
5300	36.695	-104.870	2110.8
5301	36.701	-104.877	2120.5
1004	36.704	-104.878	2182.5
5302	36.709	-104.879	2136.1
5303	36.716	-104.880	2144.3
1003	36.719	-104.881	2182.5
5304	36.723	-104.885	2160.4
5305	36.730	-104.889	2171.0
1002	36.734	-104.889	2182.6
5306	36.737	-104.893	2184.4
5307	36.744	-104.898	2208.5
1001	36.748	-104.900	2182.6
5308	36.751	-104.902	2206.3
5309	36.759	-104.903	2219.8

Station Number	**Latitude**	**Longitude**	**Elevation (m)**
5310	36.766	-104.898	2260.2
5311	36.772	-104.899	2294.5
5312	36.779	-104.865	2125.6
5313	36.786	-104.865	2092.9
5314	36.793	-104.872	2101.6
5315	36.801	-104.883	2121.9
5316	36.808	-104.891	2131.9
5317	36.815	-104.898	2133.2
5318	36.822	-104.907	2154.5
5319	36.829	-104.914	2169.4
5320	36.837	-104.921	2182.2
5321	36.843	-104.923	2191.9
5322	36.851	-104.931	2195.9
5323	36.858	-104.945	2203.5
5324	36.865	-104.960	2217.4
5325	36.873	-104.968	2226.7
5326	36.879	-104.973	2243.6
5327	36.885	-104.978	2254.0
5328	36.893	-104.991	2265.3
5329	36.902	-104.998	2284.4
5330	36.907	-105.000	2296.8
5331	36.914	-105.004	2317.8
5332	36.921	-105.016	2354.5
5333	36.929	-105.021	2386.2
5334	36.935	-105.022	2413.1
5335	36.942	-105.025	2444.6
5336	36.950	-105.027	2473.0
5337	36.957	-105.033	2507.7
5338	36.963	-105.040	2543.2
5339	36.971	-105.039	2574.7
5340	36.978	-105.041	2615.7
5341	36.985	-105.045	2660.6
5342	36.992	-105.056	2762.2
5344	37.003	-105.059	1984.6
5345	36.997	-105.053	1934.6
5345	37.011	-105.053	2084.6
5346	37.019	-104.999	2184.3
5347	37.028	-105.003	2434.7
5348	37.035	-105.001	2411.0
5349	37.042	-105.001	2377.3
5350	37.049	-105.000	2356.0
5351	37.056	-105.006	2358.2
5352	37.063	-105.012	2377.8
5353	37.070	-105.018	2400.0
5354	37.077	-105.025	2413.5

Station Number	Latitude	Longitude	Elevation (m)
5355	37.084	-105.037	2472.2
5356	37.091	-105.038	2488.5
5357	37.099	-105.041	2462.9
5358	37.105	-105.041	2447.6
5359	37.113	-105.037	2438.1
5360	37.119	-105.032	2441.8
5361	37.127	-105.027	2427.9
5362	37.134	-105.024	2398.1
5363	37.141	-105.020	2369.1
5364	37.148	-105.018	2348.3
5365	37.155	-105.042	2454.8
5366	37.163	-105.043	2474.2
5367	37.169	-105.045	2503.3
5368	37.178	-105.046	2554.3
5369	37.184	-105.048	2591.2
5370	37.191	-105.044	2590.0
5371	37.198	-105.048	2610.7
5372	37.205	-105.050	2635.6
5373	37.212	-105.050	2629.9
5374	37.219	-105.049	2630.1
5375	37.226	-105.048	2624.5
5376	37.234	-105.048	2633.5
5377	37.241	-105.045	2607.2
5378	37.247	-105.045	2608.7
5379	37.253	-105.037	2598.6
5380	37.261	-105.039	2655.0
5381	37.268	-105.043	2698.5
5382	37.276	-105.045	2711.3
5383	37.283	-105.049	2720.8
5384	37.290	-105.052	2768.8
5385	37.297	-105.054	2772.9
5386	37.304	-105.057	2820.2
5387	37.310	-105.059	2845.0
5388	37.318	-105.068	2951.4
5389	37.325	-105.084	2946.7
5390	37.333	-105.091	2814.8
5391	37.340	-105.096	2718.9
5392	37.346	-105.100	2672.1
5393	37.354	-105.107	2614.4
5394	37.361	-105.106	2613.5
5395	37.369	-105.105	2552.9
5396	37.375	-105.105	2525.4
5397	37.381	-105.099	2518.4
5398	37.388	-105.093	2484.5
5399	37.396	-105.089	2453.6

Station Number	**Latitude**	**Longitude**	**Elevation (m)**
5400	37.403	-105.078	2404.2
6001	37.408	-105.072	2423.6
6002	37.413	-105.064	2391.7
6003	37.416	-105.056	2375.8
6004	37.422	-105.051	2350.7
6005	37.428	-105.046	2338.5
6006	37.434	-105.040	2329.5
6007	37.440	-105.036	2311.6
6008	37.448	-105.036	2289.2
6009	37.455	-105.033	2261.6
6010	37.461	-105.031	2248.5
6011	37.468	-105.026	2229.5
6012	37.475	-105.024	2205.9
6013	37.481	-105.021	2189.7
6014	37.488	-105.021	2173.8
6015	37.496	-105.020	2158.6
6016	37.503	-105.013	2137.7
6017	37.510	-105.016	2122.4
6018	37.515	-105.022	2133.1
6019	37.519	-105.031	2164.4
6020	37.522	-105.041	2180.1
6021	37.528	-105.047	2200.3
6022	37.534	-105.052	2222.4
6023	37.539	-105.058	2259.8
6024	37.541	-105.066	2258.9
6025	37.542	-105.073	2268.6
6026	37.545	-105.081	2292.4
6027	37.547	-105.090	2319.2
6028	37.550	-105.100	2336.7
6029	37.553	-105.109	2365.2
6030	37.554	-105.119	2401.0
6031	37.556	-105.128	2431.4
6032	37.559	-105.135	2458.2
6033	37.563	-105.144	2503.7
6034	37.567	-105.152	2531.4
6035	37.570	-105.160	2551.4
6036	37.574	-105.169	2595.4
6037	37.579	-105.174	2614.7
6038	37.586	-105.180	2659.7
6039	37.592	-105.184	2705.5
6040	37.600	-105.185	2757.4
6041	37.606	-105.183	2800.5
6042	37.613	-105.188	2845.6
6043	37.618	-105.195	2845.2
6044	37.625	-105.227	2758.3

Station Number	Latitude	Longitude	Elevation (m)
6045	37.631	-105.220	2715.8
6046	37.637	-105.214	2685.0
6047	37.644	-105.213	2642.4
6048	37.652	-105.214	2585.4
6049	37.659	-105.217	2550.7
6050	37.665	-105.222	2522.0
6051	37.671	-105.226	2484.5
6052	37.677	-105.231	2469.7
6053	37.684	-105.234	2428.6
6054	37.692	-105.234	2392.9
6055	37.698	-105.239	2395.3
6056	37.704	-105.244	2374.5
6057	37.707	-105.252	2367.9
6058	37.714	-105.252	2363.4
6059	37.722	-105.252	2336.7
6060	37.729	-105.253	2310.1
6061	37.736	-105.253	2280.5
6062	37.742	-105.253	2258.7
6063	37.748	-105.258	2264.3
6064	37.756	-105.259	2265.0
6065	37.763	-105.252	2248.3
6066	37.769	-105.252	2258.2
6067	37.777	-105.253	2266.5
6068	37.785	-105.250	2275.1
6069	37.791	-105.254	2239.5
6070	37.798	-105.254	2228.8
6071	37.806	-105.252	2221.4
6072	37.810	-105.256	2251.8
6073	37.815	-105.273	2257.6
6074	37.820	-105.280	2280.2
6075	37.824	-105.291	2286.2
6076	37.828	-105.301	2295.8
6077	37.835	-105.307	2317.7
6078	37.843	-105.309	2330.4
6079	37.850	-105.310	2342.1
6080	37.855	-105.316	2361.1
6081	37.862	-105.321	2374.1
6082	37.869	-105.323	2392.0
6083	37.875	-105.326	2413.3
6084	37.881	-105.333	2441.5
6085	37.887	-105.333	2457.9
6086	37.895	-105.332	2479.5
6087	37.901	-105.331	2502.9
6088	37.909	-105.329	2521.7
6089	37.915	-105.329	2528.7

Station Number	Latitude	Longitude	Elevation (m)
6090	37.923	-105.328	2545.8
6091	37.931	-105.329	2582.1
6092	37.938	-105.327	2600.8
6093	37.944	-105.328	2593.9
6094	37.951	-105.327	2581.1
6095	37.958	-105.330	2573.0
6096	37.965	-105.331	2564.7
6097	37.971	-105.336	2552.1
6098	37.977	-105.342	2542.3
6099	37.983	-105.348	2534.1
6100	37.988	-105.354	2529.7
6101	37.994	-105.359	2520.6
6102	38.000	-105.365	2507.4
6103	38.007	-105.370	2495.1
6104	38.014	-105.375	2492.6
6105	38.020	-105.380	2491.9
6106	38.027	-105.386	2482.6
6107	38.033	-105.391	2475.8
6108	38.037	-105.399	2459.5
6109	38.043	-105.403	2452.6
6110	38.049	-105.408	2444.6
6111	38.056	-105.412	2441.7
6112	38.061	-105.418	2436.1
6113	38.066	-105.424	2431.4
6114	38.069	-105.432	2422.2
6115	38.073	-105.440	2412.2
6116	38.078	-105.448	2420.1
6117	38.084	-105.453	2411.8
6118	38.091	-105.455	2404.7
6119	38.098	-105.457	2408.6
6120	38.105	-105.458	2401.2
6121	38.112	-105.460	2398.4
6122	38.120	-105.461	2391.5
6123	38.127	-105.463	2387.6
6124	38.133	-105.471	2378.1
6125	38.141	-105.471	2377.8
6126	38.147	-105.476	2366.6
6127	38.154	-105.479	2365.3
6128	38.161	-105.483	2362.5
6129	38.167	-105.489	2354.5
6130	38.173	-105.501	2344.1
6131	38.180	-105.498	2343.7
6132	38.187	-105.498	2356.0
6133	38.193	-105.498	2360.6
6134	38.201	-105.501	2377.0

Station Number	Latitude	Longitude	Elevation (m)
6135	38.208	-105.500	2393.5
6136	38.215	-105.499	2387.9
6137	38.222	-105.500	2403.5
6138	38.229	-105.502	2394.7
6139	38.236	-105.502	2366.7
6140	38.244	-105.501	2349.7
6141	38.251	-105.500	2339.9
6142	38.258	-105.500	2335.0
6143	38.265	-105.501	2329.4
6144	38.272	-105.501	2306.6
6145	38.280	-105.501	2316.3
6146	38.288	-105.491	2299.8
6147	38.295	-105.491	2314.0
6148	38.301	-105.487	2323.2
6149	38.309	-105.486	2332.9
6150	38.316	-105.487	2352.0
6151	38.324	-105.488	2399.6
6152	38.330	-105.485	2355.3
6153	38.338	-105.485	2329.8
6154	38.345	-105.483	2305.6
6155	38.352	-105.482	2280.0
6156	38.358	-105.473	2278.2
6157	38.366	-105.462	2238.1
6158	38.374	-105.457	2226.5
6159	38.381	-105.456	2208.0
6160	38.388	-105.455	2189.5
6161	38.395	-105.447	2158.9
6162	38.401	-105.442	2136.4
6163	38.410	-105.437	2095.9
6164	38.417	-105.413	2019.0
6165	38.424	-105.406	1987.4
6166	38.431	-105.400	1945.4
6167	38.438	-105.380	1873.7
6168	38.445	-105.373	1834.6
6169	38.453	-105.373	1814.9
6170	38.458	-105.376	1801.6
6171	38.466	-105.377	1782.4
6172	38.473	-105.378	1772.7
6173	38.481	-105.379	1745.5
6174	38.487	-105.371	1741.9
6175	38.494	-105.363	1812.9
6176	38.501	-105.351	1872.5
6177	38.508	-105.355	1871.2
6178	38.513	-105.362	1905.8
6179	38.519	-105.366	1927.8

Station Number	Latitude	Longitude	Elevation (m)
6180	38.523	-105.374	1903.3
6181	38.527	-105.382	1882.6
6182	38.530	-105.391	1874.8
6183	38.531	-105.403	1874.6
6184	38.536	-105.410	1880.3
6185	38.539	-105.418	1881.8
6186	38.545	-105.423	1911.7
6187	38.553	-105.425	1945.0
6188	38.559	-105.426	1974.7
6189	38.566	-105.426	2011.3
6190	38.572	-105.425	2059.8
6191	38.579	-105.419	2139.7
6192	38.586	-105.419	2181.4
6193	38.593	-105.425	2195.0
6194	38.599	-105.429	2207.5
6195	38.605	-105.435	2220.1
6196	38.610	-105.440	2235.4
6197	38.617	-105.445	2243.7
6198	38.620	-105.452	2250.1
6199	38.626	-105.458	2263.8
6200	38.633	-105.463	2274.2
6201	38.638	-105.469	2286.1
6202	38.645	-105.472	2317.6
6203	38.652	-105.473	2333.8
6204	38.659	-105.474	2372.0
6205	38.665	-105.479	2397.7
6206	38.670	-105.485	2426.1
6207	38.677	-105.489	2455.5
6208	38.684	-105.490	2488.1
6209	38.691	-105.493	2515.1
6210	38.697	-105.498	2552.3
6211	38.704	-105.503	2520.9
6212	38.710	-105.507	2537.7
6213	38.716	-105.511	2560.2
6214	38.722	-105.516	2511.1
6215	38.728	-105.523	2523.2
6216	38.734	-105.528	2536.4
6217	38.736	-105.538	2549.3
6218	38.740	-105.546	2561.5
6219	38.747	-105.548	2577.8
6220	38.753	-105.552	2589.7
6221	38.760	-105.557	2607.0
6222	38.765	-105.563	2620.1
6223	38.772	-105.567	2652.1
6224	38.779	-105.569	2672.2

Station Number	Latitude	Longitude	Elevation (m)
6225	38.784	-105.576	2690.4
6226	38.787	-105.584	2685.4
6227	38.792	-105.591	2705.2
6228	38.798	-105.598	2725.4
6229	38.804	-105.603	2751.1
6230	38.809	-105.609	2755.9
6231	38.814	-105.616	2791.5
6232	38.818	-105.623	2804.0
6233	38.824	-105.627	2829.6
6234	38.832	-105.630	2847.0
6235	38.838	-105.636	2873.7
6236	38.844	-105.642	2833.2
6237	38.848	-105.648	2808.9
6238	38.855	-105.653	2794.7
6239	38.861	-105.657	2785.4
6240	38.866	-105.665	2802.1
6241	38.872	-105.669	2805.6
6242	38.878	-105.675	2825.7
6243	38.884	-105.681	2832.4
6244	38.890	-105.685	2845.3
6245	38.895	-105.690	2828.6
6246	38.902	-105.695	2813.8
6247	38.909	-105.700	2814.1
6248	38.915	-105.704	2793.3
6249	38.922	-105.709	2773.9
6250	38.927	-105.714	2742.6
6251	38.934	-105.720	2722.9
6252	38.940	-105.721	2718.9
6253	38.948	-105.722	2720.2
6254	38.955	-105.722	2716.0
6255	38.963	-105.723	2717.2
6256	38.969	-105.727	2719.8
6257	38.975	-105.732	2719.9
6258	38.980	-105.738	2713.9
6259	38.985	-105.745	2715.4
6260	38.989	-105.753	2698.0
6261	38.994	-105.761	2681.8
6262	38.998	-105.770	2678.6
6263	39.003	-105.775	2683.1
6264	39.009	-105.781	2694.6
6265	39.015	-105.787	2690.0
6266	39.019	-105.791	2690.1
6267	39.022	-105.806	2693.8
6268	39.027	-105.816	2700.9
6269	39.033	-105.822	2710.8

Station Number	Latitude	Longitude	Elevation (m)
6270	39.038	-105.827	2720.1
6271	39.044	-105.835	2725.1
6272	39.048	-105.841	2734.1
6273	39.052	-105.847	2734.5
6274	39.058	-105.852	2744.1
6275	39.064	-105.856	2754.3
6276	39.071	-105.859	2752.6
6277	39.077	-105.864	2759.5
6278	39.084	-105.867	2766.9
6279	39.090	-105.873	2766.8
6280	39.095	-105.879	2772.8
6281	39.101	-105.885	2781.7
6282	39.107	-105.890	2787.8
6283	39.114	-105.894	2795.9
6284	39.119	-105.901	2801.8
6285	39.125	-105.906	2812.6
6286	39.131	-105.913	2822.1
6287	39.136	-105.919	2843.5
6288	39.142	-105.925	2853.4
6289	39.148	-105.930	2867.9
6290	39.154	-105.935	2881.8
6291	39.159	-105.939	2890.2
6292	39.166	-105.943	2881.8
6293	39.171	-105.950	2888.1
6294	39.176	-105.957	2899.8
6295	39.181	-105.964	2912.1
6296	39.186	-105.970	2925.6
6297	39.192	-105.977	2938.1
6298	39.197	-105.983	2952.8
6299	39.202	-105.989	2968.2
6300	39.207	-105.995	2983.8
6301	39.214	-105.994	2994.1
6302	39.221	-105.995	3006.7
6303	39.228	-106.009	3055.9
6304	39.233	-106.017	3069.9
6305	39.236	-106.025	3061.8
6306	39.240	-106.032	3074.8
6307	39.246	-106.038	3083.5
6308	39.254	-106.039	3100.1
6309	39.260	-106.042	3103.9
6310	39.266	-106.045	3113.1
6311	39.273	-106.050	3123.9
6312	39.278	-106.056	3134.9
6313	39.284	-106.051	3179.3
6314	39.293	-106.066	3157.8

Station Number	**Latitude**	**Longitude**	**Elevation (m)**
6315	39.300	-106.069	3176.3
6316	39.306	-106.066	3182.4
6317	39.314	-106.063	3191.1
6318	39.320	-106.061	3198.6
6319	39.328	-106.059	3201.3
6320	39.334	-106.061	3211.0
6321	39.341	-106.059	3231.9
6322	39.348	-106.064	3235.4
6323	39.355	-106.062	3412.8
6324	39.363	-106.062	3491.1
6325	39.370	-106.060	3391.2
6326	39.377	-106.058	3340.2
6327	39.385	-106.057	3242.5
6328	39.392	-106.053	3169.5
6329	39.399	-106.051	3136.8
6330	39.406	-106.048	3111.6
6331	39.413	-106.045	3088.6
6332	39.420	-106.044	3077.8
6333	39.428	-106.044	3051.6
6334	39.434	-106.043	3064.5
6335	39.442	-106.042	3027.5
6336	39.449	-106.039	3011.7
6337	39.456	-106.037	3000.4
6338	39.463	-106.035	2970.1
6339	39.469	-106.039	2960.6
6340	39.475	-106.044	2928.8
6341	39.485	-106.049	2903.0
6342	39.492	-106.045	2884.5
6343	39.499	-106.046	2870.3
6344	39.507	-106.048	2857.5
6345	39.514	-106.049	2845.0
6346	39.521	-106.047	2834.6
6347	39.528	-106.045	2813.6
6348	39.535	-106.043	2800.4
6349	39.541	-106.041	2788.1
6350	39.548	-106.041	2778.4
6351	39.554	-106.045	2767.8
6352	39.561	-106.051	2756.2
6353	39.568	-106.048	2756.2
6354	39.576	-106.045	2808.3
6355	39.582	-106.043	2853.6
6356	39.589	-106.044	2885.2
6357	39.599	-106.038	2776.8
6358	39.605	-106.043	2762.2
6359	39.610	-106.048	2746.9

Station Number	Latitude	Longitude	Elevation (m)
6360	39.614	-106.065	2746.0
6361	39.619	-106.076	2743.8
6362	39.626	-106.076	2665.3
6363	39.633	-106.081	2658.3
6364	39.642	-106.077	2644.8
6365	39.648	-106.079	2641.0
6366	39.655	-106.081	2636.8
6367	39.662	-106.085	2625.2
6368	39.669	-106.089	2618.7
6369	39.677	-106.096	2610.5
6370	39.683	-106.100	2604.1
6371	39.691	-106.104	2592.3
6372	39.697	-106.108	2588.1
6373	39.704	-106.111	2576.7
6374	39.712	-106.114	2573.6
6375	39.718	-106.122	2547.3
6376	39.724	-106.127	2569.0
6377	39.730	-106.137	2560.3
6378	39.738	-106.134	2560.4
6379	39.745	-106.133	2543.9
6380	39.752	-106.132	2529.0
6381	39.759	-106.138	2512.2
6382	39.765	-106.146	2510.9
6383	39.771	-106.149	2504.7
6384	39.779	-106.154	2492.7
6385	39.786	-106.157	2486.5
6386	39.792	-106.160	2474.3
6387	39.799	-106.166	2470.6
6388	39.803	-106.174	2462.4
6389	39.806	-106.185	2481.7
6390	39.810	-106.193	2472.4
6391	39.816	-106.201	2453.9
6392	39.822	-106.210	2433.3
6393	39.828	-106.215	2430.1
6394	39.833	-106.221	2428.0
6395	39.840	-106.228	2426.5
6396	39.848	-106.233	2420.2
6397	39.854	-106.238	2422.9
6398	39.858	-106.248	2431.7
6399	39.862	-106.255	2435.1
6400	39.869	-106.263	2441.6
6401	39.876	-106.274	2435.5
6402	39.882	-106.281	2437.4
6403	39.887	-106.289	2419.5
6404	39.891	-106.300	2415.1

Station Number	Latitude	Longitude	Elevation (m)
6405	39.896	-106.309	2423.1
6406	39.903	-106.315	2398.4
6407	39.909	-106.321	2381.0
6408	39.916	-106.327	2357.0
6409	39.923	-106.334	2348.7
6410	39.930	-106.339	2336.6
6411	39.938	-106.344	2332.1
6412	39.945	-106.346	2339.8
6413	39.953	-106.347	2331.1
6414	39.961	-106.349	2312.3
6415	39.969	-106.351	2293.3
6416	39.978	-106.354	2287.7
6417	39.985	-106.358	2276.6
6418	39.993	-106.362	2279.6
6419	39.999	-106.367	2263.6
6420	40.006	-106.374	2272.9
6421	40.013	-106.378	2245.8
6422	40.022	-106.377	2235.2
6423	40.030	-106.376	2253.6
6424	40.038	-106.374	2262.0
6425	40.044	-106.372	2227.7
7001	40.051	-106.371	2223.9
7002	40.057	-106.393	2221.2
7003	40.063	-106.401	2228.5
7004	40.070	-106.406	2245.4
7005	40.076	-106.411	2258.8
7006	40.082	-106.415	2267.0
7007	40.089	-106.418	2294.9
7008	40.096	-106.420	2310.3
7009	40.103	-106.423	2325.5
7010	40.109	-106.426	2346.9
7011	40.115	-106.428	2342.0
7012	40.122	-106.429	2328.2
7013	40.128	-106.430	2322.0
7014	40.134	-106.431	2322.3
7015	40.141	-106.428	2315.8
7016	40.147	-106.422	2307.5
7017	40.154	-106.415	2307.5
7018	40.161	-106.415	2298.0
7019	40.167	-106.417	2306.3
7020	40.173	-106.419	2290.2
7021	40.180	-106.421	2306.4
7022	40.187	-106.424	2294.0
7023	40.193	-106.426	2295.2
7024	40.199	-106.424	2288.2

Station Number	Latitude	Longitude	Elevation (m)
7025	40.206	-106.422	2282.7
7026	40.212	-106.427	2307.7
7027	40.219	-106.431	2322.4
7028	40.226	-106.436	2315.1
7029	40.232	-106.437	2303.5
7030	40.239	-106.439	2315.2
7031	40.245	-106.445	2311.7
7032	40.252	-106.452	2334.8
7033	40.258	-106.455	2331.1
7034	40.265	-106.460	2337.5
7035	40.270	-106.467	2345.7
7036	40.278	-106.469	2377.3
7037	40.284	-106.468	2364.8
7038	40.291	-106.481	2379.7
7039	40.297	-106.499	2389.6
7040	40.303	-106.505	2406.2
7041	40.310	-106.510	2421.9
7042	40.317	-106.521	2395.9
7043	40.323	-106.526	2416.0
7044	40.329	-106.534	2446.3
7045	40.336	-106.541	2464.1
7046	40.343	-106.550	2481.6
7047	40.350	-106.559	2478.5
7048	40.355	-106.569	2495.4
7049	40.362	-106.572	2535.7
7050	40.367	-106.576	2570.3
7051	40.375	-106.578	2617.4
7052	40.382	-106.578	2629.3
7053	40.388	-106.572	2601.5
7054	40.394	-106.561	2594.2
7055	40.401	-106.546	2593.8
7056	40.407	-106.543	2580.0
7057	40.414	-106.537	2583.8
7058	40.421	-106.529	2566.7
7059	40.427	-106.515	2557.4
7060	40.435	-106.477	2540.1
7061	40.440	-106.447	2583.5
7062	40.447	-106.445	2560.6
7063	40.453	-106.445	2542.1
7064	40.460	-106.446	2550.7
7065	40.466	-106.456	2529.8
7066	40.472	-106.455	2533.8
7067	40.479	-106.446	2533.3
7068	40.486	-106.438	2511.3
7069	40.493	-106.431	2501.4

Station Number	Latitude	Longitude	Elevation (m)
7070	40.499	-106.427	2497.6
7071	40.505	-106.424	2498.1
7072	40.512	-106.420	2504.2
7073	40.518	-106.417	2500.1
7074	40.525	-106.411	2495.5
7075	40.531	-106.405	2492.8
7076	40.537	-106.398	2483.9
7077	40.544	-106.398	2473.9
7078	40.551	-106.405	2481.8
7079	40.558	-106.407	2479.1
7080	40.564	-106.407	2476.4
7081	40.570	-106.407	2478.1
7082	40.577	-106.407	2477.5
7083	40.583	-106.407	2475.8
7084	40.589	-106.407	2472.9
7085	40.596	-106.407	2468.8
7086	40.602	-106.407	2468.6
7087	40.609	-106.407	2465.8
7088	40.616	-106.404	2463.1
7089	40.622	-106.400	2460.3
7090	40.629	-106.399	2458.2
7091	40.635	-106.395	2446.3
7092	40.642	-106.395	2456.4
7093	40.648	-106.396	2477.2
7094	40.654	-106.398	2504.7
7095	40.661	-106.396	2532.6
7096	40.666	-106.390	2511.0
7097	40.674	-106.408	2487.7
7098	40.681	-106.407	2474.8
7099	40.687	-106.409	2463.5
7100	40.694	-106.409	2443.5
7101	40.700	-106.456	2463.2
7102	40.707	-106.457	2474.1
7103	40.713	-106.457	2471.4
7104	40.720	-106.455	2479.2
7105	40.726	-106.453	2478.6
7106	40.733	-106.453	2465.0
7107	40.739	-106.479	2480.9
7108	40.745	-106.480	2461.1
7109	40.752	-106.480	2477.8
7110	40.759	-106.482	2477.4
7111	40.765	-106.485	2485.0
7112	40.771	-106.486	2463.7
7113	40.778	-106.490	2486.2
7114	40.785	-106.497	2505.1

Station Number	Latitude	Longitude	Elevation (m)
7115	40.791	-106.503	2536.2
7116	40.797	-106.511	2570.5
7117	40.804	-106.517	2543.7
7118	40.811	-106.520	2534.1
7119	40.817	-106.525	2552.5
7120	40.823	-106.533	2550.8
7121	40.830	-106.536	2553.6
7122	40.837	-106.540	2551.9
7123	40.843	-106.542	2553.4
7124	40.850	-106.543	2555.8
7125	40.856	-106.545	2559.9
7126	40.862	-106.545	2588.9
7127	40.868	-106.547	2574.6
7128	40.875	-106.544	2635.9
7129	40.882	-106.548	2589.6
7130	40.889	-106.562	2587.7
7131	40.895	-106.570	2607.9
7132	40.901	-106.593	2736.7
7133	40.909	-106.595	2810.2
7134	40.915	-106.598	2804.8
7135	40.921	-106.600	2764.1
7136	40.926	-106.602	2764.8
7137	40.933	-106.605	2736.2
7138	40.941	-106.604	2709.9
7139	40.946	-106.610	2700.5
7140	40.950	-106.614	2717.5
7141	40.958	-106.635	2772.4
7142	40.963	-106.634	2748.0
7143	40.971	-106.627	2690.8
7144	40.979	-106.629	2667.6
7145	40.986	-106.663	2912.0
7146	40.992	-106.718	2859.7
7147	41.001	-106.811	2559.4
7148	41.005	-106.818	2556.9
7149	41.012	-106.828	2568.6
7150	41.018	-106.847	2522.2
7151	41.025	-106.859	2555.8
7152	41.032	-106.854	2531.4
7153	41.038	-106.853	2572.8
7154	41.043	-106.844	2666.5
7155	41.051	-106.838	2663.4
7156	41.057	-106.830	2678.1
7157	41.064	-106.828	2719.2
7158	41.070	-106.838	2807.6
7159	41.077	-106.845	2822.3

Station Number	Latitude	Longitude	Elevation (m)
7160	41.083	-106.852	2845.8
7161	41.091	-106.857	2811.5
7162	41.099	-106.862	2760.7
7163	41.106	-106.866	2782.8
7164	41.113	-106.872	2795.7
7165	41.119	-106.880	2776.7
7166	41.123	-106.883	2762.3
7167	41.129	-106.885	2717.9
7168	41.135	-106.891	2695.1
7169	41.142	-106.883	2632.2
7170	41.149	-106.883	2587.8
7171	41.155	-106.941	2833.8
7172	41.162	-107.021	2820.0
7173	41.168	-107.216	2298.9
7174	41.175	-107.217	2332.8
7175	41.181	-107.217	2410.1
7176	41.187	-107.225	2383.0
7177	41.194	-107.241	2382.9
7178	41.201	-107.247	2380.4
7179	41.207	-107.253	2370.1
7180	41.214	-107.253	2366.5
7181	41.220	-107.253	2331.7
7182	41.226	-107.253	2315.0
7183	41.233	-107.254	2300.7
7184	41.239	-107.254	2293.8
7185	41.246	-107.253	2285.7
7186	41.253	-107.253	2272.0
7187	41.259	-107.253	2252.5
7188	41.265	-107.253	2232.3
7189	41.272	-107.255	2281.1
7190	41.279	-107.256	2259.9
7191	41.285	-107.258	2238.1
7192	41.292	-107.260	2272.4
7193	41.298	-107.259	2303.0
7194	41.305	-107.257	2332.7
7195	41.311	-107.256	2341.7
7196	41.317	-107.253	2324.9
7197	41.324	-107.254	2340.2
7198	41.331	-107.248	2362.5
7199	41.337	-107.240	2381.0
7200	41.343	-107.232	2408.5
7201	41.350	-107.227	2351.1
7202	41.357	-107.227	2335.4
7203	41.363	-107.224	2374.1
7204	41.370	-107.224	2355.4

Station Number	Latitude	Longitude	Elevation (m)
7205	41.376	-107.223	2391.9
7206	41.383	-107.222	2408.4
7207	41.389	-107.226	2434.8
7208	41.396	-107.230	2448.5
7209	41.402	-107.236	2456.3
7210	41.409	-107.237	2456.5
7211	41.415	-107.228	2433.2
7212	41.421	-107.224	2418.0
7213	41.428	-107.217	2372.5
7214	41.434	-107.210	2360.6
7215	41.441	-107.205	2342.5
7216	41.448	-107.202	2292.8
7217	41.454	-107.198	2228.8
7218	41.460	-107.195	2201.5
7219	41.467	-107.194	2177.6
7220	41.474	-107.197	2148.4
7221	41.480	-107.200	2152.5
7222	41.487	-107.201	2138.0
7223	41.493	-107.204	2143.8
7224	41.500	-107.208	2131.8
7225	41.506	-107.210	2143.1
7226	41.513	-107.211	2141.7
7227	41.519	-107.217	2144.4
7228	41.525	-107.226	2155.5
7229	41.533	-107.239	2132.1
7230	41.539	-107.241	2143.9
7231	41.545	-107.246	2161.0
7232	41.551	-107.251	2171.2
7233	41.558	-107.257	2166.9
7234	41.565	-107.262	2168.2
7235	41.571	-107.262	2160.9
7236	41.578	-107.263	2143.0
7237	41.584	-107.265	2142.3
7238	41.591	-107.267	2139.0
7239	41.597	-107.269	2147.2
7240	41.603	-107.271	2131.0
7241	41.610	-107.272	2152.9
7242	41.616	-107.272	2158.0
7243	41.623	-107.272	2146.9
7244	41.630	-107.277	2174.8
7245	41.636	-107.278	2159.4
7246	41.643	-107.275	2182.9
7247	41.649	-107.270	2196.9
7248	41.656	-107.266	2202.8
7249	41.661	-107.267	2191.8

Station Number	Latitude	Longitude	Elevation (m)
7250	41.669	-107.268	2181.2
7251	41.675	-107.269	2167.5
7252	41.682	-107.269	2181.5
7253	41.688	-107.268	2183.4
7254	41.694	-107.268	2185.6
7255	41.701	-107.268	2187.5
7256	41.707	-107.268	2196.3
7257	41.714	-107.268	2189.8
7258	41.721	-107.267	2178.3
7259	41.727	-107.264	2175.7
7260	41.734	-107.265	2174.1
7261	41.740	-107.265	2171.4
7262	41.746	-107.264	2152.9
7263	41.753	-107.266	2120.1
7264	41.760	-107.268	2090.1
7265	41.766	-107.265	2081.8
7266	41.772	-107.261	2068.8
7267	41.779	-107.250	2057.6
7268	41.787	-107.244	2046.6
7269	41.792	-107.235	2051.6
7270	41.800	-107.240	2073.8
7271	41.805	-107.232	2074.4
7272	41.812	-107.227	2066.9
7273	41.818	-107.227	2080.9
7274	41.825	-107.231	2084.2
7275	41.831	-107.236	2099.1
7276	41.838	-107.241	2106.2
7277	41.844	-107.246	2119.4
7278	41.850	-107.251	2116.2
7279	41.857	-107.255	2115.6
7280	41.863	-107.260	2121.3
7281	41.870	-107.265	2129.9
7282	41.877	-107.270	2140.2
7283	41.883	-107.275	2147.8
7284	41.889	-107.281	2159.0
7285	41.896	-107.286	2176.0
7286	41.902	-107.291	2188.4
7287	41.909	-107.297	2184.8
7288	41.915	-107.302	2178.9
7289	41.923	-107.308	2175.3
7290	41.928	-107.314	2175.6
7291	41.935	-107.324	2164.7
7292	41.941	-107.332	2146.2
7293	41.948	-107.337	2134.4
7294	41.955	-107.343	2107.9

Station Number	**Latitude**	**Longitude**	**Elevation (m)**
7295	41.961	-107.349	2087.7
7296	41.968	-107.354	2054.7
7297	41.974	-107.356	2011.1
7298	41.980	-107.357	1994.5
7299	41.988	-107.359	1978.6
7300	41.994	-107.362	1975.5
7301	42.000	-107.365	1973.0
7302	42.007	-107.367	1971.9
7303	42.013	-107.370	1972.4
7304	42.020	-107.372	1971.6
7305	42.026	-107.375	1972.0
7306	42.032	-107.377	1970.2
7307	42.039	-107.380	1970.9
7308	42.046	-107.383	1971.5
7309	42.052	-107.385	1971.2
7310	42.059	-107.388	1971.1
7311	42.065	-107.391	1971.5
7312	42.072	-107.393	1970.7
7313	42.078	-107.396	1969.3
7314	42.085	-107.399	1970.1
7315	42.091	-107.403	1970.9
7316	42.097	-107.408	1969.6
7317	42.104	-107.413	1972.3
7318	42.110	-107.418	1974.5
7319	42.117	-107.421	1974.2
7320	42.123	-107.423	1977.7
7321	42.130	-107.425	1976.1
7322	42.136	-107.427	1977.8
7323	42.143	-107.429	1976.8
7324	42.149	-107.431	1977.5
7325	42.156	-107.433	1978.1
7326	42.162	-107.435	1975.8
7327	42.169	-107.438	1985.4
7328	42.176	-107.443	1989.3
7329	42.182	-107.448	1992.6
7330	42.189	-107.454	1992.6
7331	42.195	-107.459	1994.4
7332	42.201	-107.463	1995.4
7333	42.208	-107.467	1997.5
7334	42.214	-107.471	2001.3
7335	42.221	-107.475	2006.9
7336	42.228	-107.472	2010.1
7337	42.234	-107.468	2019.4
7338	42.241	-107.464	2039.5
7339	42.247	-107.459	2038.2

Station Number	**Latitude**	**Longitude**	**Elevation (m)**
7340	42.254	-107.449	2035.3
7341	42.260	-107.444	2018.2
7342	42.267	-107.443	2000.7
7343	42.273	-107.447	1983.8
7344	42.279	-107.452	1985.5
7345	42.286	-107.457	1964.4
7346	42.292	-107.458	1958.7
7347	42.299	-107.460	1954.6
7348	42.306	-107.462	1944.3
7349	42.312	-107.463	1942.1
7350	42.318	-107.465	1955.0
7351	42.325	-107.466	1936.3
7352	42.332	-107.467	1936.9
7353	42.338	-107.467	1923.9
7354	42.344	-107.463	1913.6
7355	42.351	-107.458	1912.0
7356	42.358	-107.451	1900.4
7357	42.364	-107.445	1892.3
7358	42.371	-107.450	1907.0
7359	42.377	-107.457	1916.3
7360	42.384	-107.462	1914.7
7361	42.390	-107.466	1924.4
7362	42.397	-107.476	1940.1
7363	42.403	-107.488	1942.7
7364	42.410	-107.497	1959.8
7365	42.416	-107.503	1938.2
7366	42.422	-107.510	1919.8
7367	42.429	-107.518	1906.2
7368	42.436	-107.525	1924.5
7369	42.442	-107.532	1906.9
7370	42.448	-107.540	1898.0
7371	42.455	-107.556	1879.0
7372	42.462	-107.578	1869.9
7373	42.468	-107.596	1869.4
7374	42.474	-107.608	1871.3
7375	42.481	-107.629	1878.7
7376	42.487	-107.686	1902.5
7377	42.494	-107.681	1899.1
7378	42.501	-107.674	1898.0
7379	42.507	-107.657	1906.3
7380	42.514	-107.646	1884.1
7381	42.520	-107.639	1889.7
7382	42.527	-107.635	1895.0
7383	42.533	-107.631	1906.9
7384	42.540	-107.629	1904.5

Station Number	**Latitude**	**Longitude**	**Elevation (m)**
7385	42.546	-107.627	1909.5
7386	42.552	-107.625	1907.0
7387	42.559	-107.623	1907.3
7388	42.566	-107.618	1908.5
7389	42.572	-107.611	1921.2
7390	42.578	-107.605	1950.2
7391	42.585	-107.598	1952.0
7392	42.592	-107.600	1945.6
7393	42.598	-107.611	1947.9
7394	42.604	-107.621	1954.9
7395	42.611	-107.630	1977.0
7396	42.617	-107.638	2000.0
7397	42.624	-107.646	2014.4
7398	42.631	-107.660	1972.4
7399	42.637	-107.667	1980.2
7400	42.643	-107.672	2013.3
7401	42.650	-107.679	2028.6
7402	42.656	-107.693	2050.4
7403	42.663	-107.703	2065.8
7404	42.669	-107.711	2080.6
7405	42.676	-107.712	2087.7
7406	42.683	-107.708	2090.8
7407	42.689	-107.698	2093.7
7408	42.695	-107.689	2065.3
7409	42.702	-107.684	2042.4
7410	42.709	-107.683	2026.8
7411	42.715	-107.681	2015.5

APPENIDX F

Shot Point Locations for CD-RoM ‘99

Deployment 1

Shot Name	Time (UTC)	On Time	Wt. (kgs)	Latitude	Longitude	Elevation (m)
Gardner, CO (SP 3)	1999:218:06:00:31.30	N	2727	37.822	-105.284	2296.8
Hartsel, CO (SP 5)	1999:218:06:15:00.97	N	1818	38.926	-105.662	2725.1
Day Loma, WY (SP 10)	1999:218:06:30:00.19	N	4540	42.731	-107.668	1962.0
Wagon Mound, NM (SP 2)	1999:218:06:45:00.00	Y	1818	36.101	-104.659	1921.9
Fort Sumner, NM (SP 1)	1999:218:07:00:00.00	Y	2727	34.580	-104.241	1319.6
Kremmling, CO (SP7)	1999:218:07:15:00.00	Y	2727	40.013	-106.401	2315.6
Fairplay, CO (SP 6)	1999:218:07:45:00.72	N	0	39.240	-105.966	2985.5
Canon City, CO (SP 4)	1999:218:09:00:00.72	N	909	38.392	-105.460	2229.1

Deployment 2

Shot Name	Time (UTC)	On Time	Wt. (kgs)	Latitude	Longitude	Elevation (m)
Gardner, CO (SP 3)	1999:223:06:01:08.06	N	2727	37.822	-105.284	2296.814
Hartsel, CO (SP 5)	1999:223:06:15:00.14	N	1818	38.926	-105.662	2725.154
Day Loma, WY (SP 10)	1999:223:06:30:00.00	Y	2720	42.731	-107.668	1962.027
Rawlins, WY (SP 9)	1999:223:06:45:00.00	Y	1818	41.608	-107.183	2100.705
Kremmling, CO (SP 7)	1999:223:07:00:01.00	N	2727	40.013	-106.401	2315.613
Walden, CO (SP 8)	1999:223:07:15:00.00	Y	1818	40.801	-106.479	2473.247
Canon City, CO (SP 4)	1999:223:07:31:12.86	N	909	38.392	-105.460	2229.118
Fairplay, CO (SP 6)	1999:223:07:45:00.89	N	167	39.240	-105.966	2985.573

APPENDIX G

Strike Lines along CD-RoM ‘99 Profile for Density Modeling

Latitude	Longitude
34.000	-104.125
34.577	-104.250
34.690	-104.385
35.780	-104.447
36.008	-104.708
36.312	-104.623
38.086	-105.432
38.195	-105.457
38.265	-105.501
38.501	-105.351
38.891	-105.686
39.254	-106.039
39.605	-106.043
40.013	-106.378
40.297	-106.499
41.168	-107.216
41.812	-107.227
42.715	-107.681
45.543	-109.391

APPENDIX H

Gravity Points along CD-RoM '99 Profile for Density Modeling

Distance at Start (km)	Distance From Profile (km)	Gravity Value (mGal)	Latitude	Longitude
4.06	0.25	-157.16	34.036	-104.130
14.32	0.05	-155.81	34.127	-104.152
22.57	0.97	-159.44	34.198	-104.178
27.26	0.14	-163.25	34.241	-104.178
40.54	1.76	-171.96	34.362	-104.183
45.27	1.82	-172.47	34.404	-104.192
52.93	0.69	-175.04	34.467	-104.233
53.72	1.48	-174.12	34.473	-104.243
53.73	1.48	-174.29	34.473	-104.243
57.95	0.88	-176.52	34.512	-104.245
57.95	0.88	-176.52	34.512	-104.245
62.78	0.01	-177.09	34.556	-104.245
69.48	0.99	-178.05	34.598	-104.290
73.63	0.11	-179.89	34.632	-104.313
78.90	0.61	-181.80	34.669	-104.350
82.67	0.27	-181.21	34.691	-104.382
82.90	0.31	-181.21	34.691	-104.382
87.97	0.39	-183.18	34.736	-104.383
91.81	0.11	-184.43	34.771	-104.388
97.35	1.89	-184.07	34.821	-104.372
103.05	1.81	-180.88	34.871	-104.415
107.31	1.61	-185.04	34.909	-104.415
108.86	1.99	-185.84	34.923	-104.420
112.20	0.01	-185.14	34.954	-104.400
115.48	0.65	-186.20	34.983	-104.409
116.28	0.18	-185.77	34.991	-104.400
123.60	0.20	-180.27	35.056	-104.408
134.89	0.33	-174.80	35.158	-104.408
136.81	1.84	-174.59	35.176	-104.392
153.78	1.71	-171.22	35.327	-104.440
165.42	0.14	-173.28	35.432	-104.425
169.24	0.97	-170.27	35.467	-104.418
181.30	0.93	-177.60	35.575	-104.425
186.66	1.41	-181.50	35.623	-104.422
188.00	1.70	-179.18	35.635	-104.420
220.86	0.79	-176.66	35.885	-104.579
228.94	0.49	-201.57	35.946	-104.630
238.13	0.43	-211.29	36.007	-104.700
238.76	0.75	-211.29	36.007	-104.700
240.94	0.71	-210.44	36.026	-104.695

Distance at Start (km)	Distance From Profile (km)	Gravity Value (mGal)	Latitude	Longitude
247.92	0.06	-211.16	36.088	-104.685
250.97	0.73	-207.40	36.117	-104.686
251.32	0.82	-207.08	36.117	-104.668
259.98	0.36	-200.85	36.195	-104.660
306.79	1.19	-197.14	36.598	-104.737
310.51	0.71	-195.04	36.628	-104.756
317.70	0.10	-198.81	36.687	-104.792
318.65	0.14	-198.06	36.695	-104.796
330.97	1.97	-222.63	36.805	-104.820
334.89	1.85	-233.17	36.838	-104.837
339.70	1.38	-242.35	36.869	-104.889
344.75	1.72	-248.45	36.921	-104.876
352.66	1.18	-254.65	36.979	-104.937
358.33	1.11	-254.50	37.034	-104.934
372.79	0.93	-256.23	37.156	-104.992
372.91	0.76	-256.01	37.152	-105.010
381.91	0.87	-249.82	37.227	-105.046
382.85	1.20	-247.98	37.242	-105.027
383.04	0.65	-250.39	37.242	-105.034
385.08	0.99	-247.74	37.260	-105.038
387.62	0.82	-246.82	37.281	-105.050
391.07	0.28	-245.97	37.308	-105.069
392.43	0.60	-246.65	37.321	-105.071
393.86	0.36	-243.16	37.330	-105.087
397.52	0.68	-246.08	37.360	-105.104
399.53	0.60	-243.34	37.381	-105.098
412.02	0.95	-240.96	37.482	-105.163
420.38	1.67	-233.14	37.560	-105.168
422.79	0.77	-233.99	37.578	-105.187
423.92	0.73	-231.97	37.583	-105.207
424.01	0.80	-232.18	37.583	-105.208
428.58	0.92	-234.61	37.622	-105.227
431.08	1.40	-236.18	37.650	-105.212
433.44	1.17	-237.76	37.669	-105.224
437.03	1.07	-241.76	37.699	-105.239
440.60	1.28	-242.34	37.730	-105.251
442.71	1.77	-242.21	37.738	-105.292
442.90	0.25	-244.07	37.746	-105.271
450.01	1.61	-242.19	37.810	-105.284
452.59	0.06	-239.42	37.827	-105.311
452.60	0.06	-238.65	37.827	-105.311
455.98	0.10	-236.43	37.855	-105.326
458.58	0.42	-235.42	37.879	-105.330
459.27	0.41	-234.96	37.885	-105.333

Distance at Start (km)	Distance From Profile (km)	Gravity Value (mGal)	Latitude	Longitude
460.01	0.85	-234.28	37.892	-105.331
463.56	0.58	-220.90	37.922	-105.348
469.55	1.81	-226.20	37.965	-105.397
473.36	0.47	-225.95	38.001	-105.398
474.95	1.87	-220.53	38.022	-105.379
475.57	1.72	-219.98	38.027	-105.383
476.37	1.47	-221.53	38.032	-105.389
477.77	0.84	-224.45	38.042	-105.401
478.09	1.19	-228.86	38.039	-105.424
479.30	0.51	-225.23	38.054	-105.411
480.02	0.41	-226.28	38.057	-105.424
480.86	0.12	-224.43	38.065	-105.424
481.78	0.96	-227.58	38.077	-105.416
482.23	1.25	-226.56	38.074	-105.441
483.25	0.02	-226.00	38.086	-105.432
484.85	0.39	-223.41	38.101	-105.431
486.50	0.60	-222.93	38.114	-105.445
487.86	0.18	-220.23	38.127	-105.443
488.12	0.73	-225.06	38.130	-105.434
489.16	0.57	-224.86	38.139	-105.438
489.94	0.22	-224.80	38.145	-105.448
490.98	0.42	-221.62	38.155	-105.443
491.00	0.33	-223.19	38.154	-105.451
491.38	0.83	-223.09	38.157	-105.458
491.74	0.16	-218.36	38.161	-105.447
491.89	0.25	-219.98	38.162	-105.452
492.14	0.39	-219.40	38.164	-105.454
492.37	0.26	-216.81	38.166	-105.453
492.67	0.15	-208.79	38.170	-105.449
494.40	0.55	-211.28	38.184	-105.461
495.59	0.03	-209.88	38.195	-105.457
495.95	0.52	-212.93	38.196	-105.464
497.07	0.81	-211.04	38.210	-105.456
497.48	0.12	-212.59	38.211	-105.465
500.44	1.89	-214.58	38.227	-105.501
504.01	0.08	-211.65	38.263	-105.501
506.34	0.12	-207.32	38.284	-105.490
510.43	1.81	-200.25	38.324	-105.487
516.72	1.80	-206.01	38.375	-105.455
518.78	1.26	-202.66	38.379	-105.413
521.81	0.86	-213.12	38.412	-105.419
523.62	0.37	-216.29	38.424	-105.405
527.64	0.18	-221.45	38.455	-105.378
531.06	0.89	-226.58	38.486	-105.372

Distance at Start (km)	Distance From Profile (km)	Gravity Value (mGal)	Latitude	Longitude
533.10	0.21	-226.86	38.498	-105.350
534.48	0.05	-228.89	38.509	-105.359
537.68	0.97	-235.31	38.529	-105.388
544.35	0.36	-231.93	38.585	-105.418
546.98	0.35	-235.94	38.605	-105.435
548.02	0.30	-234.30	38.612	-105.442
550.49	0.10	-236.75	38.630	-105.460
552.13	0.01	-239.45	38.642	-105.471
553.14	0.64	-239.60	38.652	-105.472
555.81	0.78	-235.87	38.673	-105.487
557.42	1.68	-233.92	38.690	-105.489
559.75	0.80	-248.66	38.695	-105.528
565.56	0.98	-246.13	38.747	-105.548
566.30	0.62	-248.05	38.744	-105.568
570.26	1.19	-250.18	38.783	-105.576
574.27	0.55	-249.15	38.810	-105.608
577.48	0.48	-257.87	38.833	-105.630
580.36	0.12	-268.66	38.853	-105.652
582.66	0.08	-270.69	38.870	-105.667
585.51	0.01	-272.99	38.891	-105.686
587.27	0.20	-272.94	38.905	-105.696
588.86	0.40	-273.17	38.917	-105.705
590.46	0.49	-271.57	38.929	-105.716
591.20	0.36	-271.08	38.934	-105.722
592.81	0.47	-268.84	38.941	-105.741
597.13	0.05	-266.50	38.974	-105.767
598.78	0.36	-264.49	38.988	-105.775
600.06	0.49	-263.05	38.998	-105.783
601.45	0.47	-266.77	39.003	-105.801
603.55	0.39	-265.37	39.023	-105.808
604.04	0.20	-267.02	39.023	-105.817
605.01	0.14	-271.10	39.032	-105.820
606.13	0.14	-276.16	39.040	-105.828
607.06	0.02	-279.81	39.046	-105.836
608.00	0.20	-283.15	39.051	-105.844
609.08	0.18	-287.70	39.059	-105.852
610.04	0.37	-289.98	39.065	-105.860
611.01	0.18	-292.66	39.075	-105.862
612.12	0.41	-294.61	39.084	-105.867
613.06	0.43	-295.66	39.091	-105.874
614.06	0.39	-296.37	39.098	-105.881
615.01	0.18	-297.25	39.104	-105.890
617.92	0.48	-294.96	39.126	-105.907
618.08	0.46	-295.12	39.127	-105.909

Distance at Start (km)	Distance From Profile (km)	Gravity Value (mGal)	Latitude	Longitude
619.07	0.40	-294.80	39.134	-105.916
620.13	0.38	-294.29	39.142	-105.924
621.11	0.41	-295.14	39.149	-105.930
622.07	0.49	-295.37	39.156	-105.936
624.95	0.46	-293.74	39.177	-105.957
625.99	0.19	-294.24	39.183	-105.966
626.05	0.41	-294.49	39.180	-105.972
627.09	0.06	-294.14	39.190	-105.975
628.18	0.01	-295.24	39.197	-105.984
629.03	0.08	-294.43	39.203	-105.990
630.02	0.25	-294.64	39.212	-105.994
631.04	0.06	-295.27	39.217	-106.004
632.14	0.45	-296.51	39.228	-106.007
633.26	0.02	-297.54	39.234	-106.019
634.03	0.35	-298.70	39.237	-106.028
635.02	0.46	-299.25	39.244	-106.036
636.16	2.00	-299.98	39.255	-106.016
637.07	1.37	-302.87	39.263	-106.023
638.02	0.77	-306.61	39.272	-106.048
639.09	0.73	-308.46	39.281	-106.048
640.23	0.10	-309.62	39.292	-106.038
642.36	0.24	-313.28	39.311	-106.042
642.93	1.47	-317.75	39.316	-106.057
643.75	0.53	-316.25	39.323	-106.034
644.10	1.06	-319.98	39.326	-106.052
645.00	0.92	-319.60	39.334	-106.051
646.34	0.49	-319.20	39.347	-106.034
647.69	0.64	-315.28	39.359	-106.033
649.21	1.33	-322.96	39.372	-106.056
650.27	1.95	-321.78	39.382	-106.063
652.52	0.77	-317.86	39.402	-106.050
654.74	0.26	-318.99	39.422	-106.044
656.30	0.19	-319.46	39.436	-106.043
658.26	0.86	-317.02	39.454	-106.031
659.43	0.64	-317.84	39.464	-106.034
660.41	1.72	-315.62	39.473	-106.021
661.24	0.02	-317.08	39.481	-106.041
662.86	1.11	-313.79	39.495	-106.029
664.44	0.69	-312.08	39.509	-106.050
665.28	1.81	-312.13	39.517	-106.063
666.05	0.36	-311.04	39.524	-106.046
668.26	1.41	-307.96	39.544	-106.059
669.92	0.64	-307.54	39.559	-106.050
671.80	0.12	-308.90	39.576	-106.044

Distance at Start (km)	**Distance From Profile (km)**	**Gravity Value (mGal)**	**Latitude**	**Longitude**
673.64	0.92	-306.38	39.592	-106.054
674.73	0.98	-304.80	39.602	-106.054
675.39	0.73	-304.16	39.611	-106.038
676.27	0.37	-303.78	39.612	-106.054
678.34	0.79	-302.85	39.626	-106.071
679.59	0.28	-302.98	39.638	-106.074
681.00	0.16	-302.98	39.649	-106.081
682.99	0.43	-302.18	39.667	-106.088
684.43	0.44	-302.13	39.678	-106.097
686.17	0.75	-300.08	39.693	-106.105
687.63	0.89	-298.69	39.705	-106.112
689.33	1.00	-295.64	39.718	-106.122
690.92	0.03	-293.50	39.726	-106.142
691.68	1.27	-291.20	39.738	-106.134
692.86	1.05	-291.95	39.735	-106.164
694.35	0.65	-287.83	39.755	-106.157
696.79	1.52	-288.14	39.763	-106.193
697.43	1.42	-289.20	39.768	-106.196
700.66	1.61	-280.13	39.808	-106.186
701.97	1.49	-277.31	39.817	-106.196
702.55	0.24	-277.54	39.815	-106.212
703.49	0.68	-276.40	39.825	-106.213
704.76	0.17	-274.28	39.832	-106.226
706.75	1.46	-273.80	39.839	-106.255
707.52	0.08	-271.93	39.852	-106.244
708.20	1.22	-271.35	39.851	-106.262
715.61	0.28	-272.07	39.915	-106.293
721.12	1.46	-262.68	39.948	-106.345
722.15	1.04	-264.99	39.968	-106.327
723.29	0.43	-261.86	39.970	-106.348
724.81	0.18	-261.49	39.983	-106.355
726.72	0.07	-261.23	39.998	-106.365
727.50	0.49	-259.85	40.006	-106.366
728.14	0.04	-259.39	40.009	-106.375
729.86	0.50	-256.83	40.024	-106.377
730.67	0.46	-254.12	40.029	-106.390
731.45	1.36	-256.50	40.040	-106.373
733.75	0.72	-251.44	40.058	-106.388
735.56	0.33	-250.58	40.071	-106.407
739.18	0.49	-248.32	40.101	-106.422
741.70	0.23	-249.57	40.124	-106.428
742.08	0.59	-250.24	40.129	-106.420
743.24	0.16	-250.91	40.138	-106.429
744.59	0.74	-252.92	40.147	-106.444

Distance at Start (km)	Distance From Profile (km)	Gravity Value (mGal)	Latitude	Longitude
750.72	0.04	-254.74	40.201	-106.459
753.80	0.90	-256.94	40.230	-106.459
754.28	0.56	-255.93	40.230	-106.477
758.49	1.63	-255.49	40.272	-106.468
760.61	1.28	-254.94	40.290	-106.480
761.89	0.06	-254.45	40.297	-106.498
762.75	0.40	-255.88	40.302	-106.508
763.25	0.01	-254.24	40.307	-106.507
764.65	0.38	-252.06	40.316	-106.520
766.09	0.36	-251.05	40.327	-106.529
767.36	0.74	-248.30	40.335	-106.540
768.61	1.01	-246.07	40.344	-106.551
769.81	1.37	-244.44	40.351	-106.562
771.23	1.34	-242.13	40.362	-106.570
773.27	0.97	-242.53	40.379	-106.579
774.64	1.46	-240.86	40.388	-106.593
775.91	1.55	-240.55	40.397	-106.602
777.84	0.57	-236.29	40.416	-106.604
779.98	1.84	-236.87	40.427	-106.630
781.09	1.18	-242.69	40.449	-106.606
785.74	0.76	-233.18	40.476	-106.655
790.17	1.08	-238.53	40.508	-106.686
791.36	0.54	-240.42	40.525	-106.677
793.39	0.62	-241.37	40.535	-106.701
795.03	0.94	-242.88	40.555	-106.696
796.55	1.86	-247.53	40.571	-106.696
799.59	0.56	-255.70	40.588	-106.728
801.02	1.95	-265.25	40.587	-106.762
808.73	1.95	-241.70	40.664	-106.771
812.93	0.35	-229.78	40.689	-106.814
813.36	1.99	-231.08	40.681	-106.840
814.63	1.60	-231.19	40.692	-106.844
815.84	1.02	-234.76	40.704	-106.846
816.39	0.81	-234.60	40.717	-106.831
818.10	0.15	-234.46	40.726	-106.851
819.80	0.16	-231.11	40.740	-106.859
825.46	0.50	-232.36	40.785	-106.891
826.68	0.18	-230.27	40.793	-106.902
827.06	1.77	-235.01	40.803	-106.888
829.44	0.46	-238.20	40.811	-106.926
833.16	0.20	-239.14	40.842	-106.943
834.56	1.86	-233.03	40.843	-106.972
835.82	0.39	-227.03	40.864	-106.957
836.06	1.86	-224.25	40.872	-106.944

Distance at Start (km)	Distance From Profile (km)	Gravity Value (mGal)	Latitude	Longitude
838.15	0.11	-220.32	40.880	-106.975
839.51	1.09	-214.48	40.895	-106.974
840.59	1.72	-207.14	40.906	-106.974
843.82	1.75	-197.21	40.931	-106.994
845.85	1.69	-190.33	40.946	-107.008
857.13	1.74	-191.87	41.016	-107.114
868.30	0.07	-201.74	41.110	-107.166
870.16	0.71	-202.44	41.127	-107.172
872.11	0.33	-203.92	41.140	-107.188
874.11	1.20	-206.84	41.148	-107.216
875.23	0.68	-205.31	41.159	-107.218
876.66	0.03	-200.55	41.174	-107.216
878.42	0.86	-196.80	41.190	-107.227
879.81	2.62	-197.28	41.202	-107.248
881.43	2.88	-192.86	41.216	-107.251
883.08	2.89	-188.25	41.231	-107.252
885.26	2.75	-186.92	41.251	-107.250
887.24	0.19	-186.39	41.269	-107.220
892.71	2.69	-185.94	41.318	-107.251
894.53	1.90	-184.47	41.334	-107.242
896.30	0.90	-185.44	41.350	-107.230
897.89	0.67	-185.98	41.365	-107.227
899.98	0.41	-188.80	41.384	-107.225
900.94	0.78	-190.13	41.392	-107.210
901.64	1.32	-195.34	41.398	-107.236
902.25	0.30	-195.73	41.404	-107.216
903.36	1.08	-198.36	41.414	-107.233
905.09	0.26	-198.46	41.430	-107.217
906.33	1.10	-200.66	41.441	-107.207
908.01	1.77	-201.77	41.456	-107.200
909.40	1.93	-203.27	41.469	-107.198
910.88	1.68	-203.89	41.482	-107.201
912.41	1.18	-204.46	41.496	-107.207
913.89	0.87	-205.19	41.509	-107.211
915.90	0.47	-206.30	41.527	-107.228
916.67	1.55	-207.21	41.534	-107.241
918.01	1.99	-208.23	41.546	-107.246
919.28	2.64	-210.61	41.557	-107.254
924.34	1.50	-218.70	41.603	-107.205
932.85	0.99	-225.70	41.679	-107.237
939.55	1.38	-222.40	41.739	-107.242
940.37	1.10	-221.97	41.747	-107.239
941.06	0.63	-221.18	41.753	-107.234
942.25	0.03	-220.26	41.764	-107.226

Distance at Start (km)	Distance From Profile (km)	Gravity Value (mGal)	Latitude	Longitude
943.57	0.40	-221.02	41.776	-107.222
944.59	0.56	-223.41	41.785	-107.233
945.27	0.62	-221.16	41.791	-107.219
946.69	0.53	-220.02	41.804	-107.233
947.99	0.20	-221.17	41.816	-107.226
949.66	0.22	-221.84	41.830	-107.233
951.27	0.13	-221.51	41.843	-107.244
952.75	0.20	-221.78	41.855	-107.251
954.29	0.43	-221.00	41.867	-107.260
955.85	0.71	-219.22	41.879	-107.270
956.93	0.78	-218.68	41.888	-107.275
957.55	1.14	-217.61	41.892	-107.282
959.25	1.37	-216.32	41.906	-107.291
961.01	1.48	-214.06	41.921	-107.300
962.89	2.21	-215.60	41.934	-107.316
964.51	2.98	-215.79	41.945	-107.332
970.79	0.40	-221.10	42.006	-107.329
971.38	1.80	-221.13	42.018	-107.306
977.33	1.68	-231.41	42.058	-107.371
978.07	0.33	-232.26	42.068	-107.359
978.85	1.02	-232.32	42.079	-107.347
979.51	2.45	-232.05	42.089	-107.333
994.06	0.70	-220.31	42.202	-107.430
995.04	1.81	-220.13	42.207	-107.447
998.88	2.09	-216.77	42.238	-107.467
999.95	0.66	-215.89	42.252	-107.455
1000.98	0.55	-212.48	42.264	-107.445
1002.50	1.27	-210.44	42.279	-107.444
1004.04	1.80	-210.66	42.294	-107.444
1005.41	1.32	-212.56	42.304	-107.455
1006.76	1.61	-212.55	42.316	-107.458
1008.37	2.12	-210.98	42.331	-107.459
1015.65	1.65	-224.12	42.381	-107.533
1016.25	0.15	-222.42	42.391	-107.518
1017.25	2.34	-212.23	42.407	-107.494
1018.57	1.96	-207.94	42.417	-107.504
1020.01	1.47	-203.19	42.427	-107.516
1021.75	0.78	-193.83	42.440	-107.531
1023.02	0.48	-186.08	42.450	-107.540
1024.24	0.68	-185.57	42.456	-107.558
1025.15	1.68	-186.76	42.461	-107.574
1026.17	2.72	-185.74	42.466	-107.590
1029.41	2.97	-182.51	42.493	-107.607
1030.18	0.06	-175.43	42.508	-107.577

Distance at Start (km)	Distance From Profile (km)	Gravity Value (mGal)	Latitude	Longitude
1030.34	0.94	-172.80	42.513	-107.566
1030.83	0.27	-171.72	42.513	-107.582
1032.45	0.10	-174.19	42.527	-107.587
1032.61	0.26	-172.24	42.528	-107.589
1033.06	0.67	-167.57	42.535	-107.581
1035.58	0.96	-168.13	42.551	-107.610
1035.75	0.05	-166.15	42.555	-107.600
1036.16	2.46	-169.35	42.551	-107.630
1037.01	1.12	-166.22	42.570	-107.592
1037.36	1.13	-166.44	42.565	-107.620
1038.68	0.00	-163.80	42.580	-107.612
1039.21	1.35	-163.51	42.589	-107.599
1041.88	0.47	-166.43	42.609	-107.621
1042.28	0.05	-171.42	42.610	-107.628
1043.01	2.53	-169.26	42.609	-107.660
1044.60	1.02	-166.76	42.627	-107.649
1046.33	2.70	-163.21	42.653	-107.614
1048.79	1.28	-162.31	42.669	-107.641
1052.25	0.80	-165.22	42.692	-107.680
1052.70	0.36	-167.48	42.699	-107.668
1056.16	3.88	-166.17	42.714	-107.732
1057.34	1.04	-169.02	42.733	-107.705
1058.54	1.63	-171.35	42.753	-107.681
1061.03	3.68	-178.99	42.780	-107.670
1070.54	4.97	-196.14	42.864	-107.700
1071.31	1.41	-197.53	42.858	-107.744
1072.68	5.00	-201.68	42.882	-107.710
1079.42	4.45	-210.89	42.904	-107.849
1113.41	4.79	-232.46	43.218	-107.908
1116.32	0.49	-231.02	43.224	-107.982
1125.28	1.48	-229.22	43.305	-108.003
1134.62	4.34	-225.27	43.362	-108.115
1136.18	4.70	-220.27	43.373	-108.127
1142.51	0.36	-189.74	43.441	-108.108
1145.17	4.51	-192.58	43.448	-108.168
1146.00	4.24	-190.91	43.456	-108.169
1147.78	3.54	-187.59	43.473	-108.170
1148.68	2.83	-184.05	43.483	-108.166
1149.63	1.64	-182.08	43.495	-108.157
1149.96	1.58	-183.14	43.498	-108.158
1151.41	2.13	-184.11	43.508	-108.172
1152.76	2.40	-183.85	43.519	-108.181
1154.13	1.40	-180.41	43.543	-108.145
1156.96	2.38	-179.56	43.553	-108.202

Distance at Start (km)	Distance From Profile (km)	Gravity Value (mGal)	Latitude	Longitude
1159.21	1.56	-178.90	43.575	-108.203
1160.56	1.86	-176.91	43.585	-108.213
1161.05	0.84	-175.70	43.593	-108.204
1163.38	3.83	-178.24	43.601	-108.250
1164.23	1.01	-175.74	43.618	-108.222
1166.75	1.09	-174.54	43.647	-108.210
1169.32	2.63	-173.88	43.673	-108.205
1183.61	3.35	-186.46	43.770	-108.344
1192.88	1.86	-198.14	43.852	-108.372
1211.92	1.69	-217.29	44.010	-108.465
1223.94	3.56	-216.14	44.102	-108.546
1235.27	4.54	-215.23	44.192	-108.614
1248.42	4.11	-218.25	44.302	-108.675
1252.54	3.60	-220.16	44.338	-108.690
1255.25	4.09	-216.59	44.388	-108.615
1258.35	0.33	-219.71	44.400	-108.674
1271.23	1.78	-221.34	44.499	-108.763
1293.08	2.86	-216.45	44.696	-108.820
1294.64	4.63	-222.92	44.682	-108.915
1296.69	1.30	-216.81	44.720	-108.857
1299.67	3.90	-220.84	44.726	-108.932
1309.40	2.31	-220.60	44.812	-108.963
1318.20	3.46	-220.28	44.880	-109.022
1327.47	4.24	-210.00	44.953	-109.078
1334.31	0.22	-216.03	45.026	-109.061
1336.11	1.87	-207.98	45.047	-109.052
1338.45	4.34	-202.35	45.075	-109.035
1342.56	4.01	-209.85	45.078	-109.153
1350.03	2.87	-184.87	45.165	-109.112
1351.06	0.81	-187.34	45.160	-109.160
1352.01	3.39	-189.63	45.158	-109.195
1353.83	3.87	-189.71	45.172	-109.210
1355.19	3.27	-182.91	45.185	-109.210
1356.13	1.28	-175.29	45.200	-109.192
1357.14	4.05	-159.59	45.228	-109.135
1358.89	1.66	-160.13	45.233	-109.172
1360.32	3.42	-165.78	45.227	-109.238
1362.13	2.90	-159.52	45.243	-109.242
1363.23	1.27	-157.20	45.258	-109.228
1365.69	1.40	-151.57	45.288	-109.210
1367.77	2.39	-154.26	45.292	-109.265
1368.66	4.85	-156.55	45.290	-109.298
1369.94	4.99	-154.75	45.300	-109.307
1370.80	1.89	-151.13	45.318	-109.275

Distance at Start (km)	Distance From Profile (km)	Gravity Value (mGal)	Latitude	Longitude
1372.34	0.35	-148.90	45.337	-109.265
1374.51	1.60	-145.90	45.362	-109.253
1376.59	2.60	-148.55	45.363	-109.313
1379.57	1.56	-146.81	45.392	-109.317
1381.54	1.74	-143.64	45.420	-109.288
1389.00	3.22	-141.60	45.487	-109.310
1389.01	0.91	-145.10	45.472	-109.358
1392.49	0.06	-146.60	45.503	-109.367
1395.30	1.37	-148.32	45.522	-109.397
1396.84	4.80	-150.54	45.522	-109.445

CURRICULUM VITAE

Catherine Mary Snelson was born on December 13, 1967 in Chicago, Illinois. The daughter of Mary Bishop and David and Dee Snelson, she graduated from St. Edwards Central High School, Elgin, Illinois, in May 1985. After several years of trying to focus, she received her Associates of Science degree from the College of DuPage, Glen Ellyn, Illinois, in June 1992. She then went on to receive her Bachelor of Science degree in Geology from California State University at Hayward, Hayward, California, in June 1995. She received her Master of Science degree in Geophysics from the University of Texas at El Paso, El Paso, Texas, in May 1998. She started her work toward a doctoral degree in the spring of 1998 continuing at the University of Texas at El Paso. While pursuing her studies, she worked as a research assistant and teaching assistant, doing various types of field work where she enhanced her blasting and acquisition expertise. She has had the opportunity to travel abroad and nationally for several seismic experiments. In addition, she taught undergraduate introductory lab courses as well as serving as a computer teaching assistant. During her time with the department, she has presented her graduate work at several regional and national meetings. Catherine completed the Doctoral program in the fall of 2001.

Permanent address:

Department of Geoscience
University of Nevada Las Vegas
4505 Maryland Parkway
Las Vegas, NV 89154-4010

This dissertation was typed by Catherine Mary Snelson